



NATIONAL TECHNICAL UNIVERSITY OF ATHENS
SCHOOL OF APPLIED MATHEMATICAL AND PHYSICAL SCIENCES
DEPARTMENT OF PHYSICS

DOCTORAL DISSERTATION

Investigation of Plasma Facing Materials at JET Tokamak

PAVLOS TSAVALAS

ADVISORY COMMITTEE

M. Kokkoris,
Professor, National Technical University of Athens

K. Mergia,
Research Director, NCSR "Demokritos"

A. Lagoyannis,
Research Director, NCSR "Demokritos"

ΑΘΗΝΑ, 2023

Contents

Contents.....	i
Acknowledgments.....	iii
List of publications	iv
Peer Reviewed International Journals	iv
Proceedings of National Conferences.....	iv
Presentations at International Conferences.....	v
Presentations at National Conferences	v
Abstract.....	vi
Περίληψη	viii
Abbreviations	x
Chapter 1: Introduction	1
1.1 Plasma – Wall Interaction: Physical Mechanisms.....	7
1.2 Plasma – ILW JET Tokamak First Wall Interaction	10
1.3 Aim of the Current Work	14
Chapter 2: Methodology: Principles and Experimental Setups	15
2.1 Ion Beam Analysis.....	15
2.1.1 Rutherford Backscattering Spectroscopy	15
2.1.2 Nuclear Reaction Analysis.....	20
2.1.3 Particle-Induced X-Ray Emission.....	21
2.1.4 IBA Experimental Setup	21
2.2 X-Ray Fluorescence Spectroscopy.....	26
2.2.1 XRF Physical Principles.....	27
2.2.2 XRF Experimental Setup.....	30
2.3 Scanning Electron Microscopy	35
2.3.1 SEM Experimental Setup	36
2.4 X-Ray Diffraction	38
4.4.1 X-ray Diffraction Setup.....	40
Chapter 3: Cross Sections of Deuteron Reaction on Beryllium.....	42
3.1 Experimental Setup.....	42
3.1 Methodology.....	43
3.2 Proton Beam Measurements.....	44
3.3 Oxygen Beam Measurements.....	46
3.4 Deuteron Beam Measurements.....	47
3.5 Benchmarking	68
3.6 Conclusions	69

Chapter 4: Sample Description	70
4.1 Be Samples	70
4.1.1 Beryllium Marker Samples Exposed to ILW1 or ILW2 Campaign	70
3.1.2 Samples from Beryllium Tiles Exposed to ILW3 or ILW1-3 Campaigns	71
4.2 Tungsten Lamellae	73
Chapter 5: Results from Beryllium Tiles	76
5.1 Be samples From the Limiters After ILW1 or ILW2	76
5.1.1 Carbon Amount and Spatial Distribution	76
5.1.2 Deuterium Retention and Spatial Distribution	83
5.1.3 Deuterium Retention Versus Carbon Deposition	87
5.1.4 Heavy Element Distribution	90
5.1.5 X-ray Fluorescence Spectroscopy Results	93
5.1.6 Surface Morphology and Stoichiometry	94
5.1.7 X-ray Diffraction Results	114
5.1.8 Summary and Conclusions	115
5.2 JET Tokamak Main Chamber After ILW1-3 and ILW3	115
5.2.1 Carbon and Oxygen Quantification	116
5.2.2 X-ray fluorescence spectroscopy results	118
5.2.3 Surface Morphology and Stoichiometry	120
5.2.4 X-ray Diffraction Results	131
5.2.5 Summary and Conclusions	131
Chapter 6: JET Tokamak Divertor Lamellae	132
6.1 Carbon, Beryllium and Oxygen Deposition	132
6.2 X-ray Fluorescence Spectroscopy Results	138
6.3 Surface Morphology and Stoichiometry	139
6.4 X-ray Diffraction Results	164
6.5 Conclusions	164
Chapter 7: Summary, Conclusions and Future Perspectives	166

Acknowledgments

I would like to express my gratitude to my supervisor Dr Konstantina Mergia for the help, the guidance and the encouragement throughout the preparation of this work. I would also like to thank Dr Anastasios Lagoyannis for the guidance in order to understand the theory of ion beam analysis and to carry out and analyze the experimental part. Additionally, I would like to thank Professor Michael Kokkoris who was always available to answer my questions.

I would like to express my thankfulness to Dr Spyros Messoloras for his advices and the urging to seek the deeper understanding and knowledge of physics. I would like to thank Dr George Provatas, Dr Stjepko Fazinic and all the technical staff of Ruder Boskovic Institute, Croatia, for the hospitality during my visit to Zagreb and the guidance in order to carry out and analyse the experiments with ^3He beam. Additionally, I would like to thank the electron microscopy laboratory head, Dr N. Boukos and his researcher group for granting me access to the SEM facility and their help during the experiments. I would like to thank Dr Michael Axiotis and the technical staff of the TANDEM accelerator at the Institute of Nuclear and Particle Physics of NCSR "Demokritos" for the excellent cooperation in order to carry out the ion beam experiments. Last but not least, I would like to thank all the FTG members for the excellent collaboration.

This work has been carried out within the framework of the EUROfusion Consortium and has received funding from the Euratom research and training programme 2014-2018, 2019-2020 and 2021-2025 under Grant Agreements Nos. 633053 and 101052200. The views and opinions expressed herein do not necessarily reflect those of the European Commission. The funding from the General Secretariat of Research and Innovation of the National Programme of the Controlled Thermonuclear Fusion of the Hellenic Republic is acknowledged. Furthermore, the current thesis was supported by "CALIBRA/EYIE" (MIS 5002799) which is implemented under the Action "Reinforcement of the Research and Innovation Infrastructure", funded by the Operational Program "Competitiveness, Entrepreneurship and Innovation" (NSRF 2014-2020) and co-financed by Greece and the European Union (European Regional Development Fund).

List of publications

Peer Reviewed International Journals

- **P. Tsavalas**, A. Lagoyannis, K. Mergia, M. Axiotis, S. Harissopulos, G. Provas, S. Fazinić, T. Tadić, A. Widdowson, M. Rubel and JET Contributors, “Fuel retention and carbon deposition on beryllium marker tiles from JET tokamak main chamber limiters investigated by ion beam analysis”, Nucl. Fusion 62 (2022) 126070 <https://doi.org/10.1088/1741-4326/ac9cf0>
- **P. Tsavalas**, A. Lagoyannis, K. Mergia, E. Ntemou, C.P. Lungu, “Differential cross sections of the deuteron reactions on beryllium at energies and angles suitable for nuclear reaction analysis”, Nucl. Instr. Meth. B 479 (2020) 205-210 <https://doi.org/10.1016/j.nimb.2020.07.002>
- E. Ntemou, M. Kokkoris, A. Lagoyannis, K. Preketes-Sigalas, **P. Tsavalas**, “Differential elastic scattering cross sections for deuterons on ^9Be , at energies and angles suitable for elastic backscattering spectroscopy” Nucl. Instr. Meth. B. 459 (2019) 90-93 <https://doi.org/10.1016/j.nimb.2019.08.032>
- A. Psaltis, A. Khaliel, E-M. Assimakopoulou, A. Kanellakopoulos, V. Lagaki, M. Lykiardopoulou, E. Malami, **P. Tsavalas**, A. Zyriliou, T.J. Mertzimekis, “Cross-section measurements of radiative proton-capture reactions in Cd-112 at energies of astrophysical interest”, Physical Review C, Phys. Rev. C 99 (2019) 065807 <https://doi.org/10.1103/PhysRevC.99.065807>
- **P. Tsavalas**, A. Lagoyannis, K. Mergia, M. Rubel, K. Triantou, S. Harissopulos, M. Kokkoris, P. Petersson and JET Contributors, “Be ITER-like wall at the JET tokamak under plasma”, Phys. Scr. **T170** (2017) 014049, <https://doi.org/10.1088/1402-4896/aa8ff4>
- A. Lagoyannis, **P. Tsavalas**, K. Mergia, G. Provas, K. Triantou, E. Tsompoulou, P. Petersson, M. Rubel, S. Harissopulos, T.J. Mertzimekis, and JET-EFDA Contributors, “Surface Analysis of the ITER-like wall divertor tiles at JET tokamak”, Nucl. Fusion **57** (2017) 0760273 <https://doi.org/10.1088/1741-4326/aa6ec1>
- 229 publications in peer-reviewed journals as JET contributor

Proceedings of National Conferences

- **P. Tsavalas**, A. Lagoyannis, K. Mergia, E. Ntemou, C.P. Lungu, “Differential Cross Sections of $^9\text{Be}(d,p_0)^{10}\text{Be}$, $^9\text{Be}(d,p_1)^{10}\text{Be}$, $^9\text{Be}(d,\alpha_0)^7\text{Li}$ and $^9\text{Be}(d,\alpha_1)^7\text{Li}$ reactions”, 27th Symposium of the Hellenic Nuclear Physics Society, Athens, 8-9 June 2018 <https://doi.org/10.12681/hnps.1811>
- E. Ntemou, M. Kokkoris, A. Lagoyannis, C. Lungu, K. Mergia, K. Preketes-Sigalas, P. Tsavalas, “First results of the differential cross sections of $\text{Be}(d,d_0)$ at energies and angles suitable for Elastic Backscattering Spectroscopy” , 27th Symposium of the Hellenic Nuclear Physics Society, Athens, 8-9 June 2018 <https://doi.org/10.12681/hnps.1812>
- **P. Tsavalas**, A. Lagoyannis, K. Mergia, K. Triantou, S. Harissopulos, M. Rubel, P. Petersson, M. Kokkoris and JET Contributors, “Investigation of JET ITER-Like Wall Be Marker Tiles”, 26th Symposium of the Hellenic Nuclear Physics Society, Anavyssos, Greece, 9-10 June 2017 <https://doi.org/10.12681/hnps.1965>

Presentations at International Conferences

- **P. Tsavalas**, A. Lagoyannis, M. Axiotis, Z. Kotsina, M. Rubel, A. Widdowson and JET Contributors, “Investigation of the ILW JET Tokamak divertor W lamellae after plasma exposure”, FusNet International Conference, 22-23 November, 2021, remote connection
- **P. Tsavalas**, K. Mergia, A. Lagoyannis, M. Axiotis, Z. Kotsina, M. Rubel, A. Widdowson and JET Contributors, “Investigation of the ILW JET Tokamak divertor W lamellae after plasma exposure”, 18th International Conference on Plasma-Facing Materials and Components for Fusion Applications, 17 – 21 May 2021, remote connection
- **P. Tsavalas**, G. Provas, M. Vuksic, S. Fazinic, A. Lagoyannis, K. Mergia, T. Tadic, M. Rubel, A. Widdowson and JET Contributors, “Investigation of Be Marker Tiles using ³He micro – beam”, 17th International Conference on Plasma-Facing Materials and Components for Fusion Applications, 20-24 May 2019, Eindhoven, the Netherlands
- **P. Tsavalas**, A. Lagoyannis, K. Mergia, M. Kokkoris, M. Rubel, P. Petersson and JET Contributors, “Investigation of JET ITER-like Wall Be Marker Tiles”, FuseNet International Conference, 6-9 November, 2018, Cadarache, France
- **P. Tsavalas**, A. Lagoyannis, K. Mergia, K. Triantou, M. Kokkoris, S. Harissopulos, M. Rubel, P. Petersson and JET Contributors, “Investigation of the JET ITER-Like Wall Be Marker Tiles”, 16th International Conference on Plasma-Facing Materials and Components for Fusion Applications, 16 – 19 May 2017, Neuss/Dusseldorf, Germany

Presentations at National Conferences

- **P. Tsavalas**, K. Mergia, A. Lagoyannis, M. Axiotis, Z. Kotsina, M. Rubel and A. Widdowson, “Investigation of the JET Tokamak divertor W lamellae after plasma exposure”, 29th Symposium of the Hellenic Nuclear Physics Society, Athens, Greece, 24-25 September 2021
- **P. Tsavalas**, A. Lagoyannis, K. Mergia, E. Ntemou, C. Lungu, M. Kokkoris, “Differential Cross Sections of ⁹Be(d,p₀)¹⁰Be, ⁹Be(d,p₁)¹⁰Be, ⁹Be(d,a₀)⁷Li and ⁹Be(d,a₁)⁷Li reactions”, 27th Symposium of the Hellenic Nuclear Physics Society, Athens, Greece, 8-9 June 2018
- **P. Tsavalas**, A. Lagoyannis, K. Mergia, K. Triantou, S. Harissopulos, M. Rubel, P. Petersson, M. Kokkoris and JET Collaborators, “Investigation of JET ITER-Like Wall Be Marker Tiles”, 26th Symposium of the Hellenic Nuclear Physics Society, Anavyssos, Greece, 9-10 June 2017

Abstract

The comprehensive understanding of the interaction between plasma and plasma-facing materials constitutes a critical issue for the safe operation of fusion devices and the prediction of the life time of the inner wall of fusion machines. The most important mechanisms that are caused by the plasma-material interaction are the surface erosion, the fuel retention and the migration and deposition of impurities on the plasma facing surfaces (PFSs) and the castellation sides of the first wall. Until 2009 the Joint European Torus (JET) tokamak operated with carbon as plasma facing material where high fuel retention was observed. So the period 2009-2011, the JET tokamak was transformed from a carbon to a full metal wall machine with beryllium in the main chamber and tungsten in the divertor (ITER-like wall), in order to investigate the results of the interaction between the plasma and the plasma facing components (PFCs) for the next generation fusion device, ITER. After the new wall installation, three D – D experimental campaigns were carried.

In this work, the phenomena of material migration and deposition, fuel retention and surface erosion in samples from a) beryllium limiters and inner wall cladding (IWC) of the main chamber and b) tungsten lamellae from the divertor were investigated. The methodology was based on nuclear reaction analysis (NRA) and particle-induced X-ray emission (PIXE) employing deuteron and ^3He ions, using milli- or micro-beams, X-ray fluorescence spectroscopy (XRF), scanning electron microscopy (SEM) with X-ray energy dispersive spectroscopy (EDS) and X-ray diffraction (XRD). Additionally, in order to obtain reliable quantitative results from the NRA measurements, the differential cross sections of the deuteron on beryllium reactions were measured for suitable angles and energies. The experiments were carried out at the Institute of Nuclear & Radiological Sciences and Technology, Energy & Safety (INRASTES), the Institute of Nuclear and Particle Physics (INPP) and the Institute of Nanoscience and Nanotechnology (INN) of NCSR “Demokritos” and at the Laboratory for Ion Beam Interaction (LIBI) of the Ruđer Bošković Institute (RBI) in Croatia.

The cross sections of the $^9\text{Be}(d,p_0)^{10}\text{Be}$, $^9\text{Be}(d,p_1)^{10}\text{Be}$, $^9\text{Be}(d,a_0)^7\text{Li}$ and $^9\text{Be}(d,a_1)^7\text{Li}$ in the energy range $E_{\text{lab}} = 0.75 - 2.2$ MeV with the non-constant energy step up to 1 MeV and then with a step of 20 keV were measured. The detection angles were 120° , 140° , 150° , 160° and 170° with respect to the beam direction. The thickness of the target was determined with proton and oxygen beams. The benchmarking using a bulk beryllium sample coated with a thin gold layer shows that the cross sections of the current work simulate the experimental spectra with deviation no more than 10%.

The samples from the beryllium limiter marker tiles from the main chamber have a nickel interlayer between the top beryllium layer and the bulk beryllium. The aim of this interlayer is to assess the erosion of the samples. Apart from the erosion, the emphasis of the investigation was put on carbon deposition and fuel (deuterium) retention. Specifically, the carbon and deuterium amounts and spatial distribution and their correlation were investigated both on the PFSs and the castellation sides. For the quantification of the carbon amount and its spatial distribution the NRA technique employing deuteron milli- and micro-beam was used. The reaction for the carbon content determination was $^{12}\text{C}(d,p_0)^{13}\text{C}$. On the other hand, for the deuterium retention a ^3He micro-beam was used as the most appropriate reaction to detect deuterium is $^2\text{H}(^3\text{He},p_0)^4\text{He}$. It was found that the carbon and deuterium amounts on the castellation sides are higher than those on the PFS. Furthermore, both the carbon and the deuterium amounts on the investigated castellation sides either stay constant or reduces with the depth from the edge of the PFS. The carbon amount is, in general, higher than the deuterium one. No systematic correlation between the carbon and the deuterium amounts have been observed. Moreover, the surface morphology, the erosion, the nickel (marker layer or deposition) distribution, the heavier material deposition, and the new compound formation were determined. Areas with melted surface, with intensive deposition, areas suffered enhanced erosion and others with mild or partial erosion were

observed. The areas with intensive deposition present the higher carbon amount. On the other hand, the areas with enhanced erosion have the lowest carbon deposition. Nickel is the only element with inhomogeneous spatial distribution originating either from deposition or the marker interlayer. On the castellation sides areas rich in aluminium, chlorine, calcium, molybdenum and tungsten were detected. BeNi is formed on most surfaces.

The carbon and oxygen amount as well as their depth profile were determined on the PFS of the inner wall cladding (IWC) and the dump plate (DP) of the main chamber. Additionally, the morphology, the heavier elemental distribution and the new compound formation were investigated. Generally, high carbon content is accompanied with high oxygen. The samples from the IWC have the highest carbon and oxygen content and their surface morphology seems unchanged after the plasma exposure. The samples of the ILWG1-3 3A8 from the DP have suffered melting. On the surfaces of the samples from the ILW3 2B2C from the DP oriented strips have been formed.

Samples from W lamellae of tile 5 from the divertor were studied in order to determine the light elemental deposition and the corresponding depth profiles. Two of the investigated lamellae consist of a molybdenum interlayer between top tungsten and bulk tungsten in order to assess the surface erosion. The results were correlated with the strike point time. Additionally, the areas with different phases, the change of the surface morphology and compound formation after the plasma exposure were determined. The amount of the deposited beryllium and carbon increases with the strike point time. Beryllium deposition increases from the first to the second campaign and from the second to the third campaign. Carbon deposition decreases from the first to the second campaign but increases from the second to the third campaign, while there is no pattern for the oxygen amount. Furthermore, the carbon and beryllium concentrations are reduced with depth in a similar way for each sample, either abruptly or smoothly. The as-fabricated W lamellae installed in JET are characterized by a network of micro-cracks on the surface. After plasma exposure the morphology of their surface shows mild or strong plasma surface interaction. The density and the width of the micro-cracks were affected in the lamellae from the stack C and after the second campaign. Plenty of heavy elements were detected, on deposition areas of all the samples. The marker lamellae have been eroded up to 6 μm maximum, which is considered as mild erosion.

Περίληψη

Η κατανόηση της αλληλεπίδρασης μεταξύ πλάσματος και των υλικών που έρχεται σε επαφή αποτελεί καίριο ζήτημα για την ασφαλή λειτουργία των αντιδραστήρων σύντηξης και την πρόβλεψη του χρόνου ζωής των εσωτερικών τοιμάτων τους. Τα πιο σημαντικά αποτελέσματα που προκαλούνται από την αλληλεπίδραση πλάσματος – υλικών του τοιχώματος είναι η διάβρωση της επιφάνειας, η κατακράτηση καυσίμου, και η μεταφορά και εναπόθεση του υλικού που διαβρώθηκε σε άλλες επιφάνειες του τοιχώματος. Μέχρι το 2019 το JET τόκαμακ λειτουργούσε με τοιχώματα άνθρακα, όπου παρατηρήθηκαν μεγάλες ποσότητες κατακράτησης καυσίμου. Για το λόγο αυτό την περίοδο 2009-2011, τα τοιχώματα του JET τόκαμακ μετατράπηκαν σε αμιγώς μεταλλικά καθώς τοποθετήθηκε βηρύλλιο (Be) στον κυρίως θάλαμο και βολφράμιο (W) στον εκτροπέα. Τα μεταλλικά τοιχώματα Be και W θα χρησιμοποιηθούν στον αντιδραστήρα σύντηξης ITER, που είναι υπό κατασκευή στη Γαλλία, και για το λόγο αυτό ονομάστηκαν ITER-like wall. Μετά την εγκατάσταση του νέου τοιχώματος στο JET τόκαμακ τρεις πειραματικές καμπάνιες αντίδρασης δευτερίου-δευτερίου έλαβαν χώρα.

Στη συγκεκριμένη εργασία, ερευνηθήκαν τα φαινόμενα της μεταφοράς και εναπόθεσης υλικού, της κατακράτησης καυσίμου και της επιφανειακής διάβρωσης σε δείγματα βηρυλλίου από α) limiters και β) inner wall cladding του κυρίως θαλάμου και γ) σε δείγματα βολφραμίου από τα lamellae του εκτροπέα. Οι πειραματικές τεχνικές που χρησιμοποιήθηκαν είναι η ανάλυση πυρηνικών αντιδράσεων (NRA), η προκαλούμενη από σωματίδια εκπομπή ακτίνων X (PIXE) χρησιμοποιώντας ιόντα δευτερίου και ^3He , μίλι- και μικρο-δέσμης, φασματοσκοπία φθορισμού ακτίνων X (XRF), ηλεκτρονική μικροσκοπία σάρωσης (SEM) με φασματοσκοπία ενεργειακής διασποράς ακτίνων X (EDS) και περίθλαση ακτίνων X (XRD). Επιπλέον για να έχουμε αξιόπιστα ποσοτικά αποτελέσματα στην ανάλυση πυρηνικών αντιδράσεων, οι διαφορικές ενεργές διατομές των αντιδράσεων του δευτερίου με το βηρύλλιο μετρήθηκαν σε γωνίες και ενέργειες κατάλληλες για τη συγκεκριμένη τεχνική. Οι μετρήσεις πραγματοποιήθηκαν στο Ινστιτούτο Πυρηνικών & Ραδιολογικών Επιστημών & Τεχνολογίας, Ενέργειας & Ασφάλειας (ΙΠΡΕΤΕΑ), στο Ινστιτούτο Πυρηνικής και Σωματιδιακής Φυσικής (ΙΠΣΦ) και στο Ινστιτούτο Νανοεπιστήμης και Νανοτεχνολογίας (INN) του ΕΚΕΦΕ «Δημόκριτος» καθώς και Ινστιτούτο Ruđer Bošković στη Κροατία.

Η διαφορική ενεργός διατομή των αντιδράσεων: $^9\text{Be}(d,p_0)^{10}\text{Be}$, $^9\text{Be}(d,p_1)^{10}\text{Be}$, $^9\text{Be}(d,a_0)^7\text{Li}$ και $^9\text{Be}(d,a_1)^7\text{Li}$ μετρήθηκαν στο ενεργειακό εύρος $E_{lab} = 0.75 - 2.2 \text{ MeV}$, έχοντας μεταβαλλόμενο βήμα μέχρι το 1 MeV ενώ στη συνέχεια το βήμα ήταν 20 keV. Οι γωνίες ανίχνευσης ήταν 120°, 140°, 150°, 160° and 170° σε σχέση με την διεύθυνση της δέσμης. Το πάχος του στόχου προσδιορίστηκε με δέσμες πρωτονίου και οξυγόνου. Η συγκριτική αξιολόγηση των αποτελεσμάτων χρησιμοποιώντας ένα παχύ δείγματα βηρυλλίου επικαλυμμένο με ένα λεπτό στρώμα χρυσού έδειξε ότι οι διαφορικές ενεργές διατομές της συγκεκριμένης εργασίας προσομοιώνουν τα πειραματικά φάσματα με απόκλιση μικρότερη του 10%.

Τα δείγματα βηρυλλίου από τα limiter marker tiles του κυρίως θαλάμου αποτελούνται από ένα interlayer νικελίου μεταξύ του επιφανειακού στρώματος βηρυλλίου και του υπόλοιπου δείγματος. Ο σκοπός του interlayer είναι να προσδιορισθεί η διάβρωση των δειγμάτων. Εκτός από τη διάβρωση, έμφαση δόθηκε στην εναπόθεση του άνθρακα και την κατακράτηση καυσίμου (δευτερίου). Συγκεκριμένα, οι ποσότητες άνθρακα και δευτερίου, η χωρική κατανομή τους και η συσχέτιση τους ερευνήθηκαν τόσο στη επιφάνεια όσο και στις ελεύθερες πλευρές (castellation sides). Για την ποσοτικοποίηση του άνθρακα και τον προσδιορισμό της χωρικής κατανομής του χρησιμοποιήθηκε η ανάλυση πυρηνικών αντιδράσεων με χρήση μίλι- και μικρο-δέσμης δευτερίου, αναλύοντας την αντίδραση $^{12}\text{C}(d,p_0)^{13}\text{C}$. Για τον προσδιορισμό της κατακράτησης δευτερίου επιλέχθηκε η χρήση μικρο-δέσμης ^3He καθώς η αντίδραση $^2\text{H}(^3\text{He},p_0)^4\text{He}$ θεωρείται η

πλέον κατάλληλη. Βρέθηκε ότι οι ποσότητες άνθρακα και δευτερίου στις ελεύθερες πλευρές που ερευνήθηκαν είτε παραμένουν σταθερές είτε μειώνονται συναρτήσει του βάθους από την ακμή της επιφάνειας. Γενικά η ποσότητα του άνθρακα είναι υψηλότερη από εκείνη του δευτερίου, ενώ δεν παρουσιάζεται συσχέτιση μεταξύ της εναπόθεσης άνθρακα και της κατακράτησης δευτερίου. Επιπλέον, ερευνήθηκαν η μορφολογία της επιφάνειας, η διάβρωση, η χωρική κατανομή του νικελίου (που προέρχεται είτε από το interlayer είτε από την εναπόθεσή του), η εναπόθεση των υπόλοιπων στοιχείων που ανιχνεύτηκαν και η δημιουργία χημικών ενώσεων. Παρατηρήθηκαν περιοχές με τηγμένη επιφάνεια, με έντονη εναπόθεση, περιοχές που υπέστησαν έντονη, ήπια ή μερική διάβρωση. Οι περιοχές με ενισχυμένη εναπόθεση παρουσιάζουν επίσης υψηλή ποσότητα άνθρακα, αντίθετα περιοχές με έντονη διάβρωση έχουν την χαμηλότερη εναπόθεση άνθρακα. Το νικέλιο είναι το μόνο στοιχείο με ανομοιογενή χωρική κατανομή στην επιφάνεια, το οποίο προέρχεται είτε από την εναπόθεση είτε από την ανάδυση του interlayer νικελίου στην επιφάνεια λόγω διάβρωσης των άνωθεν στρωμάτων. Στις ελεύθερες πλευρές ανιχνεύτηκαν περιοχές πλούσιες σε αλουμίνιο, χλώριο, ασβέστιο, μολυβδένιο και βολφράμιο. Η κρυσταλλική φάση BeNi δημιουργήθηκε στην επιφάνεια των περισσότερων δειγμάτων.

Η ποσότητα του άνθρακα και του οξυγόνου καθώς και η συγκέντρωσή τους συναρτήσει του βάθους προσδιορίστηκε στην επιφάνεια των inner wall cladding (IWC) και the dump plate (DP) του κυρίως θαλάμου. Επιπροσθέτως, ερευνήθηκαν η μορφολογία, οι επιφάνειες με διαφορετικές φάσεις και η δημιουργία χημικών ενώσεων. Γενικά, η υψηλή περιεκτικότητα σε άνθρακα συνοδεύεται με υψηλό οξυγόνο. Τα δείγματα από το IWC έχουν τη μεγαλύτερη συγκέντρωση άνθρακα και οξυγόνου και οι περιοχές τους φαίνονται αναλλοίωτες από την επίδραση του πλάσματος. Τα δείγματα του ILWG1-3 3A8 από το DP έχουν υποστεί τήξη. Στις επιφάνειες των δειγμάτων του ILW3 2B2C από το DP έχουν σχηματιστεί προσανατολισμένες λωρίδες.

Δείγματα βολφραμίου από τα lamellae του tile 5 του εκτροπέα μελετήθηκαν ώστε να καθοριστεί η εναπόθεση ελαφρών στοιχείων και η αντίστοιχη μεταβολή της συγκέντρωσης συναρτήσει του βάθους. Δυο από τα lamellae που ερευνήθηκαν έχουν ένα interlayer μολυβδενίου μεταξύ του επιφανειακού βολφραμίου και του υπόλοιπου δείγματος έτσι ώστε να προσδιοριστεί η διάβρωση της επιφάνειας των δειγμάτων. Τα αποτελέσματα συσχέτιστηκαν με το strike point time. Επιπλέον, προσδιορίστηκε η εναπόθεση βαρύτερων στοιχείων, η μεταβολή της μορφολογίας της επιφάνειας και η δημιουργία χημικών ενώσεων μετά την έκθεση στο πλάσμα. Παρατηρήθηκε η αύξηση της ποσότητας του άνθρακα και του βηρυλλίου με την αύξηση του strike point time. Επίσης, η εναπόθεση του βηρυλλίου αυξάνεται από την πρώτη στη δεύτερη πειραματική καμπάνια καθώς και από τη δεύτερη στην τρίτη. Η εναπόθεση του άνθρακα μειώνεται από την πρώτη στη δεύτερη πειραματική καμπάνια ενώ αυξάνεται από την δεύτερη στην τρίτη. Η ποσότητα του οξυγόνου δεν ακολουθεί συγκεκριμένη συμπεριφορά στις διαφορετικές πειραματικές καμπάνιες. Επιπλέον, οι συγκεντρώσεις του άνθρακα και του βηρυλλίου μειώνονται συναρτήσει του βάθους με παρόμοιο τρόπο, είτε απότομα είτε ομαλά. Η επιφάνεια των lamellae βολφραμίου πριν την έκθεση στο πλάσμα χαρακτηρίζεται από ένα δίκτυο μικρορωγμών. Μετά την έκθεση στο πλάσμα η μορφολογία της επιφάνειας παρουσιάζει ήπια ή έντονη αλληλεπίδραση πλάσματος – επιφάνειας. Η πυκνότητα και το πάχος των μικρορωγμών έχουν επηρεαστεί στα δείγματα από το stack C μετά τη δεύτερη πειραματική καμπάνια. Πληθώρα στοιχείων ανιχνεύτηκαν στις περιοχές εναπόθεσης. Τα marker lamellae δεν έχουν υποστεί διάβρωση μεγαλύτερη των 6 μm, η οποία θεωρείται ήπια διάβρωση.

Abbreviations

BSE	Backscattered Electron
DP	Dump Plate
EDS	Energy Dispersive Spectroscopy
HFGC	High Filed Gap Closure
IBA	Ion Beam Analysis
ILW	ITER-like Wall
ITER	International Thermonuclear Experimental Reactor
IWC	Inner Wall Cladding
IWGL	Inner Wall Guard Limiter
JET	Joint European Torus
LHD	Large Helical Device
NIFS	National Institute for Fusion Science
NIST	National Institute of Standards and Technology
NRA	Nuclear Reaction Analysis
OPL	Outer Poloidal Limiter
PFC	Plasma Facing Component
PFM	Plasma Facing Material
PFS	Plasma Facing Surface
PIXE	Particle-Induce X-ray Emission
SDD	Silicon Drift Detector
SE	Secondary Electron
SEM	Scanning Electron Microscopy
SOL	scrape-off layer
TDS	Thermal Desorption Spectroscopy
XRD	X-ray Diffraction
XRF	X-ray Fluorescence Spectroscopy

Chapter 1: Introduction

Searching for clear and safe energy is an issue of concern for many decades. Nowadays, the necessity of new, more efficient sources of energy is mandatory, as the population is rapidly increasing and the technology requires more and more energy consumption. The sources of energy that we already use can hardly cover our needs and most of them have some serious drawbacks. Fossil fuels are the most widespread sources that are nowadays used. Specifically, the 34% of the total energy is taken by burning oil, the 27% by coal and the 25% by natural gas. The problem with these sources is the production of CO₂. The CO₂ contributes to the greenhouse effect which increases the temperature of the surface of the earth. Additionally, the fossil fuels are finite and in the future we will face the problem of lack of resources. The nuclear energy which is already used and contributes the 5% of the total energy is the fission of the heavy nuclei, namely the uranium (²³⁵U) and the plutonium (²³⁹Pu). The drawbacks of this source are the long term radioactive waste and how to manage them [1], the finite resources of the fuel and the probability of an accident during the operation of a nuclear plant. The most promising source of energy that we use nowadays is the renewable ones, namely solar, wind, water (hydro), biomass and geothermal. In principle, which burden much less the environment but only the 12% of the total energy origins from these sources, because of the low energy density, their unreliability (they are strongly dependent on the weather condition), the difficulty to store the generated energy and the lack of suitability to power urban industrial complexes.

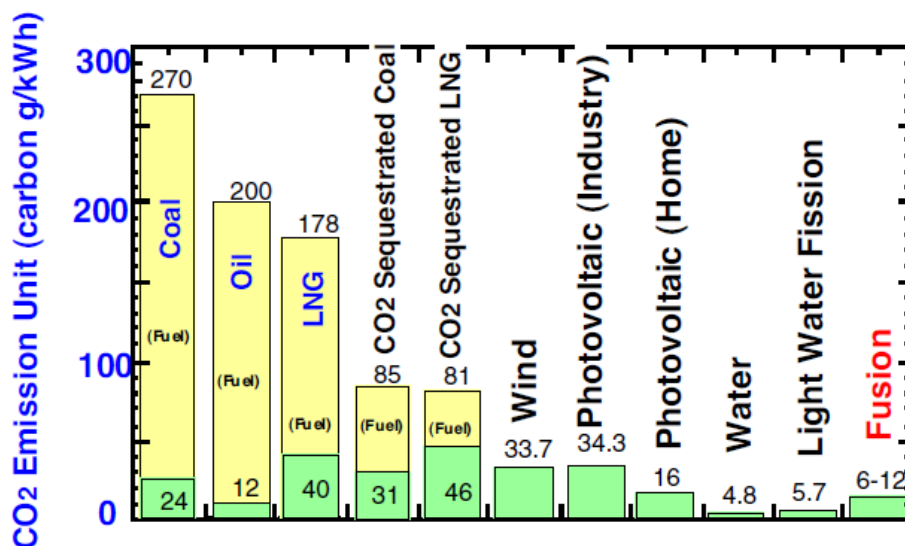


Figure 1: CO₂ emission for different sources of energy [2]. The yellow colour refers to the fuel oriented emission, while the green to the rest operations. We note the fusion with red letters.

Fusion has the potential for offering clean, abundant and affordable energy. The fusion reaction is environmentally friendly as it does not produce CO₂ and during the plant operation the CO₂ production will be very low [3] (Figure 1). Furthermore, no long-term radioactive waste is produced. Its fuel is cheap, inexhaustible (deuteron, proton) or can be produced (tritium). The plan is to produce tritium in the breeding blanket, a part of the reactor which consists of Li, via the reaction: $n + {}^7\text{Li} \rightarrow {}^3\text{H} + {}^4\text{He}$. Moreover, fusion reaction has the highest energy density (energy released per unit mass of the reactants) compared with the other sources, so less quantities of fuels are needed. For example, 1 g of fusion fuel produces as much energy as 1 t of

coal [4]. Additionally, fusion reaction is inherently safe, i.e. when the reaction is out of control, the fusion reactor switches itself off. In conclusion, nuclear fusion is a clean and safe source which offers huge amounts of energy with low cost fuels.

But what is nuclear fusion? Nuclear fusion is the reaction of two low Z nuclei producing one or more different nuclei and subatomic particles (neutron or proton). As Figure 2 presents, the binding energy per nucleon increases with the number of nucleons for elements lighter than iron (except for helium which has an extremely high binding energy), so the difference between the nuclear binding energy of the initial and the produced nuclei is offered to the latter ones as kinematic energy.

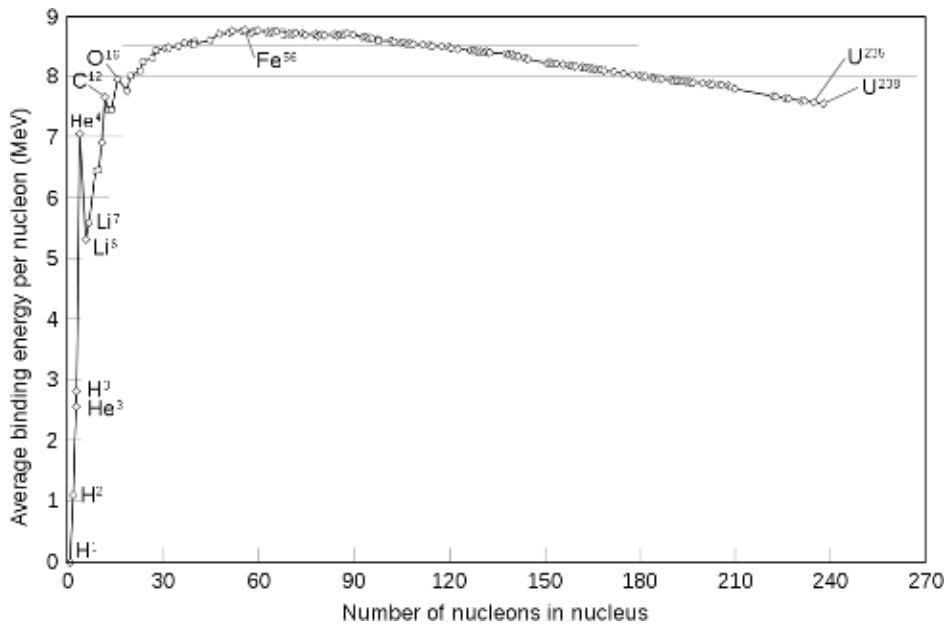
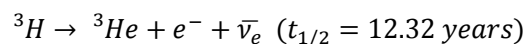


Figure 2: The binding energy per nucleon as a function of the number of the nucleons in the nucleus [5].

The production of all elements lighter than iron is performed via nuclear fusion and as it is exothermal reaction it can be used for energy production, however the candidate fusion reactions for production of electricity are the following:

1.	${}^2\text{H} + {}^3\text{H}$	\longrightarrow	${}^4\text{He} + n$	Q-value = 17.6 MeV
2.	${}^2\text{H} + {}^2\text{H}$	$\left\{ \begin{array}{l} \longrightarrow \\ \longrightarrow \end{array} \right.$	${}^3\text{H} + p$ ${}^3\text{He} + n$	Q-value = 4.03 MeV (50%) Q-value = 3.27 MeV (50%)
3.	${}^2\text{H} + {}^3\text{He}$	\longrightarrow	${}^4\text{He} + p$	Q-value = 18.3 MeV
4.	${}^3\text{H} + {}^3\text{H}$	\longrightarrow	${}^4\text{He} + 2n$	Q-value = 17.6 MeV
5.	${}^3\text{He} + {}^3\text{He}$	\longrightarrow	${}^4\text{He} + 2p$	
6.	${}^3\text{He} + {}^3\text{H}$	$\left\{ \begin{array}{l} \longrightarrow \\ \longrightarrow \end{array} \right.$	$2 {}^4\text{He} + p$ ${}^4\text{He} + {}^2\text{H}$	Q-value = 12.1 MeV (57%) Q-value = 14.3 MeV (43%)
7.	${}^2\text{H} + {}^6\text{Li}$	\longrightarrow	$2 {}^4\text{He}$	Q-value = 17.6 MeV
8.	$p + {}^6\text{Li}$	\longrightarrow	${}^4\text{He} + {}^3\text{He}$	Q-value = 4 MeV
9.	${}^3\text{He} + {}^6\text{Li}$	\longrightarrow	$2 {}^4\text{He} + p$	Q-value = 16.9 MeV
10.	$p + {}^{11}\text{B}$	\longrightarrow	$3 {}^4\text{He}$	Q-value = 8.7 MeV

The selected reaction for fusion energy production is the deuteron – tritium one (1). In this reaction 14.1 MeV neutron and 3.5 MeV helium nucleus are produced. The advantages of this reaction against the others are: a) the high Q-value, b) the low Coulomb barrier, as only two protons (positively charged particles) take place in this reaction and c) the high cross section at low particle kinetic energies (Figure 3). The high Q-value offers high energy per event. On the other hand, the low Coulomb barrier and the high cross section at low energies require low input power. The ratio of the produced power to the input power, which is called *Q* factor, is a very important factor for nuclear plants. This factor must be at least higher than one for an efficient plant and the aim is to be maximized. The disadvantages of the chosen reaction are the neutron production and the presence of the tritium. The neutron penetrates deeply in matter, is absorbed by the materials and renders the components radioactive. The 80 percent of the produced energy is carried by neutrons which are absorbed by the surrounding walls of the tokamak and their kinetic energy is transferred to the walls as heat [6]. The neutron – material interaction causes structural damage (displacement damage) and nuclear transmutation [7] and these interactions decrease the lifetime of the wall. Moreover, the tritium is a radioactive hydrogen isotope, which transmutes via beta minus decay:



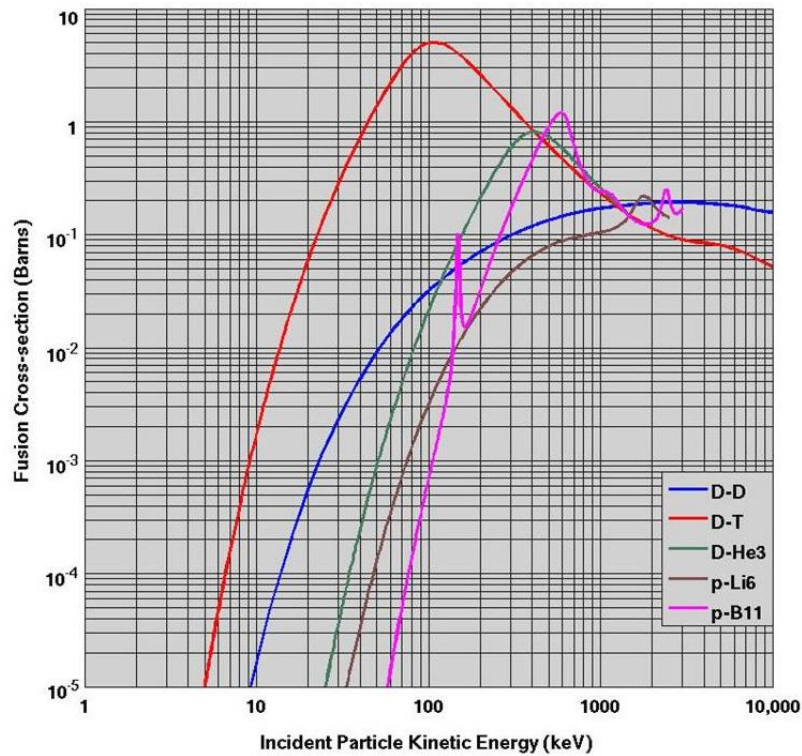


Figure 3: Cross sections of various fusion reaction as a function of the centre of mass [8]

Since 1939, when Hans Bethe presented the calculation of the proton – proton chain reaction in the stars [9], we have the full knowledge of the nuclear fusion, however controlled thermonuclear fusion for energy production has not been achieved yet. The reason is the special conditions that are needed so that two positively charged nuclei come close enough to succeed the reaction. So, in order to overcome the Coulomb barrier and reach the short range attractive strong nuclear force (Figure 4), the nuclei should obtain high kinematic energy or in other words the fuel should reach very high temperature. In the stellar core, where nuclear reaction takes place and is the inspiration of the idea, the temperature and the pressure due to gravity is high enough to achieve the reactions. For example, the temperature of the solar core is 1.5×10^7 K and the density 150 g/cm^3 [10]. On earth, it is impossible to achieve this density in large scale so the temperature should be much higher. For example, in order to have nuclei with kinetic energy of 40 keV we need a temperature of 3×10^8 K, which is one order of magnitude higher than that of the solar core. In this temperature the fuel is in plasma state and must be kept away from the wall of the reactor.

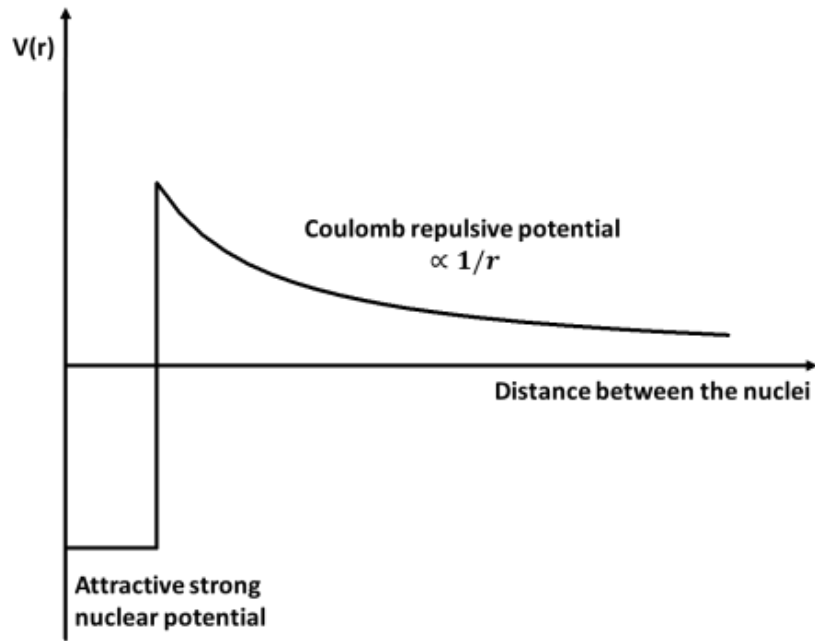


Figure 4: The potential between two nuclei.

There are two approaches to confine the plasma: a) the inertial and b) the magnetic confinement. In inertial confinement, powerful laser beams are used to compress and heat the fuel (micrograms of deuterium and tritium) which is posed in a small spherical pellet [11]. In magnetic confinement, taking advantage of the electromagnetic properties of the charged plasma particles, the plasma is trapped away from the surrounding wall of the device in a specifically designed magnetic field. The most successful way of trapping the plasma particles along the magnetic field lines has been achieved by magnetic confinement fusion based on the tokamak concept. In the tokamak (Figure 5), the plasma is formed in the shape of a torus or a doughnut, through toroidal and poloidal magnetic fields [8].

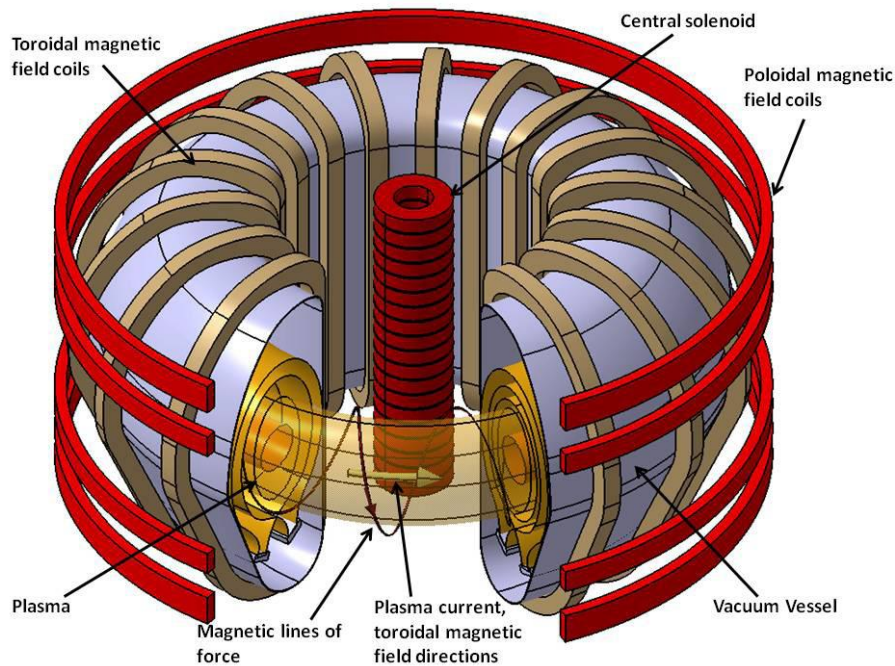


Figure 5: The magnetic configuration in the tokamak [8]

Despite the presence of the magnetic field, some particles can still escape; thus interaction between the plasma and the plasma facing materials (PFMs) takes place and affects both the stability of the plasma and the lifetime of the surrounding wall. So, the most suitable combination of elements or compounds for the first wall is now under investigation. The most favorable elements to be used as PFMs are carbon [12], tungsten [13] and beryllium [14].

The Joint European Torus (JET) at the Culham Science Centre, the largest tokamak in the world, until 2009 was operated with carbon as the main PFM (JET-C) [15]. Very high fuel inventories were measured because the presence of carbon impurities is decisive for fuel retention by co-deposition constituting the main mechanism for fuel inventory in carbon-wall machines [16]. This called for a large-scale test of a metal wall. Besides the JET Tokamak was decided to be used as a test bed for the next fusion device, the ITER, so the carbon first wall was replaced with the ITER – like wall (ILW), namely beryllium in the main chamber and tungsten in the divertor [17, 18, 19]. Beryllium is chosen due to the low Z which prevents the dilution of plasma and the power radiation loss, the high thermal conductivity ($\sim 200 \text{ Wm}^{-1}\text{K}^{-1}$) and the low fuel retention comparing to the carbon [20] which is crucial for the life time of the wall and the conservation of the fuel and constitutes the main disadvantage of the carbon. Beryllium is also an oxygen getter which reduces oxygen impurities and helps to keep the Z_{eff} (effective ionic charge, a quantity to assess the impurity content of a fusion plasma) [21] in the vessel at accessible levels, while its disadvantage is the high sputtering which is comparable to the carbon [22]. A detailed overview of the beryllium investigation as PFC is presented in [23]. On the other hand, the advantages of the tungsten are the high melting point (3695 K), low vapour pressure at melting point ($1.3 \times 10^{-7} \text{ Pa}$ at melting point), high thermal stress resistance, high thermal conductivity ($170 \text{ Wm}^{-1}\text{K}^{-1}$) and low swelling [24]. It also presents low erosion [22] and low fuel retention [20]. The main disadvantage of tungsten is the high Z , so its impurities in the core of the plasma should be limited, while it has also some other negative properties (recrystallization, high ductile to brittle transition temperature, etc.) which are described in detail in [24]. The comparison regarding the lifetime of the wall between the JET-ILW and the JET-C is presented by Roth et al [25].

Figure 6 presents an overview of the components of the ILW JET tokamak first wall. The Inner Wall Cladding (IWC) tiles (light blue) consists of a beryllium layer with nominal thickness of 7-9 μm [26] coated on Inconel substrate and were positioned 6 cm behind the limiters [27]. The Dump Plate (DP), the Inner Wall Guard Limiter (IWGL) and Outer Poloidal Limiter (OPL) tiles (light green) consist of either bulk beryllium or marker tiles with 2 μm nickel interlayer between the top beryllium (8 μm) and the bulk one [28]. The divertor consists of bulk tungsten or marker tiles with molybdenum interlayer between the top tungsten layer and the bulk tungsten (red area); or tungsten - molybdenum layers coated on CFC (purple area).

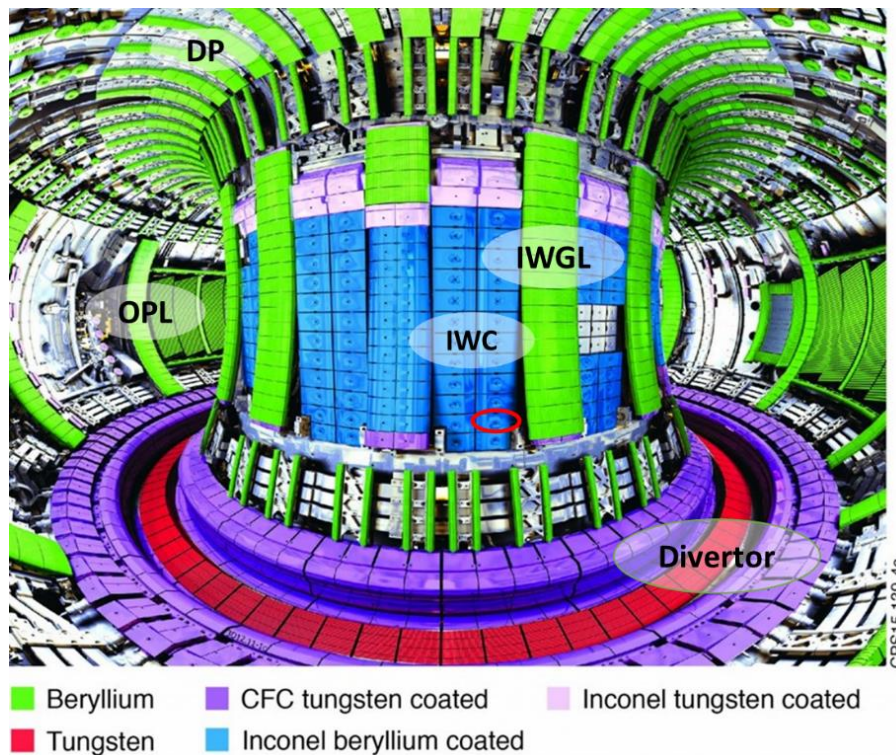


Figure 6: The Configuration of the JET ITER-like wall [29].

1.1 Plasma – Wall Interaction: Physical Mechanisms

The interaction between the plasma and the PFMs is a very large and complex field of the physics of materials. Figure 7 illustrates the results of the plasma – PFMs, the circled phenomena will be described here as there are relevant to the aims of the current work. One of the consequences of the interaction that affects both the plasma and the wall is surface erosion, which is caused by the physical and the chemical sputtering and the sublimation of the PFM. Sputtering is the removal of atoms from the surface of a solid as a result of the momentum transfer by incident ions or atoms. Physical sputtering takes place when the atoms of the material via collision with the ions obtain energy higher than the surface binding energy and leave the wall. On the other hand, chemical sputtering takes place when chemical reactions are performed between the elements of the first wall and the fuel. The physical sputtering of beryllium is higher than that of carbon (Figure 8a); however, the carbon undergoes enhanced chemical sputtering, forming CD_4 (Figure 8b). Another phenomenon which contributes to surface erosion is the sublimation. The sublimation of beryllium becomes comparable to the physical sputtering for temperature higher than 1000 K, while carbon undergoes significant radiation-enhanced sublimation during ion bombarding, above 1200 K [30].

Eventually, the total erosion of carbon and beryllium is of the same order of magnitude, while there is no erosion of tungsten for low energies (Figure 9) [22].

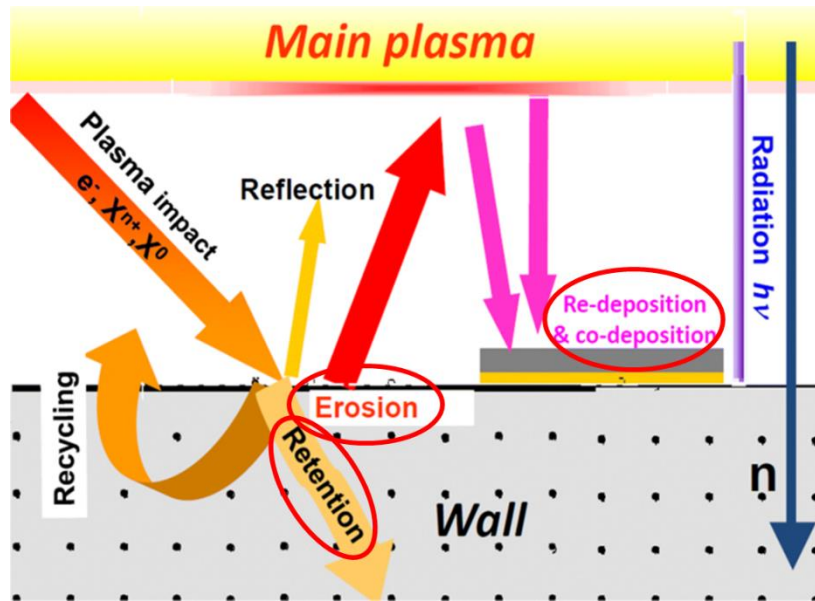


Figure 7: The results of the interaction of the plasma and the PFMs [31].

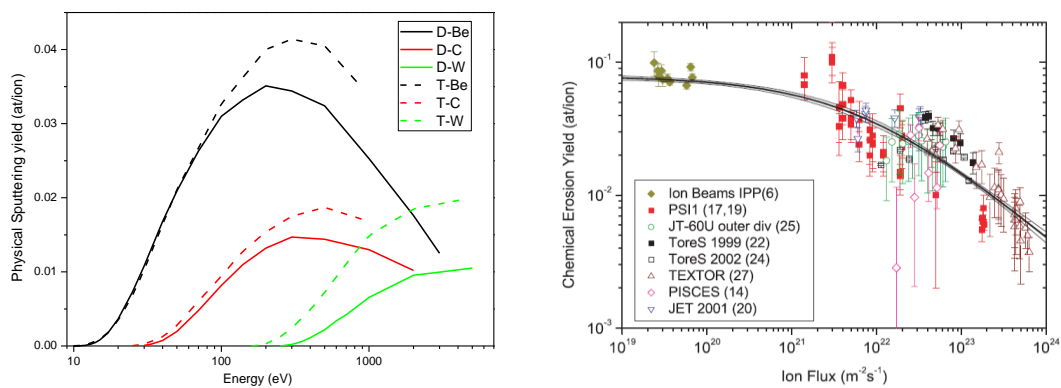


Figure 8: a) Physical sputtering of the candidate elements: Be, C, W by ions of D and T as a function of ion energy at room temperature computed by the code TRIM [32], b) flux dependence of the chemical erosion yield for T_{max} , the temperature at which the chemical erosion yield is maximum, and an ion energy of 30 eV determined by measurements in different fusion devices and plasma simulators [33].

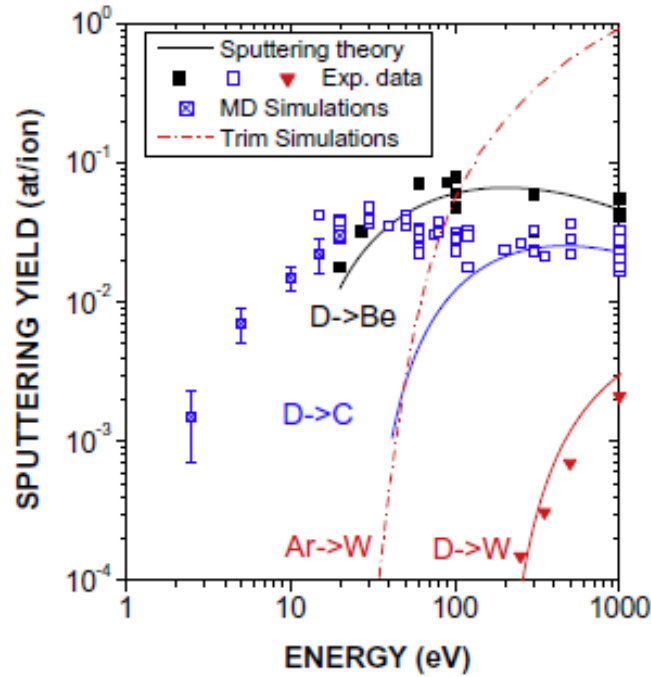


Figure 9: Sputtering yields of C, Be and W bombarded with D ions [25]

The impurities that are ejected from the wall may be re-deposited in the same place or migrate and be re-deposited in other parts of the wall. Simulations can predict the migration of the impurities from the main chamber to divertor via scrape-off layer (SOL) - the outer layer of a magnetically confined plasma, where the field lines come in contact with a material surface [34] (Figure 10a) and the post-mortem analysis determines this deposition [35] (Figure 10b). Moreover, a part of the impurities enters the core of the plasma. Another consequence of the plasma-first wall interaction is fuel retention. For carbon, the long-term fuel retention is mainly caused by the co-deposition of the released impurities with the fuel; while for the beryllium both the co-deposition and the implantation contribute to the long-term fuel retention [36]. The in situ measurements showed a reduction of one order of magnitude (factor 10-20) of the long-term retention from the JET-C to JET-ILW [20]. Surface erosion, material migration and (re-)deposition in combination with fuel retention change the properties of the wall and as a result the life time of the PFMs. On the other hand the impurities resulting from surface erosion can dilute and cool the plasma as fuel retention decreases the amount of the available fuel for the fusion reaction to take place.

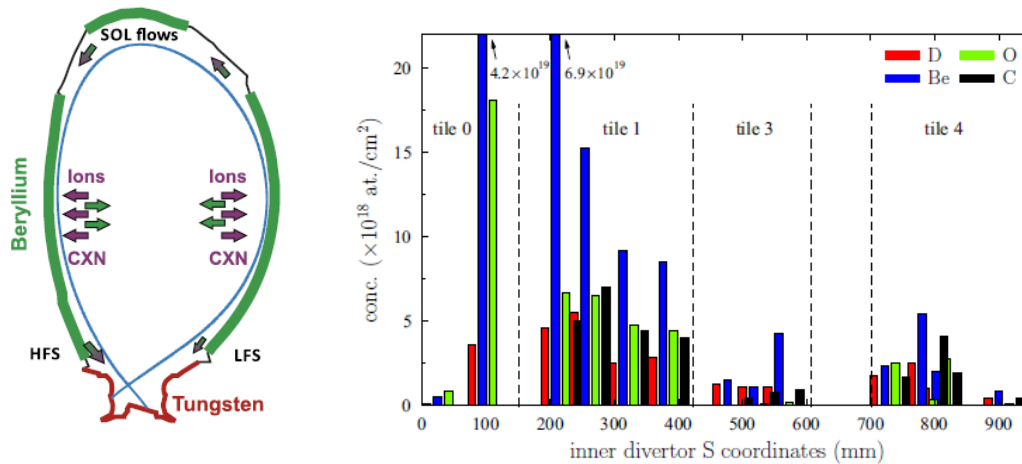


Figure 10: a) The SOL in the Tokamak and b) the results of the material deposition in the inner divertor [35]

1.2 Plasma – ILW JET Tokamak First Wall Interaction

After the wall transformation of the JET tokamak in 2011, three experimental campaigns, namely during the periods 2011-12 (ILW1), 2013-14 (ILW2) and 2015-16 (ILW3), were operated to test the plasma – wall interaction. Many works have been published, presenting the results of the investigation of the interaction of the plasma with the ILW JET tokamak first wall [37]. Regarding the divertor, the comparison between C-Wall operation and ILW shows that the material deposition was reduced by one order of magnitude after the wall transformation [38, 39, 40]. The main deposition was beryllium; carbon and oxygen constitute the 5-20%, while impurities of nickel and tungsten were detected [41]. Additionally, the fuel retention during the ILW campaigns was 10-20 times smaller than during the carbon wall ones [40, 42], while the 73% of this fuel was retained on the divertor [35, 36]. The main conclusions comparing the different tiles of the divertor (Figure 11) are that the tiles 0 and 1 have suffered the highest material (oxygen, nitrogen, carbon and beryllium) deposition [43, 44], and deuterium retention [35, 36, 40, 42, 45] after the three campaigns, while high material deposition was also detected on tile 3 [39]. The microanalysis of these tiles after the first and the second campaigns shows is that the distribution of material deposition and the fuel retention are inhomogeneous preferring cracks, pits and depressed regions [46]. The carbon decreases through the campaigns [45]. Additionally, correlation between strike-point and Be accumulation was observed [45]. Concerning the T retention, Y. Oya [47] presents a correlation between tritium and deuterium retention. Additionally, after the first campaign the band-like regions with high T retention were detected on tiles 1, 3, 4 and 6 which formed thick co-deposited layers of D, T with Be. On tiles 7 and 8 the T retention is low and uniform [48]. After the ILW2, there is a correlation between the tritium retention and the beryllium deposition, a correlation which was not noted after the ILW3. A possible reason for this may be the enhanced desorption of the tritium due to the higher temperatures of the third campaign [49]. Regarding the surface erosion, high erosion was observed only on tile 5 for all campaigns, while erosion was observed also on tile 7 after the second and the third campaigns [45].

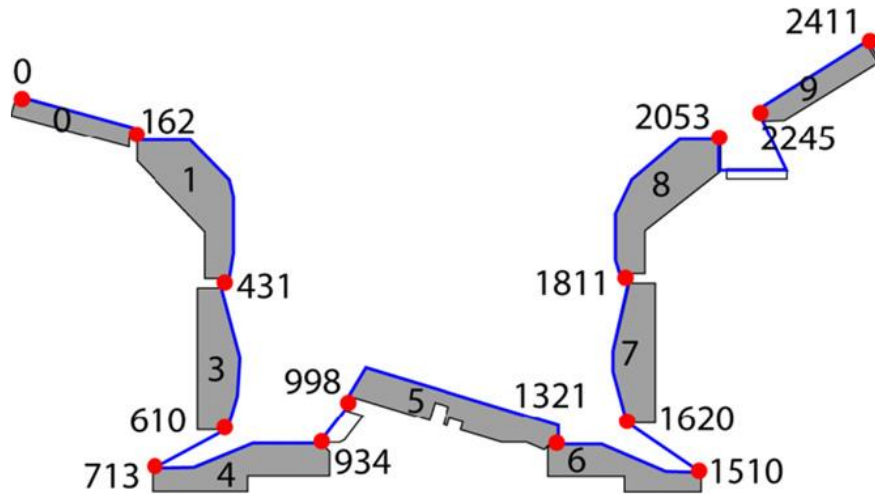


Figure 11: ILW JET tokamak divertor, the tiles numbers and s-coordinate in mm [41].

Apart from the divertor, some papers dealt with the main chamber (Figure 12) of ILW JET tokamak. The upper DPs have suffered extensive melting and arcing [39, 50], additionally D was detected on the surface (2.1×10^{22} D) [35, 36]. Details about the melting and the erosion of the different tiles from the three experimental campaigns are presented by I. Jepu et al [51].

For the IWGL, the centre part of the different tiles presents different behavior: No erosion was detected on the surface of the centre part of upper 2XR19, while tungsten and nickel deposition was observed [44]. The centre part of the 2XR15 has suffered melting [50]. The centre part of the 2XR10 presents strong erosion (up to $60 \mu\text{m}$) [39, 44]. The left side of the centre part of 2XR3 has suffered light erosion while at the same time some deposition was detected. At the ends of the tiles the original marker still exists [44], while arc tracks are presented on the left ends (for the upper tiles) or both ends (for the rest tiles) [50]. The right wing of the upper (2XR19) and mid (2XR10) tile presents high surface roughness [39]. The intermediate regions are characterized by deposition of beryllium and impurities of Ni, Mo, Cr, Fe and W [44]. The global deuterium retention as calculated by [35, 36] is 2.75×10^{22} D.

For OPL, the centre part of the midplane has suffered erosion more than $10 \mu\text{m}$, while re-deposition of beryllium and nickel was detected on the left and right sides. The transition regions between the eroded areas and the ends of the tile retain the original marker layer. The composition of the upper and the bottom tiles seems intact and only some impurities of W, Ni, Mo, Cr, and Fe were detected. Tiles B and C, which consist of CFC with a $10 \mu\text{m}$ thick tungsten layer, did not suffer any erosion, while the beryllium deposition is close to spectrum background [44, 50]. The global deuterium retention of OPL was calculated by [35] and is 5.72×10^{22} D.

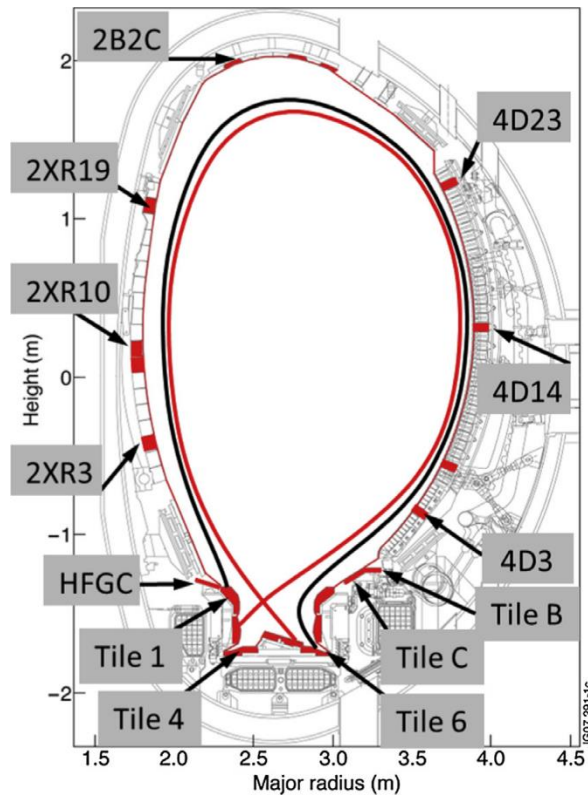


Figure 12: The Poloidal cross-section of the JET vessel and the name of the tiles that were investigated by Baron-Wiechec et al [44]

It was mentioned previously that one of the carbon disadvantages and the reason why it was replaced with metallic materials, is the high fuel retention it presents. So, many works either in JET tokamak or in other laboratories and fusion devices investigated the presence of carbon in a full metallic environment and how its presence affects the fuel retention under different conditions.

i) JET Tokamak

In the period 1994 - 1995 an experiment was carried out in JET tokamak using initially carbon and then beryllium on castellated tiles of limiters and divertor [52, 53], and the deuterium retention was associated with the carbon deposition in a number of works [54, 55, 56]. On the other hand, there is no consensus about the correlation of the deuterium retention with the carbon on the ILW JET divertor. The works [36, 40, 41, 42, 57, 58] report that deuterium retention increases with the increase of the material (carbon and beryllium) deposition on tungsten tiles. The works [45, 46, 59] claim that the increase of the deuterium retention is due to beryllium deposition, while the works [38, 60, 61] report that the carbon deposition increases the deuterium retention. P. Storm et al [62] reports that deuterium was co-deposited either with carbon or beryllium on Inconel-600 blocks and stainless steel covers for quartz microbalance crystals in IWL JET Tokamak.

ii) Other fusion devices with W wall and laboratory-prepared W samples

The deuterium-carbon correlation was investigated in different fusion tokamaks and devices around the world after plasma operation. For tungsten samples from Korea Superconducting Tokamak Advanced Research (KSTAR), two works [63, 64] focused on the carbon deposition and deuterium retention. The former [63] one presents an absolute correlation between the carbon deposition and the deuterium retention on the castellated sides of the tungsten tiles, while the latter [64] one reports that no correlation of the two elements is observed as the deuterium

retention is mainly affected by the surface temperature. For the tungsten samples of the Q-shu University Experiment with Steady-State Spherical Tokamak (QUEST), there are two works [65, 66] which investigated the effect of the carbon deposition on the deuterium retention. Y. Oya et al [65] concludes that lower H and D were detected in areas where deposition was dominant. On the other hand, A. Koike et al [66] showed that high deuterium retention was detected in areas with high carbon deposition and the retention is caused due to radiation damage. Two works [67, 68] have been published for the ASDEX-Upgrade tungsten divertor tiles. D. Schleusser et al [67] showed that the deuterium retention is associated with carbon deposition as the deuterium amount is one order of magnitude higher on inner divertor where C deposition was observed than on the outer divertor, where the erosion dominated. K. Sugiyama et al [68] reported that the carbon impurities affected the deuterium retention. The deuterium retention and carbon deposition were determined in Tokamak Experiment for technology Oriented Research (TEXTOR); in TEXTOR-94 tungsten limiters, V. Philipps et al [69] reported that 2 areas can be distinguished in the samples, one bare of carbon and deuterium and the other rich in these elements with ratio of 0.05-0.1. T. Tanabe et al [70] investigated a twin limiter from the TEXTOR-94 consisting of a tungsten and a carbon sample. Tungsten with carbon deposition presents higher deuterium retention than tungsten without carbon. Association of the deuterium retention with the carbon deposition in the gaps of the castellated tungsten limiter in the TEXTOR is reported in [71]. The deuterium retention and carbon deposition on gaps of samples from ASDEX Upgrade, DIII-D and TEXTOR tokamaks were investigated by K. Krieger et al [72]. It was found that the deuterium retention was affected by the carbon deposition and the temperature of the surface. In another fusion machine, the Large Helical Device (LHD), at the National Institute for Fusion Science (NIFS), the deuterium retention is enhanced on the carbon dominant deposited layers [73, 74].

Apart from fusion tokamaks and devices, the correlation between deuterium and carbon was investigated using laboratory-prepared sample composition and controlled experimental conditions. Many experiments have been carried out with simultaneous implantation of D and C ions or C pre-implantation and subsequently deuterium implantation. I. Bizyukov et al [75] and V. Kh. Alimov et al [76] claimed that there is no difference in the deuterium retention between deuterium and D-C ion implantation. On the other hand, F. C. Sze et al [77], Y. Ueda [78] and Y. Oya et al [79] showed that the deuterium retention is higher with C-D mixed ions than with pure deuterium ions. D. M. Fukumoto et al [80] claimed that at 500 K the D retention increases for carbon fraction higher than 1.2%; while at 700 K the retention is generally lower than that at 500 K and increases for fraction higher than 0.8%. Y. Oya et al [81] compared the deuterium retention after simultaneous deuterium and carbon implantation and after carbon pre-implantation on tungsten samples, the result is that after the simultaneous implantation the retention is higher. M. Poon et al [82] carried out experiments with different fluences of carbon which was pre-implanted on tungsten followed by different fluences of deuterium at various temperatures in order to investigate deuterium retention. Their conclusions are that with high C (10^{22} C⁺/m²) and low D fluence ($\leq 10^{23}$ D⁺/m²) the deuterium retention is higher than in pure tungsten; with low carbon (10^{21} C⁺/m²) and low deuterium ($\leq 10^{23}$ D⁺/m²) the retention is lower than in pure tungsten; with high deuterium fluence ($\geq 10^{23}$ D⁺/m²), pre-implanted and pure W present similar retention. O. V. Ogorodnikova et al [83] agreed that there was no difference with the high deuterium fluence, while at low deuterium fluence deuterium retention in carbon pre-irradiated samples was higher than in the pure tungsten. V. Kh. Alimov [84] showed that for 10 keV D retention is lower in pre-irradiated tungsten than in pure tungsten, while for 100 keV D retention is similar. T. Taguchi et al [85] claimed that carbon deposition enhances the surface deuterium retention and its re-emission but reduces deuterium diffusion. The reduction of the D diffusion was confirmed by D. A. Komarov [86].

Another route for investigation of deuterium retention and its possible correlation with carbon is deuterium bombarding on tungsten carbide or carbon coated tungsten and subsequent comparison with pure tungsten. S. Nagata et al [87], R. A. Anderl [88] and Wright et al [89] agreed that a C-coated W retains more D than the pure W. W. Wang et al [90] V. Kh. Alimov [91] claimed that tungsten carbide presents two times more than that of pure W at the room temperature;

while at 650 K their D retention is similar, on the other hand, P. Roszell [92] claimed that deuterium was not affected by the impurities (carbon and oxygen) at 300 K, while the impurities (carbon and oxygen) reduced the retention at 500 K. Y. Oya [93] concluded that the pure tungsten has more deuterium than carbon deposited on tungsten and tungsten carbide samples.

iii) laboratory-prepared Be samples

The C-D correlation has been also investigated in beryllium, using laboratory-prepared samples. Anderl et al. found the D retention in pure beryllium to be lower than in C-coated Be [94]. Also Guseva et al [95] concluded that C impurities on the beryllium surface enhance the deuterium retention. On the other hand, C. Porosnicu et al. irradiated different Be-C relative concentration with deuterium ions and found that lower carbon concentration retained higher deuterium content [96].

Based on the above findings reported in the literature, it is not clear from the literature whether the residual D retention still exists as a result of the C-D chemistry or whether deuterium is integrated into deposits irrespective of carbon.

1.3 Aim of the Current Work

The aim of the current work is to investigate samples from different areas and campaigns from the ITER-like wall JET tokamak main chamber and divertor in order to assess surface erosion and morphology change, material migration and re-deposition or co-deposition, as well as fuel retention and any possible compound formation. The emphasis will be given on carbon deposition and deuterium retention. Apart from the plasma facing surface, the castellation sides (see below the definition) of the samples were investigated. To achieve this goal, different analytical techniques were used: Nuclear Reaction Analysis with milli-beam (m-NRA) and micro-beam (μ -NRA), X-Ray Florescence Spectroscopy (XRF), Scanning Electron Microscopy (SEM) with Energy Dispersive X-Ray Spectroscopy (EDS), X-Ray Diffraction (XRD) and Particle-Induced X-ray Emission (PIXE). In order to have reliable quantitative results from the NRA technique, the cross sections of the deuteron reaction on beryllium were measured.

The carbon is an element that still exists in the ILW JET tokamak as remains from the previous wall [97] and some parts of the new wall consist of carbon (Figure 6). The investigation of the quantification of the carbon with high accuracy is missing from the literature. In the current thesis the amount of deposited carbon was studied as a function of a) the position in the main chamber of the JET tokamak, b) the ILW campaign and its depth profile was assessed. In addition, the erosion of the sample surface, the deposition of other elements and most importantly the fuel retention were also investigated. By the compilation of the results from the various techniques, a comprehensive overview of the plasma – wall interaction was achieved for the investigated positions of the JET tokamak.

It is very important to have reliable differential cross section of the detected elements in order to obtain correct quantitative NRA results. The differential cross sections of the deuteron reaction on carbon and oxygen are well defined and the evaluation values have been calculated from SigmaCalc archive [98]. On the other hand, there is a disagreement in the literature values about the differential cross sections of deuteron on beryllium. Therefore, the differential cross sections of the deuteron reaction on beryllium at energies and angles suitable for NRA measurements were measured to be used in the current and in future works.

Chapter 2: Methodology: Principles and Experimental Setups

In this chapter the basic physical principles and the experimental setup of the employed analytical techniques, namely the ion beam analysis (IBA), X-ray Florescence Spectroscopy (XRF), Scanning Electron Microscopy (SEM) along with Energy Dispersive Spectroscopy (EDS) and X-ray Diffraction (XRD) are described.

2.1 Ion Beam Analysis

IBA is a powerful tool employing accelerated ions to study the composition of a sample near the surface. The IBA includes a set of techniques. Each technique is characterized by the detected radiation or particle. In the Rutherford Backscattering Spectroscopy (RBS), the scattered particles from the nucleus-target at the back angles are detected. In the Nuclear Reaction Analysis (NRA) the products of a nuclear reaction between the projectile and the nucleus-target are detected. In the Particle-Induced X-Ray Emission (PIXE), the emitted X-rays of the atom after its excitation are detected. In the Particle Induced Gamma ray Emission (PIGE) gamma rays emitted by excited nuclei are detected.

2.1.1 Rutherford Backscattering Spectroscopy

RBS takes advantage of the energy that the particle loses in the matter and the elastic scattering between the projectile and the nucleus target and the elemental concentration and depth profile of the sample are assessed. In the following sections, we describe the three basic physical mechanisms which take place and the basic principles of the technique.

Stopping power

When a charged particle penetrates the matter, it loses energy due to the interaction with the atoms. There are two kinds of interaction that reduce the energy of the projectile: the elastic collisions with the target atom nuclei (nuclear stopping power) and the inelastic collisions with the electrons (electronic stopping power). For high mass projectiles, the electronic stopping power dominates at high energy, but when the energy is reduced the nuclear stopping power becomes dominant (Figure 13b). For low mass particles, the nuclear stopping power is negligible and only the electronic stopping power contributes to the energy decrease (Figure 13a). Knowing the energy loss, the correlation between the detected energy and the depth of the interaction is achieved.

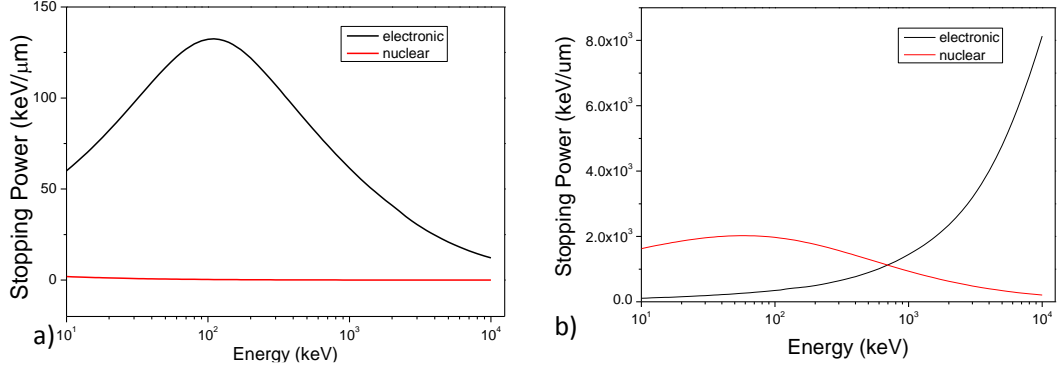


Figure 13: a) The electronic (black) and the nuclear (red) stopping power of the deuteron beam in a beryllium target and b) the electronic (black) and nuclear stopping power of iron beam in an iron target.

Now we focus on the deuteron beam in a beryllium target where only the electronic stopping power is important. There are several formulas to calculate the electronic stopping power of light elements but in our analysis the empirical Ziegler-Biersack formula was used as described below [99]. The energy loss is correlated with the stopping power via the equation:

$$-\frac{dE}{dx} = S_e(E) \quad (2.1)$$

For the energy range 10 keV/amu – 10 MeV/amu the electronic stopping power is:

$$S_e = \frac{S_{Low}S_{High}}{S_{Low} + S_{High}} \quad (2.2)$$

$$S_{Low} = C_1E^{C_2} + C_3E^{C_4} \quad (2.3)$$

$$S_{High} = \frac{C_5}{E^{C_6}} \ln\left(\frac{C_7}{E} + C_8E\right) \quad (2.4)$$

where S_{Low} and S_{High} are the stopping power from low and high energy, respectively, E is the energy of the projectile and $C_1 - C_8$ are fitting coefficients. For the energy range 10-100 MeV/amu the stopping power is given by:

$$S_e = C_9 + C_{10}x + C_{11}x^2 + \frac{C_{12}}{x} \quad (2.5)$$

where $x = \ln(E)/E$ and $C_9 - C_{12}$ are fitting coefficients. Below 10 keV/amu the electronic stopping power is given by:

$$S_e(E) = S_e(10) \left(\frac{E}{10}\right)^y \quad (2.6)$$

where $S_e(10)$ is the stopping power at 10 keV/amu and $y = 0.45$ for $Z_2 > 6$ and $y = 0.35$ for $Z_2 \leq 6$. Integrating the (2.1) we can calculate the depth where the particle have the energy we want:

$$\int_{E_0}^E -\frac{dE}{S(E)} = \int_0^x dx \quad (2.7)$$

For example choosing as initial energy, $E_0 = 1.35 \text{ MeV}$, and integrating until the deuteron stops, $E = 0$, we obtain the results depicted at Figure 14, Figure 14a gives the energy of the deuteron

with the depth inside a beryllium sample, while Figure 14b shows the stopping power as a function of the depth.

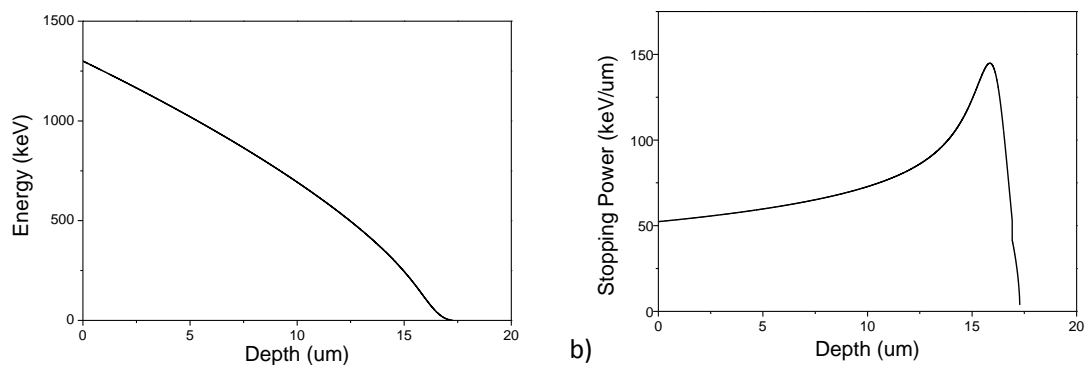


Figure 14: a) The energy of a deuteron having an initial energy of 1.35 MeV as function of depth in a beryllium target b) and the electronic stopping power as a function of depth as calculated from the Ziegler - Biersack.

Kinematic factor

During the elastic collision between the projectile and the nucleus – target, energy from the former is transferred to the latter. Using the laws of the conservation of the energy and momentum, the energy fraction of the projectile before and after the collision, E_1/E_0 , can be calculated. This fraction is named kinematic factor and is given by [100]:

$$K(\theta, M_1, M_2) = \frac{E_1}{E_0} = \left(\frac{(M_2^2 - M_1^2 \sin^2 \theta)^{\frac{1}{2}} + M_1 \cos \theta}{M_1 + M_2} \right)^2 \quad (2.8)$$

where M_1 is the mass of the projectile, M_2 is the mass of the target and θ is the scattering angle. Knowing the energy, the kind of the projectile and the scattering angle, the type of the nucleus-target is determined. Figure 15 depicts the kinematic factor dependence on the detection angle and the mass of the nucleus-target. This factor is reduced with the angle and increases with M_2 .

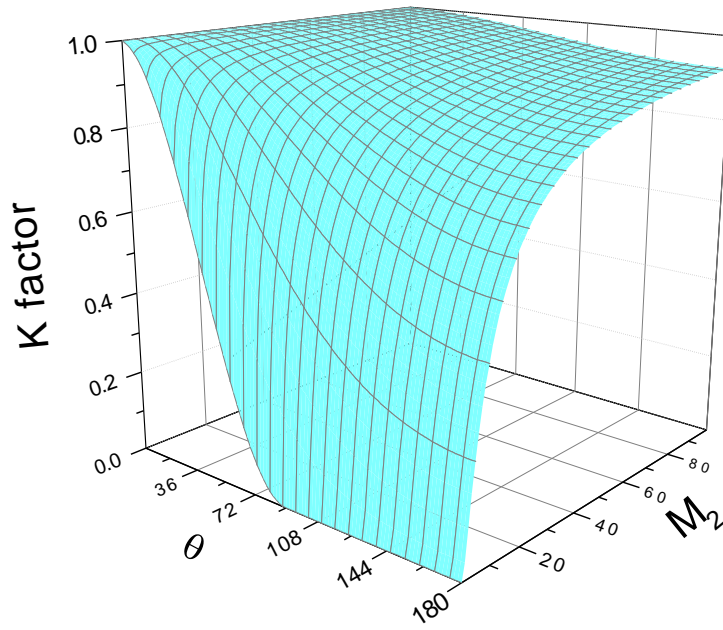


Figure 15: The kinematic factor of the deuteron as function of the scattering angle and the mass of the target.

The detected energy of the backscattered nucleus from a depth x is given by the relation:

$$E'_1 = K(E_0 - \Delta E_{in}) - \Delta E_{out} = KE_0 - \left(\frac{K}{\cos\theta_1} \left(\frac{dE}{dx} \right)_{in} + \frac{1}{\cos\theta_2} \left(\frac{dE}{dx} \right)_{out} \right) x \quad (2.9)$$

where θ_1 is the incident angle and θ_2 is the scattered angle.

Rutherford differential cross section

The previous two factors (S_e and K) determine the energy of the projectile in a certain depth (stopping power) and after the collision (kinematic factor). The number of scattered particles can be assessed by the third factor, the differential cross section which is given by the following expression:

$$\frac{d\sigma}{d\Omega} = \frac{\text{Number of scattered particles per unit time into solid angle } d\Omega}{\text{Number of incident particles per unit time per unit area}} \quad (2.10)$$

The differential cross section of the elastic scattering is called Rutherford differential cross section and can be calculated by the following equation:

$$\left(\frac{d\sigma}{d\Omega} \right)_{lab} = \left(\frac{Z_1 Z_2 e^2}{8\pi\epsilon_0 E} \right)^2 \frac{1}{\sin^4\theta} \frac{(M_2 \cos\theta + M_2^2 - M_1^2 \sin^2\theta)^{1/2}}{M_2(M_2^2 - M_1^2 \sin^2\theta)^{1/2}} \quad (2.11)$$

For $M_2 \gg M_1$ the previous equation is written:

$$\left(\frac{d\sigma}{d\Omega} \right)_{lab} = \left(\frac{Z_1 Z_2 e^2}{16\pi\epsilon_0 E} \right)^2 \frac{1}{\sin^4(\theta/2)} \quad (2.12)$$

where Z_1 and Z_2 are the atomic number of the projectile and the target, respectively. The differential cross section decreases with the scattering angle and the projectile energy and

increases with the masses of the projectile and the nucleus-target. By definition (2.10), the cross section for one nucleus-target can be written:

$$\frac{d\sigma}{d\Omega} = \frac{dY/d\Omega t}{Q/S_A t} \quad (2.13)$$

where dY is number of particles in solid angle $d\Omega$, t is the time, Q is number of the incident particles and S_A is the area. For a thin layer having a number of target nuclei equal to $N S_A$ where N is the atomic areal density of the layer the cross section is written:

$$\frac{d\sigma}{d\Omega} = \frac{dY/d\Omega}{Q/S_A} N S_A \quad (2.14)$$

Integrating for the solid angle of the detector, the yield of the detected particles is given by the equation:

$$Y(E, \theta) = Q \Omega N \frac{d\sigma}{d\Omega}(E, \theta) \quad (2.13)$$

Figure 16 presents the simulated spectrum of a carbon sample coated by a thin layer with gold and silver radiated by a He beam with an energy of 2 MeV. The mass of the gold is higher than silver so the energy and the yield of the scattered He by gold is higher than that by silver.

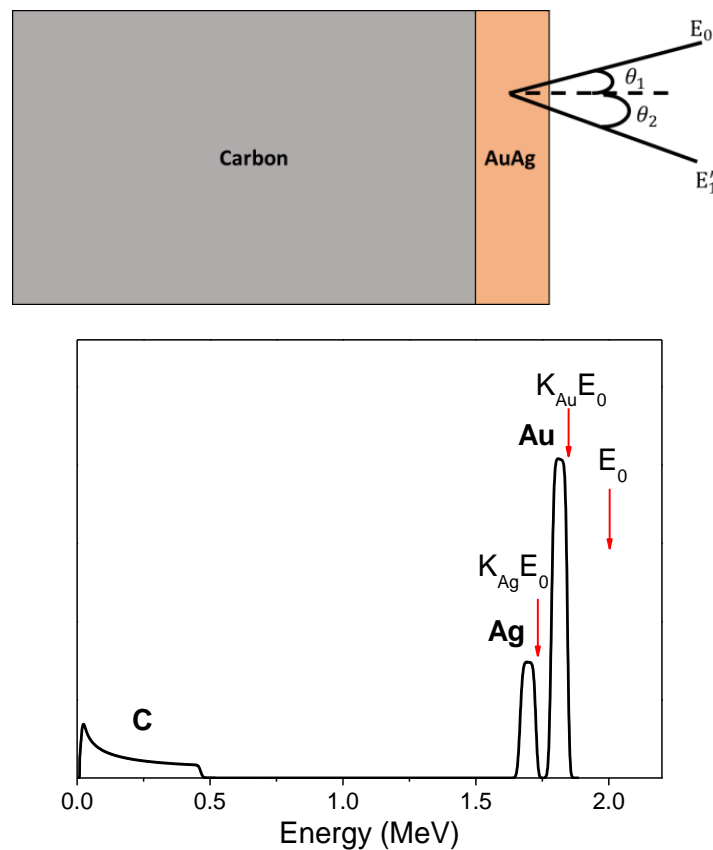


Figure 16: The simulation spectrum of the RBS technique using He beam on a sample with a thin layer of AuAg on C substrate. The beam energy is 2 MeV and the detector is placed at 170°.

2.1.2 Nuclear Reaction Analysis

NRA is another analytical technique employing light ion beams to detect light elements. The only difference with RBS is that the projectile and the nucleus-target undergo a nuclear reaction. The factors of this technique are the stopping power, which is the same as in RBS, the Q-value of the reaction and the differential cross section.

Q-value

In a nuclear reaction the sum of the masses of the reactants and the products is different. This difference is called Q-value. If the reaction is exothermic - the mass of the reactants is higher than the mass of the products - the light product will be detected with energy higher than that of the projectile. This property is very useful to detect light elements deposited on heavy substrate. Using the relativistic two-body reaction kinematic we can calculate the energy of the out-going particle 3 (Figure 17) with the relation:

$$E_3 = \left(\frac{1}{E_{tot}^2 - p_1^2 \cos^2 \theta_3} \right) \left\{ E_{tot} \left(m_2 E_1 + \frac{m_1^2 + m_2^2 + m_3^2 - m_4^2}{2} \right) \pm p_1 \cos \theta_3 \left[\left(m_2 E_1 + \frac{m_1^2 + m_2^2 - m_3^2 - m_4^2}{2} \right)^2 - m_3^2 m_4^2 - p_1^2 m_3^2 \sin^2 \theta_3 \right]^{\frac{1}{2}} \right\} \quad (2.14)$$

where m_1 is the mass of the projectile, m_2 is the mass of the target and m_3 and m_4 are the masses of the products. In the relativistic frame the energies, the momenta and the masses are connected via the relations:

$$E_1 = E_{kin1} + m_1, E_{tot} = E_1 + m_2, p_1 = \sqrt{E_1^2 - m_1^2}, E_{cm,tot} = (m_1^2 + m_2^2 + 2m_2 E_1)^{1/2}$$

The sign in (2.14) depends on the factor:

$$a = \frac{p_1}{E_{tot}} * \left(\frac{1 + \frac{m_3^2 - m_4^2}{E_{cm,tot}^2}}{\left\{ \left[1 - \left(\frac{m_3 + m_4}{E_{cm,tot}} \right)^2 \right] \left[1 - \left(\frac{m_3 - m_4}{E_{cm,tot}} \right)^2 \right] \right\}^{\frac{1}{2}}} \right) \quad (2.15)$$

If $\alpha > 1$ both signs of equation (2.14) are allowed and two solutions exist for the scattering angle θ_3 , else only the positive sign is acceptable [101].

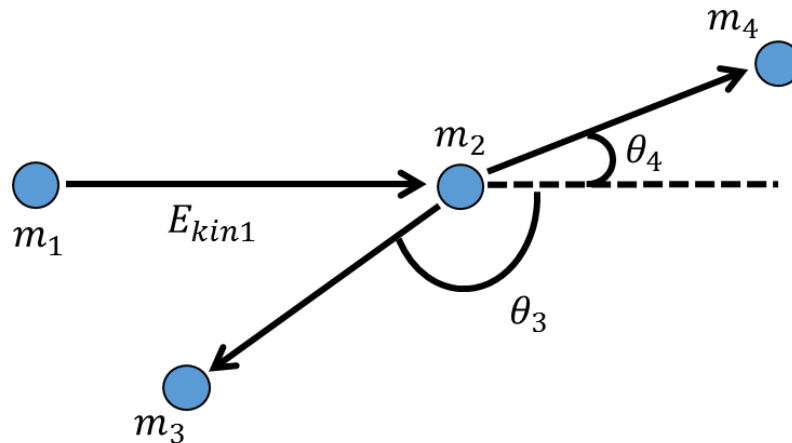


Figure 17: The nuclear reaction in the laboratory frame

Differential Cross Section

In contrast to RBS, there is no general formula to calculate the differential cross sections of the nuclear reactions, so it is necessary to measure them with suitable experiments. For the need of our work, the differential cross sections of the deuteron reactions on beryllium were measured (see Chapter 4).

2.1.3 Particle-Induced X-Ray Emission

The particle-induced X-ray emission (PIXE) technique is similar to XRF (its basic physical principles are presented in section 2.3), apart from the exciter source, which in this case is a beam of particles (proton, helium, or heavier ion of $1 - 3 \text{ MeV } amu^{-1}$). The beam is accelerated with a particle accelerator and the characteristic X-rays are detected by Si(Li), SDD or intrinsic Ge semiconductor detectors [100].

2.1.4 IBA Experimental Setup

The RBS, NRA and PIXE techniques can be carried out in the same experimental setup. For the ion accelerator of our experiment, a tandem Van de Graaff generator was used. Figure 18 presents schematically the parts of a Van de Graaff generator. The basic operation of the Van de Graaff generator is the following: the belt (4) is moving, charging the acrylic glass (3) positively taking electrons via the triboelectric effect [102]. The strong electric field around the positive upper roller (3) creates a very high electric field near the points of the comp (2). The electric field of the points of comp (2) ionize the air molecules. The electrons from the air molecules are attracted by the positively charged roller (3) and the comp neutralizes the air taking electron form the metal sphere (1). As a result, the metal sphere gets positive charged. On the other hand, the metal roller (6) picks the electrons from the negatively charged belt (5) which through the lower electrode are transferred to the spherical device (8) [103].

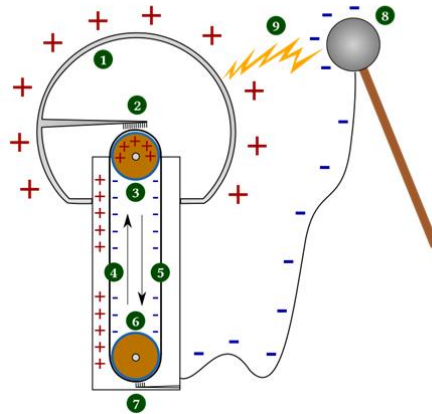


Figure 18: Schematic presentation of the Van de Graaff generator operation [103]

Another part of the experimental setup is the ion source. Two kinds of source will be described here: the sputtering and the duoplasmatron one. The sputtering source (Figure 19) is used to accelerate heavy ions such as O, C, Li etc positioned in the cathode. Neutral Cs atoms are extracted from the oven (300° C), come in contact with the ionizers, which consist of tungsten at 1000° C, and are ionized. Then the Cs ions hit the cathode and negatively charged ions are scattered by the cathode [104], which is the reason why the Cs is used. The applied voltage drives these ions out of the source in order to be accelerated by the Van de Graaff accelerator.

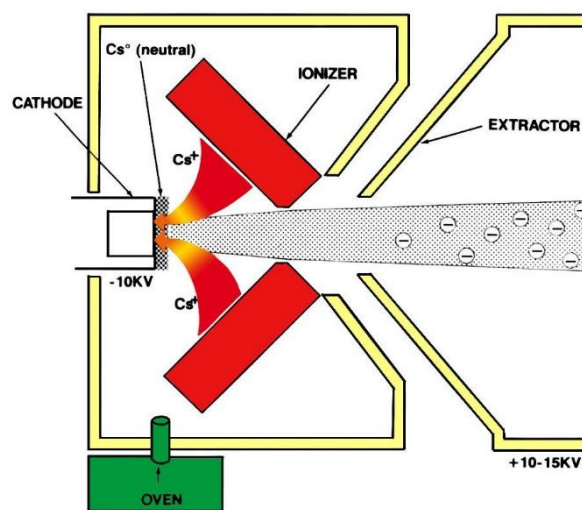


Figure 19: Schematic of the operation of the sputtering source [105].

The duoplasmatron source (Figure 20) is used for the acceleration of light ions such as hydrogen and deuteron. The basic parts of the source are: the filament, the intermediate electrode and the solenoid. The target inside the chamber is in plasma condition due to the low pressure and the high temperature. The cathode filament, which has “U” shape and consists of Pt coated with BaCO₃, is heated by a current of about 25 A. The BaCO₃ loses electrons, and creates negative charged ions. The role of the solenoid is to confine the plasma in the center of the chamber. While the use of the intermediate electrode is to “funnel” the ions and create higher density near the extraction hole. The ions area extracted from the source by applying a voltage of 20 kV [106].

In case of He ions, the duoplasmatron source can only produce positive He ions. In order to produce negative He ions additional 'exchange channel' is needed where positive He ions from duoplasmatron are transferred to negative ions with the help of vapours of Cs or Rb. For ^3He measurements done at RBI, another source was used, so called RF ion source that also produce positive ^3He ions, which are then converted to negative ions in the exchange channel using rubidium low vacuum vapours.

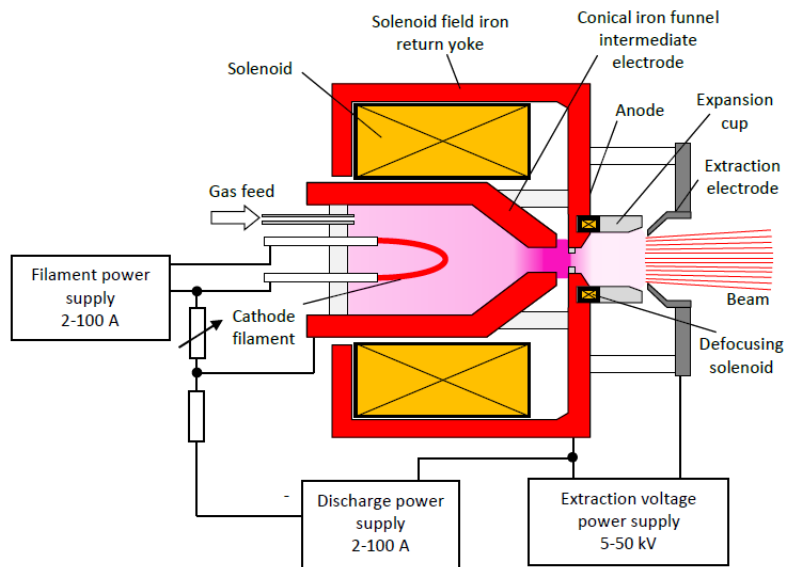


Figure 20: Schematic illustration of duoplasma source [106].

Figure 21 presents the whole experimental setup of the 5.5 MV HV Tandem accelerator at NCSR "Demokritos". Apart from the sources and the Van de Graaf generator, which have been already described, the setup comprises three magnets, two lens, two quadrupoles, three cups and two slits. The magnets change the direction of the ion beam and more specifically the first switching magnet chooses the source, the analyzing magnet defines the required energy of the beam and the second switching chooses the experimental line. The lens is used to focus the beam at low energies while the quadrupoles at high energies. The slits are used to collimate the beam and the cups measure the current of the beam.

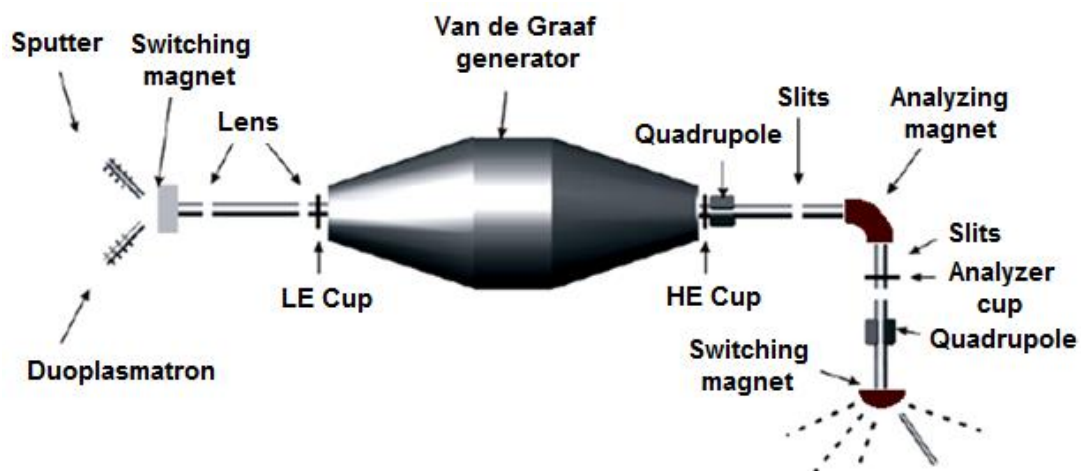


Figure 21: The parts of the Tandem accelerator at NCSR "Demokritos"

For the detection of the produced or scattered particles a silicon surface barrier (SSB) detector is used. The SSB (Figure 22) is a type of semiconductor detector, which consists of an n-type silicon coated with a thin p-type silicon in order to create the depletion layer. One surface is coated with a thin gold layer (typically $\sim 40 \text{ mg/cm}^2$) and the other one with aluminum (typically $\sim 40 \text{ mg/cm}^2$) to provide electrical contact. Depending on the applied voltage, the detector can be partially depleted (inactive entrance layer, Figure 22), totally depleted (no inactive layer), or over-depleted (higher applied potential than required for total depletion) [107].

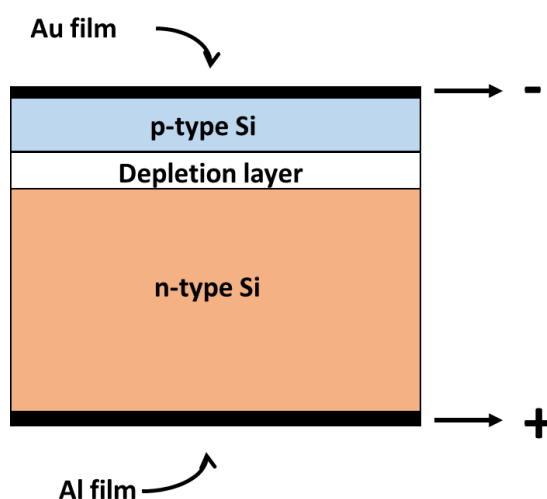


Figure 22: The silicon surface barrier detector with partial depletion

2.1.4.1 Deuteron Mili-Beam Measurements

The measurements were carried out at the 5.5 MV Tandem Accelerator Laboratory of NCSR “Demokritos”, Athens, Greece using NRA employing a 1.35 MeV deuteron beam. In a C. Evans & Assoc. scattering chamber, a silicon surface-barrier (SSB) detector was used to detect the products of the reactions and was placed at 170° with respect to the beam axis. During the measurement, the chamber was under vacuum (10^{-7} bar). The total charge of the tungsten lamellae measurement was obtained from the Rutherford backscattering of deuteron on tungsten. The total charge for the beryllium samples was obtained from the ${}^9\text{Be}(d,p_0){}^{10}\text{Be}$ peak. Additionally for the Be samples, a Kapton foil, having a thickness of $12.5 \mu\text{m}$, was employed in front of the detector in order to separate the ${}^{12}\text{C}(d,p_0){}^{13}\text{C}$ peak from the alpha particle produced from the beryllium via the ${}^9\text{Be}(d,\alpha_0,1){}^7\text{Li}$ reactions. For the quantification of the C, the ${}^{12}\text{C}(d,p_0){}^{13}\text{C}$ peak was chosen using the cross section of the reaction from the SigmaCalc archive [98] and the O content was assessed simulating the ${}^{16}\text{O}(d,p_0){}^{17}\text{O}$ with the evaluated cross section. To simulate the Be peaks, the cross sections assessed in chapter 4 were used. For tungsten peak the Rutherford cross section was used. Figure 23 presents the chamber where all the deuteron milli-beam NRA measurements were carried out.



Figure 23: The chamber for the ion milli-beam measurements of Tandem Accelerator at NCSR “Demokritos” in Athens.

2.1.4.2 Deuteron Micro-Beam Measurements

The ^2H micro-beam measurements were also performed using the 5.5 MT TN11 HV Tandem Accelerator at NCSR “Demokritos”, in Athens, Greece. The beam energy was 1.35 MeV and a silicon surface barrier (SSB) detector with depletion depth of 1000 μm was placed at an angle of 170° with respect to the beam axis. A kapton foil of 12.5 μm was also positioned to separate the $^9\text{C}(d,p_0)^{10}\text{C}$ peak from the alpha particles. The chamber was kept under vacuum (10^{-6} mbar). The beam spot of the micro-beam had a diameter smaller than 100 μm and the current was around 100 pA. The mapping area was $1.5 \times 1.5 \text{ mm}^2$ and the resolution 64×64 pixels. The data acquisition and the mapping was performed using the OMDAQ2007 software and appropriate hardware [108]. Figure 24 present the experiment line where the deuteron μbeam measurements were carried out.



Figure 24: The micro-beam experimental line of the of the Tandem accelerator at NCSR “Demokritos”

2.1.4.3 Helium Micro-Beam Measurements

The ^3He measurements were carried out at Ruder Boskovic Institute, in Zagreb, Croatia. The ^3He beam was accelerated by the 6 MV tandem Van de Graaff accelerator and 1.0 MV Tandetron

accelerator. The beam energies varied between 2 and 3 MeV, and the mapping areas were either $1 \times 1 \text{ mm}^2$ or $300 \times 300 \text{ }\mu\text{m}^2$. For the NRA spectra, a Partially Depleted Silicon Surface Barrier detector (PDSSB) with depletion depth of $2000 \text{ }\mu\text{m}$, with nominal active area of 300 mm^2 collimated to 230 mm^2 was used and placed at an angle of $135^\circ \pm 19^\circ$ with respect to the beam axis. The distance between the target and the detector was approximately 2.5 cm, which corresponds to a solid angle of 0.462 sr. For the PIXE spectra, a 30 mm^2 Si(Li) detector with a $12.5 \text{ }\mu\text{m}$ Be window was placed at 135° with respect to the beam axis at a distance of about 4 cm from the target covering a solid angle of 0.0176 sr. The effective detector X-ray energy resolution was about 160 eV (for the Mn K α line). A homemade chopper was used in order to estimate the current of the measurements. The data acquisition of the measured spectra and 2D intensity maps was performed using the in-house developed software package SPECTOR [109] and the hardware based on Xilinx Virtex 6 FPGAs. Figure 25 depicts some parts of the experimental setup of the Tandem accelerator at Ruđer Bošković Institute, in Zagreb.



Figure 25: a) The Van der Graaff accelerator, b) the source of the ^3He and c) the experimental line for the micro beam measurements at Ruđer Bošković Institute, in Zagreb.

For the deuterium quantification, the V. Kh. Alimov et al [110] cross section data for the $^2\text{H}(^3\text{He},p_0)^4\text{He}$ reaction and the N. P. Barradas et al [111] for the $^9\text{Be}(^3\text{He},p_{0,1})^{11}\text{B}$ reactions were used.

The quantitative analysis of all the NRA spectra was performed with the SIMNRA software [112].

2.2 X-Ray Fluorescence Spectroscopy

X-ray fluorescence (XRF) spectroscopy is a nondestructive analytical technique which is based on the emitted characteristic X-rays of a matter when it is bombarded with X- or γ - ray. This technique

is used to identify the elements of a sample with $Z > 11$ and assess their relevant concentrations with sensitivity of the order of some ppm (particles per million).

2.2.1 XRF Physical Principles

According to the Rutherford-Bohr model [113], the atom consists of a nucleus (with protons and neutrons) and electrons, which are revolving around it in determined orbits. These orbits are named shells and are characterized with the letters K, L, M etc. The electrons of the K-shell have the highest binding energy and are depicted as the nearest to the nucleus, then the L-shell follows and so on. Every shell is divided in one or more subshells as the quantum mechanics and the Pauli Exclusion Principle require [114]. For example, the L-shell consists of L_I, L_{II}, L_{III} with different energies (Figure 26).

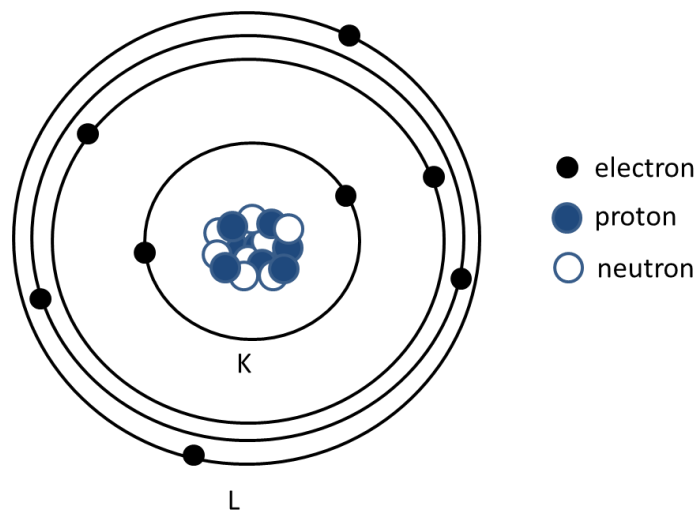


Figure 26: Structure of the oxygen atom showing the nucleus consisting of protons and neutrons and the K- and L- shells of electrons.

Generally when a photon passes through the matter, it can interact with the electron, the nucleus, the electric field and the meson field surrounding nucleons of an atom [115]. In the range of energy (1-100 keV) that we are interested, the photon interacts with the atomic electron via photoabsorption, Compton or Rayleigh scattering.

Photoabsorption is the process when a bound electron absorbs a photon (photoelectric effect). In this process the photon is completely absorbed and the electron is ejected from the orbit. The photon energy should be higher than the binding energy and the energy of the ejected electron is described by the following equation:

$$E = hf - W \quad (2.16)$$

where E is the kinetic energy of the electron which absorbs the photon, hf is the photon energy and W is the binding energy of the electron to the nucleus.

The cross section of the interaction, τ , is proportional to Z^4 for low energies and Z^5 for higher ones [116] and presents peaks when the photon energy is just higher than the binding energy of a shell. These peaks are named edges and they are characterized by the name of the shell which they are originated from, for example K-edge.

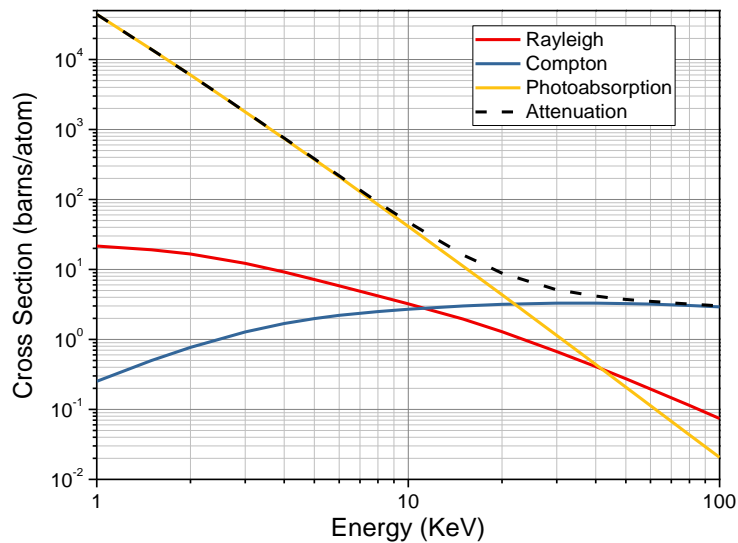
Rayleigh scattering constitutes the elastic scattering of a photon with an electron. A low-energy photon can be deflected by a tightly bound electron without losing energy while the atom is neither ionized nor excited. Rayleigh scattering occurs mostly at low energies and for high-Z materials and its cross section, σ_R , is proportional to Z^2 [116].

In Compton scattering, a photon collides with an electron, loses some of its energy and is deflected from the original direction of motion. The theory of this interaction was developed initially, assuming the electron to be free and rest [117]. In order to apply this theory to an atomic electron, Jauch and Rohrlich [118] generalized the theory to the case where the electron is free but in motion. Approximation of the binding correction have also been done, taking into account all the atomic electrons (incoherent scattering function $S(q,Z)$ [119]). The cross section, σ_C , of this interaction is proportional to Z [116].

Figure 27 presents the cross sections of a light (carbon) and a heavy (tungsten) element. The attenuation cross section constitutes the sum of the cross sections of the previous interactions:

$$\sigma_{at} = \tau + \sigma_R + \sigma_C \quad (2.17)$$

For light elements the cross section of the photoabsorption is dominant for energies up to 20 keV. Above this energy the Compton scattering becomes significant. For heavy elements the attenuation cross section is almost equal to the photoabsorption for the whole energy range, as the other cross sections are of lower order of magnitude. Additionally, the K-, L- and M- edges are distinguished.



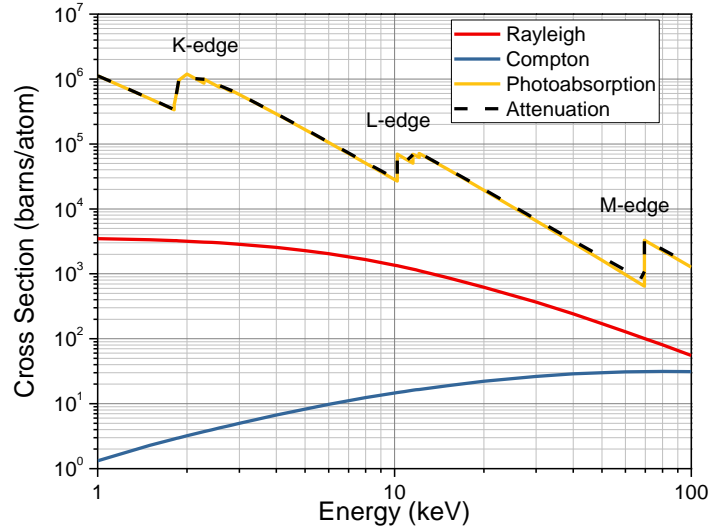


Figure 27: Cross section of Rayleigh and Compton scattering, photoabsorption and attenuation of the elements: a) carbon and b) tungsten [120].

The attenuation of a monoenergetic beam of photons in homogeneous matter is described by the Beer-Lambert law:

$$I = I_0 e^{-\mu x} = I_0 e^{-\kappa \rho x} \quad (2.18)$$

where I is the transmitted intensity, I_0 is the incident intensity, x is the length over which attenuation takes place, $\kappa = \mu/\rho$ is the mass attenuation coefficient, μ the linear attenuation coefficient and ρ the mass density. μ/ρ can be calculated by the equation:

$$\mu/\rho = \sigma_{tot} \frac{N_0}{A} \quad (2.19)$$

where N_0 is Avogadro number and A is the mass number. According to Eq. 2.19 the mass attenuation coefficient has the same behavior as the attenuation cross section, i.e. K-edge etc. Eq. 2.18 is used to calculate the maximum depth of X-rays inside matter.

As we have already discussed, an electron can absorb a photon being ejected from the shell and leaving a vacancy. Then another electron from an outer subshell (or even a free electron) fills the vacancy emitting a photon with energy of the difference between the final and the initial shell. This procedure constitutes one expression of the general phenomenon of fluorescence. The energy of the emitted photon is between 1-100 keV depending on the element, namely in the X-rays region.

In this work, we will use the Siegbahn notation [121] to refer to a transition, i.e. for example the transition $L_{III} \rightarrow K$ is named K_{α_1} line. Additionally, for the transition energy values the database of the National Physical Laboratory is used [122].

Every transition has a unique energy value for each element, as any subshell has an individual energy. For example, the K_{α_1} and K_{β_1} for W have energies of 59.318 keV and 67.244 keV, respectively. Additionally, for different elements the same noted transitions have different energy values, for example the K_{α_1} transition for the elements of Mo and W has $E = 17.479 \text{ keV}$ and $E = 59.318 \text{ keV}$, respectively. Taking advantage of these properties, one can determine the elements of an analyte. Figure 28 presents the process of X-ray fluorescence.

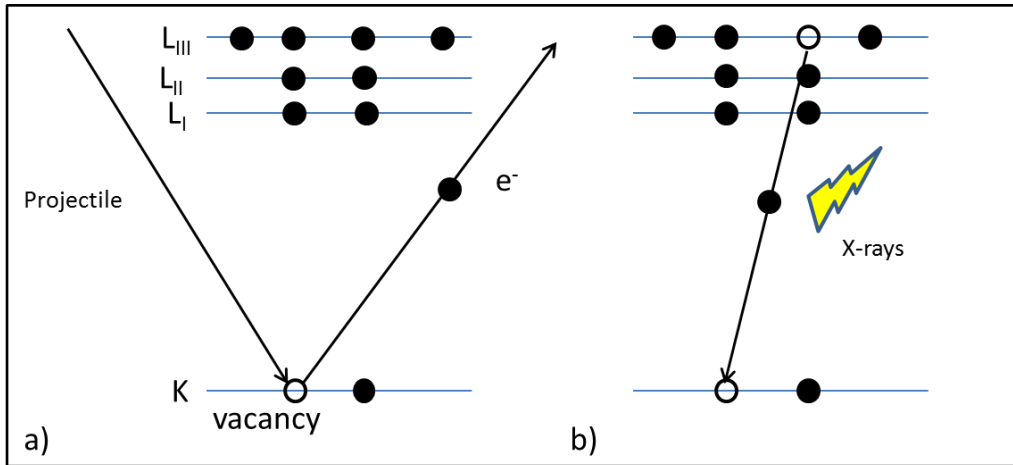


Figure 28: a) Photoabsorption of a K shell electron and its ejection from the atom leaving a vacancy; b) the filling of the vacancy by an electron from the L_{III} subshell with X-ray emission.

2.2.2 XRF Experimental Setup

The XRF experimental setup consists of the primary X-ray source, the filters, the sample holder and the detector of the X-rays produced by the analyte.

The X-ray source emits the primary X-rays which excite the atoms of the analyte. It is known that if a charged particle is accelerated or decelerated, it radiates (Bremsstrahlung) [123]. This radiation is continuum and its maximum value is the energy of the particle. In practice, a heated filament emits electrons by thermionic emission, a high voltage accelerates these electrons in order to hit a target with high Z (as Au or Ag) which is placed in the anode and decelerates them abruptly (Figure 29). It is important to mention here that if the electron energy is higher than the K edge of the anode target element, apart from the continuum radiation, the source emits also the characteristic X-rays. Additionally, we must underline that both the continuum and discrete radiations contribute to the excitation of the atoms of the sample. Figure 30 presents the spectra of a source with Ag anode with different voltage accelerations.

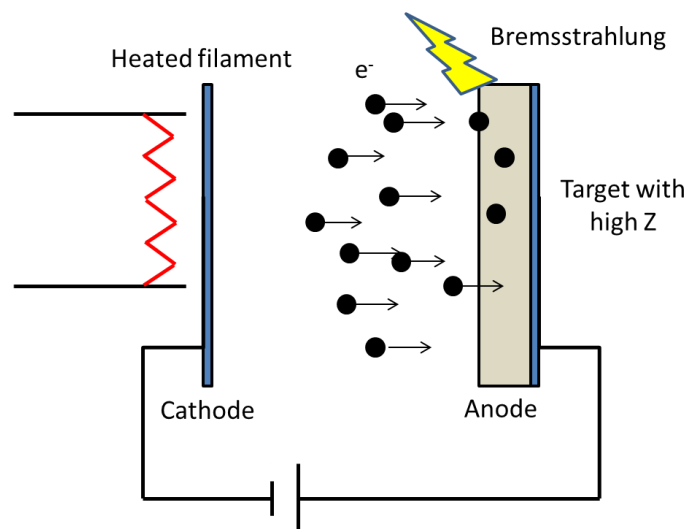


Figure 29: The operation of an X-ray source

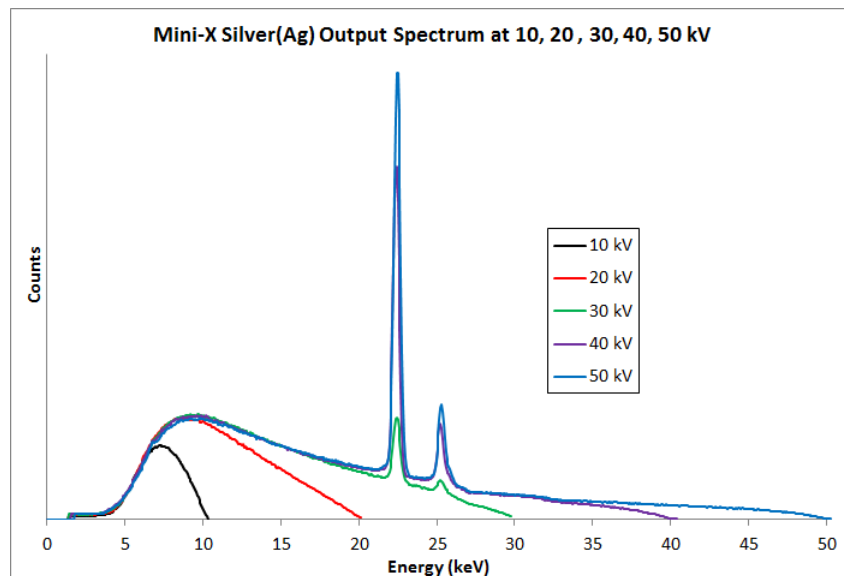
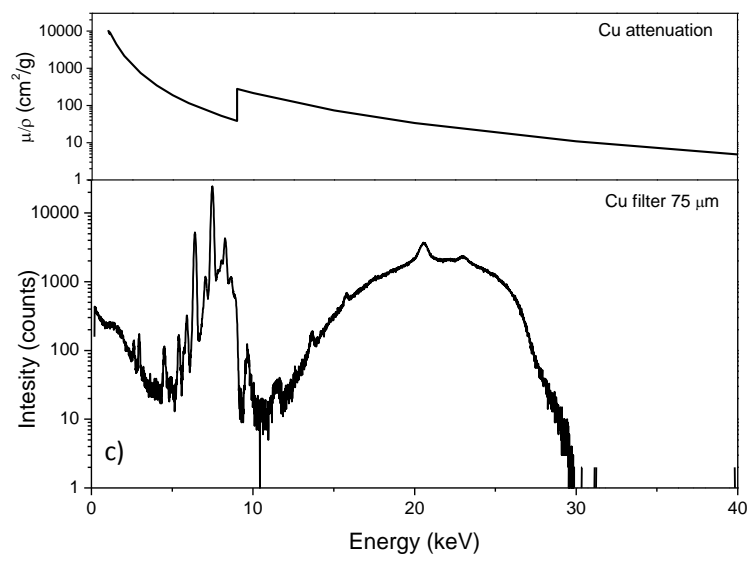
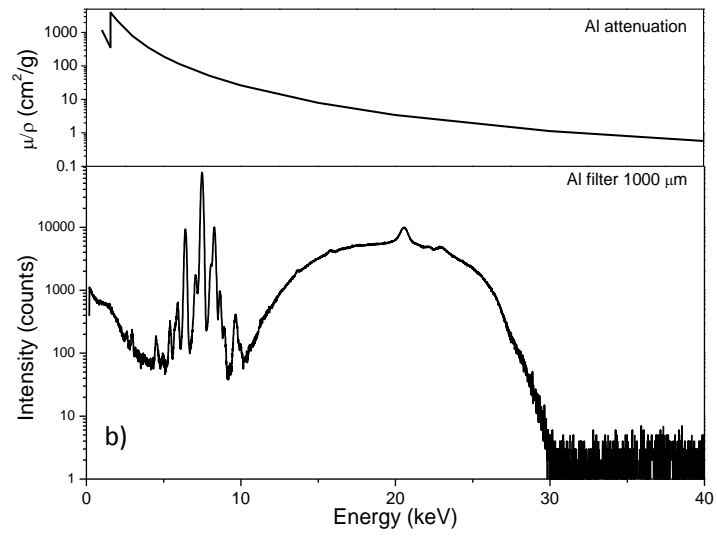
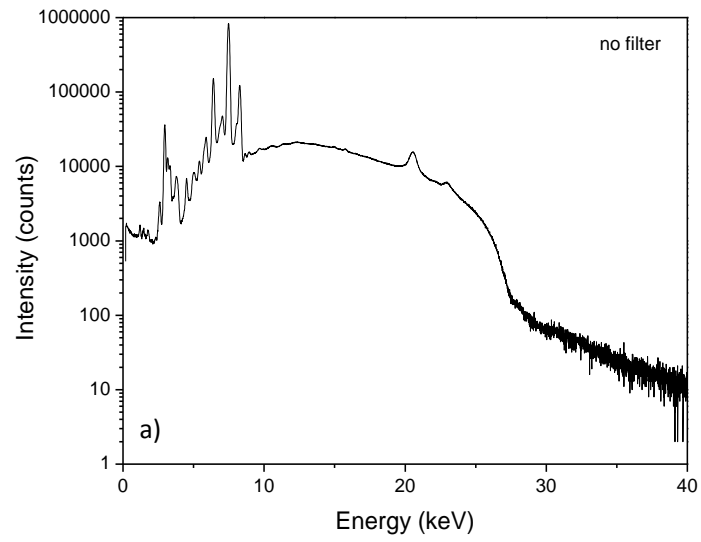


Figure 30: Spectra of Ag source using different voltage (electron). Above 20 keV the characteristic X-ray of the source is produced [124]

Another type of excitation source is a radioactive source which emits X-rays with appropriate energy. The energy of X-rays is discrete and depends on the source. A common source is ^{109}Cd , which has half-life 470 days and emits X-rays with energies of 22.16 keV, 24.94 keV and 88.03 keV [125].

A part of the X-rays from the source can be scattered by the analyte and thus it can reach the detector. These X-rays constitute the background of the measurement. The use of filters helps to reduce the background of a chosen region of energies. The filter is placed between source and sample and absorbs a percentage of the continuum primary radiation. The absorption cross section depends on the energy of the X-ray and the filter element. Using the appropriate filter, we can choose which region of X-ray energies will be absorbed more efficiently. So it is important to know how a matter attenuates the photons. In the frame of the filter choice for the measurement of the beryllium samples, different elements and thicknesses as filters were tested. Figure 31 shows the XRF spectra of the ILW-1 IWGL outer (27), see the sample description below, with filters of different elements and the corresponding attenuation.



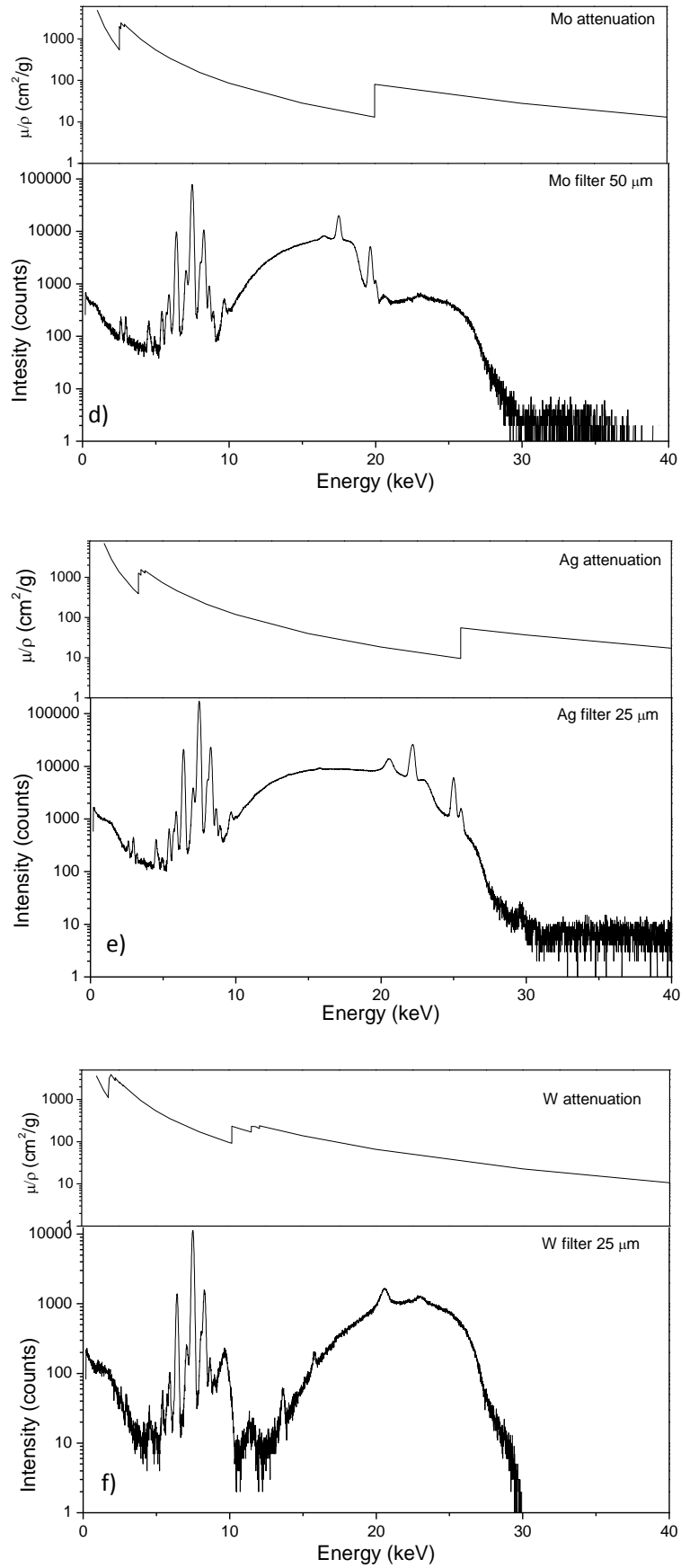


Figure 31: The ILW-1 IWGL outer (27) XRF spectra using a) no any filter, b) Al, c) Cu, d) Mo, e) Ag and f) W

The XRF spectrum of the ILW-1 IWGL outer (27) without any filter (Figure 31a) has a very high background and the use of filter is mandatory; additionally, it is clear that the interesting energy area is 0 – 12 keV, where the peaks of the elements were detected. The Al filter (Figure 31b) reduces the background uniformly as the K edge is at low energies and the peaks stand out. The Cu filter (Figure 31c) have the intense absorption above the energy of 10 keV and the interested peaks are not so clear. The Mo (Figure 31d) and Ag (Figure 31e) filters absorb intensely above the energy of 20 keV and 25 keV, respectively. Moreover, the Ka and Kb peaks of these elements are observed. The W filter (Figure 31f) absorbs efficiently the energy range of 0 – 12 keV, but the L peaks of the W were detected, an element that is also observed in sample. So, the Al filter is decided to be used for the measurements as its absorption is efficient in the energy range, we are interested in, and no extra peaks are added in the spectrum.

Silicon Drift Detector

The detector which is used in this technique is a silicon drift detector. Its operating principle are same with a common semiconductor detector (see details about this kind of detector in [126]). Except for the different electrode structure which consists of a series of drift rings which produce a radial field guiding the electron to the anode (Figure 32) [127].

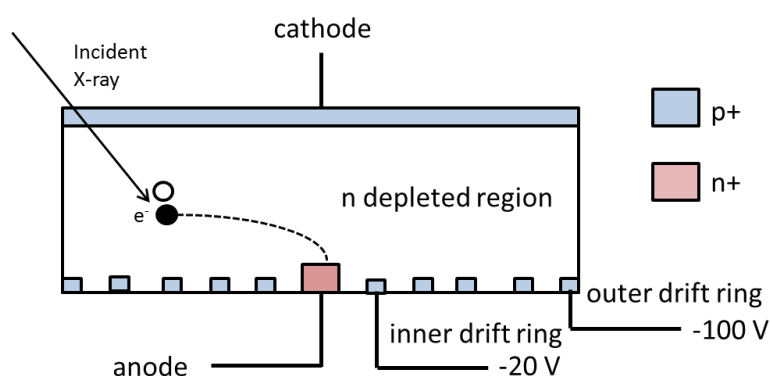


Figure 32: Cross section of a silicon drift detector

XRF spectrum

Apart from the secondary X-rays of the analyte and the primary (continuum and characteristic) X-rays which are emitted from the source and reflected by the analyte, the detector records two kinds of X-rays which are originated from the secondary X-rays, but their energies have been changed producing the following additional peaks:

- Escape peak:* if the secondary X-ray of the analyte excites the silicon of the detector and the photon of the Si fluorescence is not detected then the detector records the energy of the secondary X-ray reduced by the characteristic X-ray energy of the Si (1.75 keV).
- Sum peak:* If two X-rays come to detector in so close time that it cannot separates them, then they are recorded as one with energy the sum of their energies [128].

The XRF measurements were carried out using Amptek's system with an Ag x-ray tube, a high voltage of 30 kV and a silicon drift detector [129]. A collimator of 1 mm diameter and an aluminium filter of 500 μm or 1000 μm was used. Quantification was achieved employing XRF-FP x-ray analysis software [129] and using a NIST stainless steel 316 standard [130]. Figure 33 depicts the

experimental setup where we observe the fan to cool the source, the Ag source, the detector and the sample holder made of Teflon.

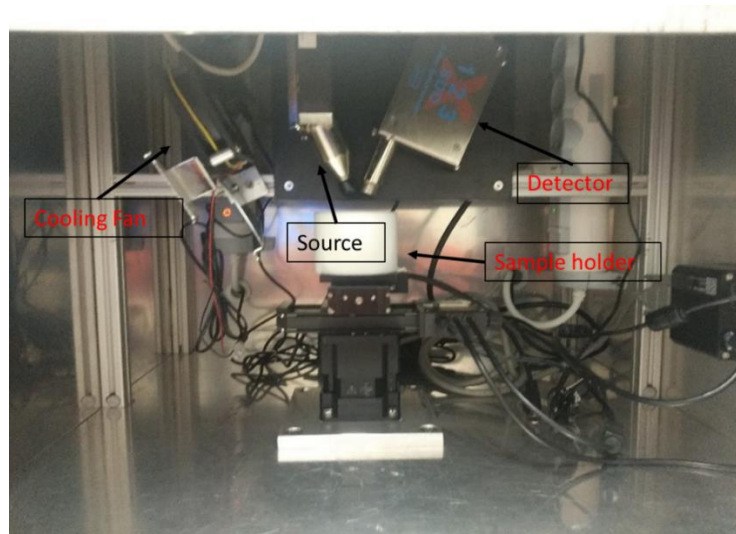


Figure 33: The experimental setup of the XRF technique

2.3 Scanning Electron Microscopy

Scanning electron microscopy (SEM) is a non-destructive analytical technique which based on the interaction of an electron beam with the atoms of the sample, provides qualitative information about the surface morphology and the composition of the sample. The electron can also excite the atoms of the sample with the same way as the X-rays do (see section 2.2.1) and the relative concentrations of the detected elements can be assessed.

The electrons can be scattered by the atoms of the matter with two ways: elastically or inelastically. The electrons which are scattered elastically at large angles, after one or more scattering process, can leave the sample and provide one way of sample surface imaging. The equation for the total elastic scattering cross section is given by the relation [131]:

$$\sigma_T = \frac{3.0 \times 10^{-18} Z^{1.7}}{(E + 0.005Z^{1.7}E^{0.5} + (0.007Z^2)/E^{0.5})} \text{ cm}^2 \quad (2.20)$$

For a certain energy beam, the cross section is proportional to approximately Z^2 , so the backscattered electrons give information about the material composition.

The electrons can also interact inelastically with the electrons of the atomic shells giving a part of their energy. The bound electrons leave the atom creating a vacancy and as they have low energy only these which are near the surface can leave sample (secondary electrons), providing information about the morphology of the sample surface. The vacancy will be filled with the same mechanism as in XRF spectroscopy by the emission of X-rays (see section 2.2.1). The emitted X-rays may leave the sample and be detected or be absorbed by an electron which also may leave the sample (Auger electron). So at the same time with the production of surface images, we can detect the produced X-rays and have a quantitative result for the same area but not for the same volume (Figure 34) [132].

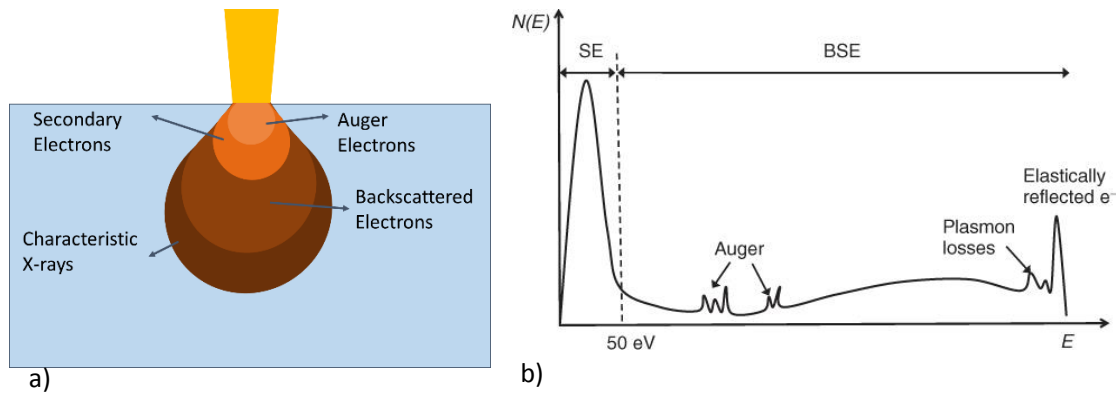


Figure 34: a) The volumes where the Auger, the secondary, the backscattered electrons and the characteristic X-rays come from and b) the energy spectrum of the electrons [132]

2.3.1 SEM Experimental Setup

The electron microscope (Figure 35) consists of four main components:

a) Electron source (electron gun): The most common electron source is the thermionic one which emit electrons via a filament (cathode) made of a thin W wire by heating it at high temperature (about 2800 K). The thermionic emission is described by the Richardson's law:

$$J = AT^2 e^{-\frac{\phi}{kT}} \quad (2.21)$$

where J is the current density, T is the temperature, k is the Boltzmann's constant, A is the Richardson's constant and ϕ is the work function. From the equation it is clear that an element with high melting point and low work function is required this is the reason why the W is used.

b) Lens system: The beam enters the lens system in order to be focused and exits to hit the specimen surface. There are two kinds of lens: the electrostatic and the magnetic one. The electrostatic lens produces appropriate electric fields while the magnetic lens uses coils to create magnetic field to focus the beam (Figure 36).

c) Scan unit: The scan generator signal, fed to the deflection systems, moves the beam in a raster pattern over the specimen area. The electrical voltage changes as it rasters, which provides serial information of the specimen surface. This signal, modulated by the detection system signal, produces the onscreen image.

d) Detection unit: Electrons striking the specimen react with its surface producing three basic types of signal: backscatter electrons, secondary electrons and X-rays. The detection system picks up these signals, converts them into an amplified electrical signal which is sent to the control PC and displayed on the monitor [133]. The most common detector for electrons is the Everhart Thornley detector, a scintillator photo-multiplier type one.

The scintillator (Figure 37) consists of materials which convert the kinematic energy of charged particles into light with high scintillation efficiency. The conversion should be linear which means that the light yield should be proportional to deposited energy. Additionally, the medium should be transparent to the wavelength of its own emission for good light collection. Moreover, the decay time of the induced luminescence should be short so that fast signal pulses can be generated. The produced light is converted into an electrical signal via the photomultiplier: The photon interacts with the photocathode due to the photoelectric phenomenon and a low energy electron is ejected. This electron is accelerated and interact with the second dynodes creating more electrons. After 12 dynodes, a well-enhanced sign has been produced [126].

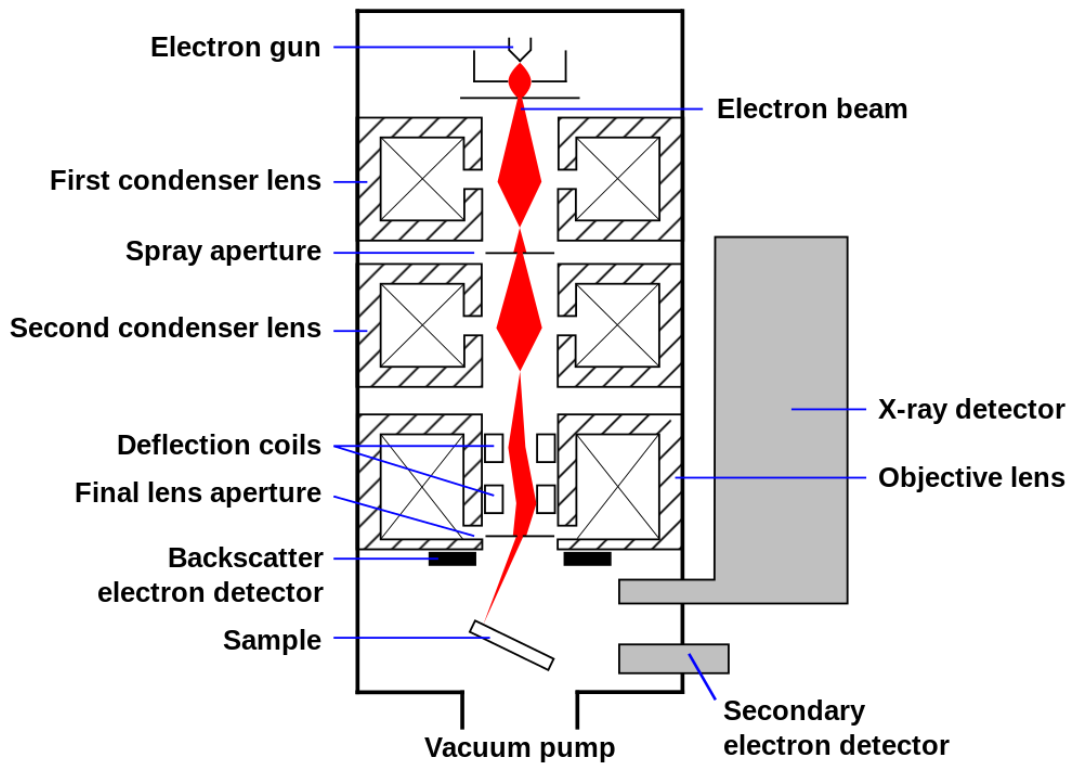


Figure 35: The experimental setup of the Scanning Electron Microscopy [134].

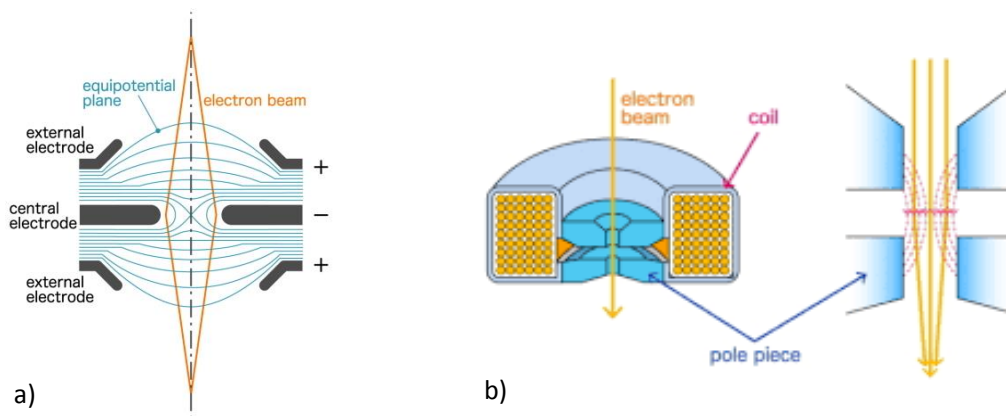


Figure 36: A schematic presentation of the operation of a) an electrostatic lens and b) a magnetic one [135].

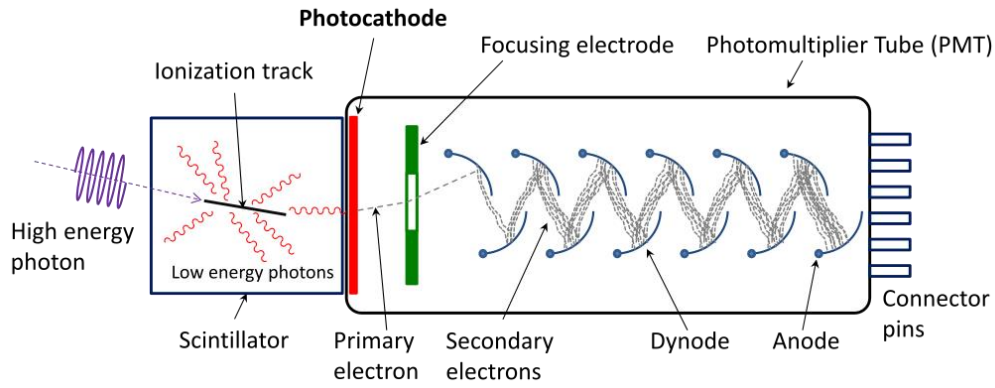


Figure 37: The parts and the operation of the scintillator [136].

SEM measurements were carried out on a FEI Quanta Inspect SEM (Figure 38) coupled with EDS.



Figure 38: The experimental setup of the SEM technique.

2.4 X-Ray Diffraction

X-ray diffraction is a non-destructive technique for characterizing crystalline materials. It provides information on structures, phases, preferred crystal orientation, and other structural parameters, such as average grain size, crystallinity, stain, and crystal defects.

Crystals are materials in solid state composed of atoms, ions or molecules arranged in periodic pattern in three dimensions, creating a lattice. When the periodicity extends throughout a certain piece of material, it is called single-crystal. On the other hand, in the polycrystalline materials the periodicity of structure is interrupted at the grain boundaries [137]. A lattice in three dimensions is defined by three fundamental translation vectors \vec{a} , \vec{b} and \vec{c} such that the atomic arrangement looks like the same when viewed from a point $\vec{r} = n_1\vec{a} + n_2\vec{b} + n_3\vec{c}$, where n_1 , n_2 and n_3 are

integers. Unit cell is the smallest volume which is repeated in all directions. The unit cell is determined by the three edges (a_1 , a_2 and a_3) and the angles between them (α_{12} , α_{13} and α_{23}). If the unit cell has one lattice point per unit cell is called primitive otherwise it is called non primitive [138]. Figure 39 presents the Bravais lattice, the 14 different 3-dimensional configurations into which atoms can be arranged in crystals.

The crystal lattice may be regarded as made up of an infinite set of parallel equidistant planes passing through the lattice points which are known as lattice planes. The orientation of planes or faces in a crystal can be described in terms of their intercepts on the three axes. Miller introduced a system to designate a plane in a crystal i.e. a set of three numbers to specify a plane in a crystal. This set of three numbers is known as “Miller Indices” of the concerned plane. Miller indices (hkl) is defined as the reciprocals of the intercepts made by the plane on the three axes [138].

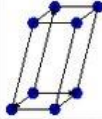
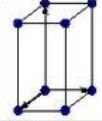


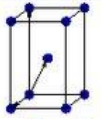

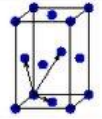
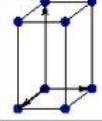
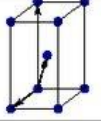
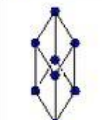
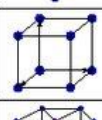
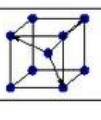
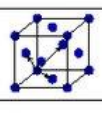
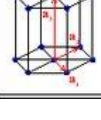
Bravais lattice	Parameters	Simple (P)	Volume centered (I)	Base centered (C)	Face centered (F)
Triclinic	$a_1 \neq a_2 \neq a_3$ $\alpha_{12} \neq \alpha_{23} \neq \alpha_{31}$				
Monoclinic	$a_1 \neq a_2 \neq a_3$ $\alpha_{23} = \alpha_{31} = 90^\circ$ $\alpha_{12} \neq 90^\circ$				
Orthorhombic	$a_1 \neq a_2 \neq a_3$ $\alpha_{12} = \alpha_{23} = \alpha_{31} = 90^\circ$				
Tetragonal	$a_1 = a_2 \neq a_3$ $\alpha_{12} = \alpha_{23} = \alpha_{31} = 90^\circ$				
Trigonal	$a_1 = a_2 = a_3$ $\alpha_{12} = \alpha_{23} = \alpha_{31} < 120^\circ$				
Cubic	$a_1 = a_2 = a_3$ $\alpha_{12} = \alpha_{23} = \alpha_{31} = 90^\circ$				
Hexagonal	$a_1 = a_2 \neq a_3$ $\alpha_{12} = 120^\circ$ $\alpha_{23} = \alpha_{31} = 90^\circ$				

Figure 39: The 14 Bravais lattice in three dimensions [139].

X-ray diffraction occurs when the reflected photons from the atoms of a crystalline material interfere constructively. The condition for X-ray diffraction is expressed by Bragg's law,

$$\vec{G}(hkl) = \vec{k}' - \vec{k} = \vec{Q} \quad (2.21)$$

where $\vec{k} = \frac{2\pi}{\lambda} \hat{n}$ and $\vec{k}' = \frac{2\pi}{\lambda} \hat{n}'$ is the incident and scattered wave vector of the X-ray beam, λ is the wavelength and \hat{n} and \hat{n}' are the incident and the scattered waves direction. The vector $\vec{G}(hkl)$ is the reciprocal lattice vector of the (hkl) set of crystal lattice planes with magnitude,

$$|\vec{G}(hkl)| = \frac{2\pi}{d_{hkl}} \quad (2.22)$$

where d_{hkl} is the interplanar distance. The second form of Bragg's law results from the combination of Equations 2.21 and 2.22,

$$2d_{hkl} \sin \theta_B = \lambda \quad (2.23)$$

Using Bragg's law for a given position $2\theta_B$ where a strong peak is recorded at the XRD spectrum the interplanar distance d_{hkl} of the specific hkl set of lattice planes can be computed.

There are two XRD experimental configurations,

a. The *symmetric or asymmetric X-ray diffraction*: In this setup the motion of the X-ray tube and detector is coupled, i.e.

$$\begin{aligned} \theta_n &= \theta_0 - n\delta\theta \\ \theta_n &= \theta_0 + n\delta\theta \end{aligned} \quad (2.24)$$

b. with n steps. During the scan the direction of the scattering vector is constant while its magnitude varies, thus it provides the ability to investigate selectively crystal planes of a specific orientation determined by the direction of the scattering vector that is chosen.

The *grazing incidence X-ray diffraction (GIXRD)*: In this mode the incident beam is kept fixed at a small angle and detector rotates around the center of the goniometer (Figure 40). During a 2θ scan both direction and magnitude of the scattering vector change enabling the investigation of the in-plane crystal strain in polycrystalline films. The X-ray penetration depth reduces the smaller the incident angle hence this technique is surface sensitive.

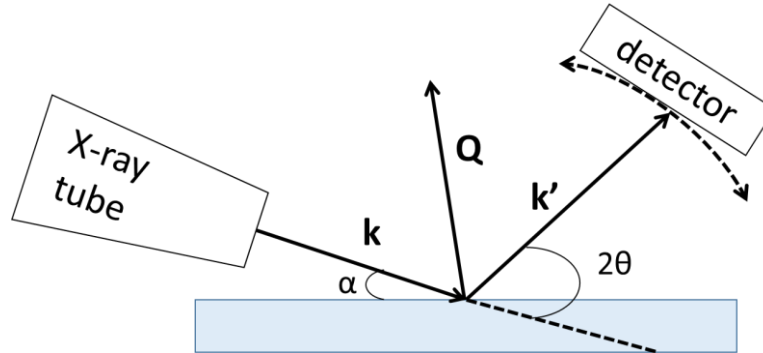


Figure 40: Grazing Incidence X-Ray Diffraction geometry.

4.4.1 X-ray Diffraction Setup

XRD measurements were carried out on a Bruker D8 spectrometer using Cu K_α radiation, a parallel beam stemming from a Göbbel mirror and a scintillator point or a linear position sensitive detector. Figure 41 depicts the experimental setup, where we observe the Cu source, the sample holder and the detector.

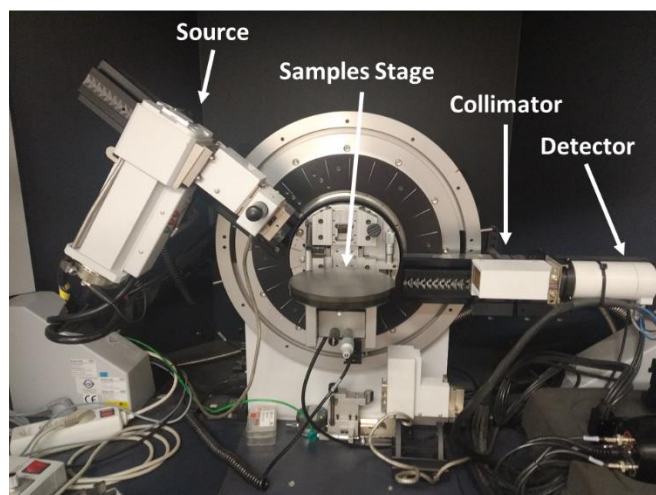


Figure 41: XRD experimental setup with the scintillator point detector.

Chapter 3: Cross Sections of Deuteron Reaction on Beryllium

The quantification of the NRA measurements of the beryllium samples requires the prior knowledge of the differential cross sections of the deuteron reactions on beryllium. Figure 42 shows the differential cross section of the ${}^9\text{Be}(d,p_0){}^{10}\text{Be}$ reaction as measured by T. Ishematsu et al [140], E. Friedland et al [141], I. I. Bondouk et al [142] and A. S. Deineko et al [143] in the detection angle range of $140^\circ - 165.2^\circ$. It is obvious that the literature differential cross section values are not reliable as there is a disagreement among each other. Thus the measurements of the differential cross sections of the ${}^9\text{Be}(d,p_0){}^{10}\text{Be}$, ${}^9\text{Be}(d,p_1){}^{10}\text{Be}$, ${}^9\text{Be}(d,\alpha_0){}^7\text{Li}$ and ${}^9\text{Be}(d,\alpha_1){}^7\text{Li}$ reactions at deuteron beam energies and detection angles suitable for nuclear reaction analysis are imperative and the results of these measurements are presented in the current chapter.

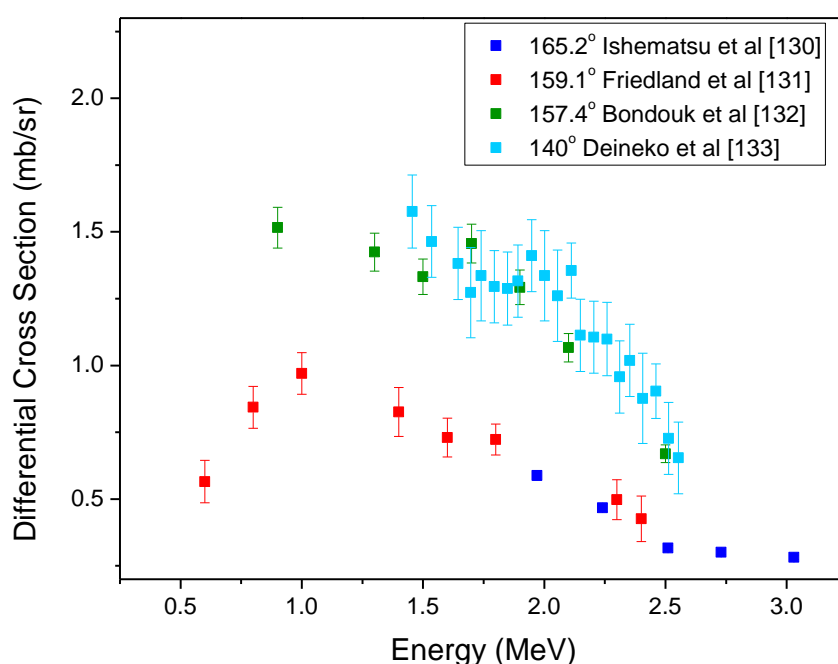


Figure 42: The differential cross section of the ${}^9\text{Be}(d,p_0){}^{10}\text{Be}$ reaction as measured by Ishematsu et al, Friedland et al, Bondouk et al, and Deineko et al.

3.1 Experimental Setup

The measurements were carried out using the 5.5 MV TN11 HV Tandem Accelerator at NCSR “Demokritos” in Athens, Greece. The detection system consisted of five silicon surface barrier detectors with thickness of $500\ \mu\text{m}$ which were placed at angles of 120° , 140° , 150° , 160° and 170° with respect to the beam direction, in a cylindrical scattering chamber with a radius of 40 cm, equipped with a high precision goniometer (0.1°). The detectors were equipped with orthogonal slits in front of them and were placed at a distance of ~ 10 cm from the target resulting at an angular uncertainty of $\pm \sim 1^\circ$. During the measurements, the vacuum was kept at around 1×10^{-6} mbar. A set of two collimators was placed at a distance of 40 and 90 cm before the target forming a circular beam spot with a radius of around 0.5 mm. The energy of the deuterons varied in the range $E_{\text{lab}} = 0.75 - 2.2$ MeV using a non-constant beam energy step up to 1 MeV and then a

constant step of 20 keV. The beam energy was measured constantly using a nuclear magnetic resonance probe at the 90° magnet of the accelerator. The beam energy was calibrated, using the 991.89 keV resonance of the $^{27}\text{Al}(p,\gamma)^{28}\text{Si}$ reaction employing a 18% HPGe detector. The offset was found to be (1.18 ± 0.36) keV. The sample consisted of a Be layer having measured thickness of 77 nm deposited on a Si_3N_4 (50 nm) membrane using the thermionic vacuum arc method (TVA) [28].

For the determination of the ratio of the areal atomic density of the Si to Be and the Be thickness, proton beam measurements were performed at energies $E_{\text{lab}} = 1.2$ MeV and $E_{\text{lab}} = 1.5$ MeV, for which the differential cross section of proton elastic scattering on Be presents a plateau at the detection angles of 120°, 150° and 170° where literature data exist [144, 145, 146]. For the cross section of the $^{\text{nat}}\text{Si}(p,p_0)^{\text{nat}}\text{Si}$, the evaluated values as calculated by sigmaCalc [98] were used. Additionally, transmission Elastic Recoil Detection Analysis (ERDA) measurements employing an O beam were carried out in the energy range 11.75 – 12.5 MeV and at the detection angle of 30°. In these measurements, the Rutherford cross section was used for the calculation of the ratio in question and the obtained value was used as a confirmation of the value acquired from the proton beam.

A benchmarking experiment was also carried out in order to confirm the energy dependence and the absolute values of the measured cross sections. This procedure was performed, measuring a bulk beryllium target with a thin gold layer of known thickness, deposited on its surface. The measured differential cross sections were used as an input in the simulation and the simulated spectra were compared against the experimental ones in order to check the validity of these cross sections.

All simulations were performed using the SIMNRA software [112].

3.1 Methodology

Solving the equation (2.13) for the differential cross section, we have:

$$\frac{d\sigma}{d\Omega}(E, \theta) = \frac{Y(E, \theta)}{Q \Omega N} \quad (3.1)$$

where $\frac{d\sigma}{d\Omega}(E, \theta)$ is the differential cross section of the reaction, which we are looking for, $Y(E, \theta)$ is the number of light particle produced by the reaction, Q is the number of the incident particles, Ω is the solid angle of the detector and N is atomic areal density.

For a homogenous layer the atomic areal density (N) is related with the thickness via the equation:

$$N = N_A \rho t \quad (3.2)$$

where N_A is the Avogadro's number, ρ is the mass density and t is the thickness of the target.

In the current work, the differential cross sections of the deuteron reactions on beryllium were determined using the corresponding formula of the relative measurement technique [147]. Using the differential cross section of the deuteron elastic scattering on Si, the differential cross sections of the Be can be obtained by:

$$\frac{d\sigma_{Be}}{d\Omega} = \frac{Y_{Be}}{Y_{Si}} \frac{N_{Si}}{N_{Be}} \frac{d\sigma_{Si}}{d\Omega} \quad (3.3)$$

where the Y_{Be} and Y_{Si} are determined experimentally and simultaneously from the measured spectra as the target consists of Be and Si (in the substrate), $d\sigma_{Si}/d\Omega$ has been measured recently [148] and the ratio N_{Si}/N_{Be} is determined employing the proton and the O beams using the known

differential cross sections, either analytically with Rutherford method or from the literature, as it is described below. The use of this method rules out systematic errors from the direct measurement of the beam charge and solid angle. On the other hand, as this is a relative method based on the recently measured deuteron elastic scattering on Si, the error of the cross sections ($\sim 1.5\%$) and of the ratio N_{Si}/N_{Be} (5.5%) contribute to the error of the measurements.

Using Equation (3.1) for the proton and O beam, the calculation of the ratio N_{Si}/N_{Be} (Equation (3.4)) is feasible as the differential cross section for both elements is known either from the literature in case of the proton beam or from the Rutherford cross section for the O beam:

$$\frac{N_{Si}}{N_{Be}} = \frac{Y_{Si} \frac{d\sigma_{Be}}{d\Omega}}{Y_{Be} \frac{d\sigma_{Si}}{d\Omega}} \quad (3.4)$$

The integration of all peaks was performed with Origin program [149] where the peaks were fitted with a Gaussian (Figure 43).

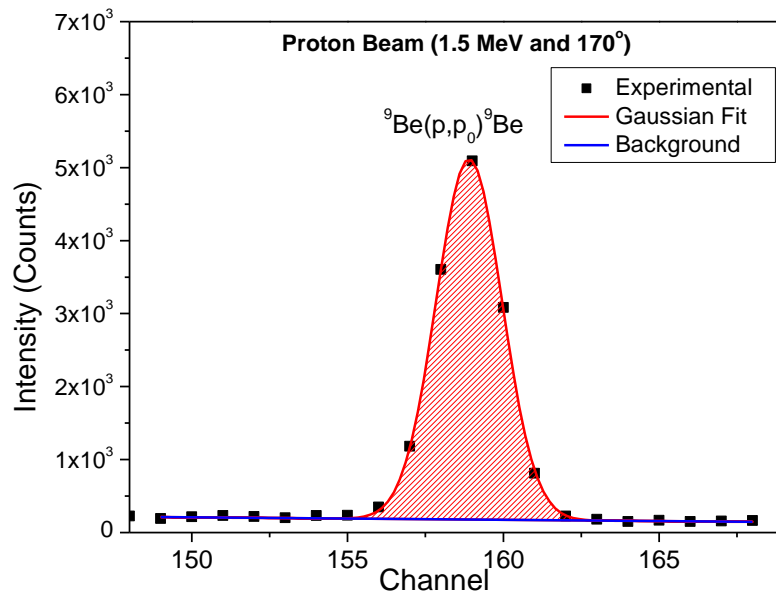


Figure 43: Experimental spectrum and gaussian fit of the ${}^9\text{Be}(p, p_0){}^9\text{Be}$ peak

3.2 Proton Beam Measurements

Figure 44 depicts a typical experimental and simulated spectrum of the proton beam measurements, with an energy of 1.5 MeV and a detection angle of 170°. The integrals of the peaks of the ${}^9\text{Be}(p, p_0){}^9\text{Be}$ and the ${}^{28}\text{Si}(p, p_0){}^{28}\text{Si}$ reactions constitute the values of the Y_{Be} and Y_{Si} , respectively. Using Equation 3.4 and the literature cross sections [144, 145, 146], the ratio N_{Si}/N_{Be} was calculated for different energies and detection angles (Table 1).

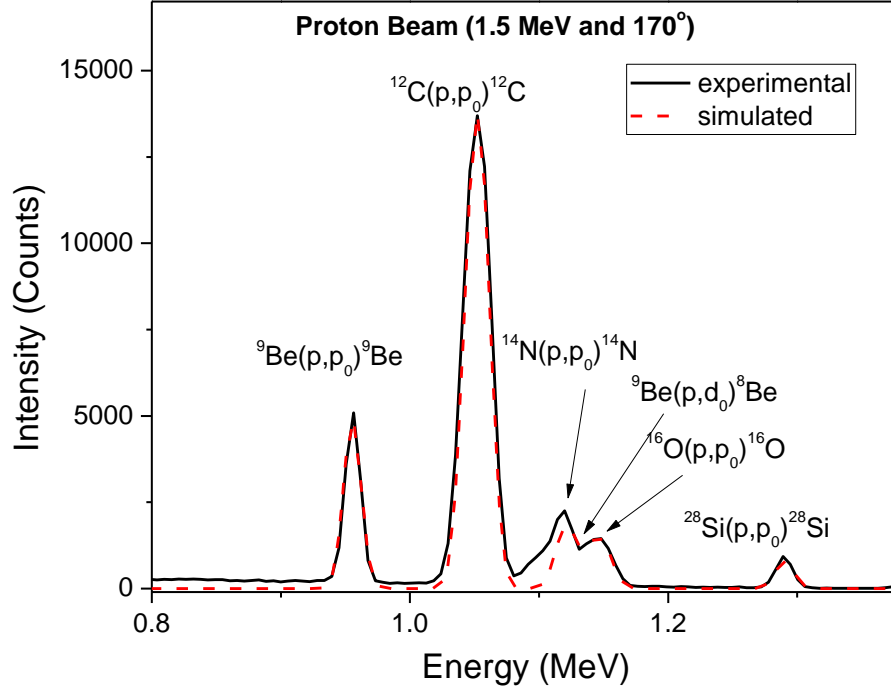


Figure 44: Experimental (solid line) and simulated (dash line) spectrum using a proton beam of 1.5 MeV energy and a detection angle of 170° .

Table 1: The values of the cross section at specific energies and angles from the literature data and the calculated ratio N_{Si}/N_{Be} .

Energy (MeV)	Angle	Work Author	Be (p,p ₀)Be C. S. (mb/sr)	$\frac{N_{Si}}{N_{Be}}$
1.2	120°	M. Tsan [144]	92 ± 6	0.227 ± 0.025
	150°	N. Catarino [145]	93 ± 6	0.226 ± 0.016
	170°	Z. Liu [146]	98.00 ± 0.03	0.210 ± 0.005
1.5	120°	M. Tsan [144]	117 ± 8	0.200 ± 0.013
	150°	N. Catarino [145]	97 ± 8	0.211 ± 0.017
	170°	Z. Liu [146]	103.00 ± 0.04	0.231 ± 0.004
Average				0.218 ± 0.012

The average of the ratios for the different energies and detection angles of the ${}^9\text{Be}(p,p_0){}^9\text{Be}$ reaction is $\frac{N_{Si}}{N_{Be}} = 0.218 \pm 0.012$. Knowing the nominal thickness $t_{Si_3N_4,nom} = 50 \text{ nm}$ and using the mass density $\rho_{Si_3N_4} = 3.17 \text{ g/cm}^3$ of the Si_3N_4 , we can find that the thickness of Be is $t_{Be} = 77 \text{ nm}$, which is in the range of the nominal value $t_{Be,nom} = 65 \pm 15 \text{ nm}$.

3.3 Oxygen Beam Measurements

Figure 45 shows a typical experimental and simulated spectrum of the O beam with energy of 11.75 MeV and at detection angle of 30°. The yields of Be, Y_{Be} , and Si, Y_{Si} , are determined with the integration of their peaks. Applying Equation (3.4) for the O beam measurements, the ratio N_{Si}/N_{Be} was calculated using the Rutherford cross section. Table 2 summarizes this ratio for the different energies.

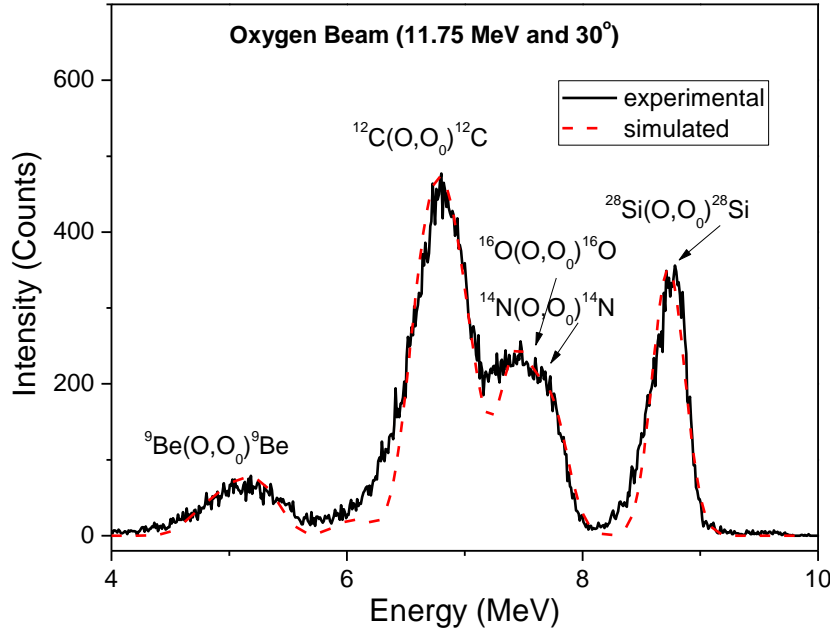


Figure 45: Experimental (black solid line) and simulated (red dash line) spectrum from the O beam measurement. The beam energy was 11.75 MeV and the detection angle 30°.

Table 2: O beam energy and the calculated ratio N_{Si}/N_{Be} .

Energy (MeV)	$\frac{N_{Si}}{N_{Be}}$
11.75	0.216 ± 0.003
12.00	0.210 ± 0.003
12.25	0.226 ± 0.004
12.5	0.221 ± 0.003
Average	0.219 ± 0.007

The resulting ratio N_{Si}/N_{Be} from the proton and O beam experiments is the same within error bars, namely 0.218 ± 0.012 for the proton beam and 0.219 ± 0.007 for the O beam. The value of the proton beam was used for the calculation of the differential cross section of the deuteron beam reactions on Be, as the error of the proton beam covers up the value obtained using the oxygen beam.

3.4 Deuteron Beam Measurements

Below we discuss the determination of the differential cross section values of ${}^9\text{Be}(d,p_0){}^{10}\text{Be}$, ${}^9\text{Be}(d,p_1){}^{10}\text{Be}$, ${}^9\text{Be}(d,a_0){}^7\text{Li}$ and ${}^9\text{Be}(d,a_1){}^7\text{Li}$ reactions. Figure 46 presents a typical deuteron beam spectrum with $E_{\text{lab}} = 2.2$ MeV and at the detection angle of 170° . The statistical error of the cross sections came from the error of the integration of the Be and the Si peaks. Moreover, the uncertainty of the ratio $N_{\text{Si}}/N_{\text{Be}}$ (5.5%) and the error of the cross sections of ${}^{\text{nat}}\text{Si}(d,d_0){}^{\text{nat}}\text{Si}$ ($\pm \sim 1.5\%$) constitute the systematic error of the measurements ($\sim 7\%$).

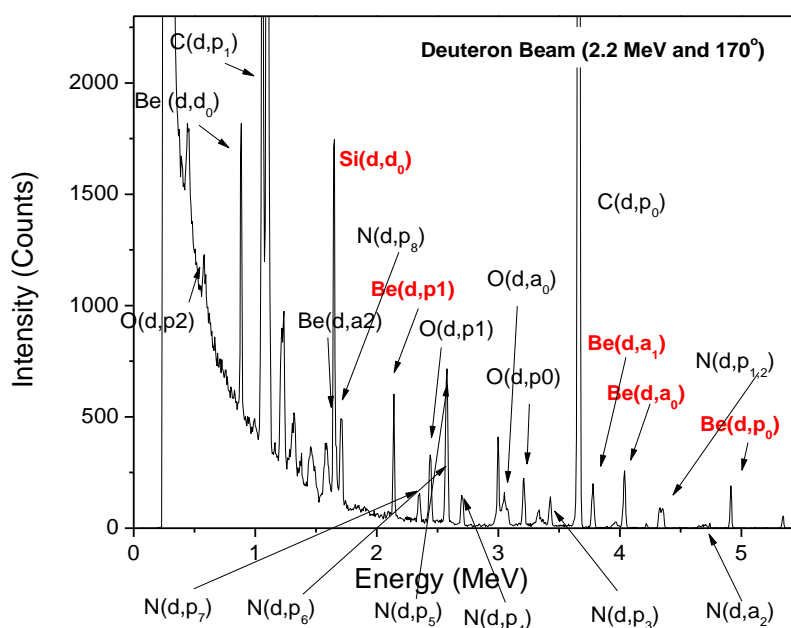


Figure 46: A typical spectrum of deuteron beam with energy 2.2 MeV and at detection angle of 170° . The peaks noted with red-bold were used for the analysis.

A number of nitrogen (N) peaks is observed in the spectrum, some of which overlap with the Be peaks for specific energy ranges where the differential cross sections could not be calculated and were excluded from the final results. Below peaks of N and the energy ranges where the peaks overlap with the measured reactions are presented.

${}^9\text{Be}(d,p_0){}^9\text{Be}$

The ${}^9\text{Be}(d,p_0){}^9\text{Be}$ peak is quite clear and the peak of the ${}^{14}\text{N}(d,a_2){}^{12}\text{C}$ is too short to affect the integral.

${}^9\text{Be}(d,p_1){}^9\text{Be}$

The ${}^9\text{Be}(d,p_1){}^9\text{Be}$ peak has been surrounded by many peaks. Figure 47 presents the overlapping of the Be peak with an unidentified one which is referred as unknown peak. The Table 3 shows the energy ranges where the integral was not determined for each detection angle.

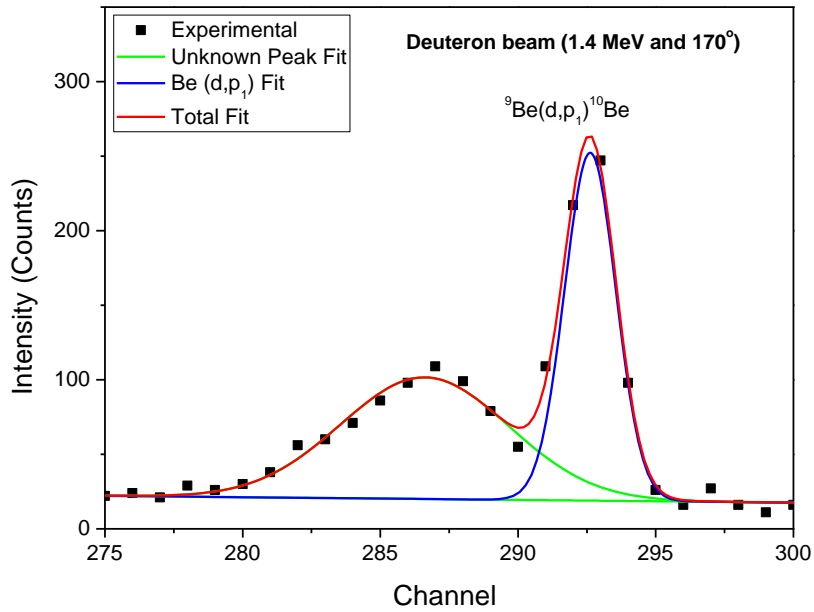


Figure 47: The overlapping of the ${}^9\text{Be}(d,p_1){}^{10}\text{Be}$ peak with an unidentified one. The deuteron energy is 1.4 MeV and the detection angle 170° .

Table 3: The energy ranges for each detection angle where the cross section of ${}^9\text{Be}(d,p_1){}^{10}\text{Be}$ was not calculated

Detection Angle	Energy Range (MeV)
120°	0.72 - 1.18 / 1.4 - 1.54 / 1.68 - 1.8
140°	0.72 - 1.02 / 1.24 - 1.34 / 1.46 - 1.54
150°	0.72 - 0.88
160°	0.72 - 0.88
170°	1.12 - 1.22 / 1.32 - 1.38

${}^9\text{Be}(d, a_0){}^7\text{Li}$

The ${}^9\text{Be}(d, a_0){}^7\text{Li}$ peak overlaps with ${}^{14}\text{N}(d, p_{1,2}){}^{15}\text{N}$ ones in the energy range which depends on the detection angle. Figure 48 presents the overlapping of these two peaks with the Be one and the Gaussian Fit created to assess the integral of the ${}^9\text{Be}(d, a_0){}^7\text{Li}$ peak. The Table 4 shows the energy range where the integral cannot be determined for each detection angle.

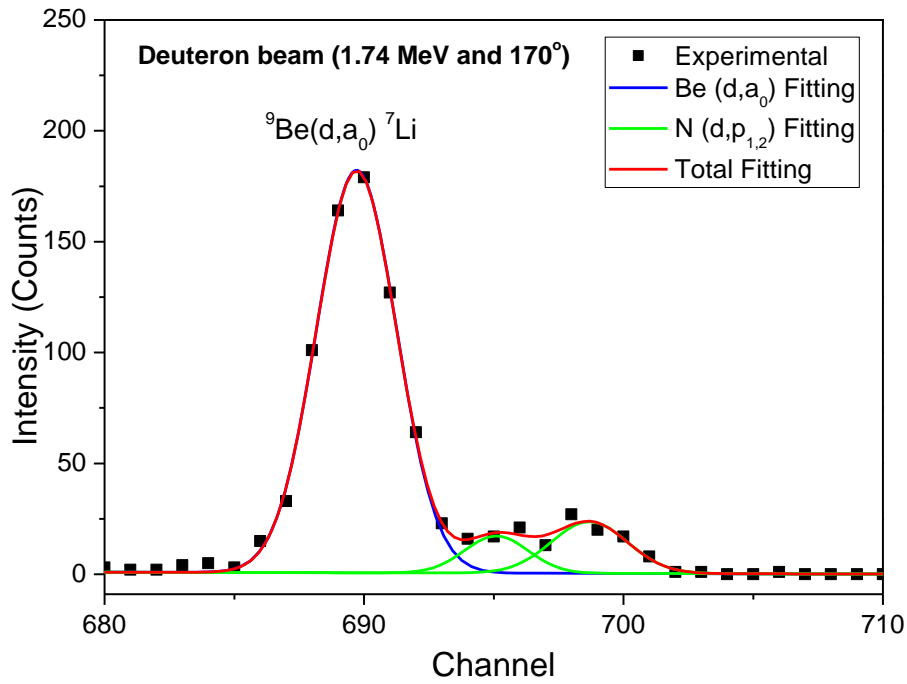


Figure 48: The overlapping of the ${}^9\text{Be}(d,a_0){}^7\text{Li}$ peak with the ${}^{14}\text{N}(d,p_{1,2}){}^{15}\text{N}$ ones.

Table 4: The energy range for each detection angle where the cross section of ${}^9\text{Be}(d,a_0){}^7\text{Li}$ was not calculated due to the overlapping with ${}^{14}\text{N}(d,p_{1,2}){}^{15}\text{N}$ peaks.

Detection Angle	Energy Range (MeV)
120°	-
140°	1.9-2.1
150°	1.76-1.9
160°	1.64-1.78
170°	1.6-1.72

${}^9\text{Be}(d,a_1){}^7\text{Li}$

The ${}^9\text{Be}(d,a_1){}^7\text{Li}$ peak also overlaps with ${}^{14}\text{N}(d,p_{1,2}){}^{15}\text{N}$ peaks at lower energies. Figure 49 presents the overlapping of these peaks and the Gaussian Fit. Table 5 shows the energy range where the integral cannot be determined for each detection angle.

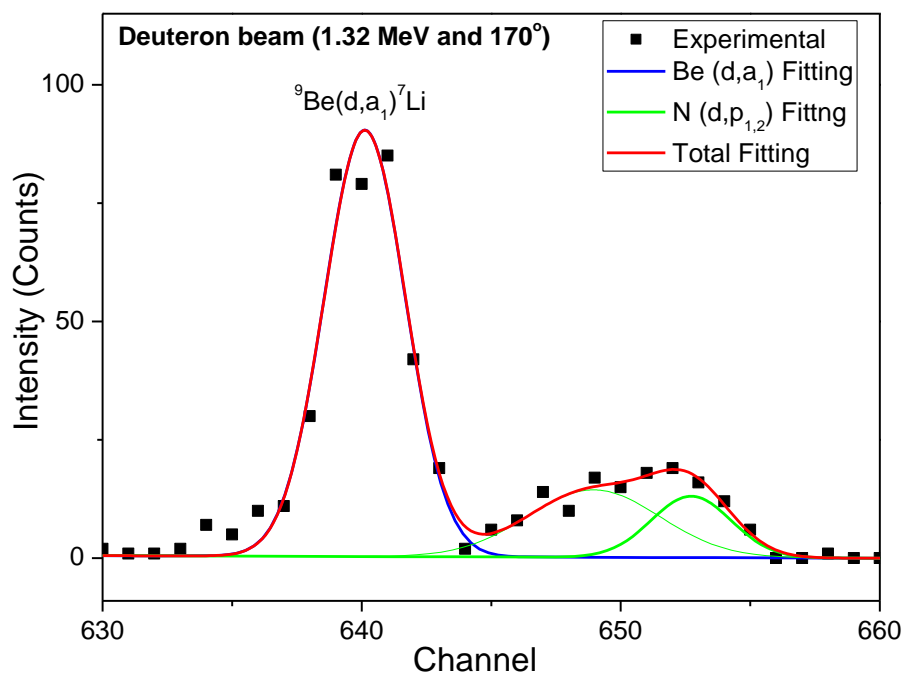


Figure 49: The overlapping of the ${}^9\text{Be}(d,a_1){}^{10}\text{Be}$ peak with the ${}^{14}\text{N}(d,p_{1,2}){}^{15}\text{N}$ one.

Table 5: The energy range for each detection angle where the cross section of ${}^9\text{Be}(d,a_1){}^{10}\text{Be}$ was not calculated due to the overlapping with ${}^{14}\text{N}(d,p_{1,2}){}^{15}\text{N}$ peak.

Detection Angle	Energy Range (keV)
120°	1740-1980
140°	1380-2100
150°	1280-1420
160°	1200-1320
170°	1160-1300

Using the methodology that was described in the Section 3.4 and determining the integral of the peaks with Gaussian Fit, we calculated the cross sections of deuteron beam reactions on beryllium.

The statistical error results from the integration of the Be and Si peaks. Having excluded the Be peaks which overlap with the surround peaks, the statistical error of each point does not exceed 10% and in the most of the cases, it is around 6-8%.

During the deuterium – beryllium reaction, a compound nucleus is formed. The time scale of compound nucleus reactions is $10^{-18} \text{ s} - 10^{-16} \text{ s}$, which is much longer than the time of transit of an incident ion across the nucleus ($\sim 10^{-22} \text{ s}$). The consequence of thermal equilibrium inside a compound is that the mode of decay of the compound nucleus does not depend on how the compound nucleus is formed [150]. Additionally the excitation levels of compound can affect the cross sections of the reactions. Figure 50 shows the excitation levels of boron, the compound nucleus of the deuteron - beryllium reactions, in the deuteron beam energy range of 0.72 – 2.2 MeV.

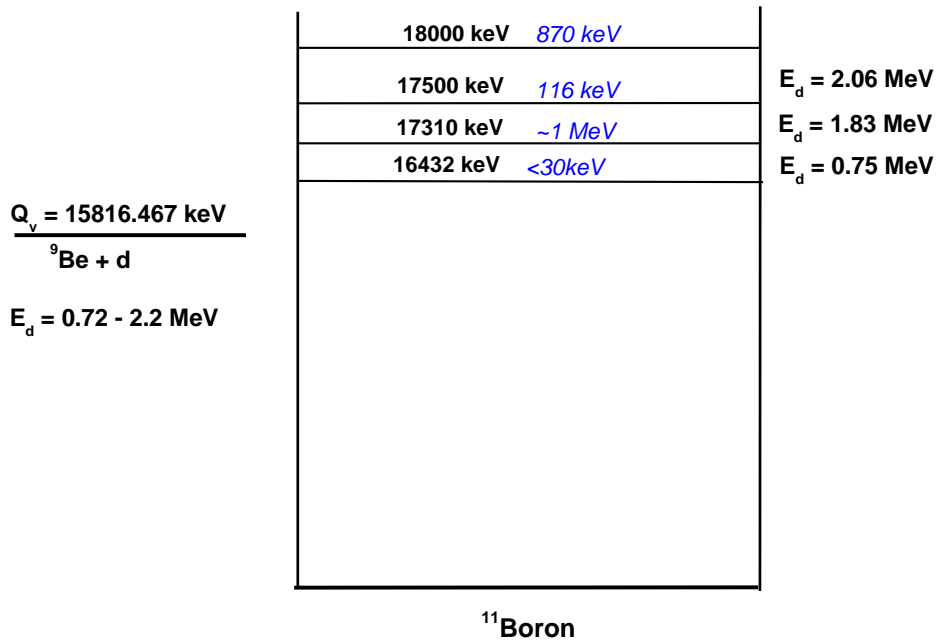
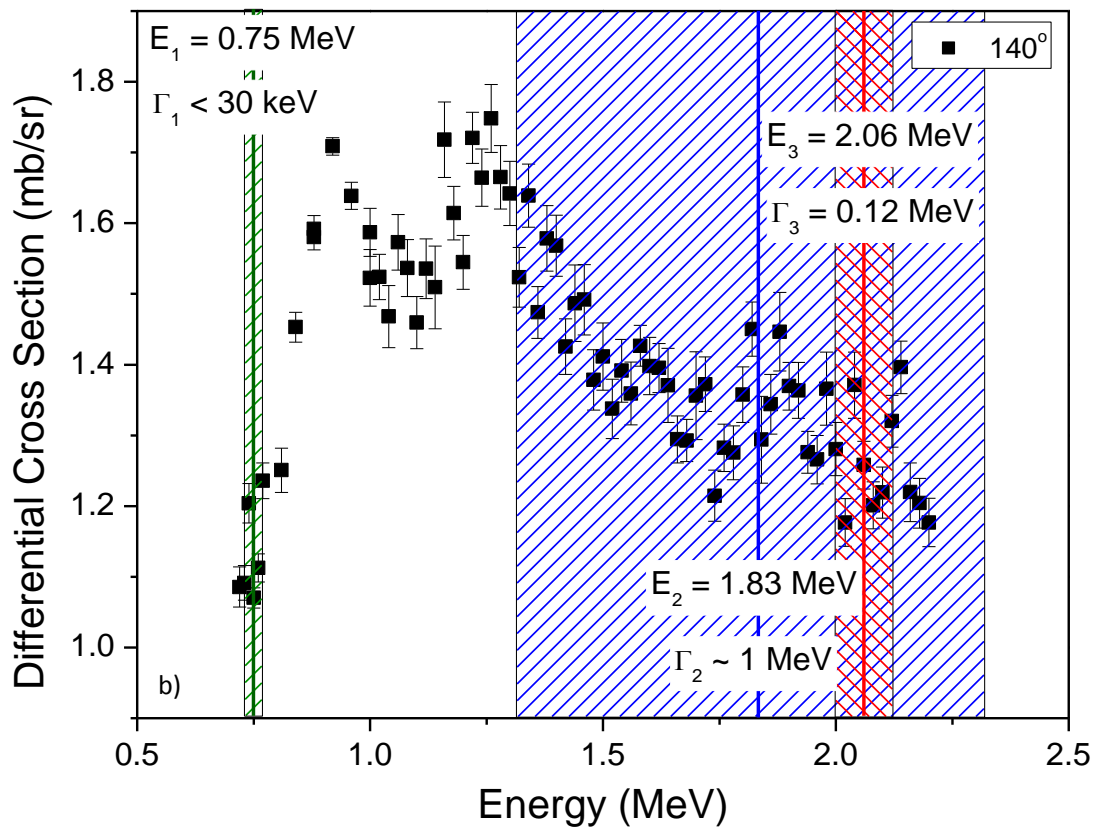
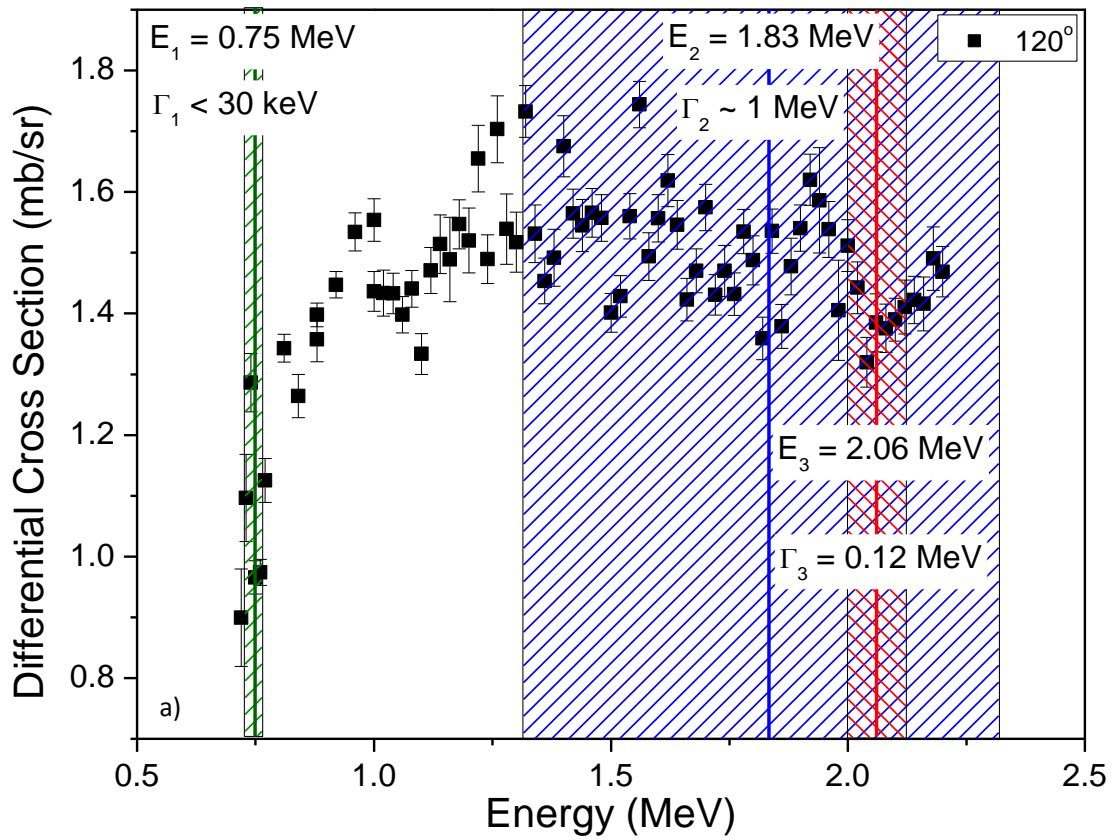
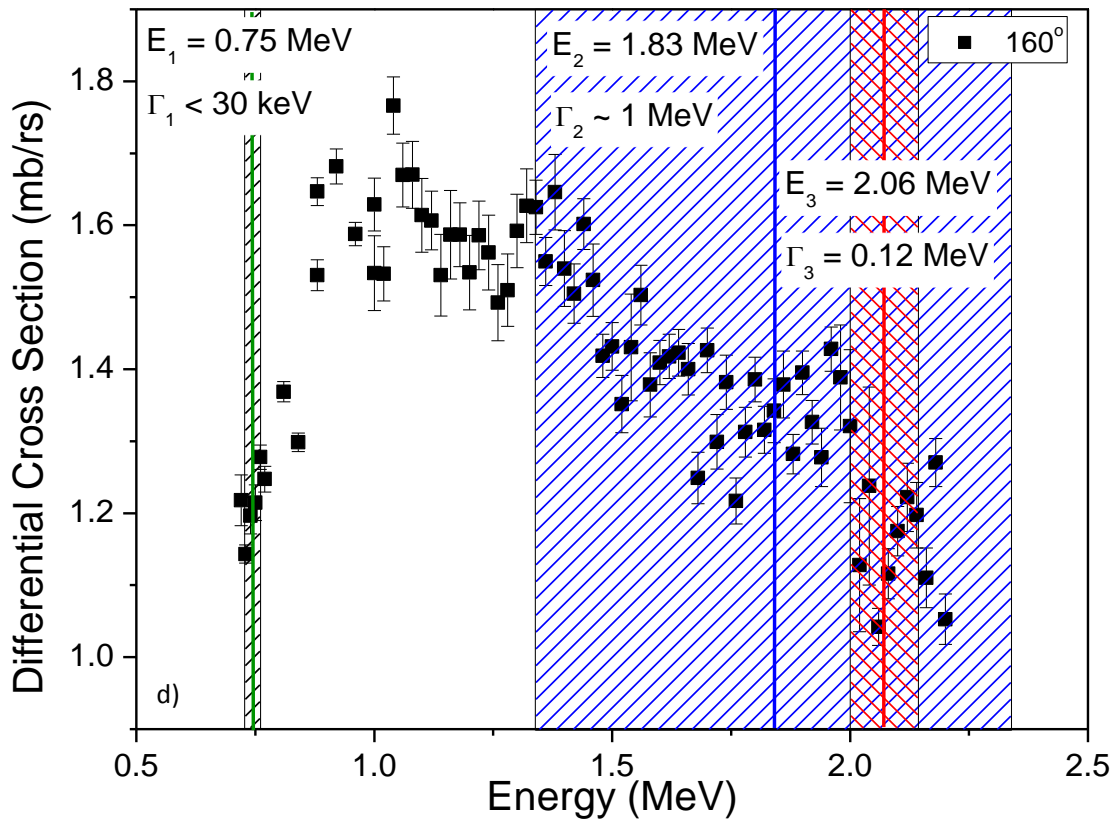
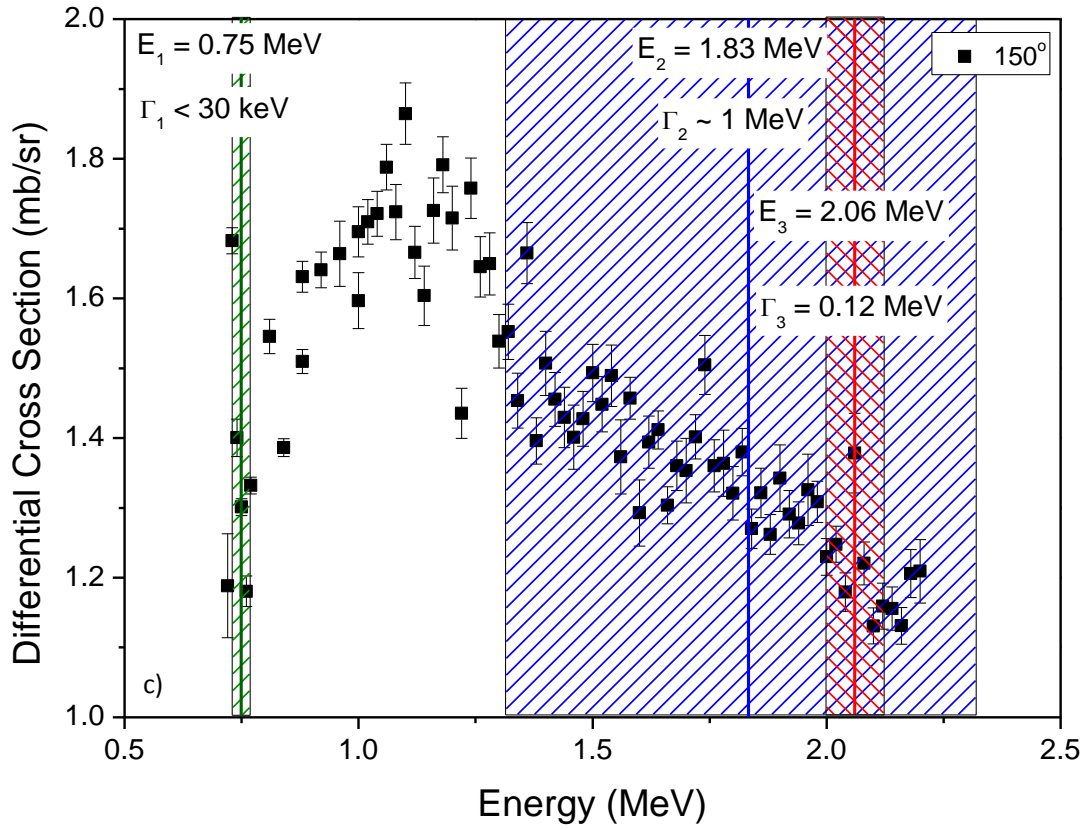


Figure 50: The B excitation levels in the deuteron energy range 0.72 – 2.2 MeV.

The values of the differential cross section for the ${}^9\text{Be}(d,p_0){}^{10}\text{Be}$ reaction (Figure 51), ${}^9\text{Be}(d,p_1){}^{10}\text{Be}$ (Figure 53), ${}^9\text{Be}(d,\alpha_0){}^7\text{Li}$ (Figure 55) and ${}^9\text{Be}(d,\alpha_1){}^7\text{Li}$ (Figure 57) are presented at the chosen detection angles. Additionally, the results of the current work are compared with literature values (Figure 52, Figure 54, Figure 56, Figure 58).





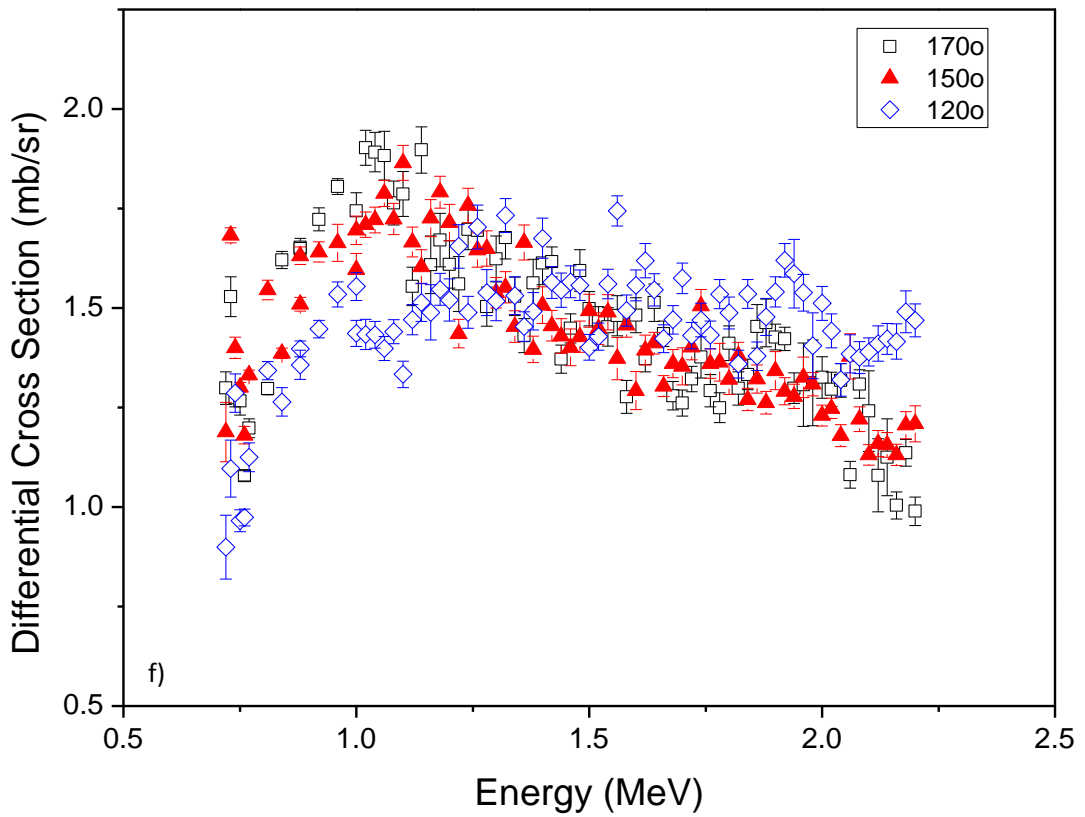
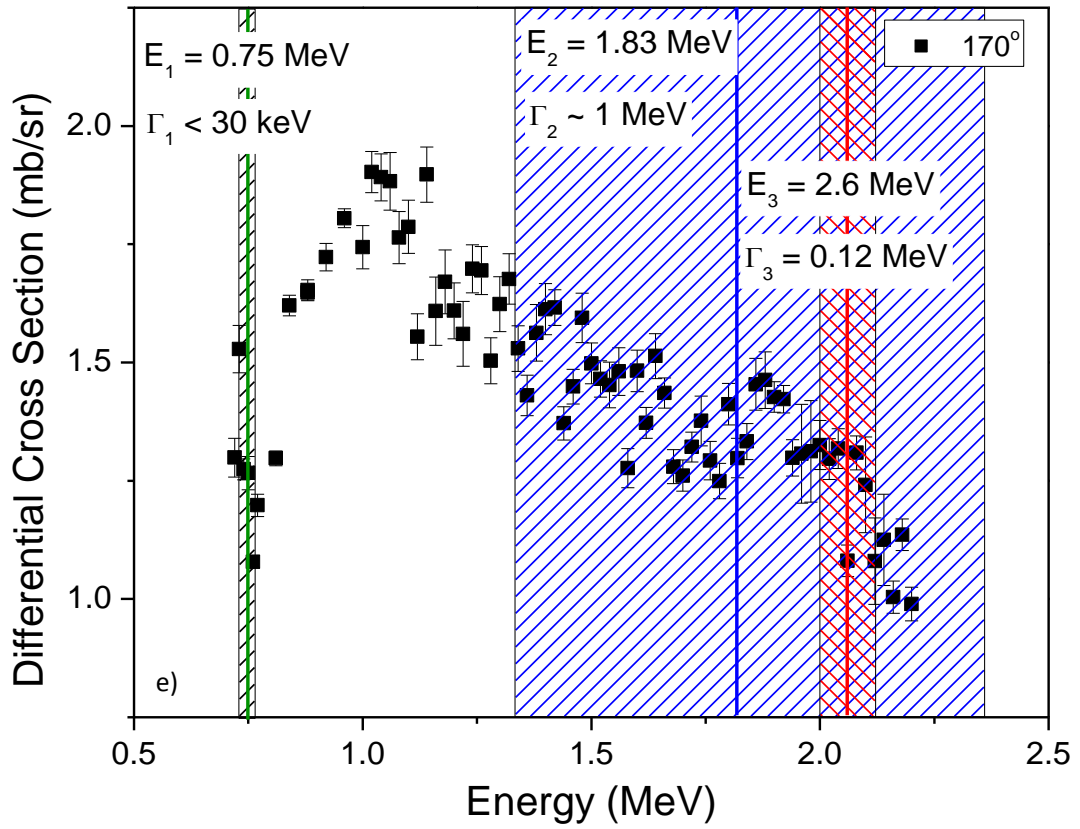


Figure 51: Measured differential cross section of the $^{10}\text{Be}(d,p_0)^9\text{Be}$ at detection angles of a) 120° , b) 140° , c) 150° , d) 160° , e) 170° and f) a comparison of differential cross section from 120° , 150° and 170° .

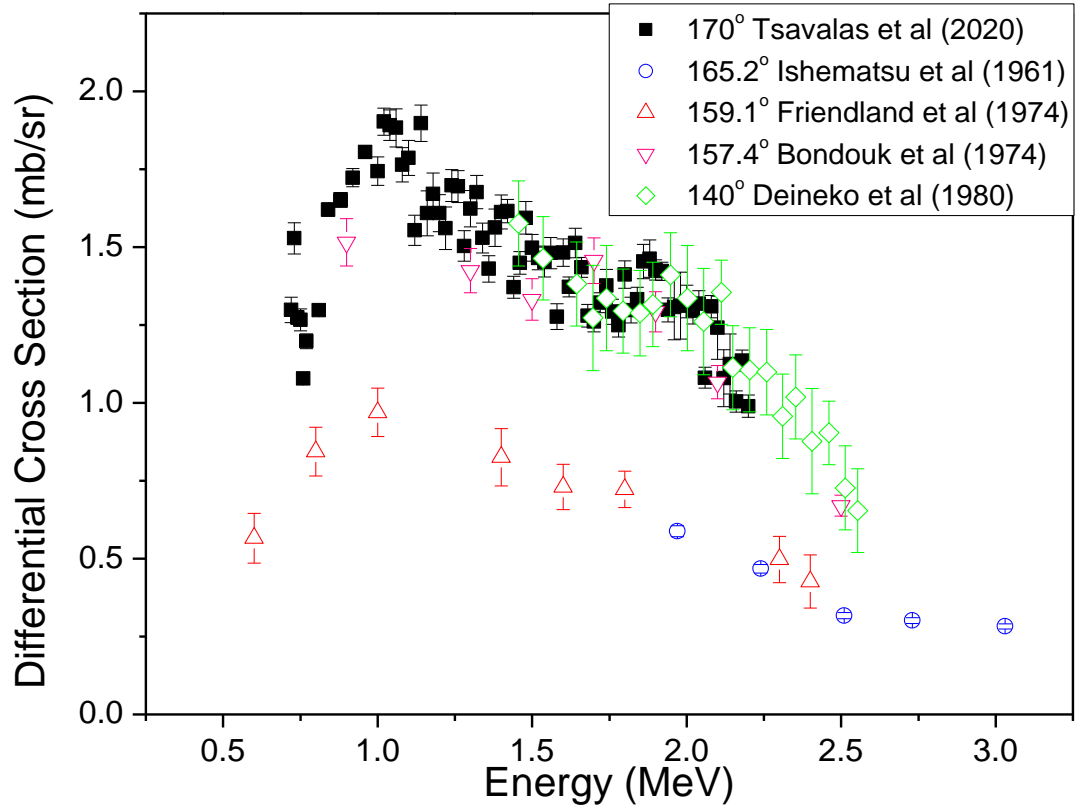
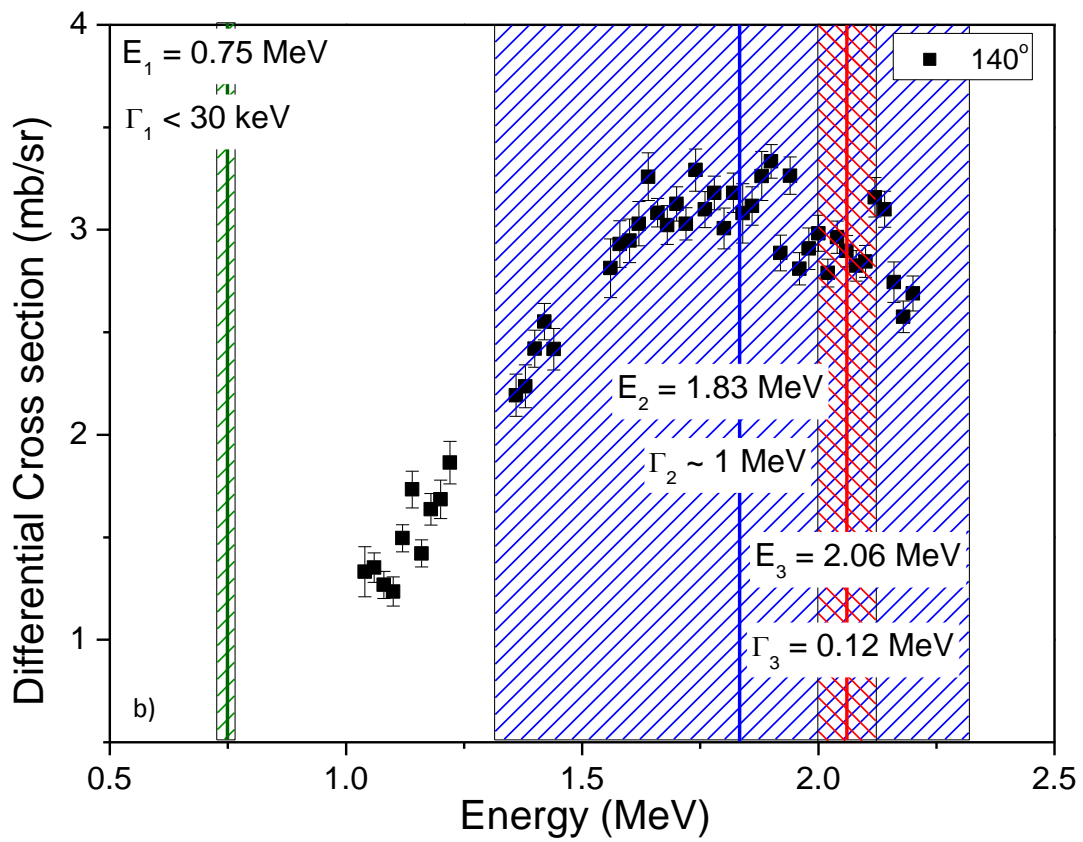
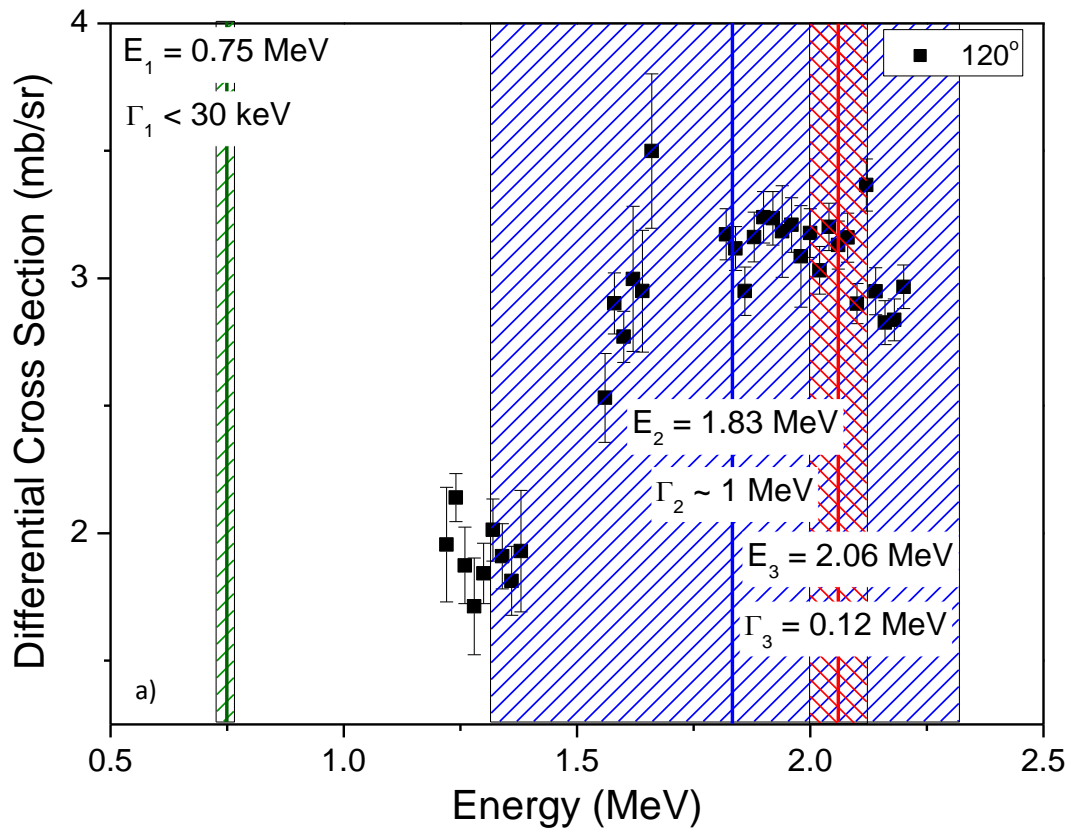
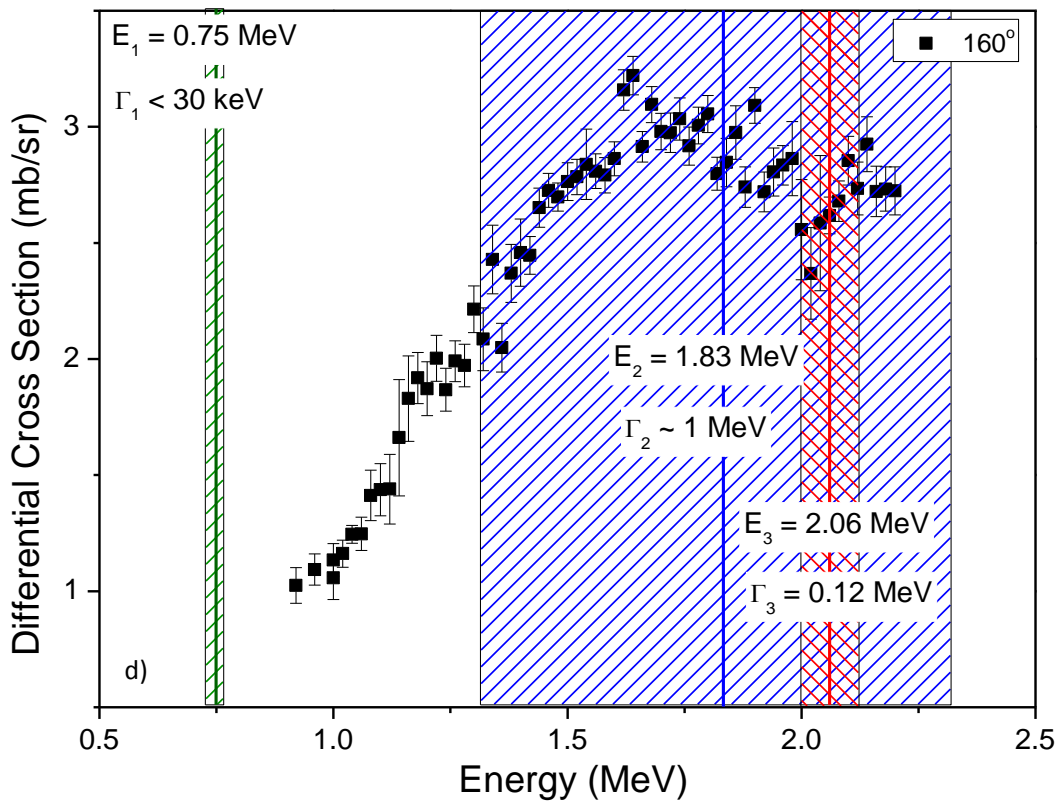
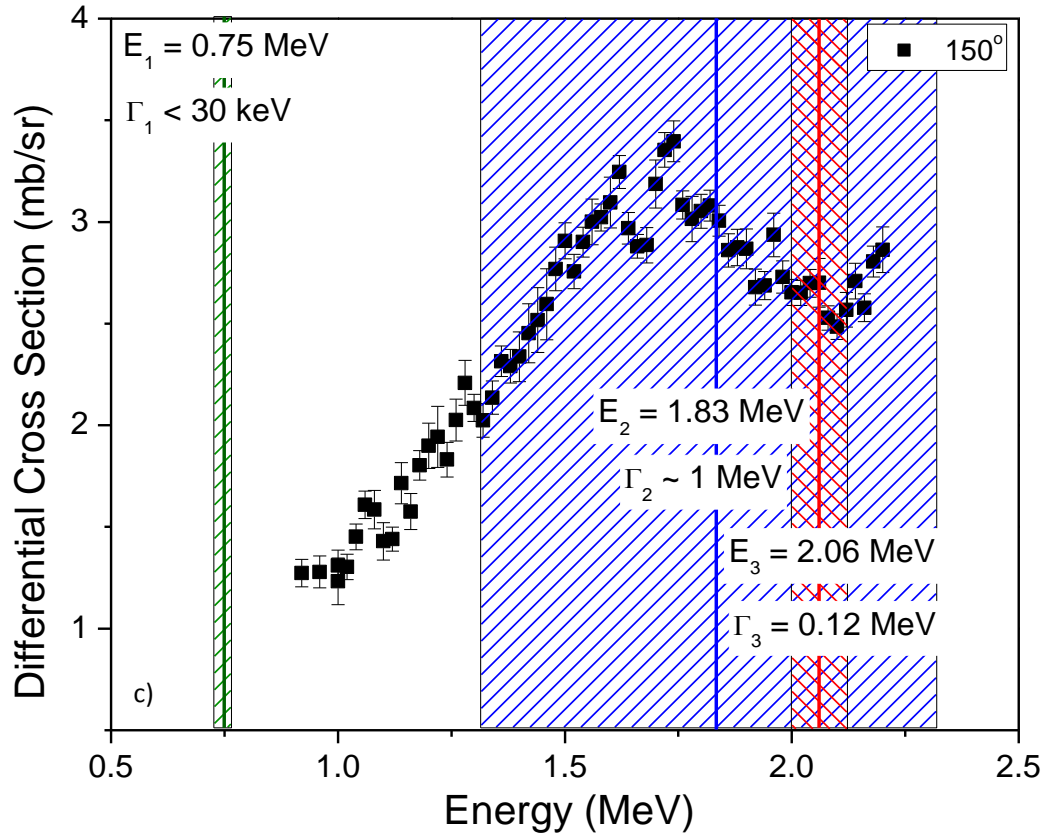


Figure 52: Comparison of the differential cross section of the ${}^9\text{Be}(d,p_0){}^{10}\text{Be}$ reaction of the current work with that of T. Ishematsu et al [140], E. Friedland et al [141], I. I. Bondouk et al [142] and A. S Deineko et al [143].

For the detection angles of $150^\circ - 170^\circ$, the cross section of the ${}^9\text{Be}(d,p_0){}^{10}\text{Be}$ reaction shows an abrupt increase with the energy for the energy range 0.76 - 1 MeV and then its values decrease almost linearly with the increase of the energy. As the detection angle decreases the slope decreases. For the detection angle of 170° , the cross section is 1.9 mbarn at 1.0 MeV and decreases to 1 mbarn at 2.2 MeV. For the 140° , the behaviour looks like detection angles $150^\circ - 170^\circ$, but there is a local minimum in the energy range of 1.04 - 1.1 MeV. On the other hand, the cross section of 120° presents different behaviour for energies higher than 1 MeV as it is almost constant around the value of 1.5 mb/sr (with fluctuations) (Figure 51a). Regarding the levels of the boron, the level with 16.4 MeV, which corresponds to energy beam of 0.75 MeV (Figure 50), seems to cause a sharp peak at the detection angles of 120° , 150° and 170° , while the rest of the levels, it is not clear if they affect the cross sections.

In Figure 52, the data of the current work are compared with datasets from previous works. As there is no significant angle dependence for energies between 1.3 MeV and 2.2 MeV (Figure 51f), the comparison of cross sections from different angles is valid. The present results agree with those of I. I. Bondouk et al [142] and A. S. Deineko et al [143], while there is disagreement in absolute values, but not in the energy dependence, with E. Friedland et al [141] and T. Ishematsu et al [140], which are 45% lower than the present values.





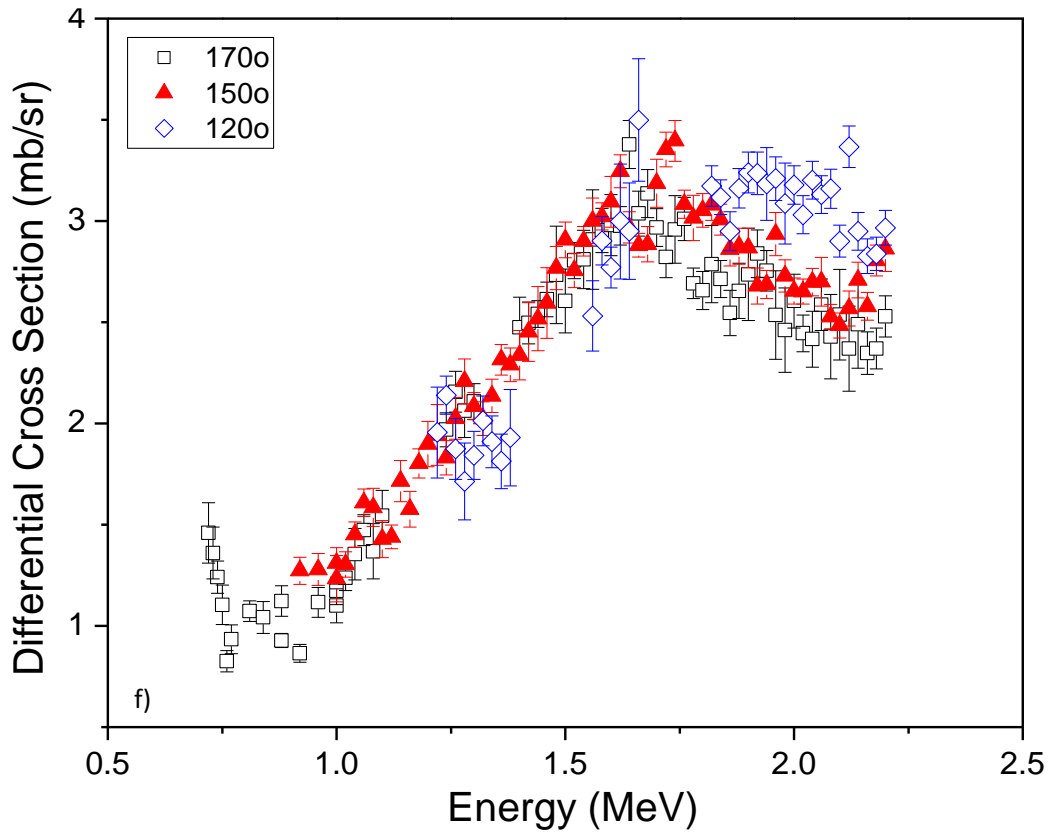
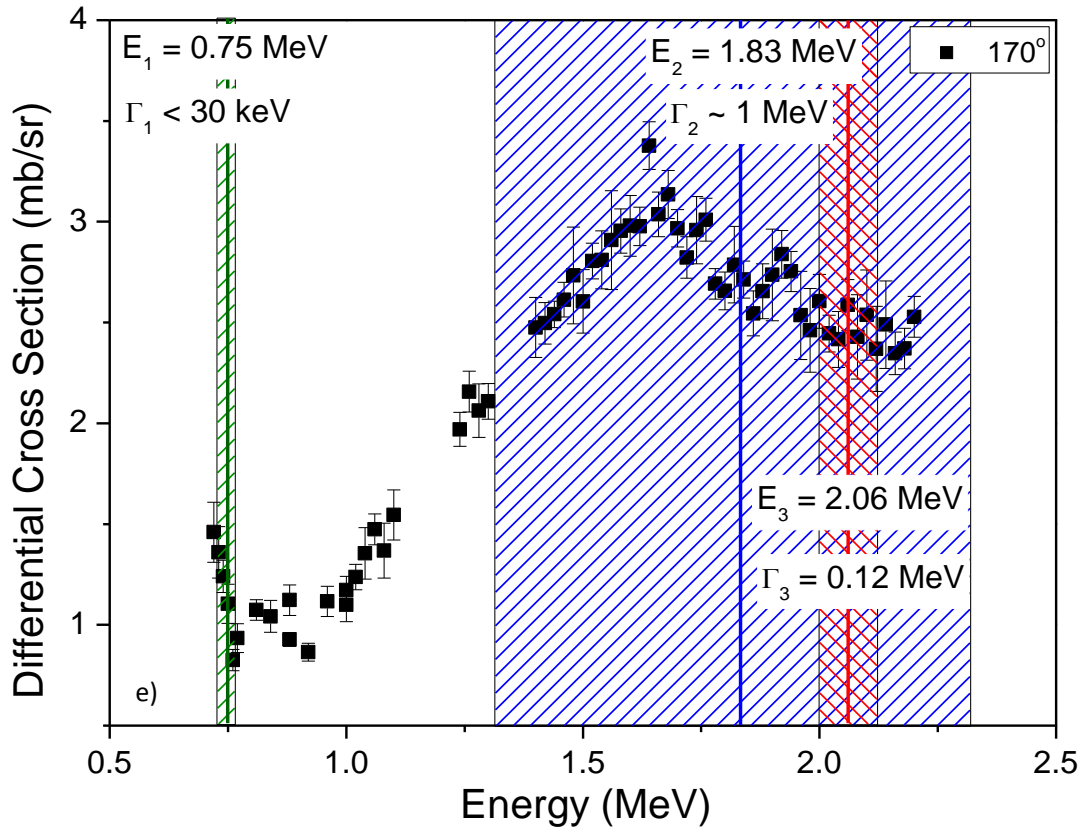


Figure 53: Measured differential cross section of the $^{10}\text{Be}(d,p_1)^9\text{Be}$ at detection angles of a) 120° , b) 140° , c) 150° , d) 160° , e) 170° and f) a comparison of differential cross section from 120° , 150° and 170° .

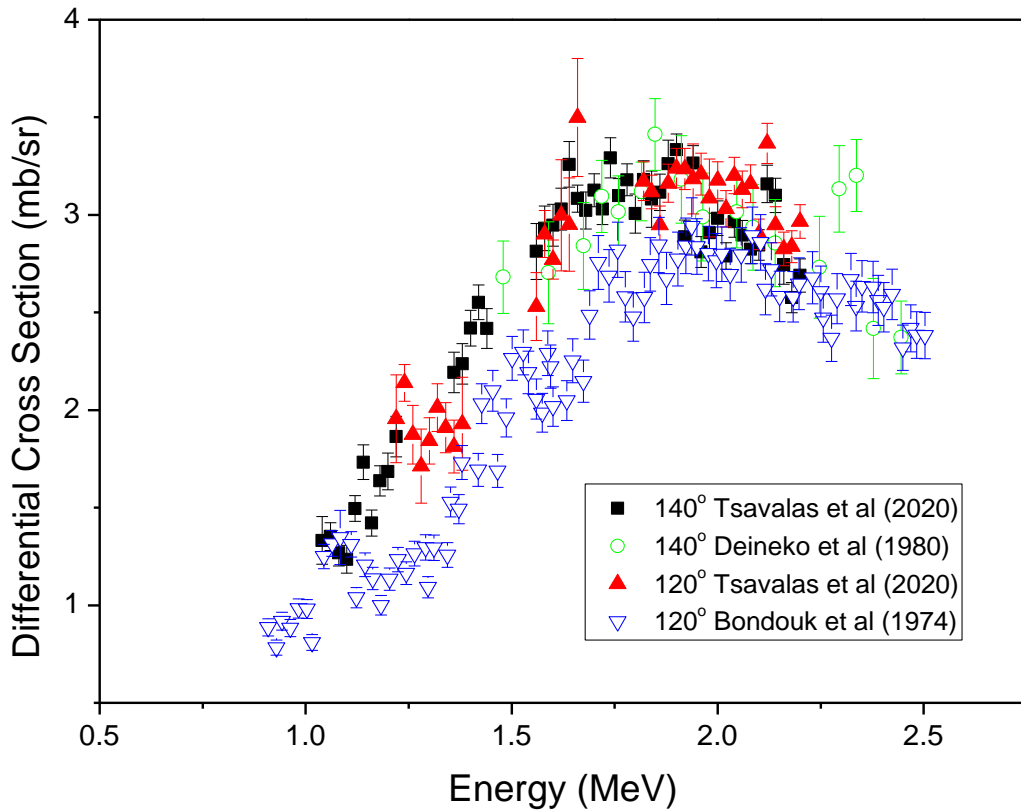
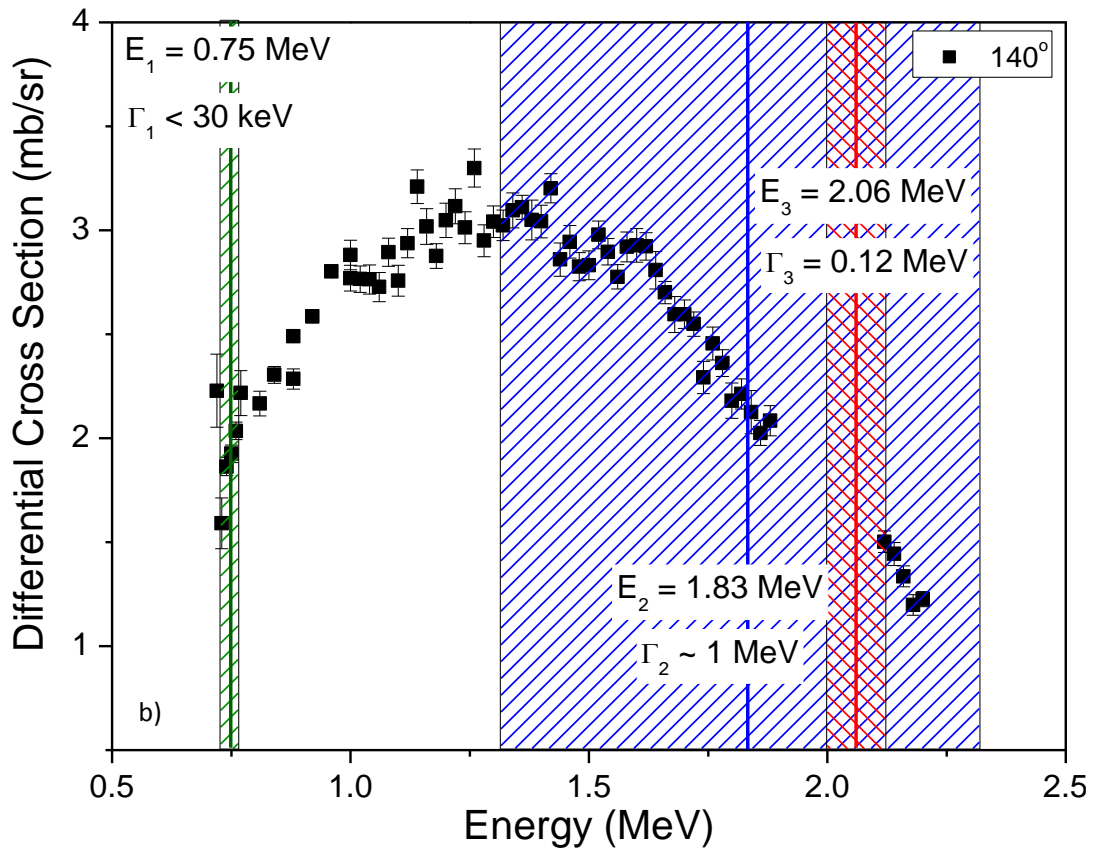
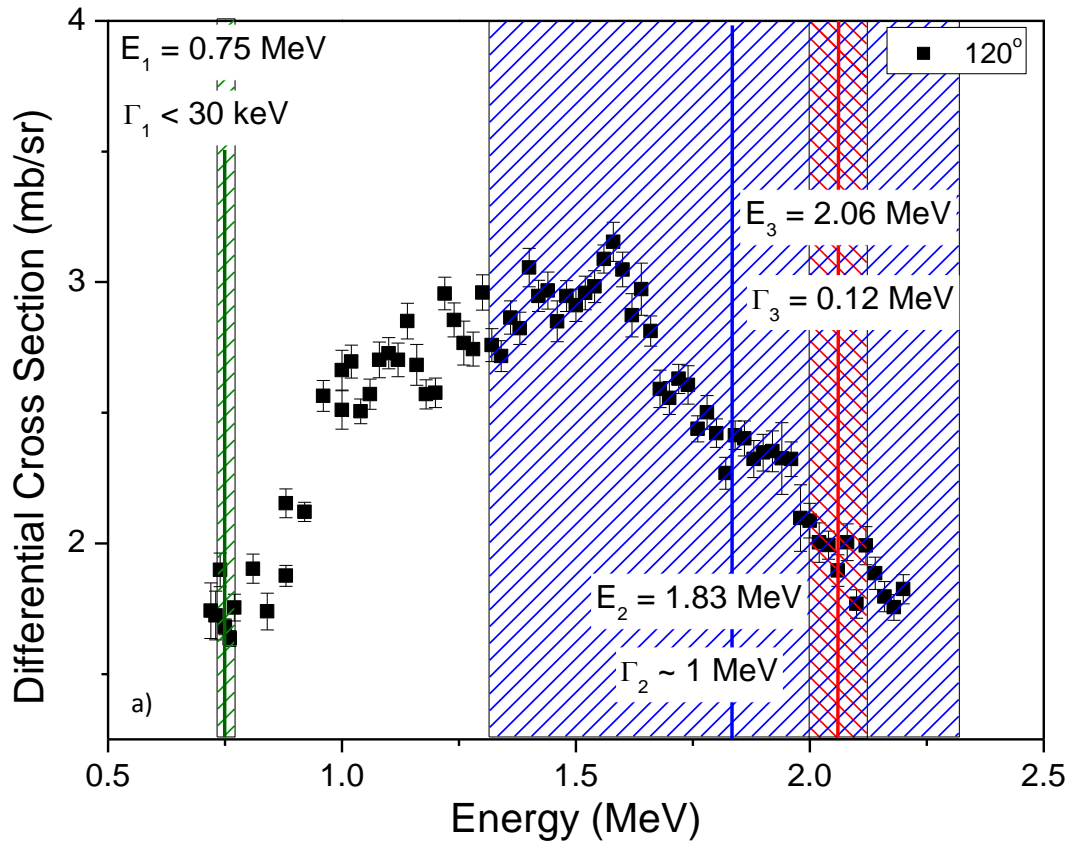
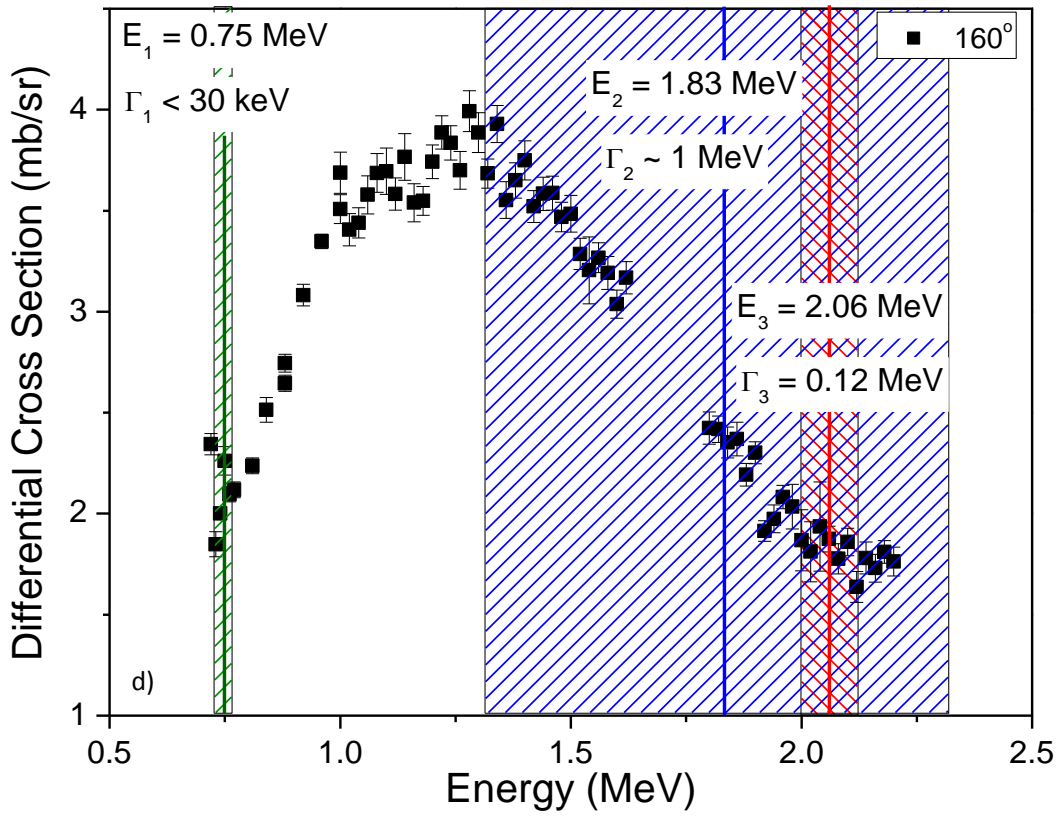
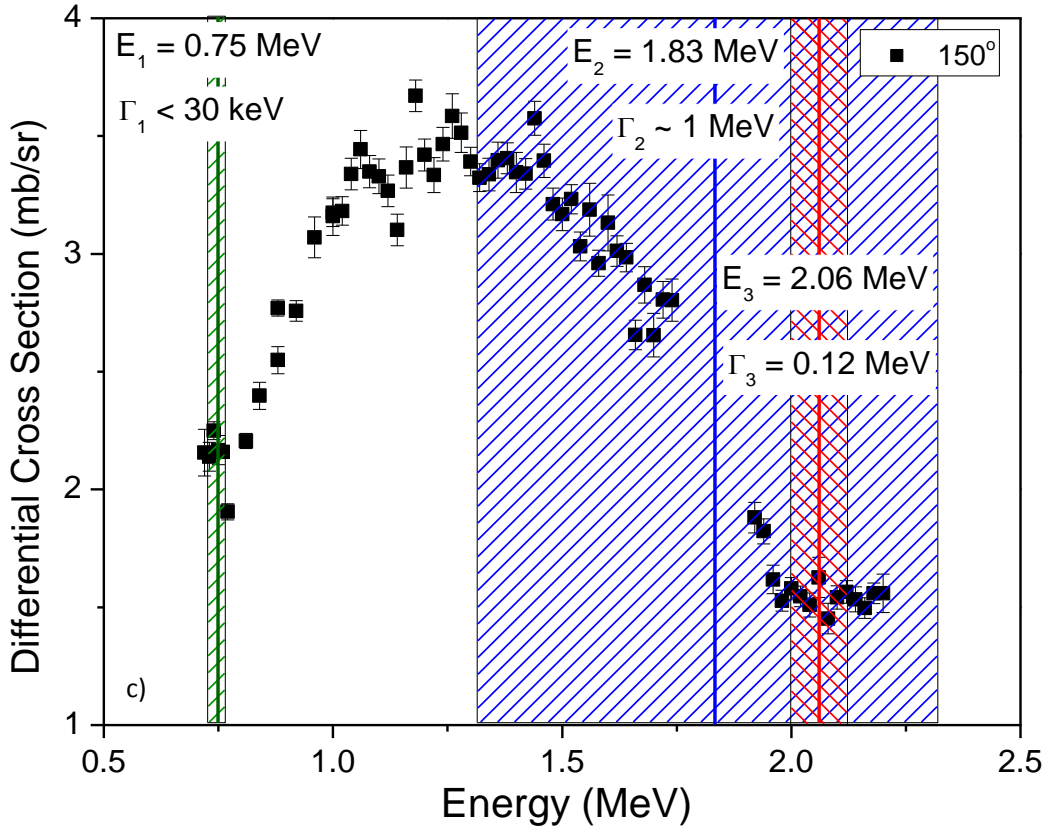


Figure 54: Comparison of the ${}^9\text{Be}(d,p_1){}^{10}\text{Be}$ reaction differential cross section of the Tsavalas et al with A. S. Deineko et al [143] and the I. I. Bondouk et al [142] for the detection angles of 120° and 140° .

The differential cross section of the ${}^9\text{Be}(d,p_1){}^{10}\text{Be}$ reaction starts from 1 mb/sr and increases up to 3.1 mb/sr at the energy $E_{\text{lab}} = 1.7$ MeV for all detection angles. For higher energies, the cross section decreases with the energy, while the slope of the cross section depends on the angle, as the slope becomes steeper with the increase of the detection angle (Figure 53). Unfortunately, only the values of the cross section at the detection angle of 170° could be determined, in the energy range near the lowest boron level (16.4 MeV, energy beam of 0.75 MeV) where an abrupt increase is observed. The other levels do not affect the values of the cross section.

The results of the current work agree with those of A. S. Deineko et al [143], while the data of I. I. Bondouk et al [142] exhibit 15 - 20% lower values, but with the same energy dependence (Figure 54).





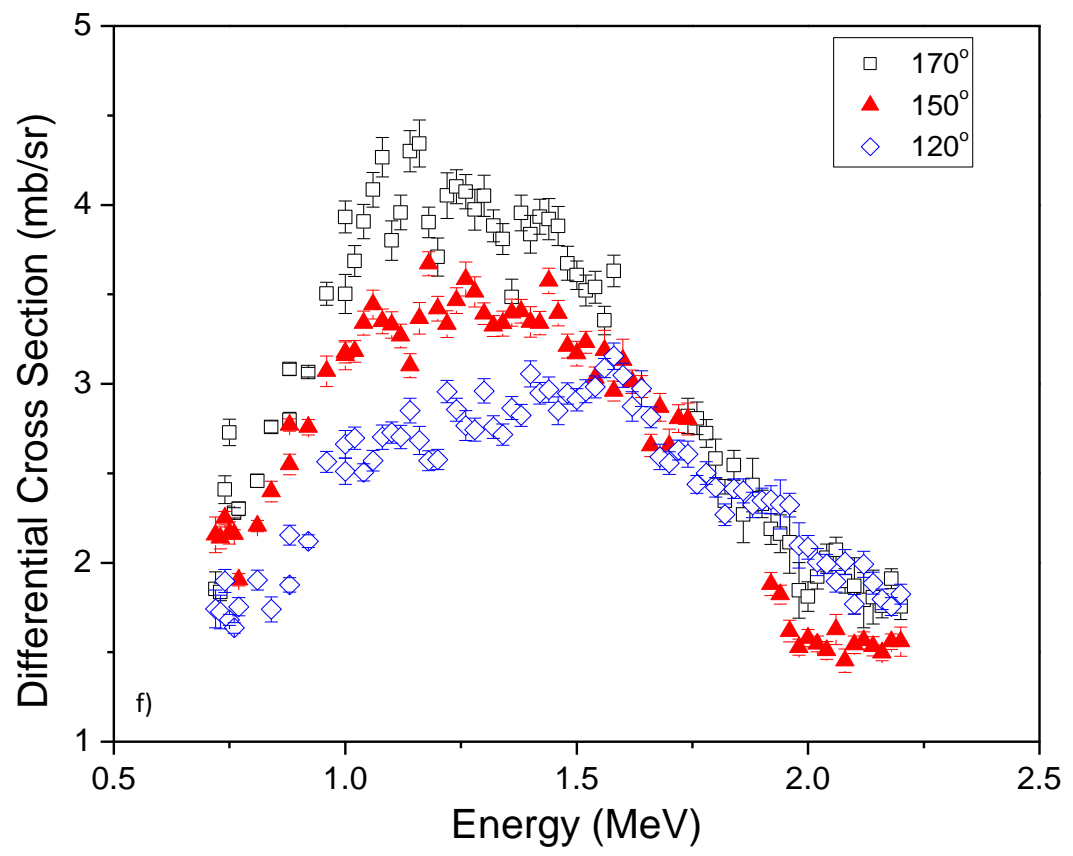
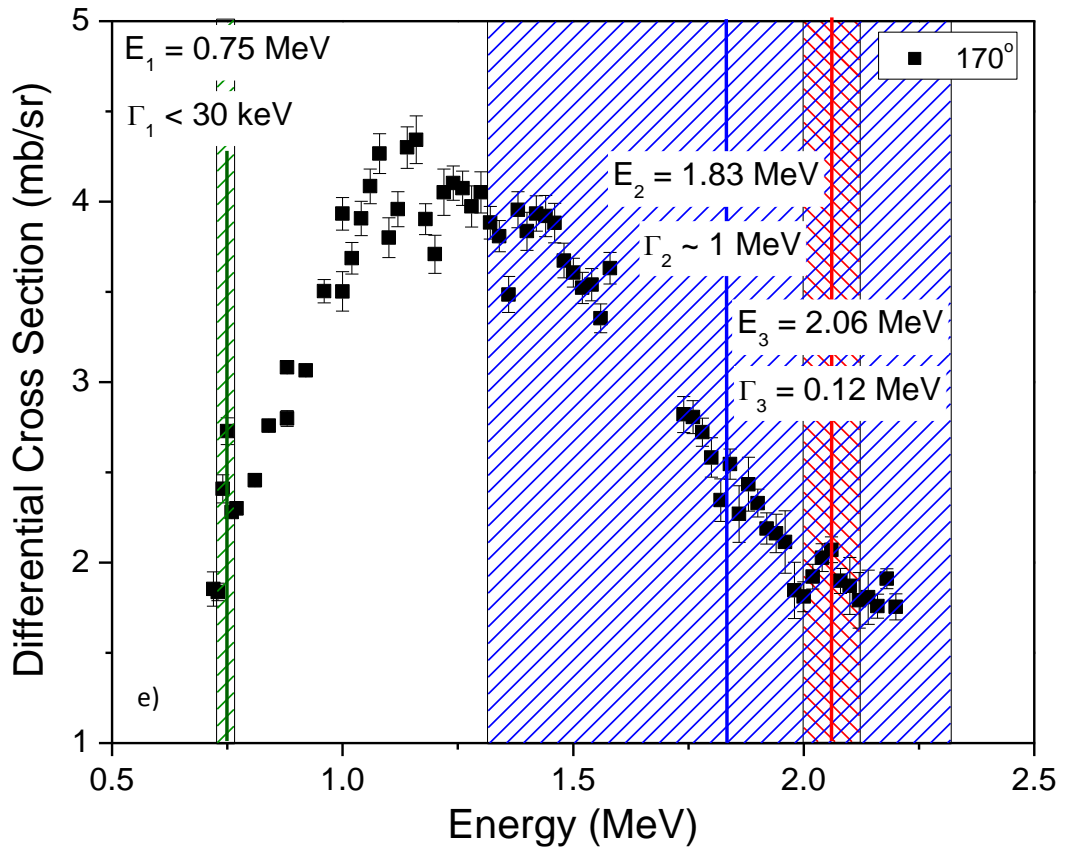


Figure 55: Measured differential cross section of the $^{10}\text{Be}(d, \alpha_0)^7\text{Li}$ at detection angles of a) 120° , b) 140° , c) 150° , d) 160° , e) 170° and f) a comparison of differential cross section from 120° , 150° and 170° .

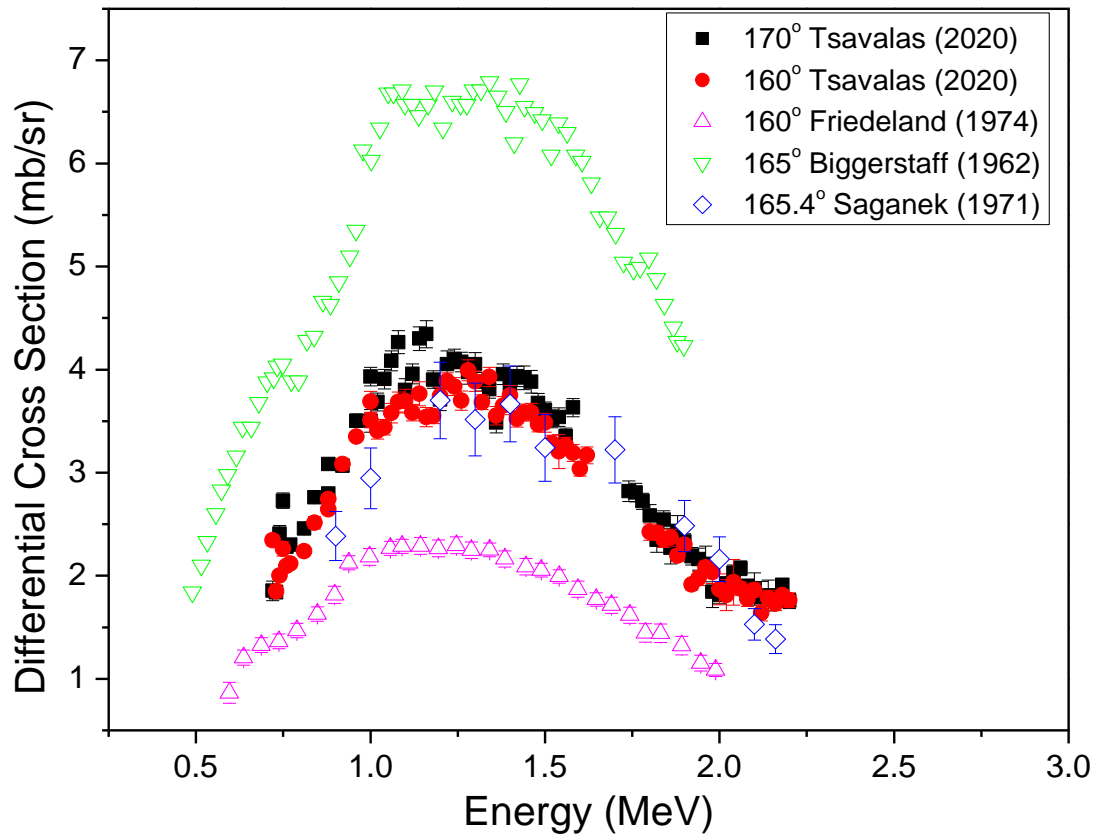
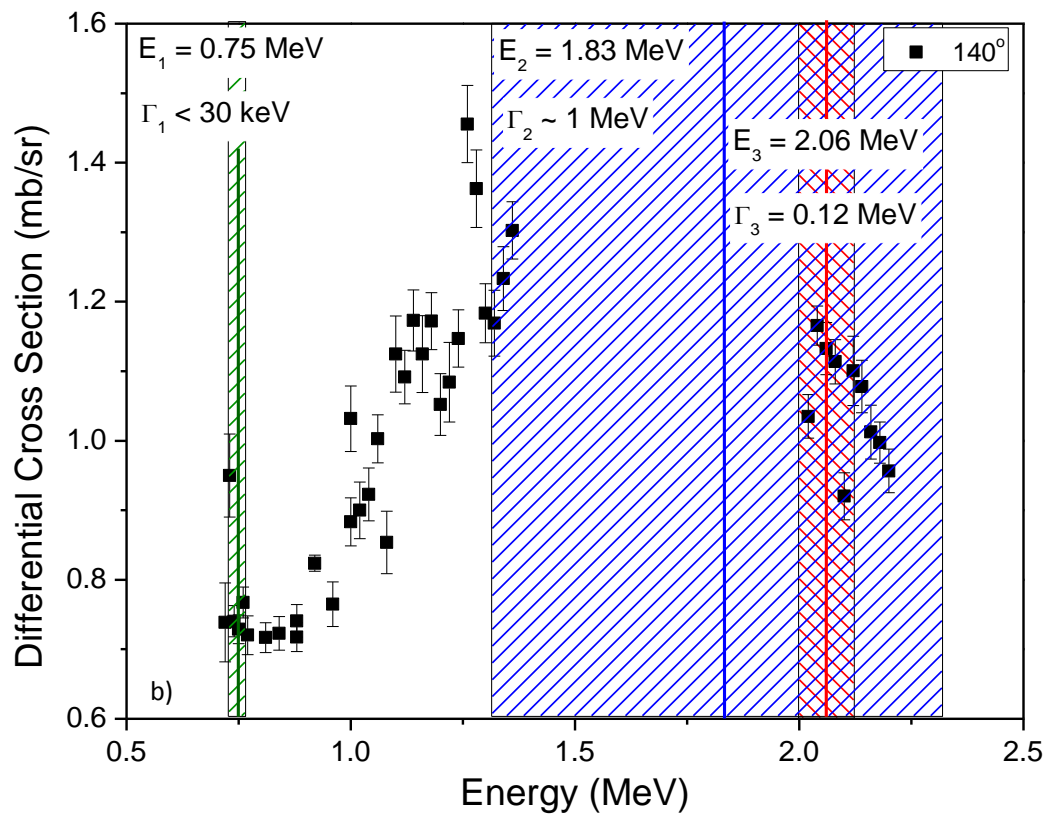
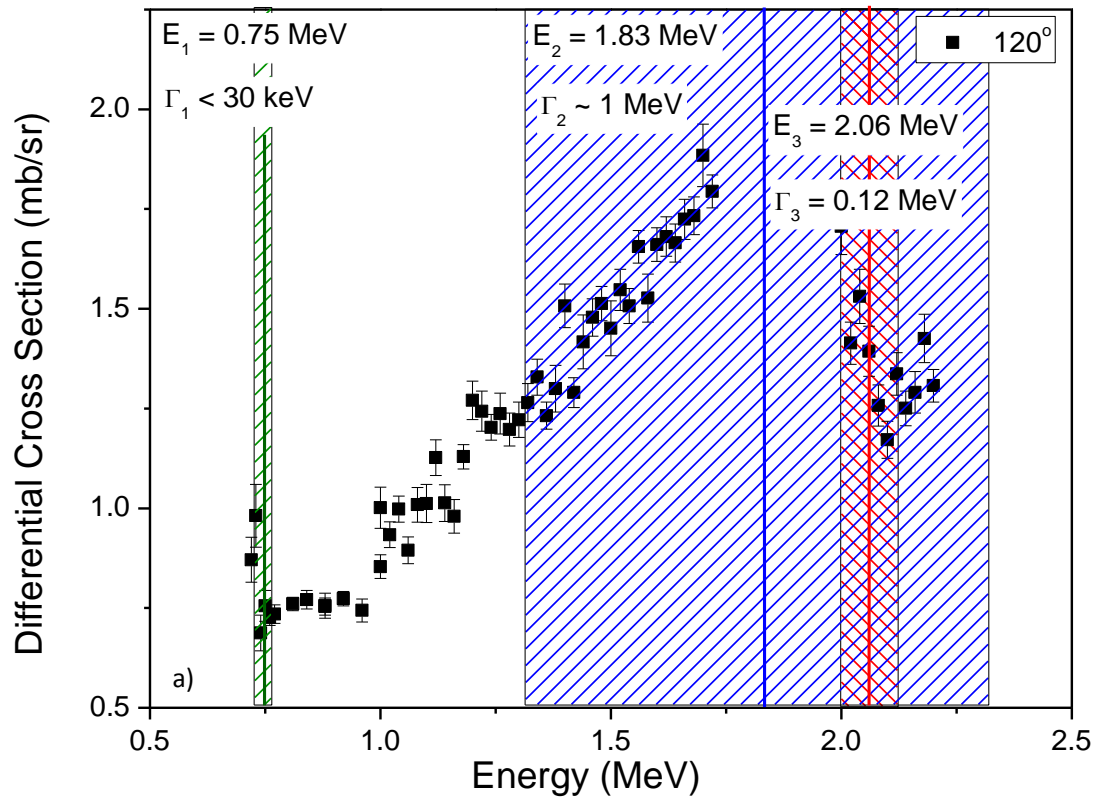
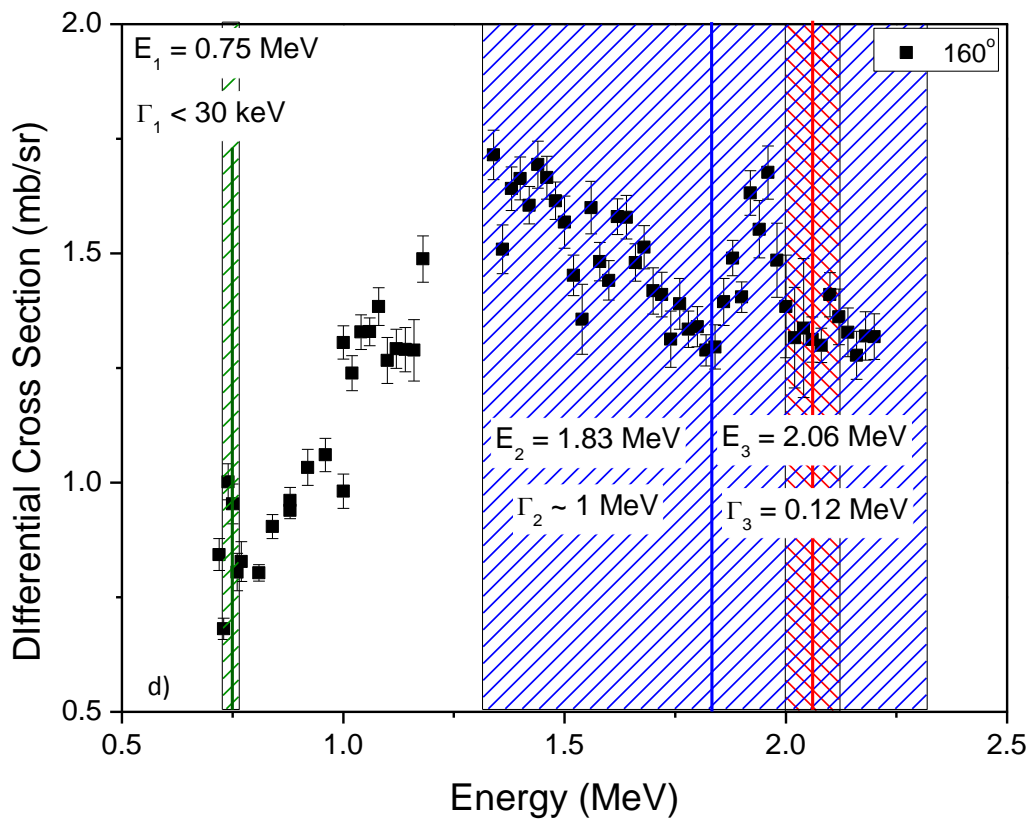
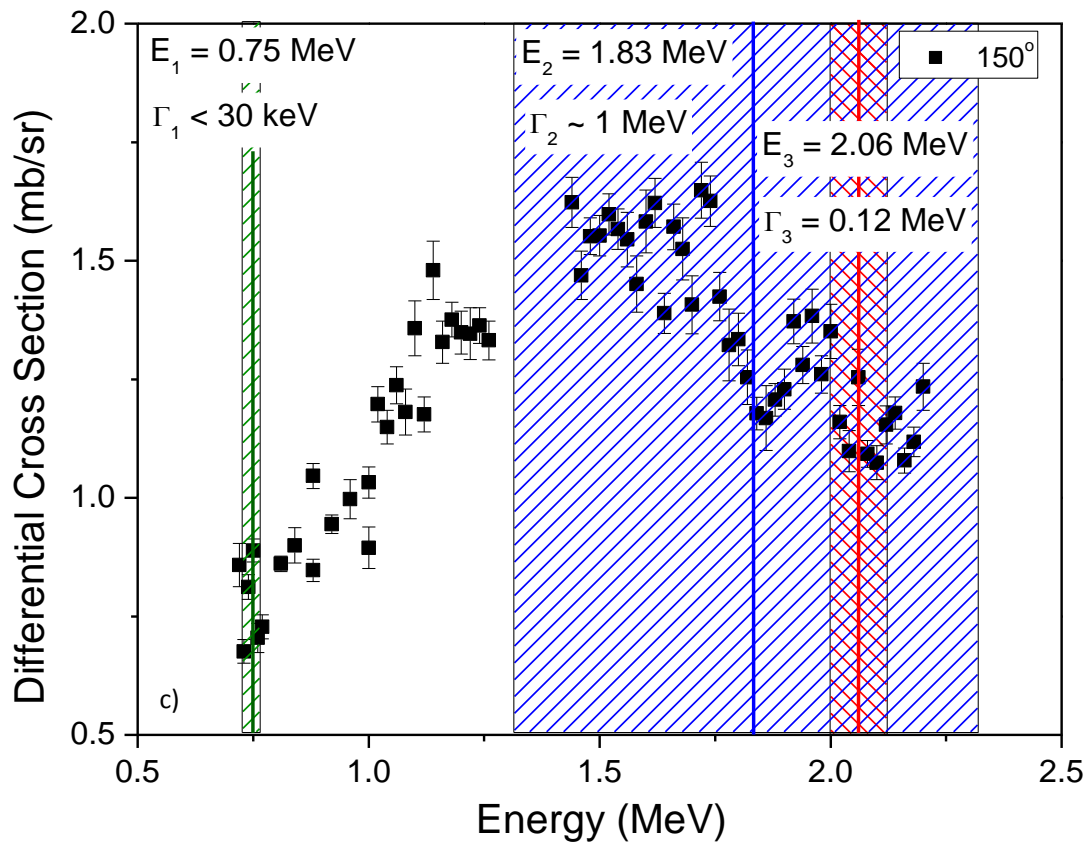


Figure 56: **Differential cross section comparison for the ${}^9\text{Be}(d,\alpha_0){}^7\text{Li}$ reaction between the Tsavalas et al and the E. Fredland et al [141], J. A. Biggerstaff et al [151] and A. Saganek et al [152] for the detection angle range between 160° - 170° .**

The differential cross section of the ${}^9\text{Be}(d,\alpha_0){}^7\text{Li}$ reaction presents angular dependence for energies lower than about 1.5 MeV with its value increasing with the increase of the detection angle. For energies higher than 1.5 MeV, the cross section decreases with the energy, displaying values from 3 mb/sr at $E_{\text{lab}} = 1.6$ MeV to 1.5 mb/sr at $E_{\text{lab}} = 2.2$ MeV, for all detection angles (Figure 55). The boron level of 16.4 MeV (energy beam of 0.75 MeV) seems to affect the cross section of all detection angles. At the detection angle of 170° , the boron level of 17.5 MeV (energy beam of 2.06 MeV) creates a peak to the differential cross section.

In Figure 56, the results of the current work are compared with the data sets of the literature for similar detection angles. The results of the current work agree with A. Saganek et al [152] data within errors bars, while the datasets of E. Freidland et al [141] and J A Biggerstaff et al [151] have the same energy dependence but considerably different absolute values. Specifically, the cross section of E. Freidland et al [141] is 45% lower, while that of J. A. Biggerstaff et al [151] is 1.6 - 1.8 times higher than the present data. These differences can be attributed to the accuracy of the thickness determination as we observe a constant discrepancy between the data.





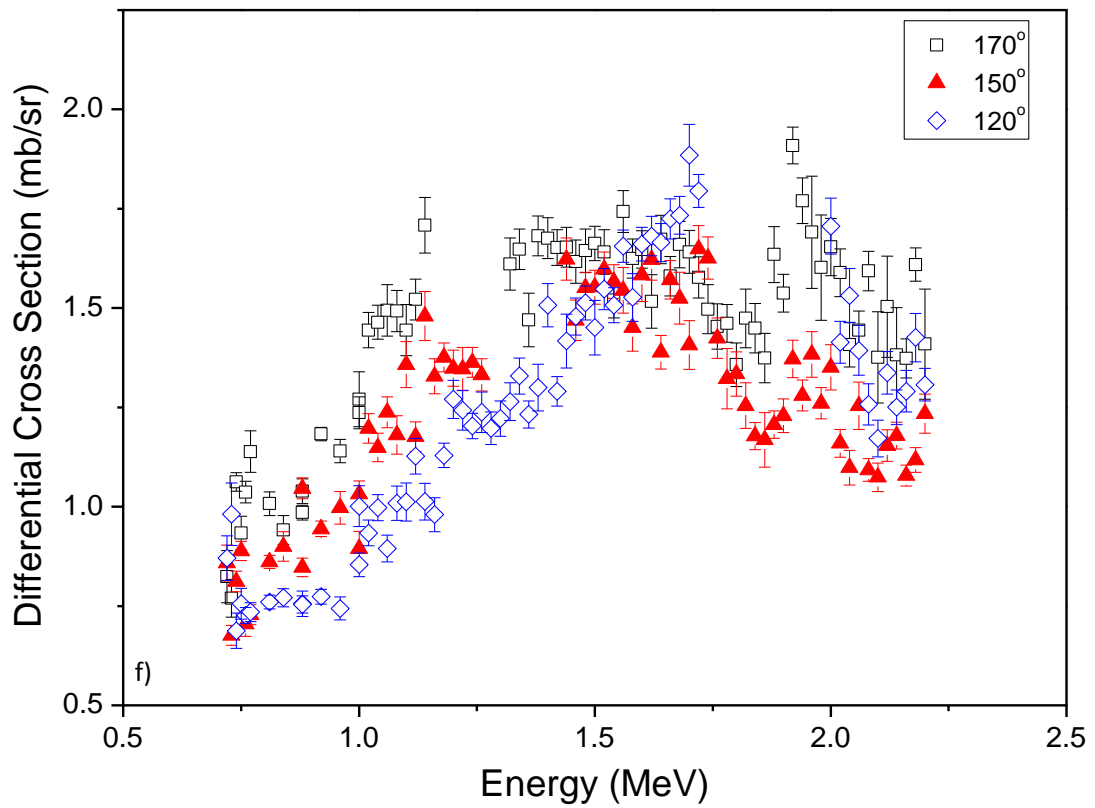
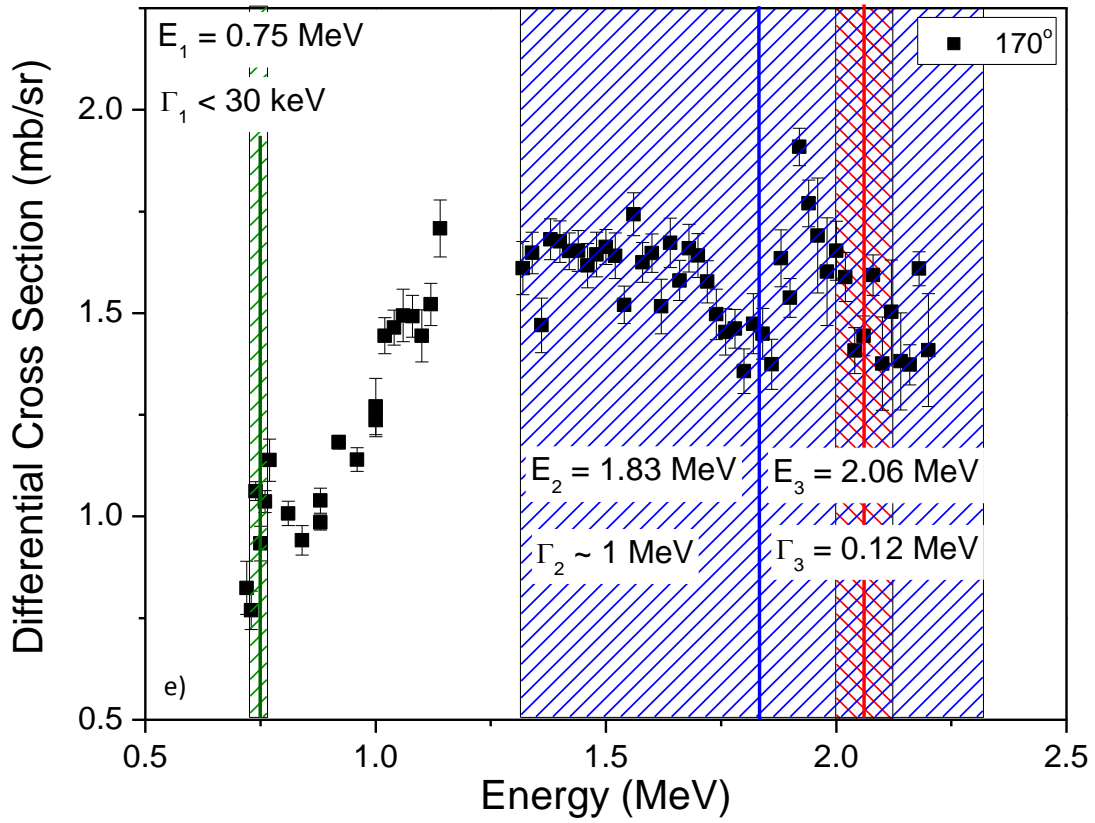


Figure 57: Measured differential cross section of the $^{10}\text{Be}(d, a_1)^7\text{Li}$ at detection angles of a) 120° ,

b) 140°, c) 150°, d) 160°, e) 170° and f) a comparison of differential cross section from 120°, 150° and 170°.

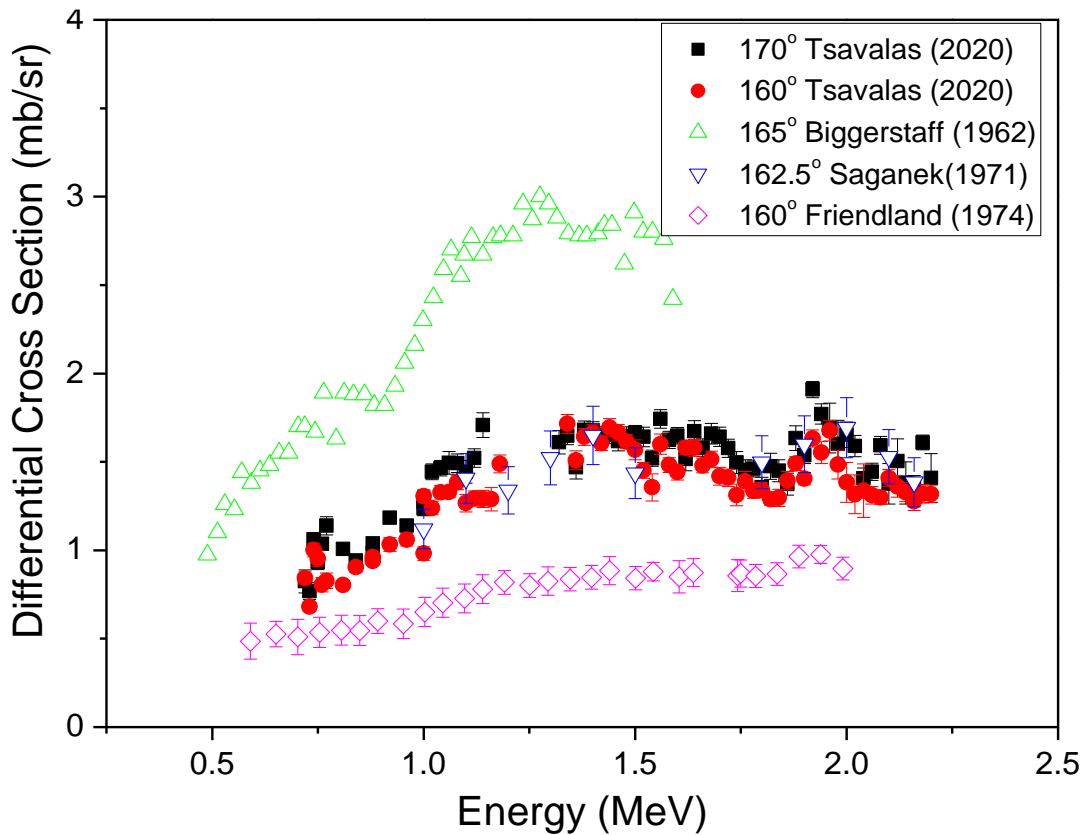


Figure 58: Comparison of the differential cross section for the ${}^9\text{Be}(d,\alpha_1){}^7\text{Li}$ reaction between the current work and that of J. A. Biggerstaff et al [151], A. Saganek et al [152] and E. Friedland [141].

The differential cross section of the ${}^9\text{Be}(d,\alpha_1){}^7\text{Li}$ reaction presents angle dependence in the whole energy range and its value increases as the detection angle increases, with the exception of the cross section for 120° detection angle and energy higher than 1.5 MeV. A peak in the energy range of 1.75 - 2 MeV is observed at detection angles where the differential cross section can be assessed (150°, 160°, 170°). A sharp peak is created due to the boron level of 16.4 MeV (energy beam of 0.75 MeV) at all the detection angles (Figure 57).

Figure 58 presents the comparison between the differential cross section of the ${}^9\text{Be}(d,\alpha_1){}^7\text{Li}$ reaction of the current work and previous ones for similar detection angles. The differential cross section of this study agrees with that of A. Saganek et al [152], while the data of E. Friedland et al [141] and J. A. Biggerstaff et al [151] have similar energy dependence with the present results but different absolute values, 45% lower and 1.7 times higher than present ones, respectively. These differences are similar to the differences in the differential cross sections of the ${}^9\text{Be}(d,\alpha_0){}^7\text{Li}$ reaction and can be attributed to the accuracy of their target thickness measurements.

3.5 Benchmarking

In order to validate the energy dependence and the absolute values of the determined cross sections, a bulk Be target with a thin Au layer deposited on its surface was constructed and measured with XRF technique to determine its thickness and NRA technique at different energies and angles to check the measured cross sections. Figure 59 presents the XRF spectrum without background and the deconvolution spectrum focused on the Au peaks of the target using a collimator of 1mm diameter, aluminum filter of 1000 μm and voltage of 30 kV. The thickness of the Au layer is determined 9.42 nm with an error of 7%.

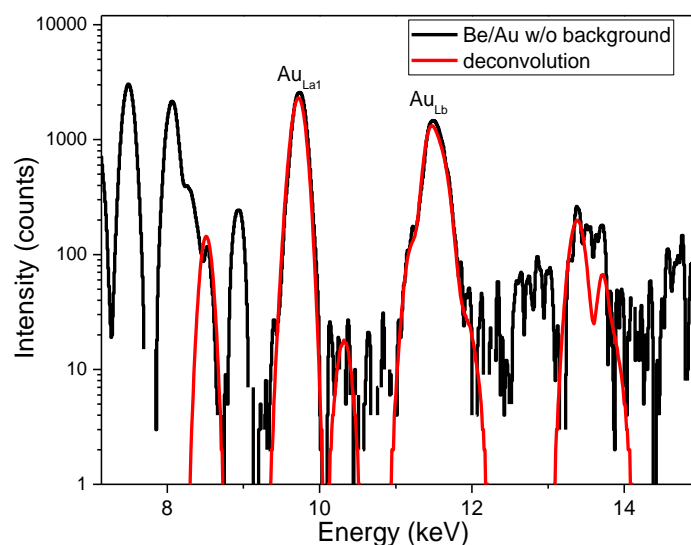


Figure 59: The XRF spectrum of the sample for the benchmarking focused on the Au peaks.

For the NRA measurements, the energy of the deuteron beam varied in the range 1.2 – 2.2 MeV with a step of 0.2 MeV and the detection angles were 120°, 140°, 150°, 160° and 170°. For the benchmarking of the cross sections, the ${}^9\text{Be}(d,p_0){}^{10}\text{Be}$ reaction was used as it was the only one which does not overlap with other reactions existing in the experimental spectra. However, there is a strong indication that the results obtained from the benchmarking experiment of the ${}^9\text{Be}(d,p_0){}^{10}\text{Be}$ reaction are also valid for the reactions ${}^9\text{Be}(d,p_1){}^{10}\text{Be}$, ${}^9\text{Be}(d,a_0){}^7\text{Li}$, ${}^9\text{Be}(d,a_1){}^7\text{Li}$, since it was a coherent measurement. The thin gold layer was used in order to calculate the $Q \cdot \Omega$ term at each energy and scattering angle through the elastic backscattering of deuterons on the gold layer which follows the Rutherford formula. Using the value of the calculated charge, the ${}^9\text{Be}(d,p_0){}^{10}\text{Be}$ reaction spectrum was simulated at each energy and scattering angle combination employing the measured cross sections. Figure 60 shows a typical experimental and simulated spectrum of the thick target measurements with the deuteron beam energy of 2 MeV and at the detection angle of 170° focused on the ${}^9\text{Be}(d,p_0){}^{10}\text{Be}$ reaction energy range.

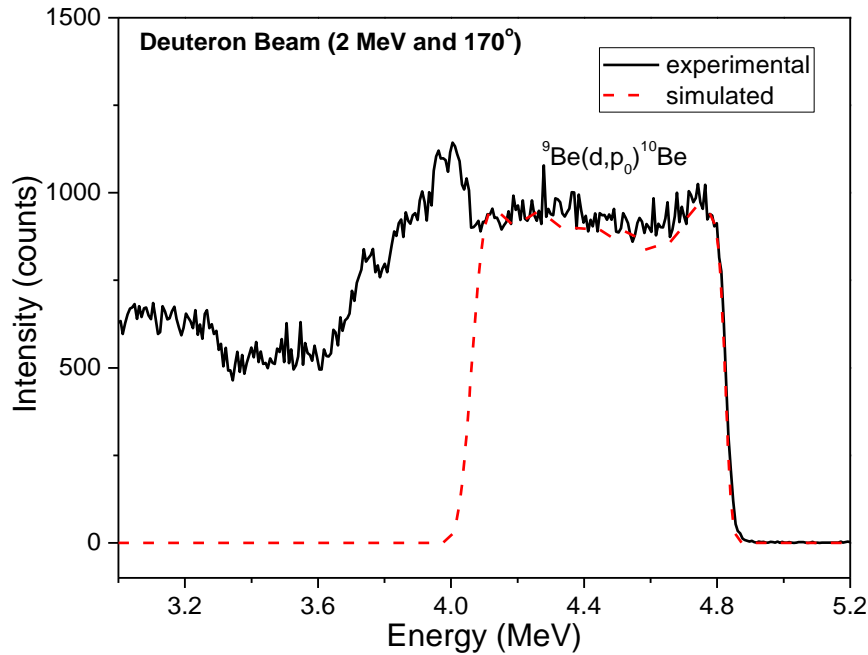


Figure 60: Experimental (black line) and simulated (red dish line) spectrum of the target consists of bulk beryllium with a thin gold layer

As Figure 60 shows, the energy dependence of the cross section agrees well with the experimental spectrum. This agreement applies to all beam energies and detection angles. The simulated spectrum of Figure 60 agrees within 3% with the experimental thick target spectrum, with the simulated one being systematically below the experimental spectrum. For all the thick target measurements, the difference between the experimental and the simulated spectra does not exceed 10%.

3.6 Conclusions

The differential cross section values of the deuteron reactions on beryllium were measured in the energy range 0.72 – 2.2 MeV at the detection angles of 120°, 140°, 150°, 160° and 170° in order to be used for the implementation of the NRA technique. The target used was a beryllium layer deposited on a Si₃N₄ membrane. The determination of the target thickness was performed using proton and O beams. The values of the cross sections were determined using the cross sections of the ^{nat}Si(d,d)^{nat}Si elastic scattering. The B excitation level with energy of 16.4 MeV, which corresponds to 0.75 MeV deuteron beam energy, affects the most of the cross sections. Comparing the results with the previous data, the current differential cross sections of the ⁹Be(d,p_{0,1})¹⁰Be reactions agree with A. S. Deineko et al [143] and the differential cross sections of the ⁹Be(d,α_{0,1})⁷Li reactions agree with A. Saganek et al [152]. The benchmarking shows that the energy dependence of the differential cross section is consistent with the acquired thick target spectra for all detection angles with the difference between the experimental and the simulated spectra not exceeding 10%.

Chapter 4: Sample Description

Samples from different parts of the ILW JET tokamak and exposed on one (ILW1, ILW2 or ILW3) or three (ILW1-3) experimental campaigns were investigated. The beryllium samples are from the limiter and the inner wall cladding of the main chamber, while the tungsten ones are from the Tile 5 of the divertor.

4.1 Be Samples

In the following section the configuration and the composition of the beryllium tiles from the different areas of the main chamber before the plasma exposure will be described. This information is very useful to interpret the results of the analysis and understand the effects of the plasma – PFMs interaction

4.1.1 Beryllium Marker Samples Exposed to ILW1 or ILW2 Campaign

Samples from beryllium marker tiles of the Dump Plate (DP), the Outer Poloidal Limiter (OPL) and the Inner Wall Guard Limiter (IWGL) from the ITER-like wall JET main chamber after the first (2011-2012) or the second (2013-2014) experimental periods were investigated (Figure 61). The marker tiles before the exposure have a special configuration with a nickel interlayer between the top beryllium layer and the bulk beryllium: Be (Bulk)/(Ni ($2.5 \pm 0.5 \mu\text{m}$)/Be ($8.5 \pm 0.5 \mu\text{m}$) [28]. The aim of the Ni interlayer is to assess surface erosion due to plasma exposure. Additionally, a sample with similar configuration with that of the marker tiles but without plasma exposure was measured and used as reference. After the cut, one of the castellation sides was noted with an engraved number. The configuration of the tiles and the samples as well as the labelling of the castellation sides based on the ion/electron drift direction are presented schematically in Figure 62, using as an example the sample 27 from ILW1 IWGL outer.

Table 6: The experimental campaign, the origin and the code of the investigated samples

Exp. Campaign	Tile	Sample Code
ILW1	Dump Plate 2B2C very top Octant 2	80
ILW1	OPL 4D14 outer midplane Octant 4 W3 RH	120
ILW2	OPL 4D14 outer midplane Octant 4 W3 RH	320
ILW1	IWGL 2XR10 inner midplane Octant 2 RH Outer	27
ILW2	IWGL 2XR10 inner midplane Octant 2 RH Outer	191
ILW1	IWGL 2XR10 inner midplane Octant 2 Centre Tile	174
ILW1	IWGL 2XR10 inner midplane Octant 2 RH Wing	76

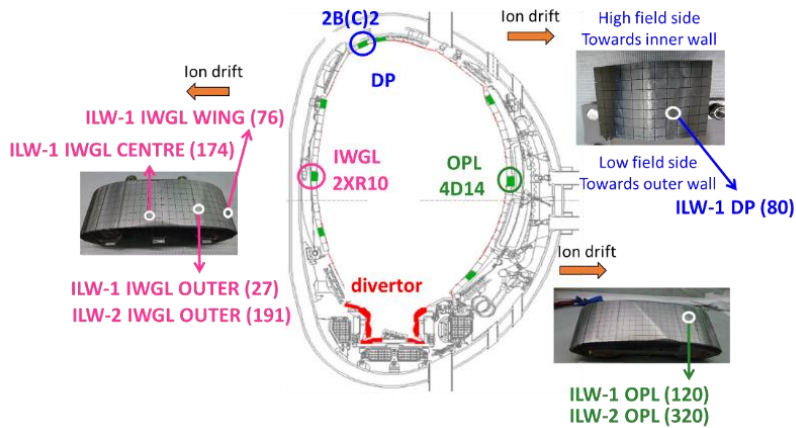


Figure 61: Position of the samples from the Be limiters in the ILW JET tokamak.

The beryllium limiter tiles have a castellation configuration, i.e. there is a gap between the samples (Figure 62). Specifically, the width of the groove of the castellation side is 0.4-0.5 mm for all samples, except for ILW-1 IWGL OUTER, where the corresponding width is 0.8 mm. This configuration enhances the thermo-mechanical durability and integrity of materials under high heat flux loads [153].

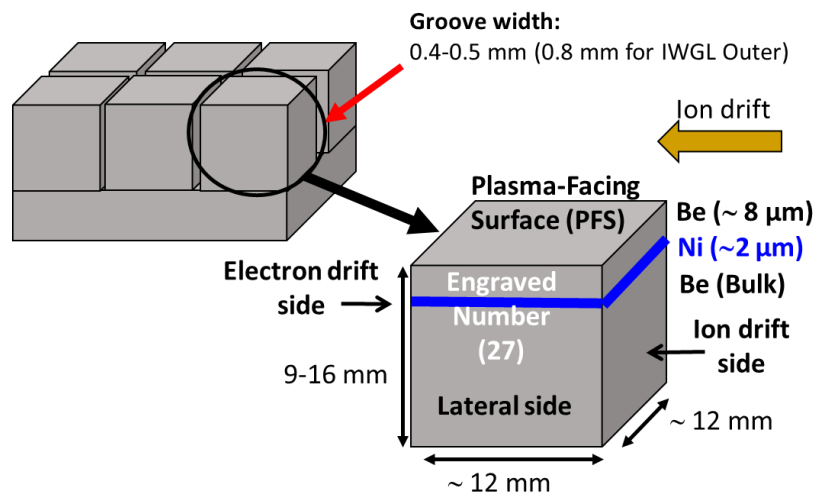


Figure 62: Schematic of the castellation configuration of the beryllium tiles and the configuration of the ILW1 IWGL outer (27) sample from the marker tiles. The castellation sides are labelled based on the ion/electron drift direction.

3.1.2 Samples from Beryllium Tiles Exposed to ILW3 or ILW1-3 Campaigns

The samples originate from the limiters and the cladding of the ILW JET Tokamak main chamber exposed to ILW1-3 or ILW3 campaign (Table 7). Specifically, two of the samples (23 and 38) are from IWC 412 and were exposed to the three experimental campaigns (ILW1-3); sample 23 is from the region A and sample 38 from the region B (Figure 63a and b). The configuration of this tile is a beryllium layer with nominal thickness of 7-9 μm coated on Inconel substrate and was placed 6 cm behind the limiters. Two samples, 390 and 418, are from the DP 3A8 exposed to three experiment

campaigns (ILW1-3) (Figure 64a). The samples 449 and 451 are from the DP 2B2C exposed to the third experimental campaign (Figure 64b).

Table 7: The list of the samples exposed to ILW3 or ILW1-3

Exp. Campaign	Tile	Sample No
ILW1-3	Inner Wall Cladding 412	23
ILW1-3	Inner Wall Cladding 412	38
ILW1-3	Dump Plate 3A8	390
ILW1-3	Dump Plate 3A8	418
ILW3	Dump Plate 2B2C	449
ILW3	Dump Plate 2B2C	451

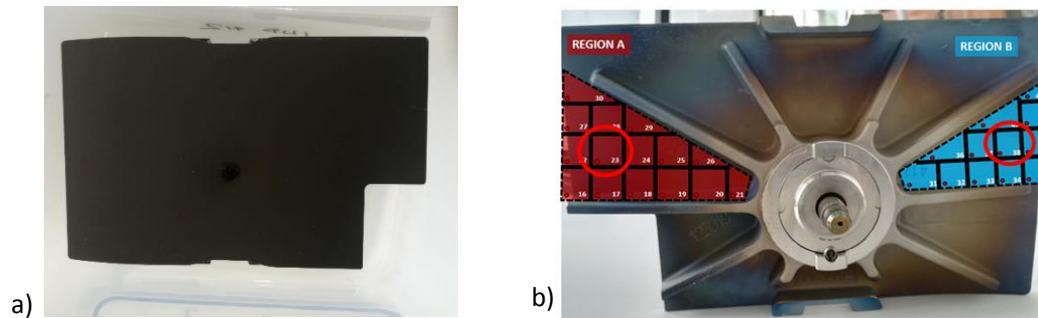


Figure 63: Images of a) the surface and b) the position of the samples of the IWC 412

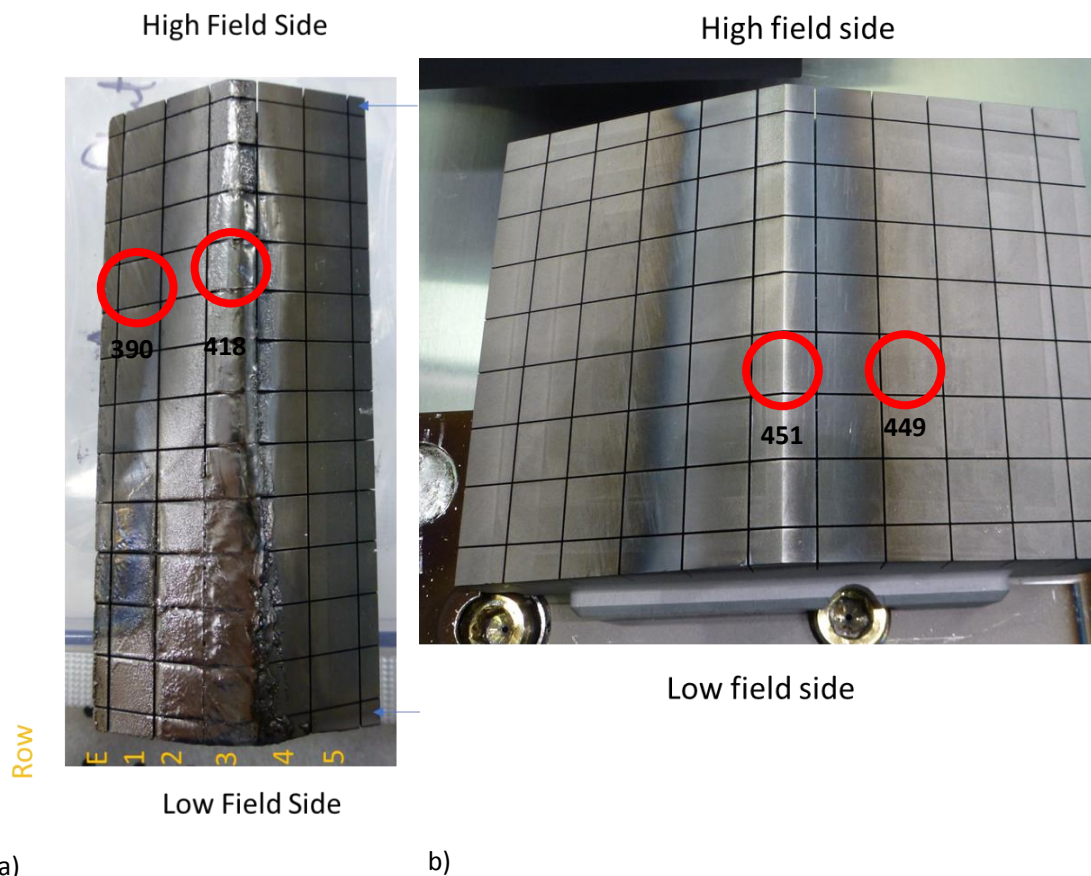


Figure 64: Images of a) the tile 3A8 exposed in ILW1-3 and b) tile 2B2C after the ILW3.

4.2 Tungsten Lamellae

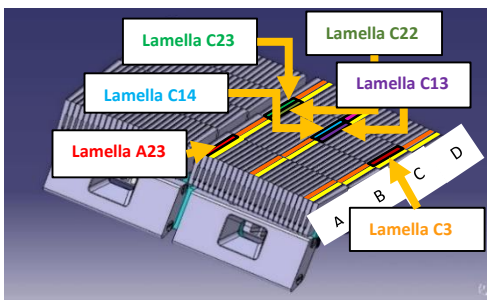
Twelve samples from the tile 5 tungsten lamellae of the JET Tokamak after one of the three ITER-like wall campaigns (ILW1, ILW2 and ILW3): five samples from the A23 (Figure 65b, e and k), one from the C3 (Figure 65c), one from the C13 (Figure 65f), three from the C14 (Figure 65d, g), one from the C22 (Figure 65h) and one from the C23 (Figure 65) lamella were analysed. The C13 and C22 constitute marker lamellae with a composition of bulk W/6 μm Mo/6 μm W, while the rest lamellae consist of bulk tungsten. Table 8 presents the full description of the analyzed samples. Figure 65 shows the tile 5 of the JET tokamak divertor, the segmentation of the lamellae and the position of the measured samples.

Table 8: The Description of the samples from the tile 5 of the JET Tokamak divertor

Exp. Period	W Lamella	Sample No	Same position	S coordinate	Description
ILW1	A23	1	as 48	1120	Bulk tungsten
	A23	7		1064	Bulk tungsten
	C3	12		1191	Bulk tungsten
	C14	15	as 63	1248	Bulk tungsten
ILW2	A23	48	as 1	1248	Bulk tungsten

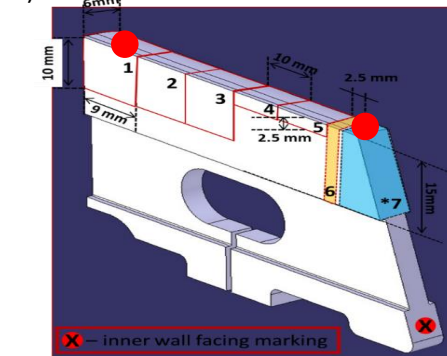
	A23	51	as 93	1085	Bulk tungsten
	C13	61		1248	Marker tile
	C14	63	as 15	1248	Bulk tungsten
	C14	67		1201	Bulk tungsten
	C22	70		1248	Marker tile
	C23	72		1248	Bulk tungsten
ILW3	A23	93	as 51	1084	Bulk tungsten

a) ILW Jet tokamak divertor Tile 5

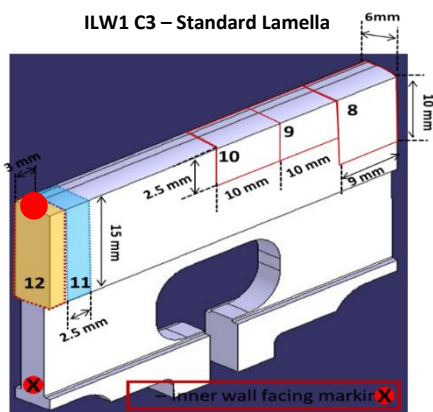


■ Marker coated lamellae 6 μm Mo/6
■ Standard lamellae; lines 3, 14, 23

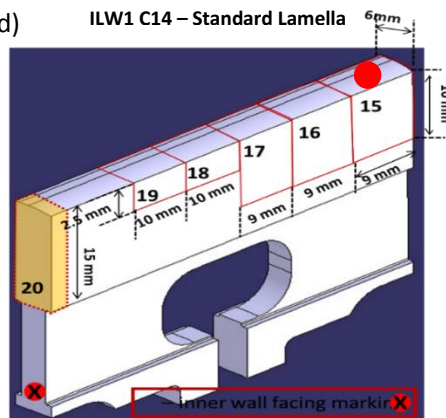
b) ILW1 A23 – Standard Lamella



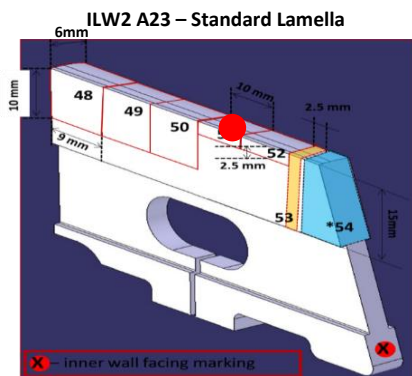
c) ILW1 C3 – Standard Lamella



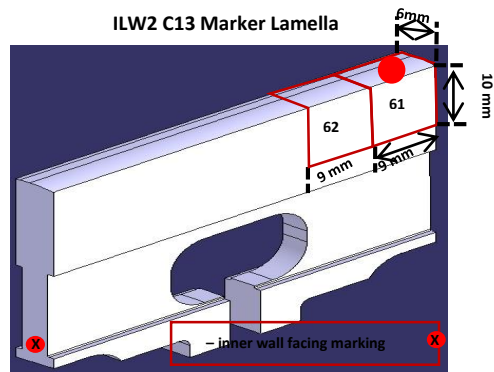
d) ILW1 C14 – Standard Lamella



e) ILW2 A23 – Standard Lamella



f) ILW2 C13 Marker Lamella



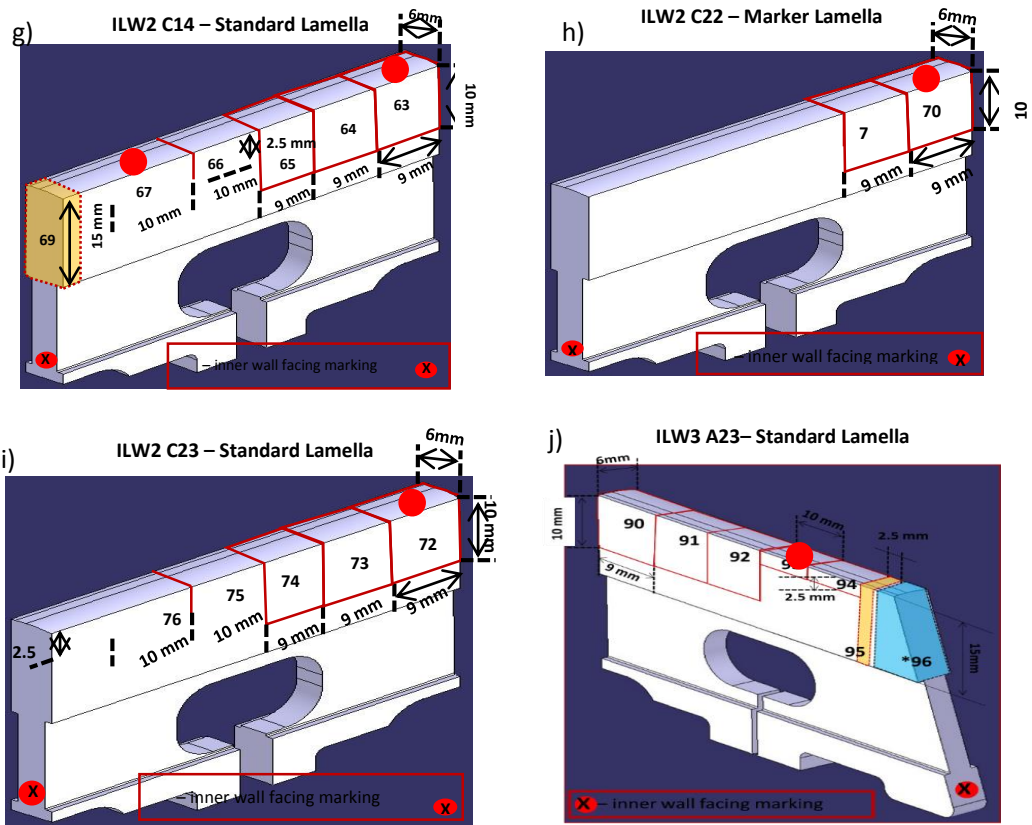


Figure 65: a) The position of the lamellae in tile 5 of the divertor and b) – k) the investigated samples and sides

Chapter 5: Results from Beryllium Tiles

In this chapter the quantitative results, the material mapping and the surface images of the measurements of plasma facing surfaces (PFSs) and the castellation sides of the beryllium samples from the JET tokamak main chamber, which were described analytically in the Section 4.1, are presented. The analytical techniques that we used are milli-beam and micro-beam NRA, XRF, SEM with EDS, XRD and PIXE.

5.1 Be samples From the Limiters After ILW1 or ILW2

The samples from the Be limiter were analysed with the mentioned set of techniques and useful conclusions were drawn about the material migration and deposition, focusing on carbon amount and spatial distribution, the deuterium retention and correlation with the carbon, the surface erosion, the surface morphology and the compound formation.

5.1.1 Carbon Amount and Spatial Distribution

The C amount and depth profile of PFS and castellation sides were determined with sensitivity of 1×10^{15} C/cm². Additionally, the maps of the castellation using the micro-beam scanning illustrate the C distribution near the PMS edge.

5.1.1.1 Plasma Facing Surface

Figure 66 shows the NRA spectrum of the PFS of ILW-1 IWGL wing (76) sample which is a representative spectrum for all the samples. The peaks from the ${}^9\text{Be}(d,p_0){}^{10}\text{Be}$, ${}^9\text{Be}(d,t){}^8\text{Be}$ and ${}^9\text{Be}(d,a_0){}^7\text{Li}$ reactions are clearly observed. On most of the samples, the O peaks of ${}^{16}\text{O}(d,p_0){}^{17}\text{O}$ and ${}^{16}\text{O}(d,p_1){}^{17}\text{O}$ reactions were also detected. However, there is contribution from the ${}^9\text{Be}(d,t){}^8\text{Be}$ and ${}^9\text{Be}(d,a_{0,1}){}^7\text{Li}$ peaks to the oxygen peaks. Therefore, the quantification of the O cannot be achieved with accuracy. In addition, for ILW1 OPL (120) and ILW-1 IWGL wing (76) samples the peak of the ${}^2\text{H}(d,p){}^3\text{H}$ was detected.

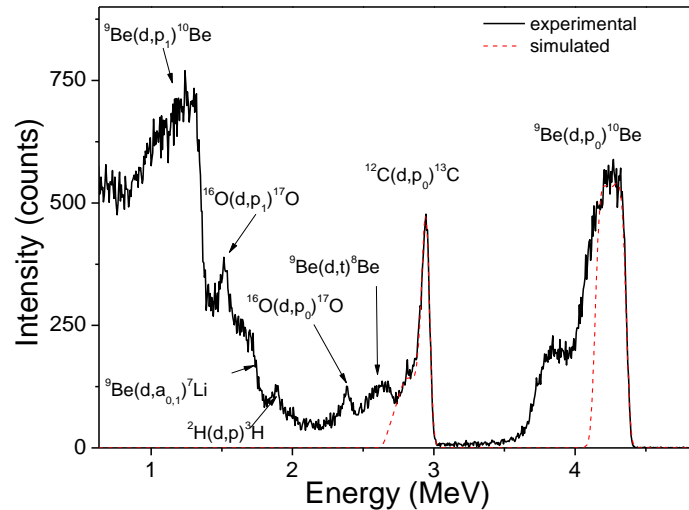


Figure 66: Experimental (black-solid line) and simulated (red-dash line) spectrum of PFS of the ILW1 IWGL wing (76) sample.

From the simulation (dotted line in Figure 66) of the NRA spectrum, in the range of energy where the $^{12}\text{C}(d,p_0)^{13}\text{C}$ and $^9\text{Be}(d,p_0)^{10}\text{Be}$ reactions were detected, the carbon depth profile was determined. The peak on the left of the $^{12}\text{C}(d,p_0)^{13}\text{C}$ peak, which corresponds to the $^9\text{Be}(d,t)^8\text{Be}$ reaction cannot be simulated due to the lack of the required cross section. This is the reason why the simulated spectrum for the $^9\text{Be}(d,p_0)^{10}\text{Be}$ reaction in Figure 66 is limited in the energy range 4 to 4.5 MeV. It is noted that the energy range 3.5 to 4 MeV of the $^9\text{Be}(d,p_0)^{10}\text{Be}$ peak is related with Be erosion and Be/Ni mixing, as it will be discussed below. The total atomic surface density and the extent of the deposition layer with the presence of C are presented for all the samples in Table 9. There are differences in the C content between respective samples, but the total carbon content is rather small (maximum content of $(11.8 \pm 0.6) \times 10^{17}$ at/cm²) reflecting low C fluxes during the ILW operation. It also indicates that the plasma erosion of the W coatings deposited on carbon fiber composite (CFC) is limited, since CFC material could provide a source of C.

The largest amount of C ($(11.8 \pm 0.6) \times 10^{17}$ at/cm²) co-deposited in a layer of 6.7 μm has been measured on the PFS of ILW1 DP (80). The lowest amount ($(0.35 \pm 0.07) \times 10^{17}$ at/cm²) with the smallest layer thickness of 0.4 μm has been detected on ILW2 OPL (320). The lower carbon deposition on OPL during the second campaign compared to the first one must be related with the enhanced erosion of the sample 320 from OPL during the second campaign, as it will be discussed below. The low amount of C in the central part of the ILW1 IWGL centre (174) is explained by the fact that the sample originates from the erosion zone.

Table 9: Total C amount on PFS and the surface thickness of the carbon-containing layer.

Campaign	Sample Code	C surface content (10^{17} at/cm ²)	C deposition thickness (μm)
ILW1	DP (80)	11.8 ± 0.6	6.7
ILW1	OPL (120)	2.9 ± 0.2	3
ILW2	OPL (320)	0.35 ± 0.07	0.4

ILW1	IWGL center(174)	0.70 ± 0.05	0.8
ILW1	IWGL outer (27)	3.6 ± 0.3	2.3
ILW2	IWGL outer (191)	4.0 ± 0.3	3.7
ILW1	IWGL wing (76)	7.6 ± 0.3	5.5

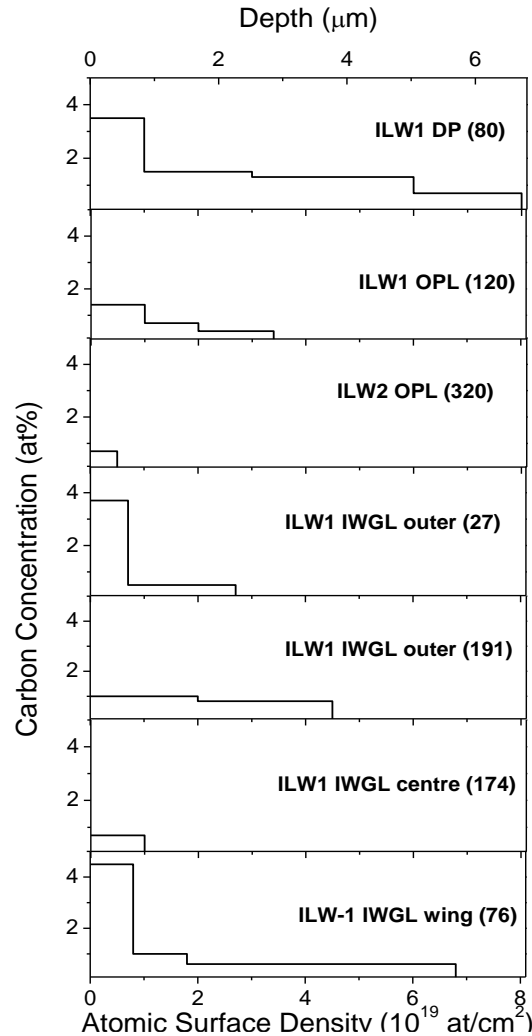


Figure 67: Carbon concentration in at% plotted versus atomic surface density (bottom x axis) and depth (top x axis) for the different samples of the JET tokamak for the ILW1 and ILW2 campaigns.

The depth profile of the carbon concentration in the deposition layer is depicted in Figure 67. In Figure 67 the top x-axis corresponds to the depth in the sample, which is calculated using the elemental concentration of each sublayer and its approximate mass density. It is perceived that the concentration decreases as a function of depth in all the investigated samples and moreover the decrease is drastic at about 1 μm depth. Carbon was detected in depth higher than 6 μm (highest depth) on the surface of the ILW1 DP (80), on the other hand carbon on the ILW2 IWGL (320) is superficial. Additionally, The highest surface concentration (4.5 at%) was detected on the ILW1 IWGL wing (76). A significant difference is observed in OPL and IWGL areas between the first and the second campaign. Specifically, the carbon deposition in both areas is higher at the surface

layers in ILW1 (on OPL (120) is 1.4 at% and on IWGL (27) 3.7 at%) than in ILW2 (on OPL (320) is 0.7 at% and on IWGL (191) 1 at%) .

Figure 68 presents the NRA spectrum in the energy range of the ${}^9\text{Be}(d,p_0){}^{10}\text{Be}$ reaction of the samples exposed to plasma compared to the non-exposed (reference) one. The maximum and the minimum energy of each peak correspond to the energy of the outgoing particles from the top and the bottom surface of each layer, respectively. Consequently, the range of the energies covered by a peak is a first indication of the thickness of the layer. The reference sample has the nominal structure of Be (bulk)/Ni(2.5 μm)/Be(10 μm). The simulation of the NRA spectrum of the reference sample gives a thickness for the top Be layer of (7.6 \pm 0.1) μm and for the Ni interlayer of (2.6 \pm 0.1) μm .

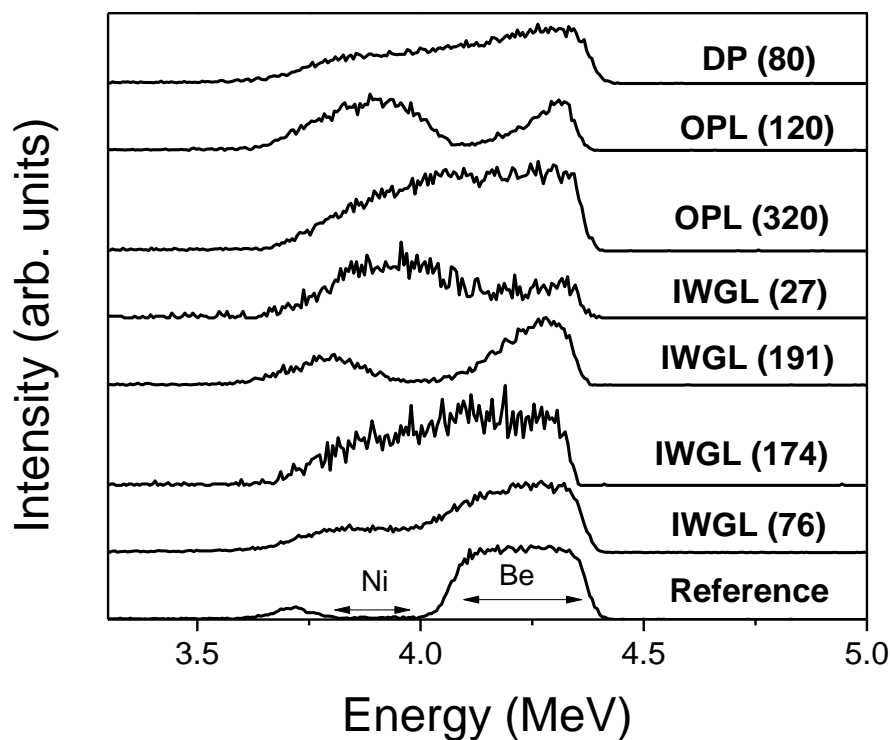


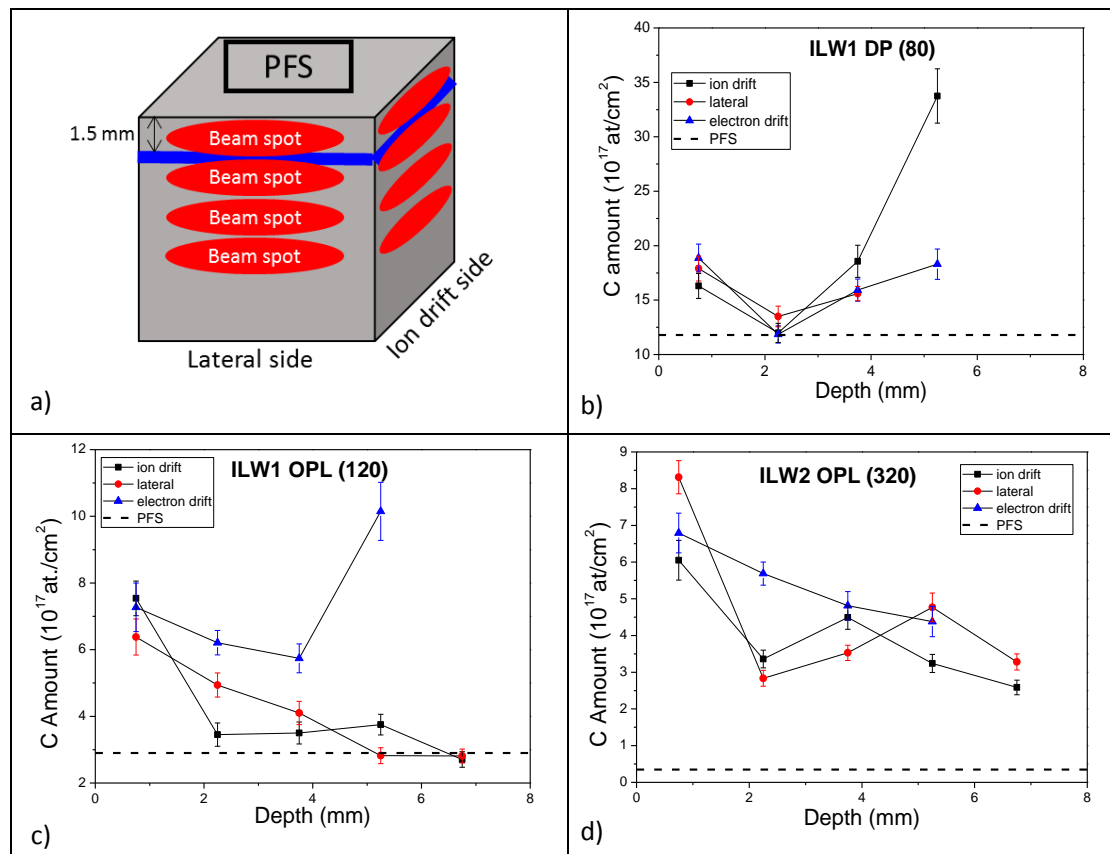
Figure 68: Comparison of ${}^9\text{Be}(d,p_0){}^{10}\text{Be}$ peak between the reference and the exposed to plasma samples.

In the reference sample the absence of the ${}^9\text{Be}(d,p_0){}^{10}\text{Be}$ peak in the energy range 3.8 to 4 MeV (Figure 68) is related with the presence of the Ni interlayer at a depth of about 8 μm . The small peak between 3.6 and 3.8 MeV corresponds to the Be bulk below the Ni interlayer. The spectra of the ILW2 OPL (320) and ILW-1 IWGL centre (174) samples indicate that either both the Ni interlayer and Be top layer have been eroded or a thick beryllium layer, of at least 7 μm thickness, has been deposited. The picture will be clarified later with the aid of the XRF results as it will be discussed below. In the ILW-1 OPL (120) and ILW2 IWGL outer (191) samples the surface beryllium is thinner than in the reference sample, leading to the conclusion that these samples had suffered erosion which is less than 8 μm . In ILW1 IWGL outer (27) the beryllium top layer has suffered larger erosion

than that of the samples ILW1 OPL (120) and ILW2 IWGL outer (191), and either the nickel layer has been mixed with the beryllium bulk or erosion of parts of the top Be layer has taken place. This will be also clarified below with the aid of the quantitative results of XRF (Section 5.1.5) and the SEM images (Section 5.1.6). The comparison of the reference sample with the samples ILW1 DP (80) and IWL1 IWGL wing (76) shows that in these two samples the nickel interlayer is mixed with the beryllium. On the other hand, in ILW1 IWGL outer (191) the presence of the nickel interlayer is clearly indicated.

5.1.1.2 Castellation Side

NRA measurements with mili- beam were also performed on the various sides and depths located inside the castellated grooves. The step for the various depths was 1.5 mm starting from the areas near to the PFS of the sample. Figure 69 illustrates schematically the beam spots of the mili-beam on the castellation sites of a sample and presents the carbon content for different depths of the ion drift, lateral and electron drift castellation sides of the samples under investigation compared with the carbon content of the PFS of the sample.



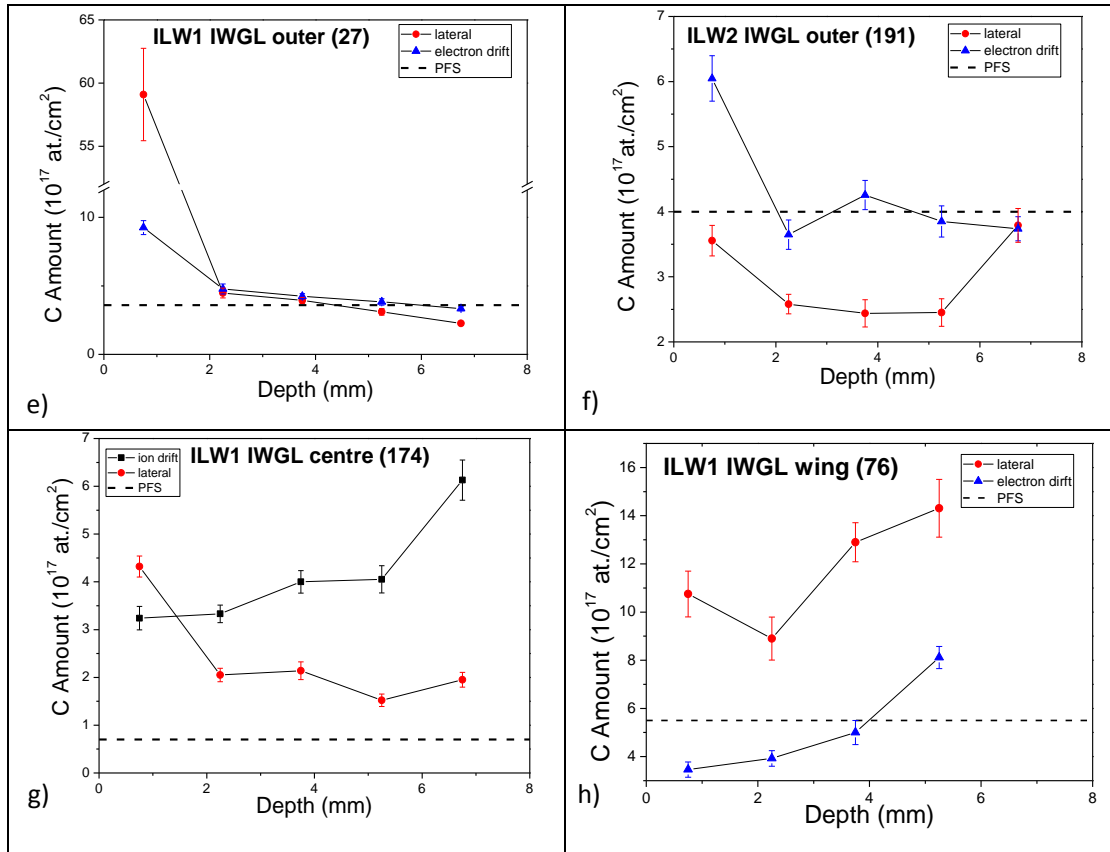
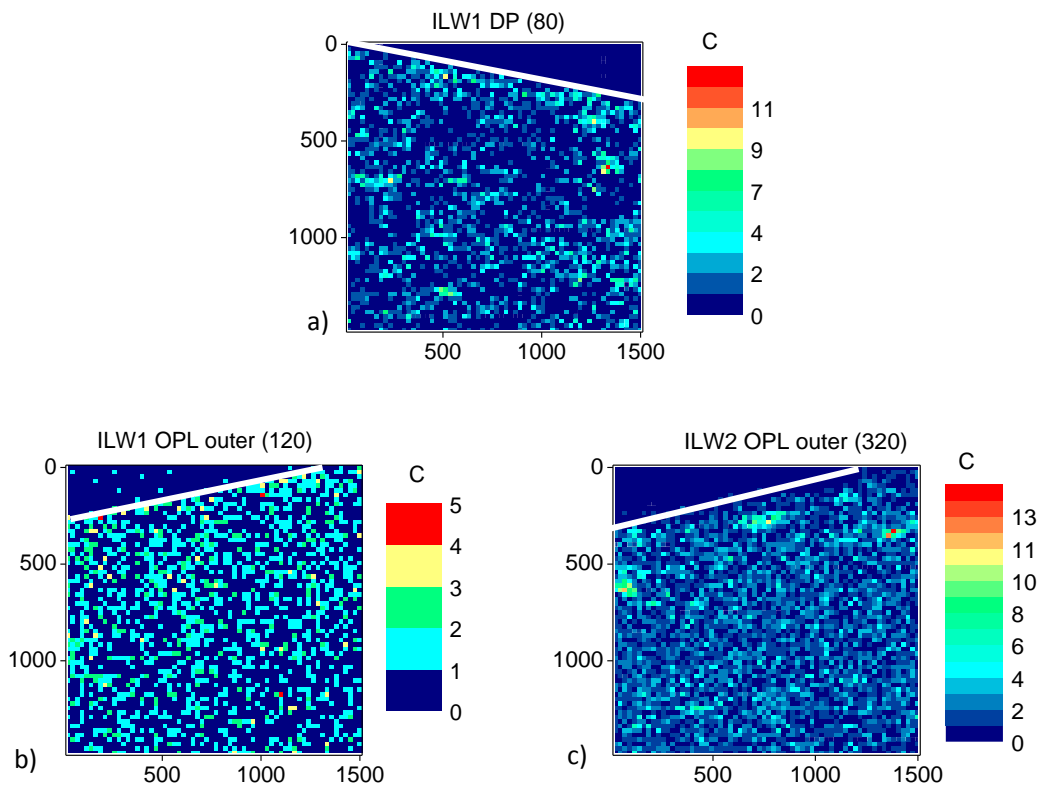


Figure 69: a) The schematic of the milli-beam measurements of the castellation sides and b-h) the carbon content of the castellation sides from different depths inside the grooves. The dash line is the carbon content of the PFS.

In most of the samples, the carbon content on the different castellation sides follows the same pattern. The castellation sides of the ILW-1 DP (80) have similar carbon amount for the first 4 mm, while in deeper positions the carbon content on the ion drift side increases with depth. For the ILW-1 OPL (120), the carbon on the ion drift and lateral castellation sides has similar depth dependence, i.e. the carbon content decreases with depth and its values are quite similar. Moreover these castellation sides have higher carbon content than the PFS and on the deepest position (depth higher than 5 mm) the carbon content becomes similar to that on the PFS. On the other hand the electron drift side has same carbon content with the other castellation sides near the PFS, its content reduces smoothly with depth but there is an abrupt increase in the deepest position. The carbon content has more or less the same behaviour on the castellation sides of the ILW2 OPL (320) as its value decreases from $(6 - 8.3) \times 10^{17} \text{at./cm}^2$ to $(2.5 - 4.4) \times 10^{17} \text{at./cm}^2$. The position near the PFS of the ILW1 IWGL outer (27) lateral castellation side presents by far the highest C amount $((59 \pm 4) \times 10^{17} \text{at./cm}^2)$, the carbon amount decreases slightly with depth on both castellation sides presenting similar values and very close to those of the PFS at depths larger than 2 mm. The electron drift castellation side of ILW-2 IWGL outer (191), after the position near the PFS, presents a constant carbon content around the value of the PFS ($4 \times 10^{17} \text{at./cm}^2$), while carbon content at the lateral castellation side decreases with depth, except for the deepest position (depth higher than 6 mm); additionally, the carbon amount of the electron drift side is 1.4 to 1.8 times higher than that of the lateral one for any depth apart from the deepest one where the two castellation sides present the same carbon content. The carbon content of ILW1 IWGL centre (174) lateral castellation side decreases with depth, whereas that of the ion drift side has the opposite behaviour and higher values for depths larger than 2 mm. The carbon content on both castellation

sides of 174 sample is higher than that of surface. The carbon content on the ILW1 IWGL wing (76) presents similar depth dependence for the castellation sides increasing with depth, but its value on the lateral side is 2 to 3 times higher than that on electron drift one.

For the area up to depth of around 1.5 mm from the PFS of various castellation sides, ^2H micro-beam measurements were carried out in order to depict the carbon spatial distribution. In Figure 70 the carbon mapping of the lateral side of all samples is depicted, with the exception of the ILW1 IWGL centre (174) sample, for which the ion drift side is presented. The PFS of the samples is at the top of the mapping and it is defined by a white line in Figure 70. On the ILW1 DP (80), some carbon agglomerates with diameter of about $150\ \mu\text{m}$ have been formed over the whole side. On the ILW1 OPL outer (120), we observe a slight decrease of the carbon with the depth, from $3 \times 10^{18}\ \text{at}/\text{cm}^2$, close to the PFS, to $1.2 \times 10^{18}\ \text{at}/\text{cm}^2$ at the depth of about 1.5 mm from the PFS. On the ILW2 OPL outer (320), carbon agglomerates with diameter in the range $100 - 200\ \mu\text{m}$ are observed near the PFS of the sample. On ILW1 IWGL outer (27), at a depth of about $800\ \mu\text{m}$ from the PFS, a stripe having a width of about $500\ \mu\text{m}$ with carbon content of $5.8 \times 10^{19}\ \text{at}/\text{cm}^2$, has been formed. On ILW2 IWGL outer (191), the amount of carbon decreases as a function of depth, from $2 \times 10^{18}\ \text{at}/\text{cm}^2$ at the top to $0.5 \times 10^{18}\ \text{at}/\text{cm}^2$ at the bottom of the investigated area. On the ILW1 IWGL centre (174), $400\ \mu\text{m}$ from the PFS, there is a thin stripe having a width of about $200\ \mu\text{m}$ depleted of carbon. On the IWL1 IWGL wing (76), a drastic decrease of the carbon content is observed from the PFS ($9 \times 10^{18}\ \text{at}/\text{cm}^2$) to the bottom of the measured area ($0.8 \times 10^{18}\ \text{at}/\text{cm}^2$).



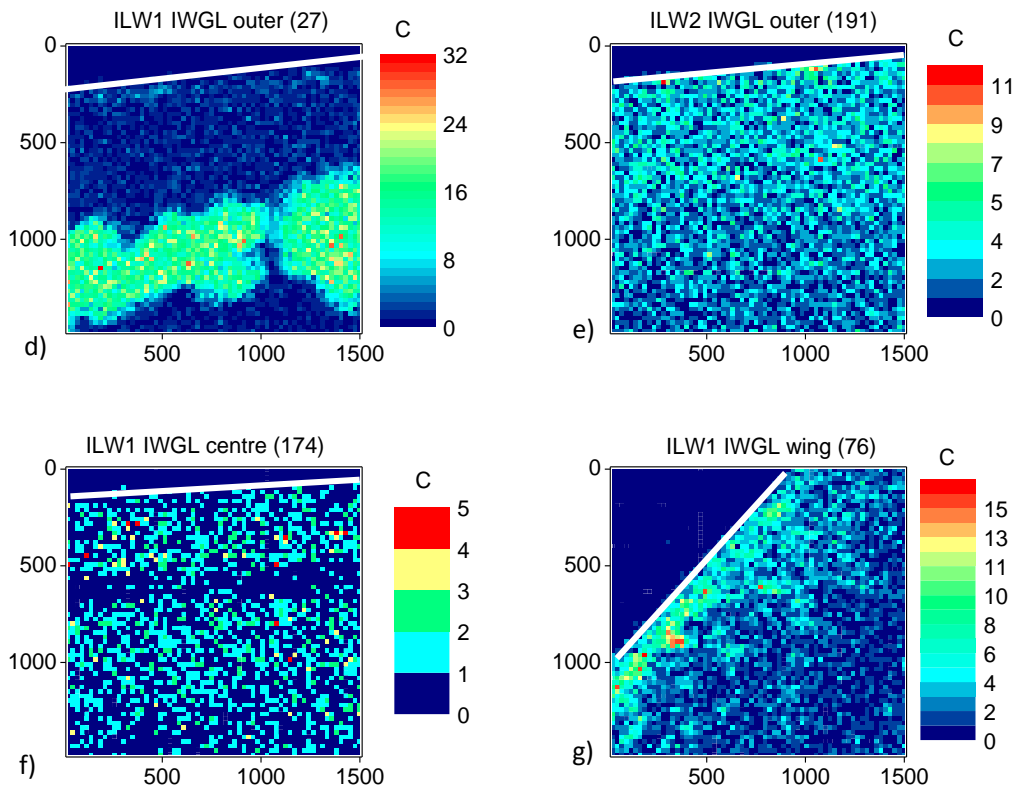


Figure 70: Mapping of the deposited carbon on the lateral side (a, b, c, d, e, g) and the ion drift side of the ILW-1 IWGL centre (174) (f). The white line defines the edge of the plasma-facing surface. The unit of the axes is μm .

5.1.2 Deuterium Retention and Spatial Distribution

The PFS and at least one castellation side of all samples were measured using a ^3He micro-beam. Figure 71 depicts representative experimental and simulated spectra of the ion drift side from the ILW1 Dump Plate (80) employing a ^3He micro-beam. The determined deuterium content using a ^3He beam is presented in Figure 72 together with the carbon content determined using a ^2H milli-beam (as described above in Section 5.1.1) for the same area.

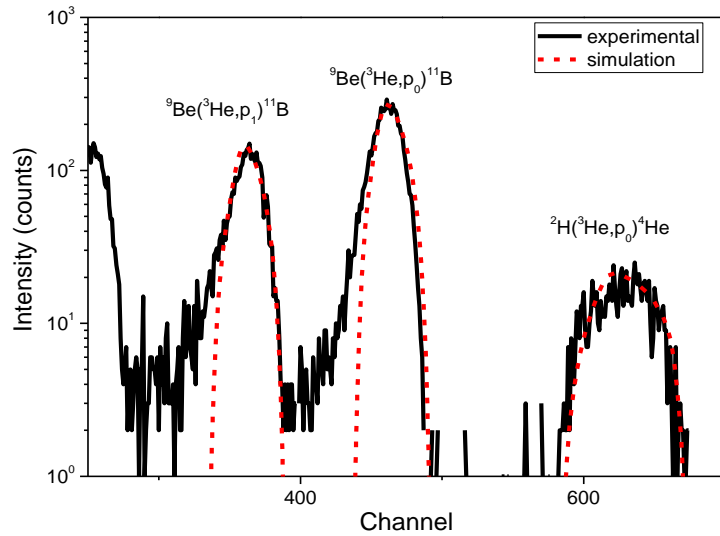


Figure 71: The experimental (solid, black) and the simulated (dash, red) NRA spectra of the ion drift side of sample 80 from the ILW1 Dump Plate.

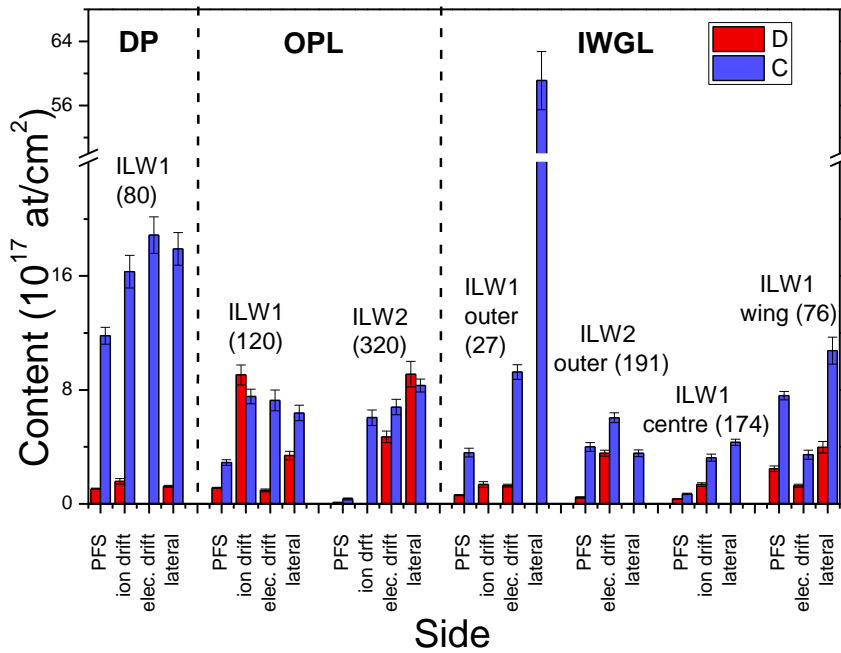


Figure 72: Deuterium and carbon content of the PFS and the castellation sides as measured by ^3He and deuteron beams, respectively.

The deuterium content on the PFS of the samples is found to vary one order of magnitude, ranging from $(0.090 \pm 0.003) \times 10^{17}$ at/cm² (sample 320 from ILW2 OPL outer) to $(2.5 \pm 0.2) \times 10^{17}$ at/cm² (76 sample from IWGL 2XR10 wing). The deuterium amount determined in the current work on the PFS of ILW1 DP ($(1.05 \pm 0.05) \times 10^{17}$ at/cm²) is in reasonable agreement with that reported in [44] ($(3.4 \pm 1.2) \times 10^{17}$ at/cm²). Additionally, integrating the mean D content (1.2×10^{17} at/cm²) of the different areas over the whole ILW1 IWGL tile, we observe that the total D content, 3.51×10^{19} at., is half of the corresponding value (6.76×10^{19} at.) reported in [44].

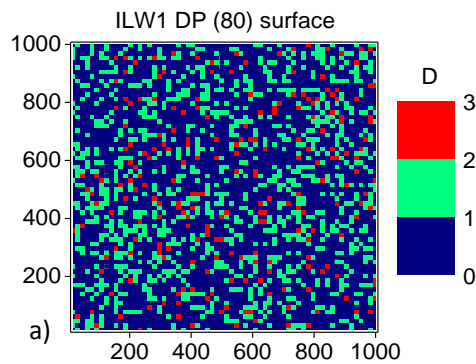
On the castellation sides, the variation of the fuel retention between the various locations is reduced with the deuterium content ranging between $(0.96 \pm 0.10) \times 10^{17}$ at/cm² (ILW1 OPL (120)

electron drift side) and $(9.1 \pm 0.9) \times 10^{17}$ at/cm² (ILW1 OPL (120) ion drift side and ILW2 OPL (320) lateral side). In general the castellation sides retain higher amounts of deuterium than the PFS.

From the first to the second campaign, the deuterium content on the PFS decreased; for the OPL from $(1.13 \pm 0.04) \times 10^{17}$ at/cm² to $(0.090 \pm 0.003) \times 10^{17}$ at/cm² and for IWGL outer from $(0.61 \pm 0.04) \times 10^{17}$ at/cm² to $(0.45 \pm 0.05) \times 10^{17}$ at/cm². On the contrary, deuterium amount on the castellation sides during ILW2 increases with respect to ILW1; for OPL from $(0.95 \pm 0.10) \times 10^{17}$ at/cm² to $(4.7 \pm 0.4) \times 10^{17}$ at/cm² (electron drift side) and from $(3.4 \pm 0.3) \times 10^{17}$ at/cm² to $(9.1 \pm 0.9) \times 10^{17}$ at/cm² (lateral side); and for IWGL outer from $(1.4 \pm 0.2) \times 10^{17}$ at/cm² to $(3.8 \pm 0.2) \times 10^{17}$ at/cm² (electron drift side).

The mean values of the deuterium content on the castellation sides are compared with those reported in [35]. There is agreement that the ILW1 DP castellation sides present the lowest deuterium retention with $(1.4 \pm 0.3) \times 10^{17}$ at/cm² found in the current work and $<10^{17}$ at/cm² reported in [35]. For the ILW1 OPL castellation side, the value found in the current work $((4.5 \pm 2.4) \times 10^{17}$ at/cm²) is close with that reported in [35] ($\sim 6 \times 10^{17}$ at/cm²). For the ILW1 IWGL, we find lower deuterium amount $((1.8 \pm 0.5) \times 10^{17}$ at/cm²) than the low limit of the range reported in [35] $((7 - 20) \times 10^{17}$ at/cm²). The comparison between the carbon deposition and the deuterium retention will be presented in Section 5.1.3.

Figure 73 depicts deuterium mappings of the PFS of the analysed samples, as determined with the ³He micro-beam. The deuterium distribution on the PFS is homogeneous for all samples. Figure 74 depicts deuterium mappings of two of the castellation sides for IWL1 OPL (120), ILW2 OPL (320) and ILW1 IWGL outer (27). Deuterium is reduced with depth on the castellation sides of all samples apart from the ILW2 OPL outer (320) (Figure 74c and d) where a deuterium stripe of about 400 μm width, 200 μm from the PFS, is observed for both castellation sides. The deuterium distribution is similar on the castellation sides of ILW1 OPL (120) (Figure 74a and b). On the ion drift side of the IWL1 IWGL outer (27) the deuterium is reduced with depth more abruptly than on electron drift one.



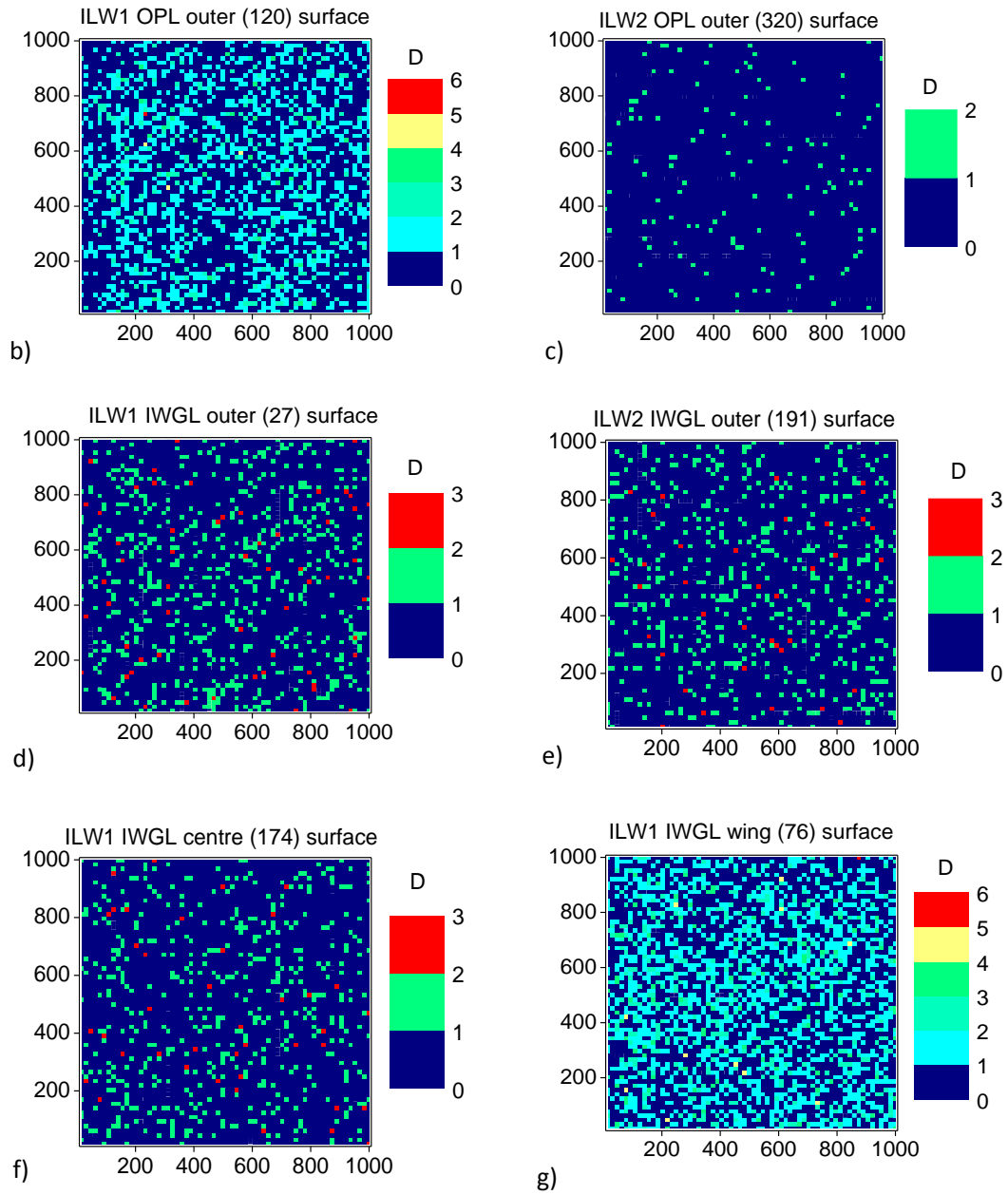
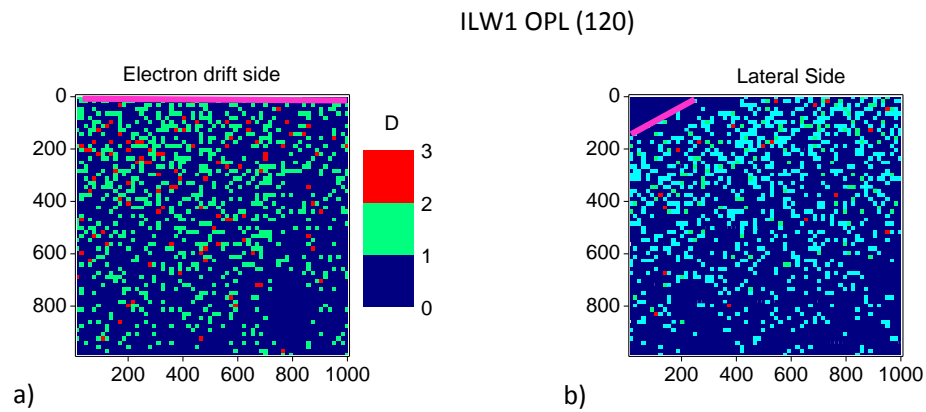


Figure 73: The deuterium mapping of PFS of the investigated samples. The unit of the axes is μm .



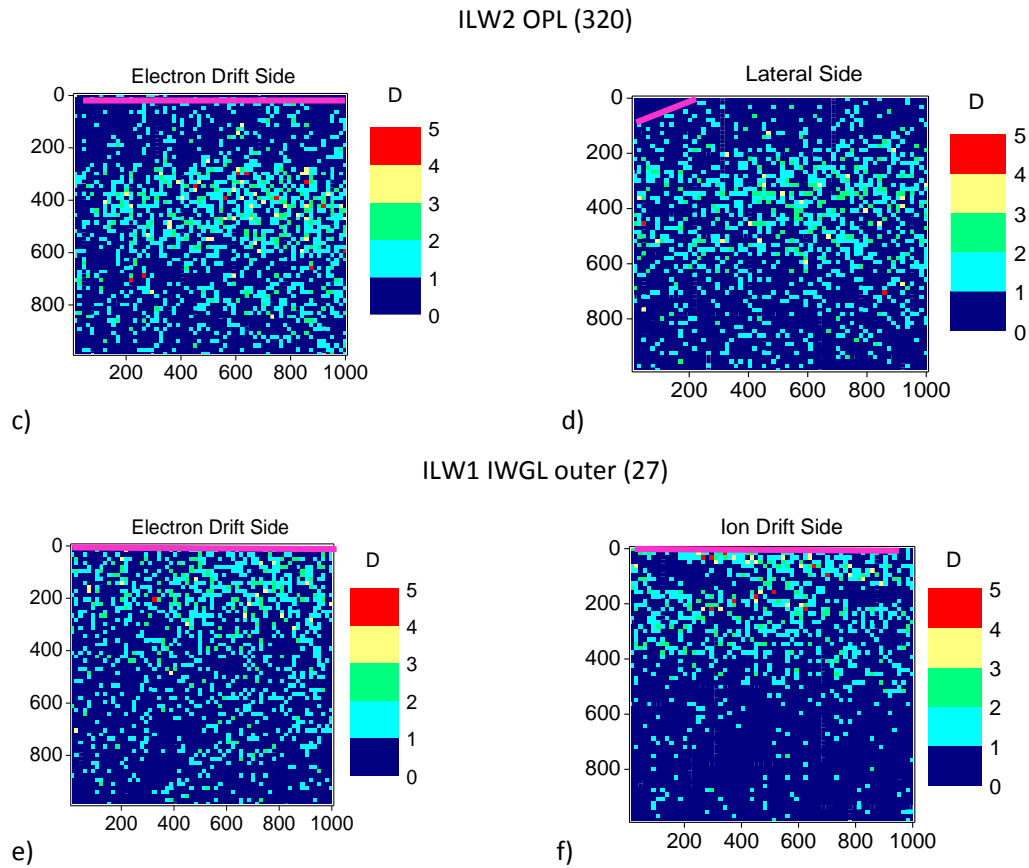


Figure 74: Deuterium mapping of vertical and parallel castellation sides. The top magenta line defines the edge of the plasma-facing surface. The unit of the axes is μm .

5.1.3 Deuterium Retention Versus Carbon Deposition

In this section we discuss possible correlation between deuterium retention and carbon deposition. From Figure 72, we conclude that high carbon amount is not necessarily accompanied by high deuterium content.

In Figure 75 the deuterium over carbon ratio (D/C) is presented for the PFS and the castellated sides. For the castellation side the average of the measured castellation sides has been used. The D/C ratio ranges from 0.07 to 1.16 with DP presenting the smallest ratio (< 0.1) and the castellation side of OPL after the second campaign the highest one (~ 1). Similar D/C ratios for the PFS and the castellation sides are observed during ILW1 campaign, whereas during ILW2 campaign the ratio is larger on the castellation sides compared to that of the PFS, being in the range of 3.6 - 6.0.

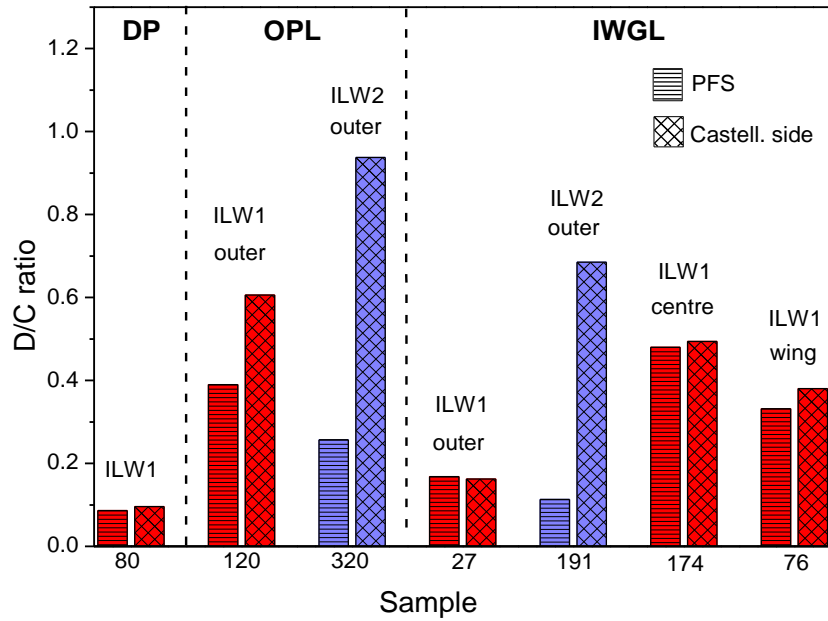
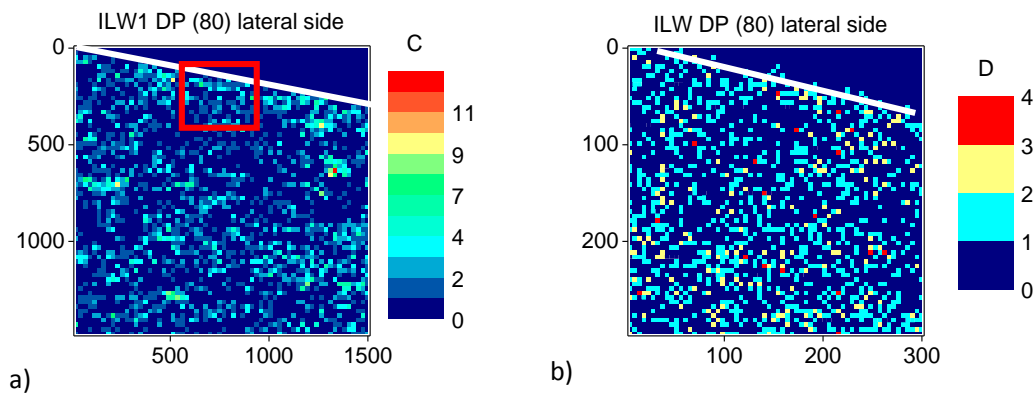


Figure 75: The deuterium over carbon (D/C) ratio of the plasma-facing surface (PFS) and the castellated side. For the castellated side the average of the measured castellation sides has been used.

Figure 76 displays representative carbon and deuterium mappings of the same castellation sides. On ILW1 DP (80) lateral side (Figure 76a and b), carbon and deuterium have similar homogeneous distributions all over the mapped area. On the ILW1 OPL (120) lateral side the carbon distribution is nearly homogeneous (Figure 76c) while the deuterium decreases with depth (Figure 76d). On the ILW2 OPL (320) lateral side the stripe rich in deuterium (Figure 76f) is not observed on the carbon mapping (Figure 76e). On the ILW1 IWGL centre (174) ion drift side, there is a zone depleted of carbon (Figure 76g), while the amount of deuterium decreases smoothly with depth (Figure 76h). On ILW1 IWGL wing (76) lateral side, a similar stripe with high amount of carbon and deuterium is detected near the PFS (Figure 76i and j).



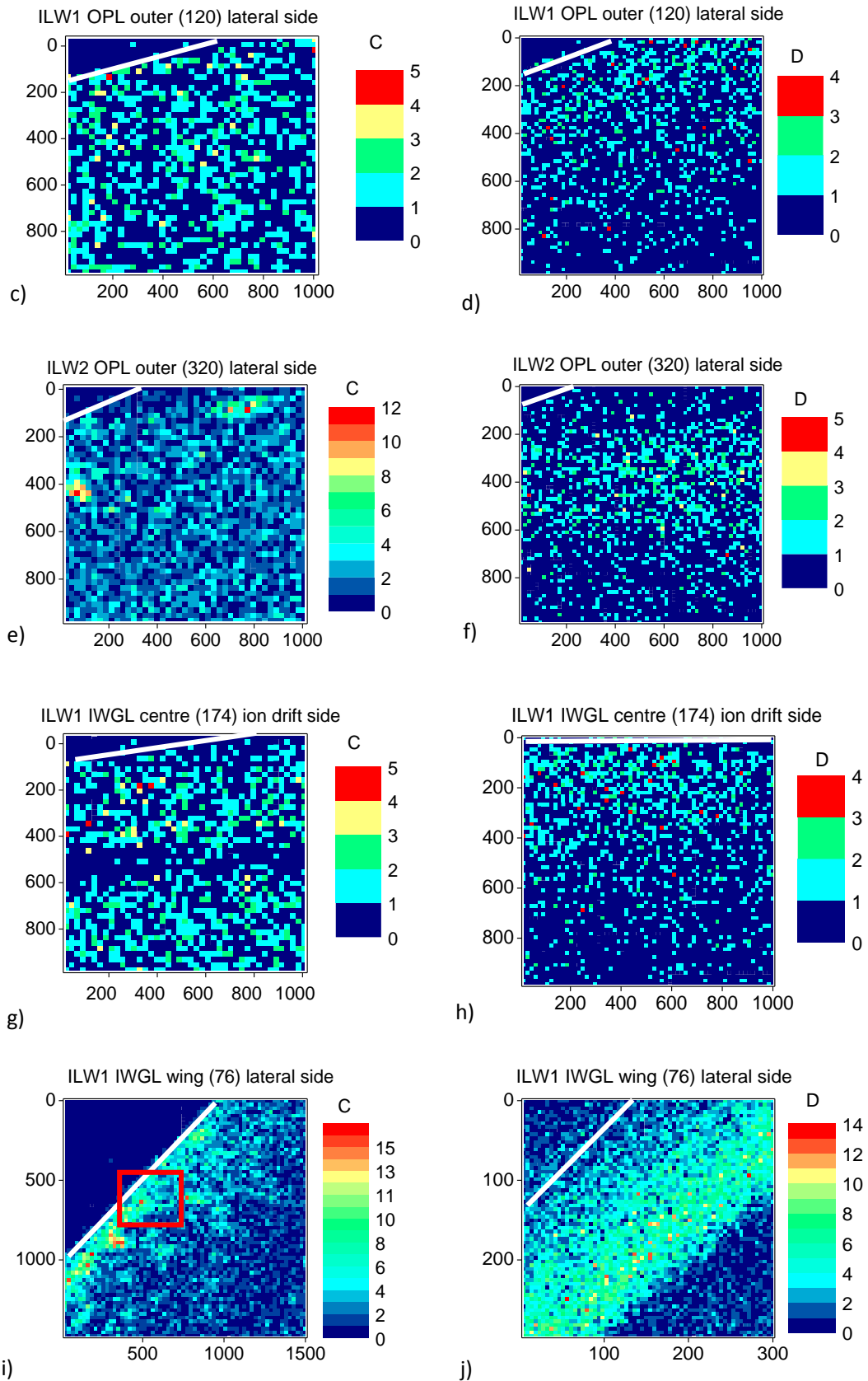


Figure 76: Carbon and deuterium mapping on the same castellation side of ILW1 DP (80) (a and b), ILW1 OPL outer (120) (c and d), ILW2 OPL outer (320) (e and f), ILW1 IWGL centre (174) (g and h) and ILW1 IWGL wing (76) (i and j). The area of deuterium mapping for b) and j) corresponds to the red box in i).

the red square of the corresponding carbon mapping (a and i, respectively). The white line defines the edge of the plasma-facing surface. The unit of the axes is μm .

5.1.4 Heavy Element Distribution

Heavy elements, such as aluminium (Al), chlorine (Cl), calcium (Ca), chromium (Cr), manganese (Mn), iron (Fe), nickel (Ni), molybdenum (Mo) and tungsten (W) were detected using PIXE on both the PFS and the castellation sides. Ni originates from either the interlayer of the samples or from parts of the tokamak that consist of Inconel. Cr, Mn and Fe are also from the Inconel parts, while Mo and W have probably migrated from the divertor. The Al may be deposited from the remote handling tool. The origin of the rest of the detected elements is not clear. Figure 77 depicts a representative PIXE spectrum of the ILW1 DP (80) lateral side. Ni is the only element with significant amount and inhomogeneous distribution on the PFS of the samples. Ni maps along with representative SEM images from the PFS are presented in Figure 78. The sample PFSs present quite different morphology. It is noted that the white areas in the SEM images correspond to heavy elements whereas light elements are depicted grey. It is observed that Ni distribution on the PFS is in agreement with the observed SEM morphologies. Specifically, areas rich in Ni are detected on the PFS of the ILW1 DP (80) and ILW1 OPL (120) (Figure 78a and b). On the PFS of the former sample, Ni particles have been deposited, while the latter one has suffered partial erosion of the top beryllium layer. The ILW1 IWGL outer (27) PFS has suffered erosion, so the Ni from the interlayer is detected on the surface (Figure 78e). The distribution of Ni on the ILW1 IWGL wing (76) (Figure 78g) is almost homogeneous. This sample must have suffered some heat load that probably caused the melting of the deposit and/or marker coating [44, 154]. The analysis of the SEM and EDS measurements will be presented analytically in section 5.1.6.

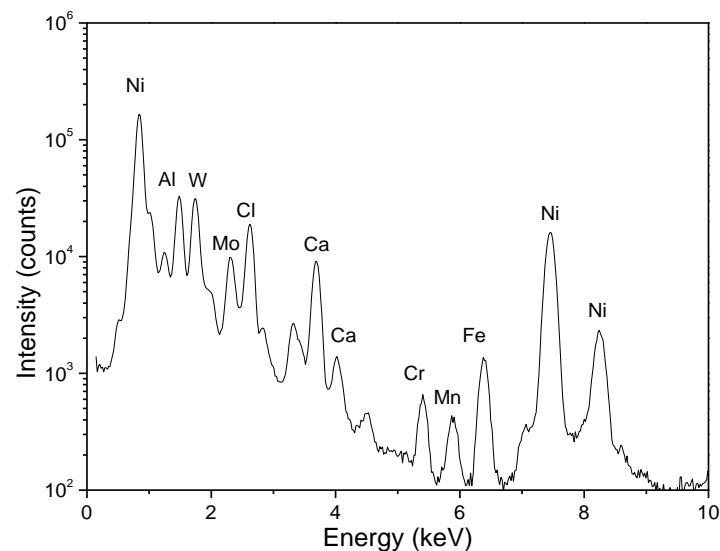


Figure 77: PIXE spectrum and peak identification of the ILW1 DP (80) lateral side using a ^3He micro-beam.

ILW1 DP (80) PFS

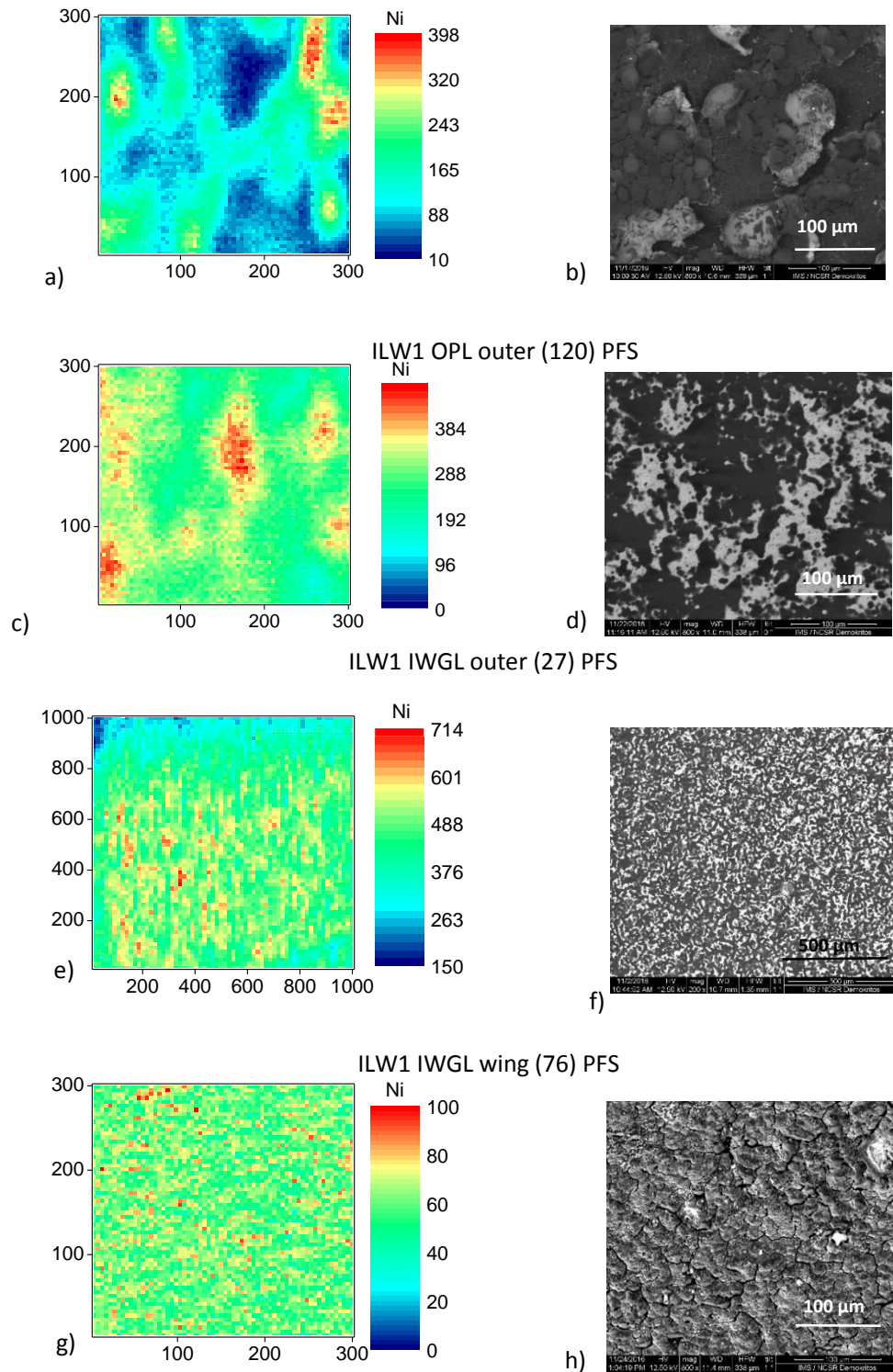
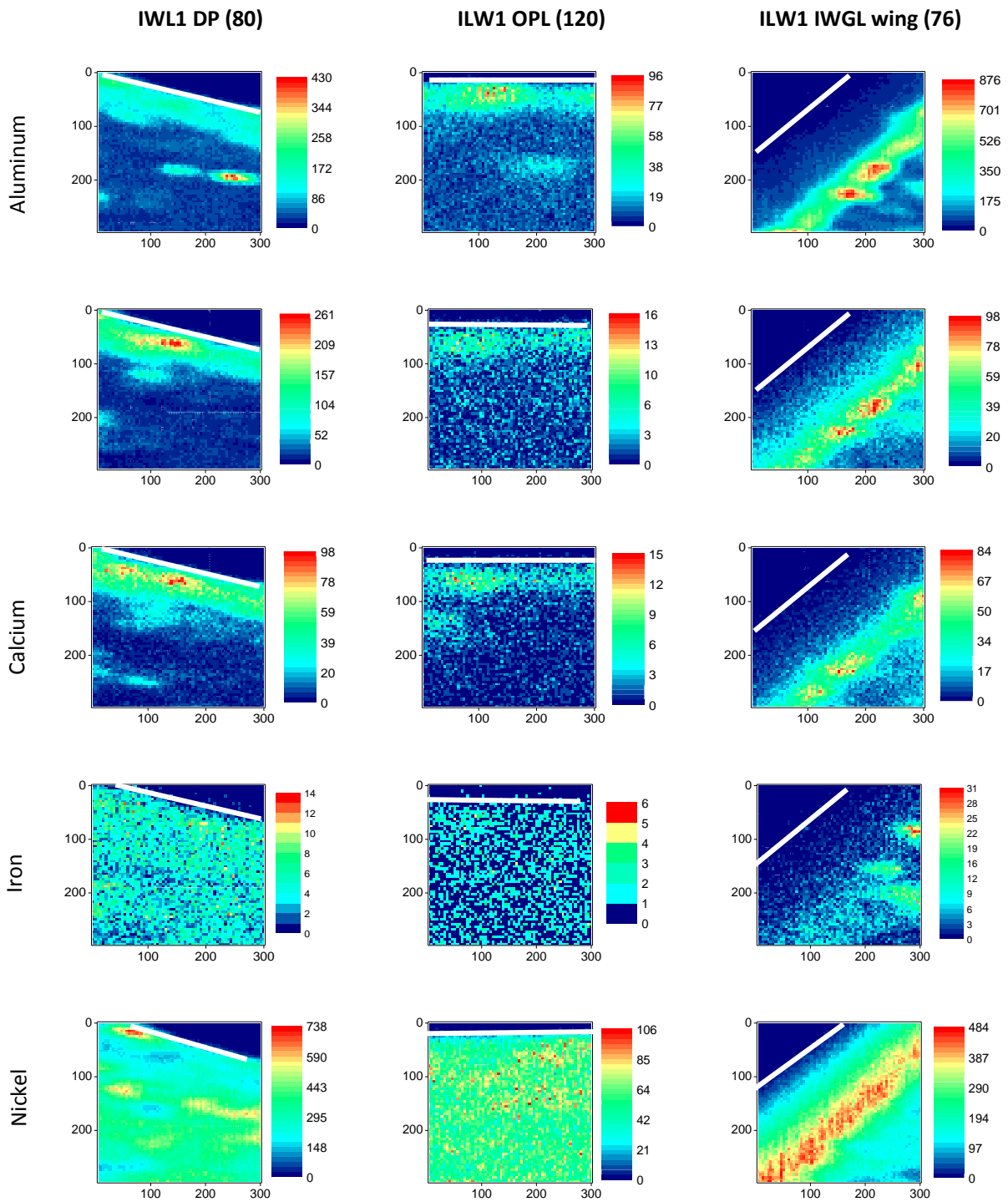


Figure 78: Representative Ni mapping and SEM images of the PFS of ILW1 DP (80), ILW1 OPL outer (120), ILW1 IWGL outer (27) and ILW1 IWGL wing (76).

Figure 79 depicts the mapping of selected heavy elements on the lateral side of ILW1 DP (80) and ILW1 IWGL wing (76) and the ion drift side of ILW1 OPL outer (120). For the ILW1 DP (80), all the elements, except for Ni and Fe, present a strong depth dependent distribution peaking at about 30 μm from the PFS and decreasing abruptly for depths larger than 80-100 μm. This zone of high

Al/Cl/Ca/Mo/W elemental concentration presents low concentration in Ni. Additionally, areas rich in one or more elements were detected in depths higher than 100 μm (Figure 79). For the ILW1 OPL outer (120), a stripe rich in Al, Cl, Ca and having a width of around 80 μm is observed, presenting no correlation with the Ni concentration. Inhomogeneous areas rich in Al or Ca are observed for depths larger than 100 μm . For the ILW1 IWGL wing (76), the detected elements form a zone of high concentration with a width varying between 50 and 150 μm at a depth of about more than 100 μm . Al, Cl, Ca, Mo and W follow similar deposition pattern.



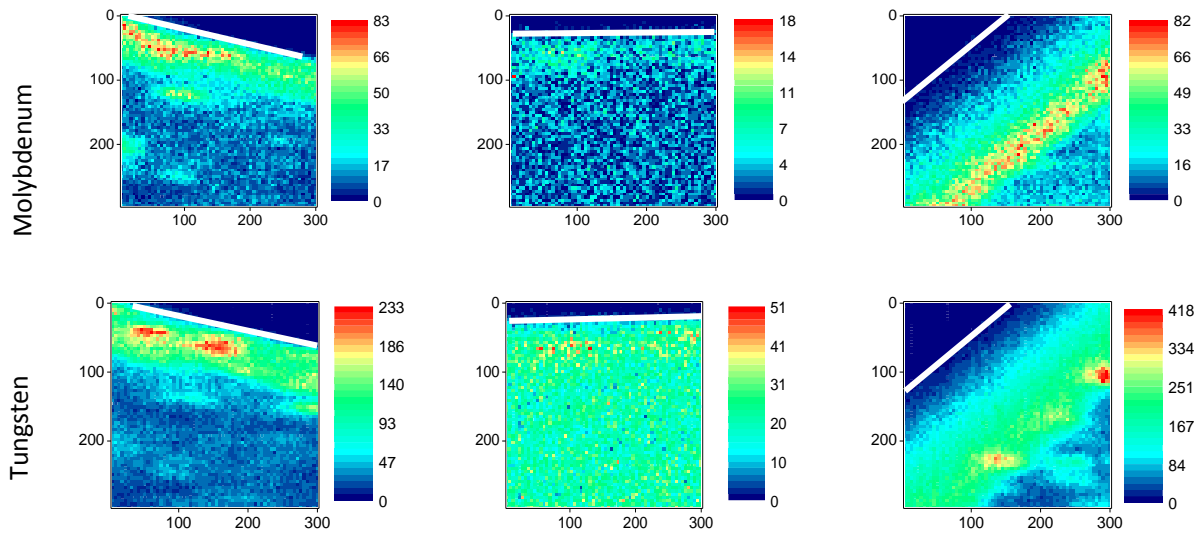


Figure 79: Mapping of the metallic elements of the castellated side of IWL1 DP (80), ILW1 OPL (120) and ILW1 IWGL wing (76). The white line defines the edge of the plasma-facing surface. The unit of the axes is μm .

5.1.5 X-ray Fluorescence Spectroscopy Results

XRF measurements were carried out in order to determine the concentration of elements heavier than Na ($Z > 11$) from higher depth of the samples. The representative XRF spectrum of the ILW1 IWGL outer (27) focused on the energy that we are interested in, using Al filter with thickness of 1000 μm and the identification of the peaks are presented in Figure 80. Figure 81 presents the quantitative XRF results of the samples from the JET tokamak main chamber and a reference one.

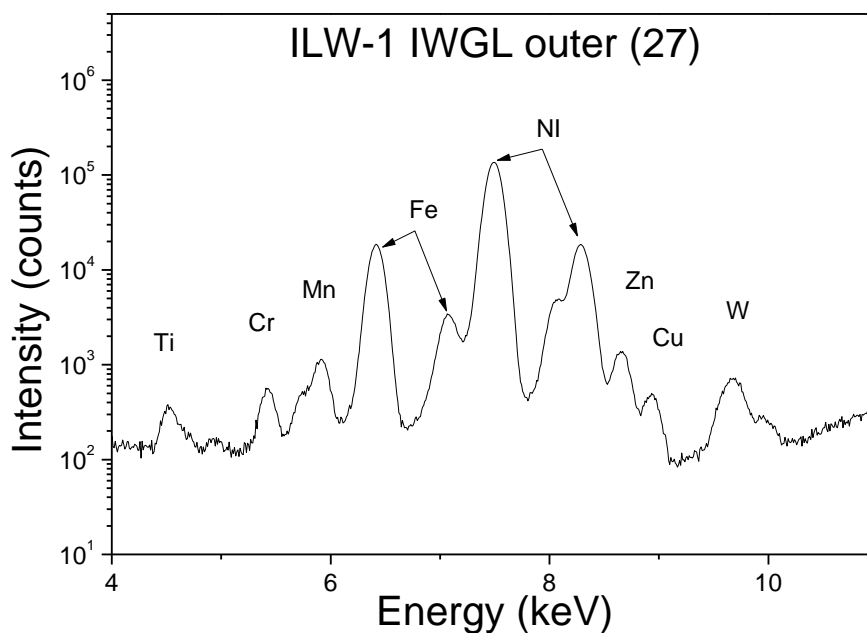


Figure 80: The XRF spectrum of ILW-1 IWGL outer (27) and the peak identification.

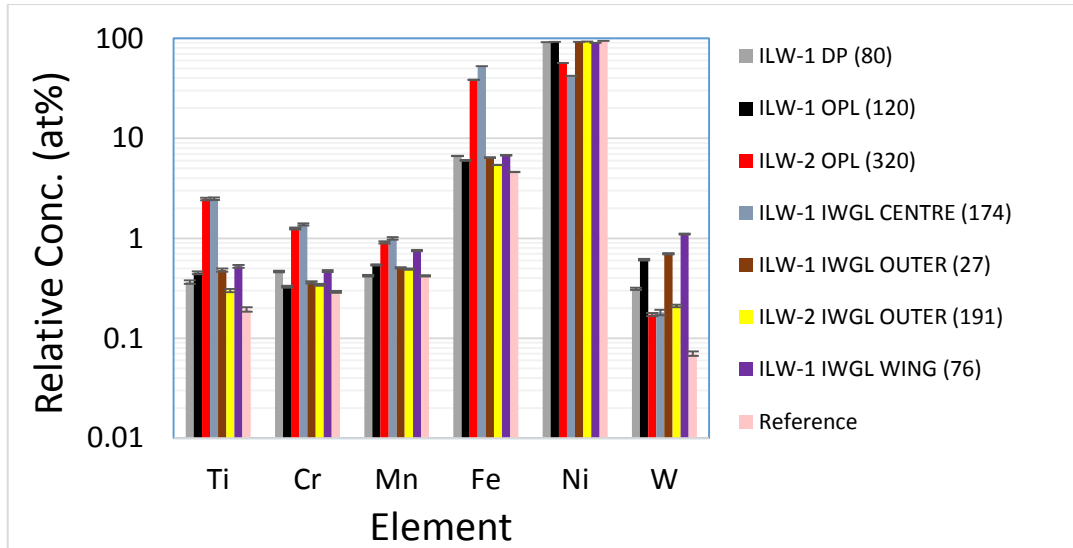
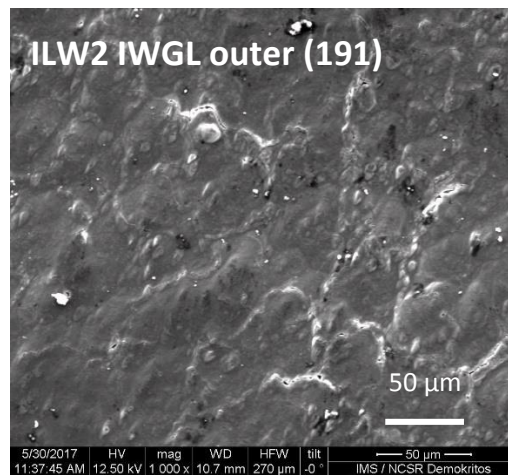
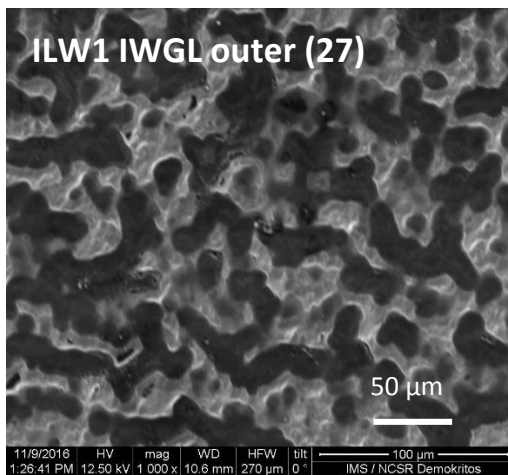
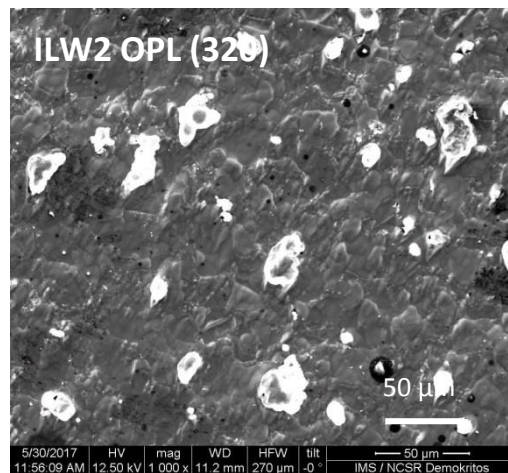
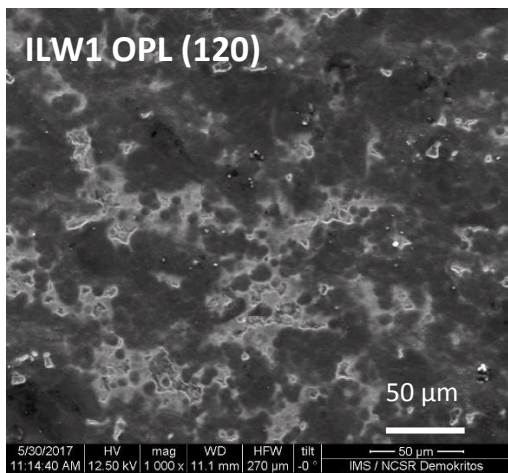
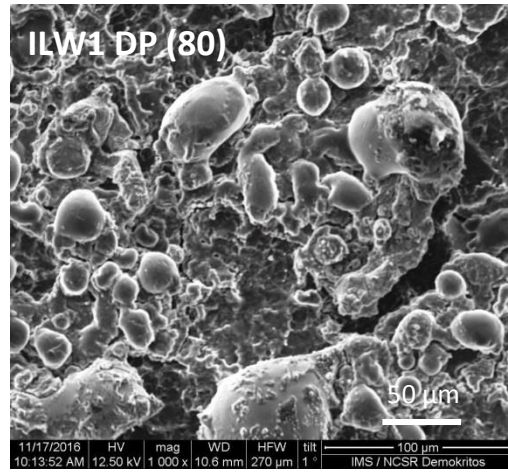
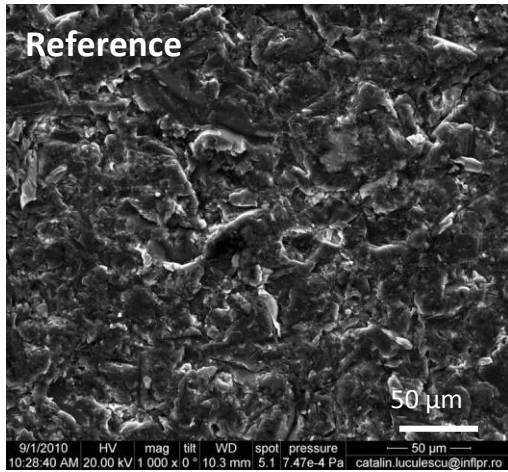


Figure 81: XRF results of the analysed samples. The concentration refers to elements with $Z > 11$.

The elements: Cr, Mn, Fe, Ni, Ti and W were detected in all samples, including the reference one. The content of these elements, except Ni, in the reference sample is smaller than in the samples exposed to plasma. The higher content of Cr, Fe, Mn and Ti in the plasma exposed samples must be related to the deposition of the eroded Inconel parts present in the JET main chamber. Ni comes from the nickel interlayer and its decrease with respect to the reference sample must be due to the erosion of the Ni interlayer. Thus, it is concluded that only the picture of enhanced erosion of the Ni interlayer for the samples ILW1 OPL (320) and ILW1 IWGL centre (174) can support both the XRF and NRA data discussed above (see Figure 68). The strong erosion of the centre area of the 2XR10 tile is confirmed by the results of [39] where an erosion of more than $>50 \mu\text{m}$ is found in the mid-plane of ILW-1 IWGL. The increased content of W in the exposed samples might be due to its migration from the JET divertor and the tungsten coated CFC tiles which are present in the main tokamak chamber. W migration is increased (almost one order of magnitude with respect to the reference sample) in ILW1 OPL (120), ILW1 IWGL outer (27) and ILW1 IWGL wing (76). It is noted that the peaks of Cu and Zn are present in the XRF spectra because of the beam collimator made from brass and their content in the samples, if any, cannot be quantified. However, EDS analysis (section 5.1.6) does not show the presence of Cu and Zn.

5.1.6 Surface Morphology and Stoichiometry

In this section the SE and the BSE images of the PFs of the investigated samples from the SEM measurements are illustrated in order to understand the morphology and the different phases. Additionally, the EDS measurements were carried out on large areas, which have dimensions $1 \times 0.5 \text{ mm}^2$ for all samples except for ILW1 IWGL outer ($0.4 \times 0.2 \text{ mm}^2$) and white or dark areas which is characterized by color in the BSE images. Generally the white areas conclude heavier elements than the dark ones. The energy beam for the EDS measurements was 12.5 keV



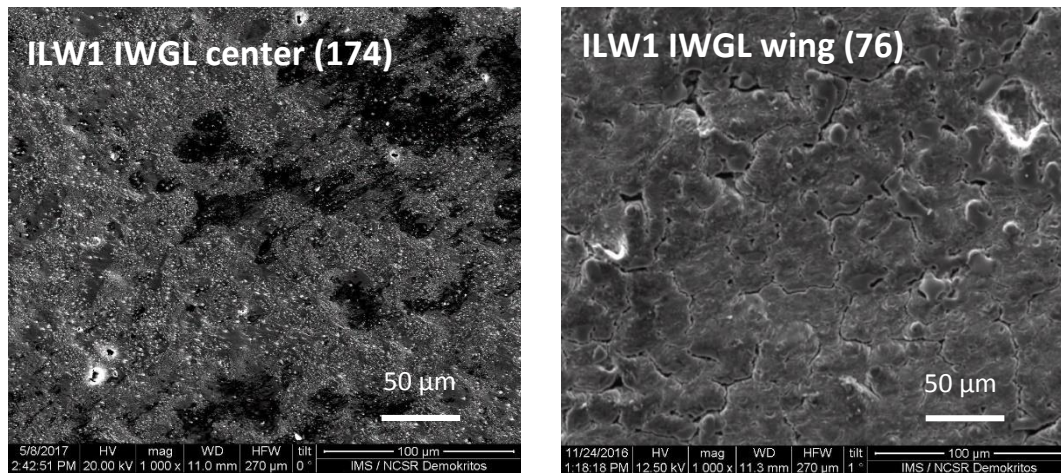


Figure 82: Comparison of the sample morphology after the plasma exposure with the reference.

Figure 82 presents the SEM images with secondary electrons with the same magnification of the reference and the samples after the plasma exposure. The surfaces of the samples have been altered and none of them looks like the reference. Additionally, the morphology of each plasma exposed sample is unique and no similarity between the sample surfaces is observed.

Figure 83 shows the EDS spectrum of the ILW1 IWGL outer (174), where C, O, Ni, Al, W, Ca and Fe are detected. Figure 84 - Figure 118 present the SEM images of the measured samples with different magnifications and the quantitative results of the EDS spectra for large and focused areas.

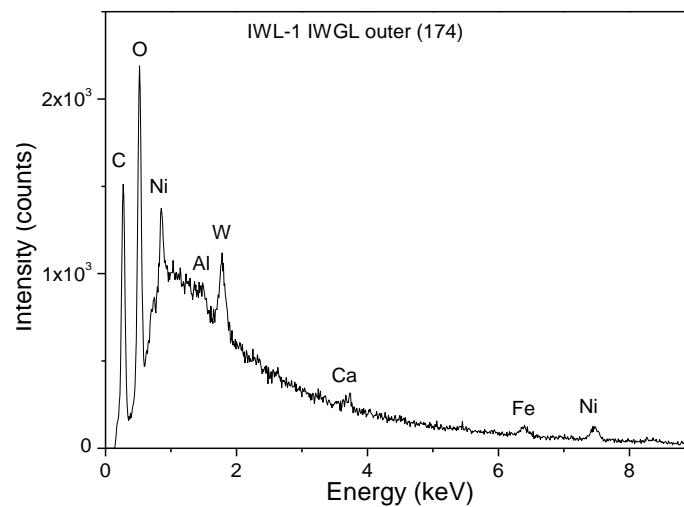


Figure 83: The EDS spectrum of the IWL1 IWGL outer (174)

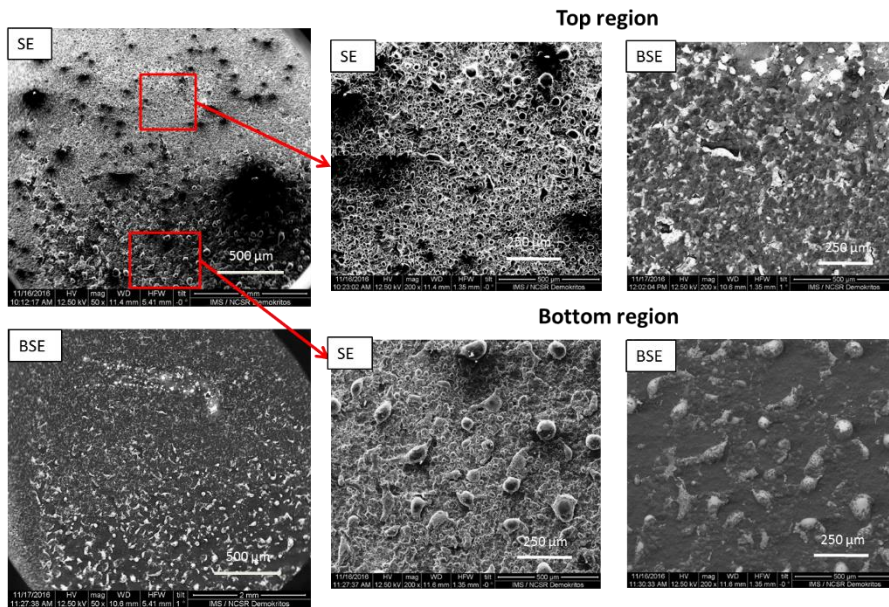


Figure 84: SEM images of the ILW1 DP (80) different areas using secondary and backscattered electrons.

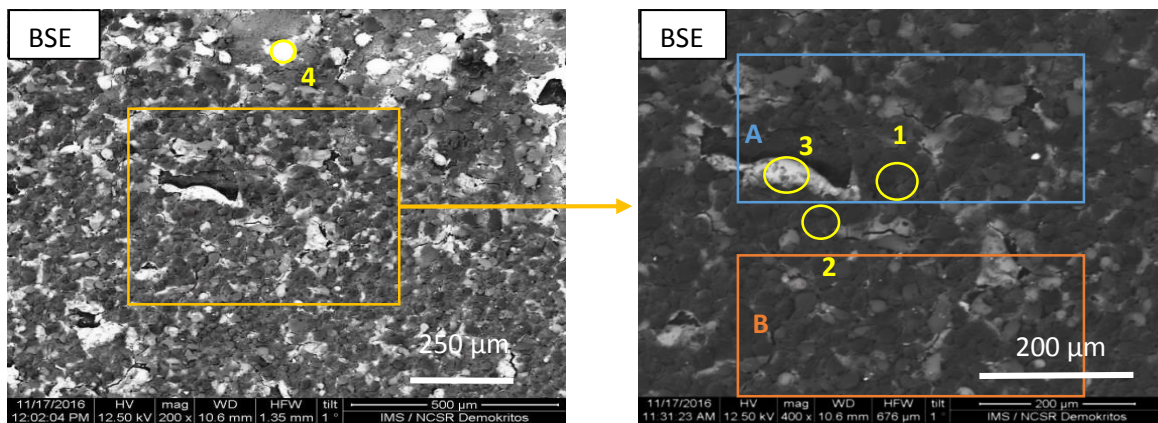


Figure 85: SEM image of the ILW1 DP (80) top region and the quantified areas.

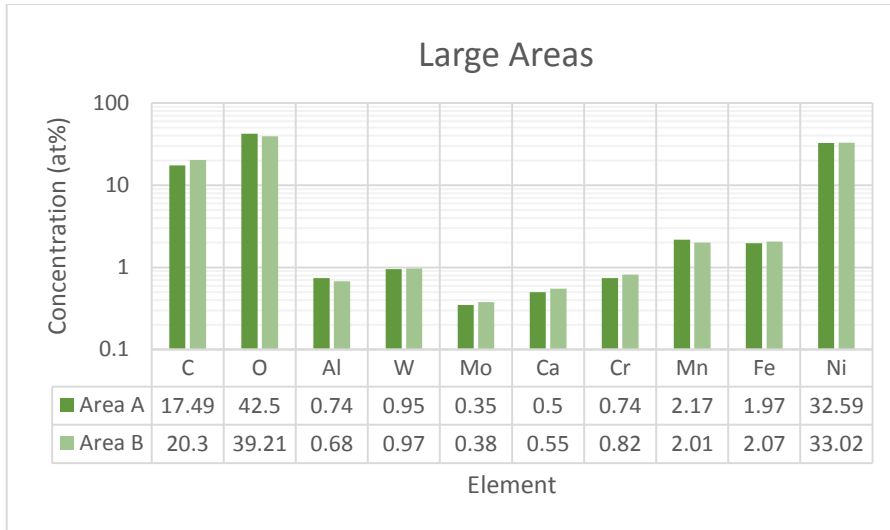


Figure 86: The quantification of the large areas of the ILW1 DP (80) top region shown in Figure 85.

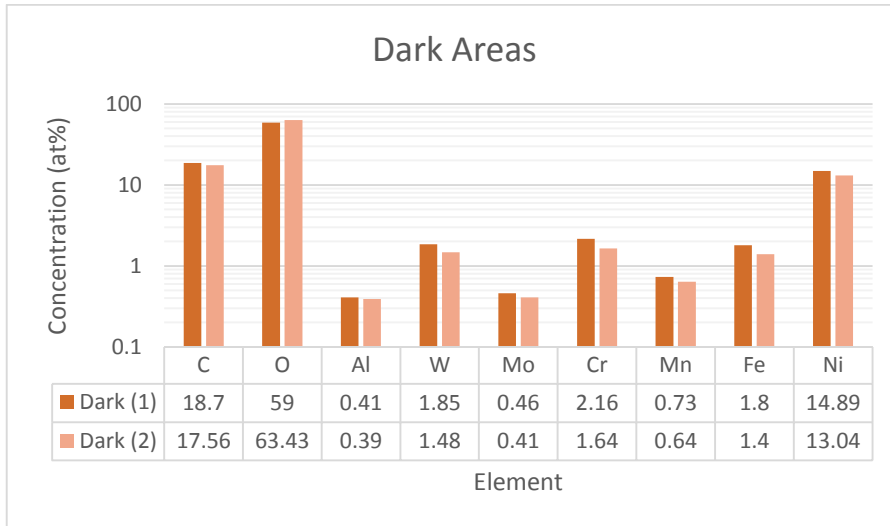


Figure 87: The quantification of the dark areas of the ILW1 DP (80) top region shown in Figure 85.

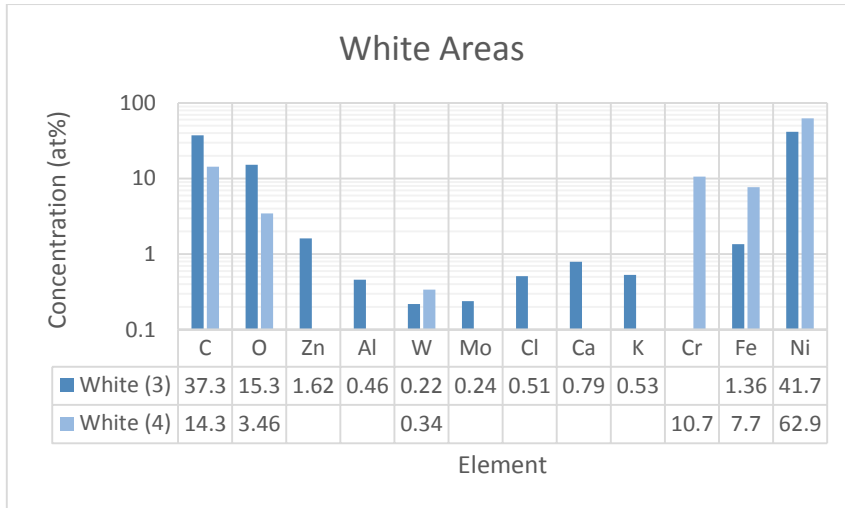


Figure 88: The quantification of the white areas of the ILW1 DP (80) top region shown in Figure 85.

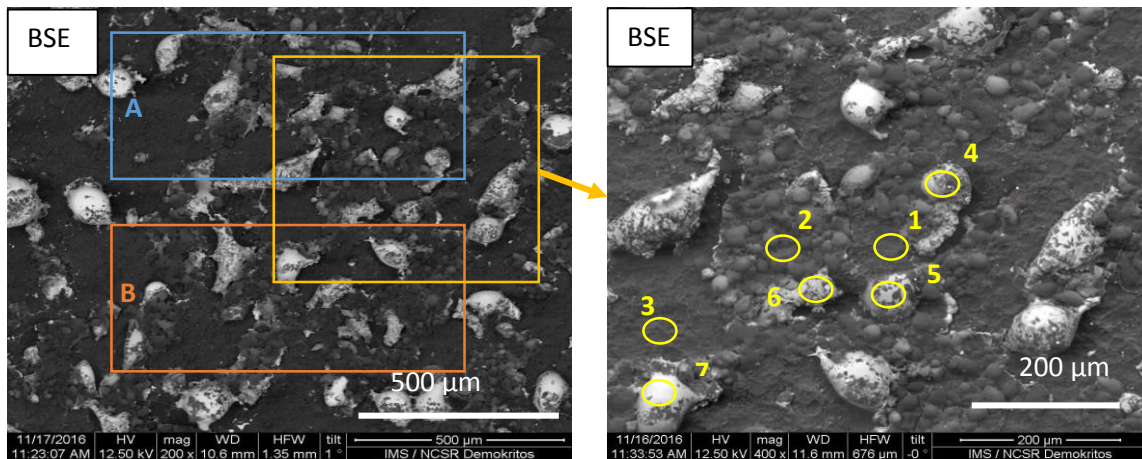


Figure 89: SEM image of the ILW1 DP (80) bottom region and the quantified areas.

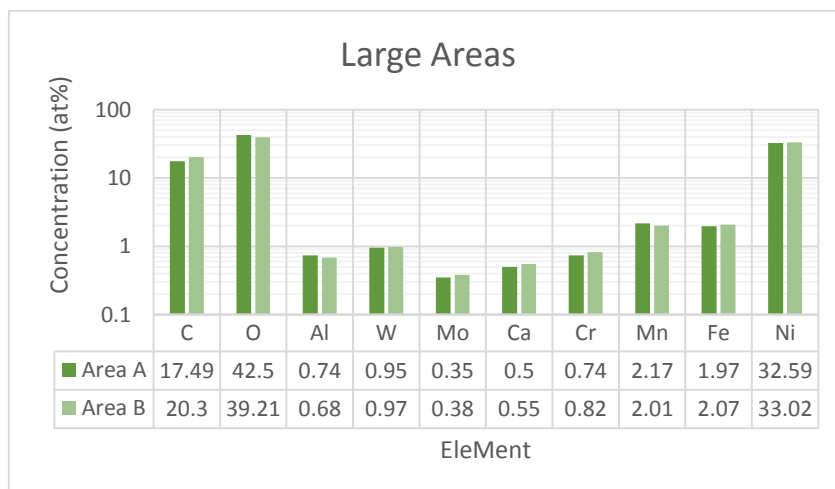


Figure 90: The quantification of the large areas of the ILW1 DP (80) bottom region shown in Figure 89.

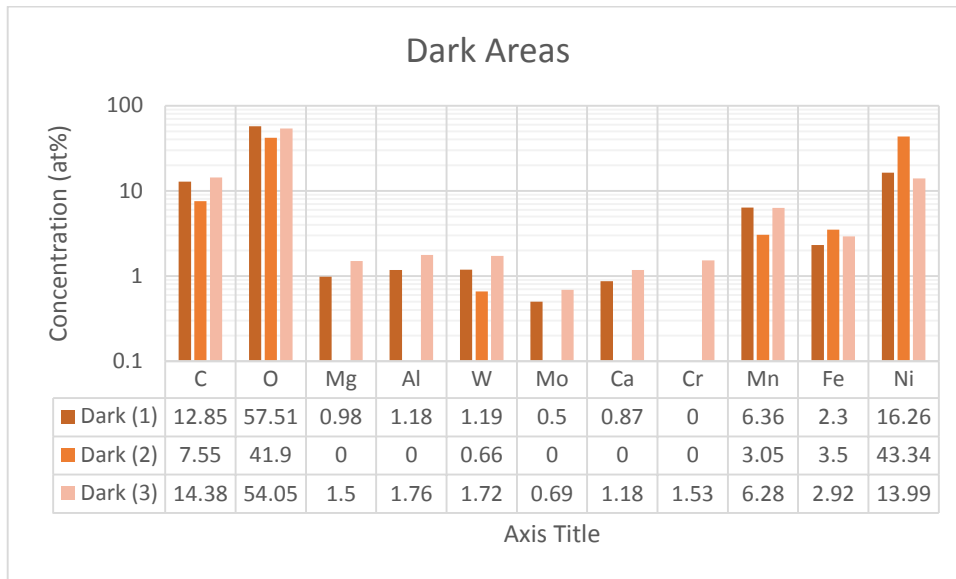


Figure 91: The quantification of the dark areas of the ILW1 DP (80) bottom region shown in Figure 89

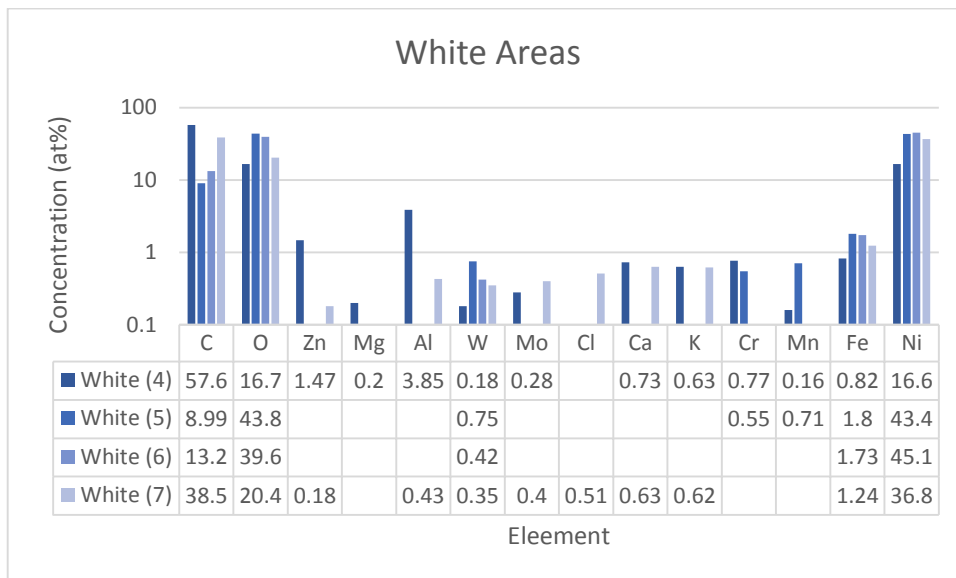


Figure 92: The quantification of the white areas of the ILW1 DP (80) bottom region shown in Figure 89.

Figure 84 depicts the surface of the ILW1 DP (80) where two different areas are observed. The upper region seems smoother than the bottom one. Comparing the quantitative results of the large areas, we observe that both regions have the same elements (C, O, Al, W, Mo, Cr, Mn, Fe and Ni) (Figure 86 and Figure 90) and their concentrations are quite similar for the elements with high concentration (Ni, O, C and W). The analysis of specific areas of the top region shows that the dark ones have similar elemental concentration to each other (Figure 87), but lower concentration of Ni and higher concentration of the rest elements than the large and the white ones. On the other hand, the white areas have very high Ni concentration and one of them has elements (Zn, Cl, K and

Ca) that are absent in the other one. For the chosen areas of the bottom region, the white ones (Figure 92) have more Ni and greater variety of elements than the large areas (Figure 91). Combining the morphology of the surface, the quantification of all the areas and the mili-beam NRA results, we observe that the nickel interlayer is not clear (Figure 68) and particles rich in nickel are detected on the surface so we conclude that IWL1 DP (80) has suffered intense deposition or erosion and re-deposition and the white particles are deposited particles consist mainly of nickel.

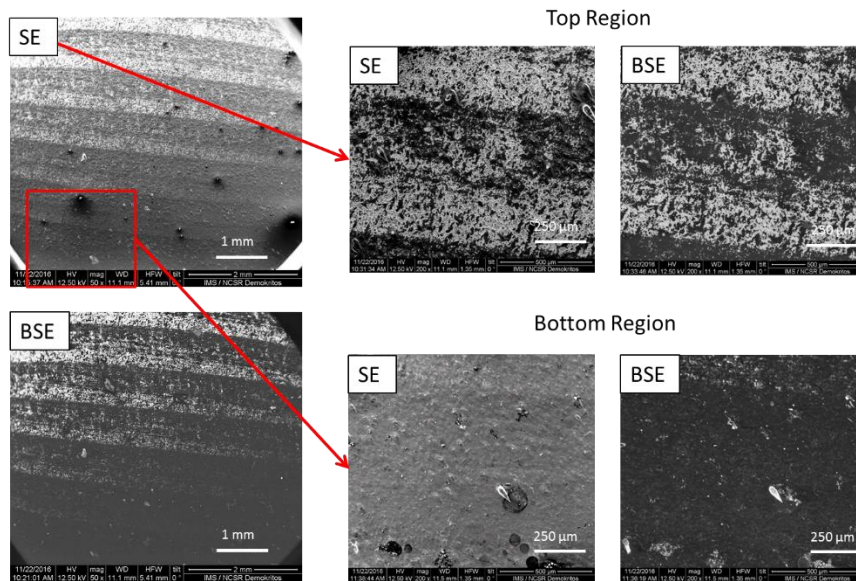


Figure 93: SEM images of the ILW1 OPL (120) different areas.

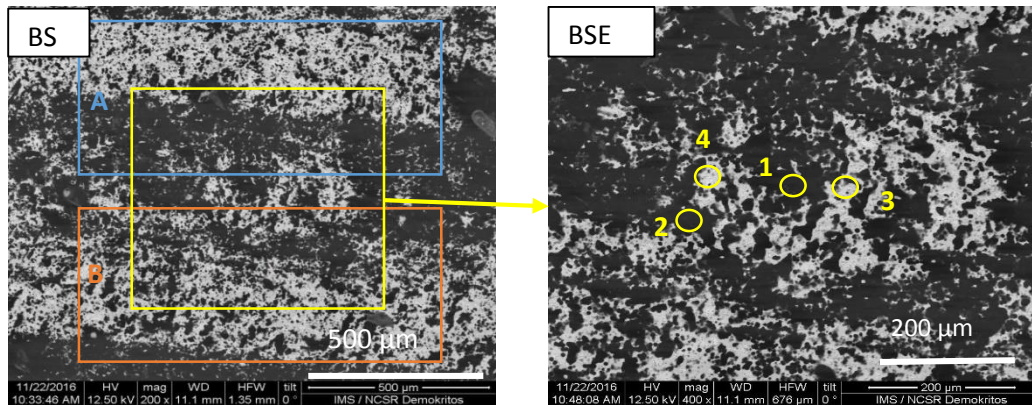


Figure 94: SEM images of the ILW1 OPL (120) top region and the quantified areas.

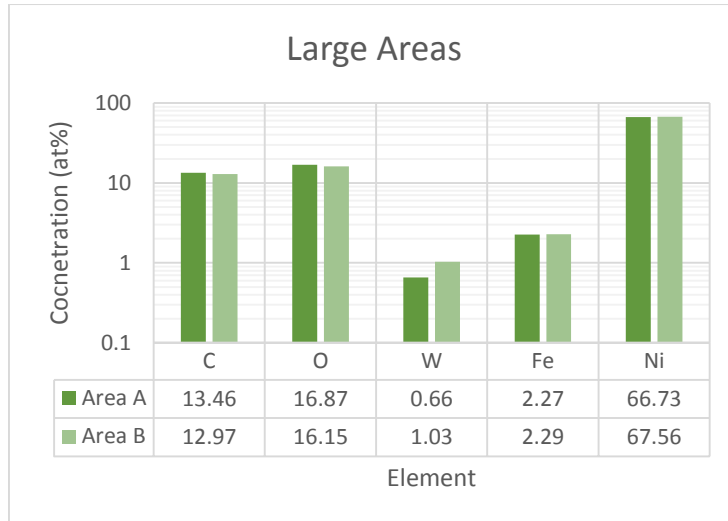


Figure 95: The quantification of the large areas of the ILW1 OPL (120) top region shown in Figure 94.

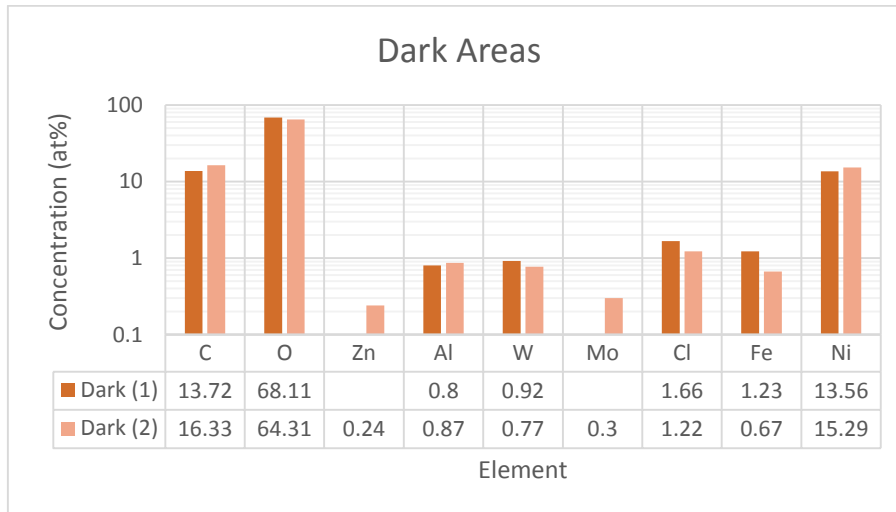


Figure 96: The quantification of the dark areas of the ILW1 OPL (120) top region shown in Figure 94.

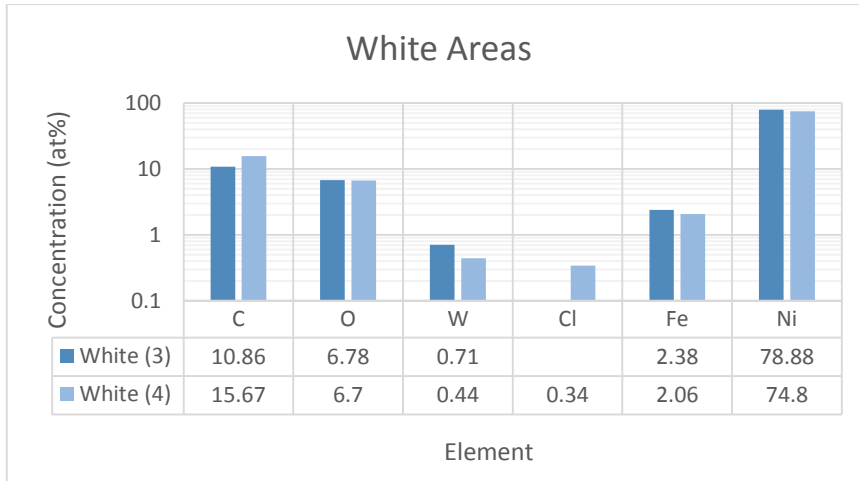


Figure 97: The quantification of the white areas of the ILW1 OPL (120) top region shown in Figure 94.

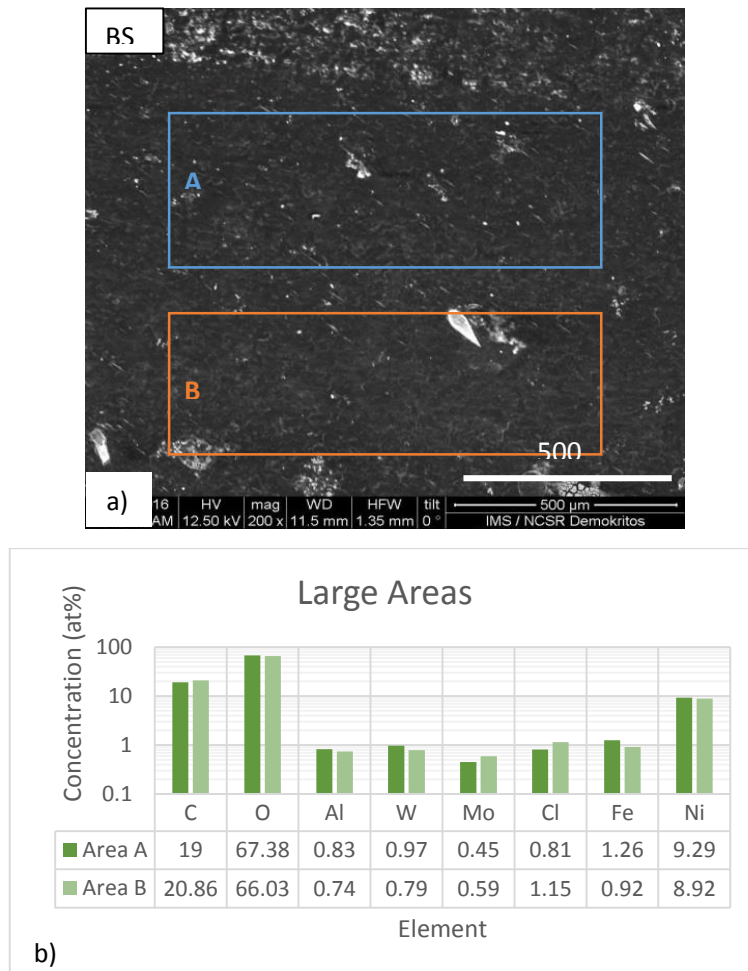


Figure 98: a) SEM image of the ILW1 OPL (120) bottom region and b) the large area quantification as determined in the SEM image.

Figure 93 depicts the SEM images of the ILW1 OPL (120) surface where strips with different composition are detected in the top region, while the bottom one seems homogeneous. The top

region has higher Ni concentration ((66.73 – 67.56) at%, the dominant element) and less elements (C, O, W, Fe, Ni)) (Figure 95) than the bottom one, where the Ni concentration is (8.92 – 9.26) at%, the detected elements are C, O, Al, W, Mo, Cl, Fe and Ni, while O is the dominant element (Figure 98b). The dark areas (Figure 96) of the top region have less Ni ((13.56 – 15.29) at%) and greater variety of elements (C, O, Zn, Al, W, Mo, Cl, Fe and Ni) than the white ones, where Ni is the dominant element with concentration of (74.8 – 78.88) at% and the detected elements are C, O, W, Cl, Fe and Ni (Figure 97). The ²H mili-beam spectrum shows that the top beryllium layer is thinner than that of the reference (Figure 68). Additionally, Ni was detected on the surface of the sample and its spatial distribution does not look like deposition but it looks like strips with a specific orientation, having revealed from the Ni interlayer due to the erosion. The conclusion is that the IWL1 OPL (120) has undergone erosion of its beryllium layer in the area towards the centre of the tile and the areas rich in Ni appear from the interlayer of the sample.

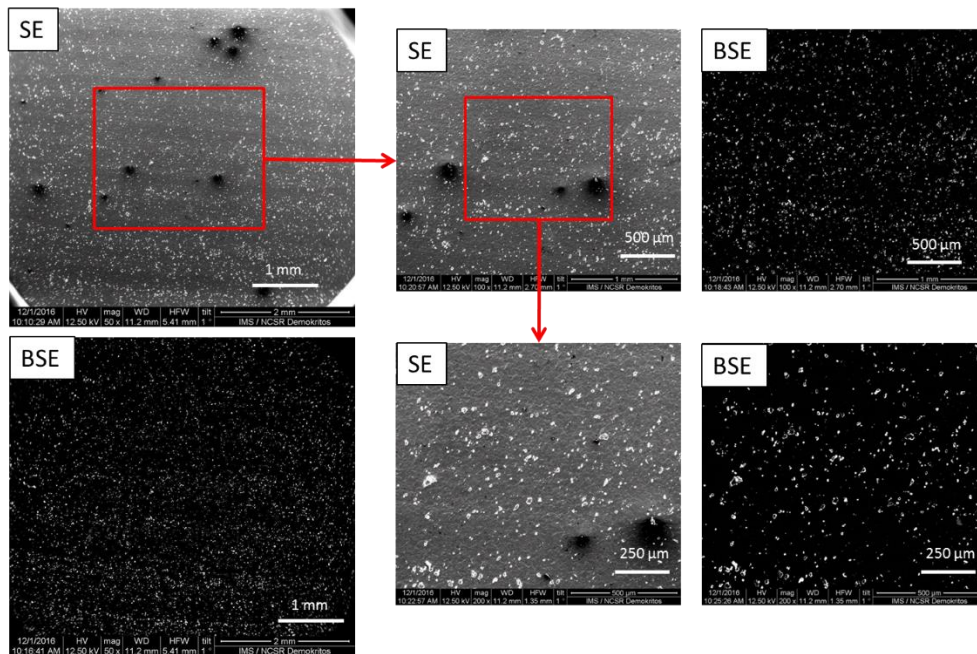


Figure 99: SEM images of ILW2 OPL (320) with different magnifications

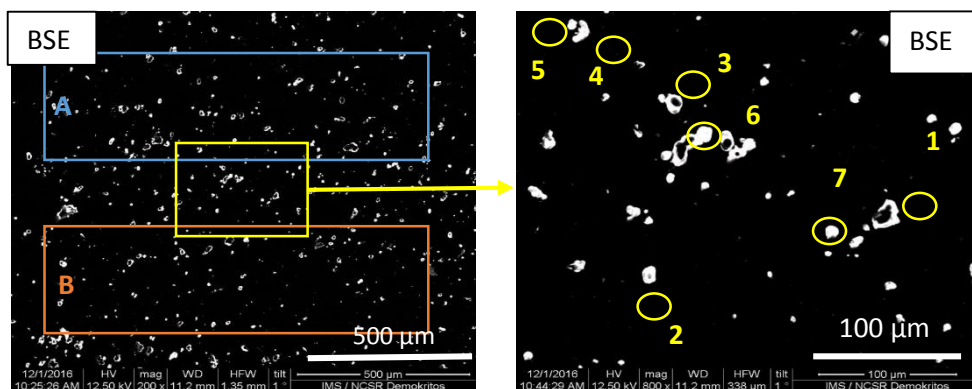


Figure 100: SEM images of the backscattered electrons and the quantified areas of the IWL2 OPL (320).

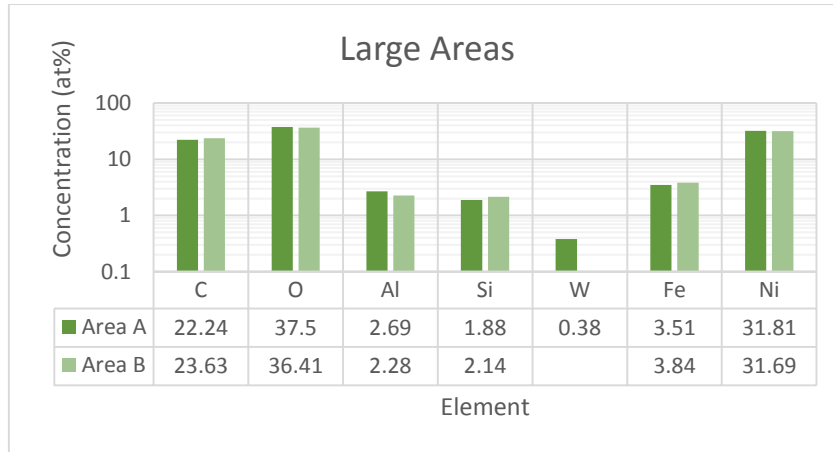


Figure 101: The quantification of the large areas of the ILW2 OPL (320) shown in Figure 100.

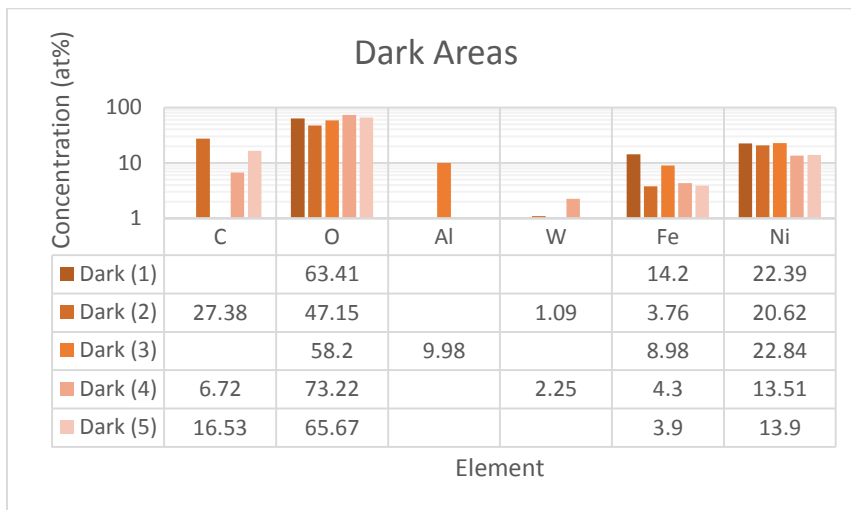


Figure 102: The quantification of the dark areas of the ILW2 OPL (320) shown in Figure 100.

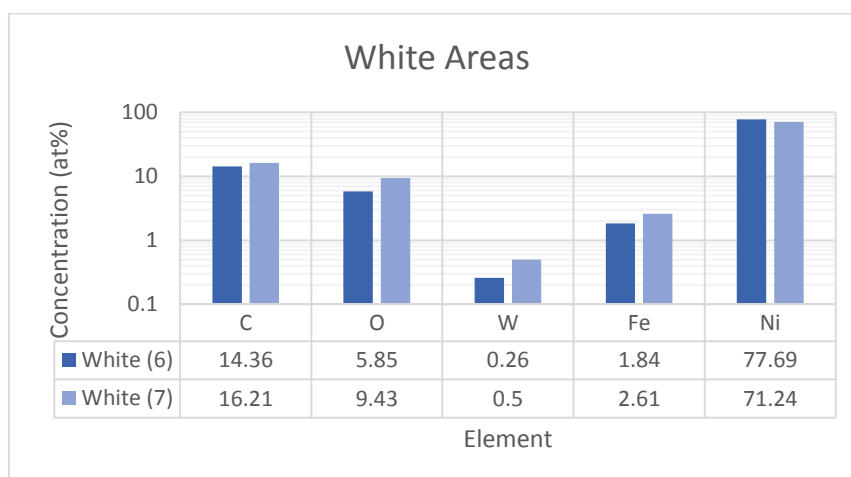


Figure 103: The quantification of the white areas of the ILW2 OPL (320) shown in Figure 100.

Figure 99 depicts the SEM image of the ILW2 OPL (320) surface with different magnifications where small white areas homogeneously distributed, with different concentration were detected. The quantification (Figure 100) shows that Ni, C and O are the dominant elements in the sample, where Al, Si, W and Fe were also detected. As Figure 102 presents, the dark areas are very rich in O ((47.15 – 73.22) at%) which implies high beryllium content, while the white ones have higher Ni ((71.24- 77.69) at%) concentration (Figure 103). The ^2H mili-beam spectrum (Figure 68) shows that the nickel interlayer is missing and the XRF analysis confirms that the Ni is lower than that of the reference sample. In addition, the surface has only small particles rich in Ni so the conclusion is that the ILW2 OPL (320) has undergone enhanced erosion of more than 11 μm , while the rich in Ni particles either where deposited or have been left from the Ni interlayer.

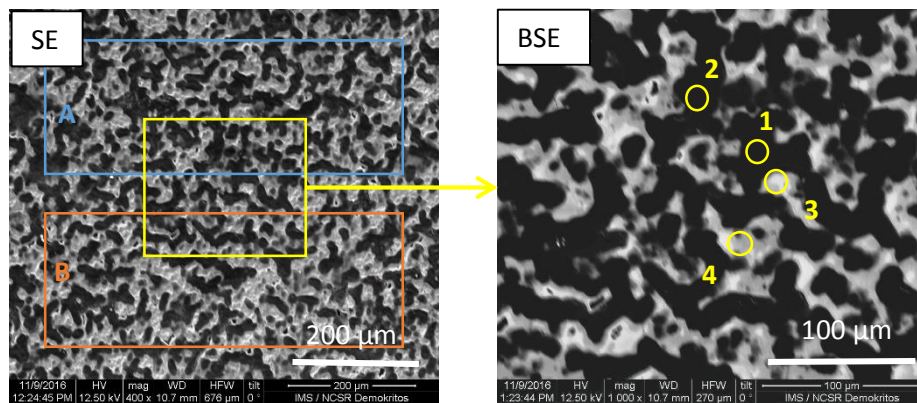


Figure 104: SEM images and the quantified areas of the IWL1 IWGL outer (27).

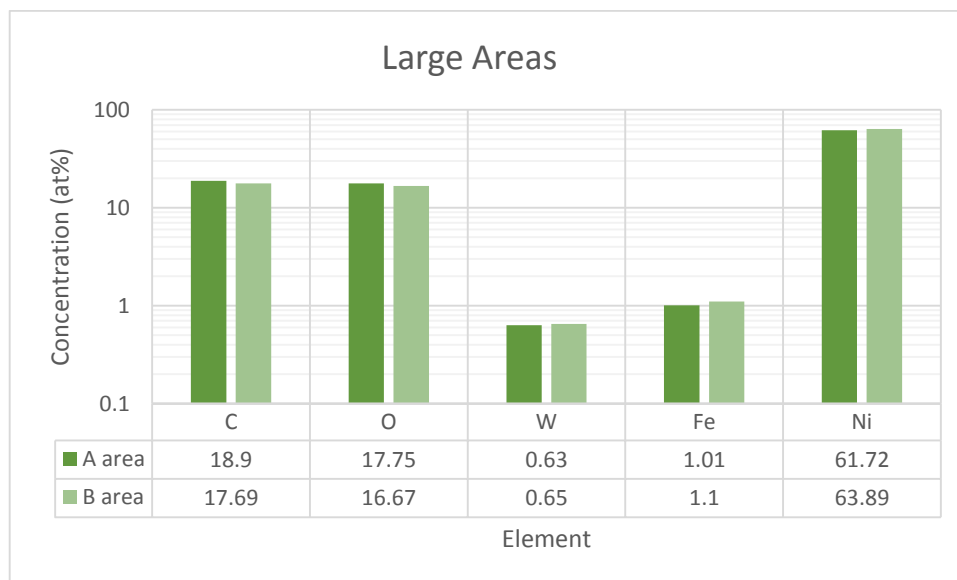


Figure 105: The quantification of the large areas of the ILW1 IWGL outer (27) shown in Figure 104.

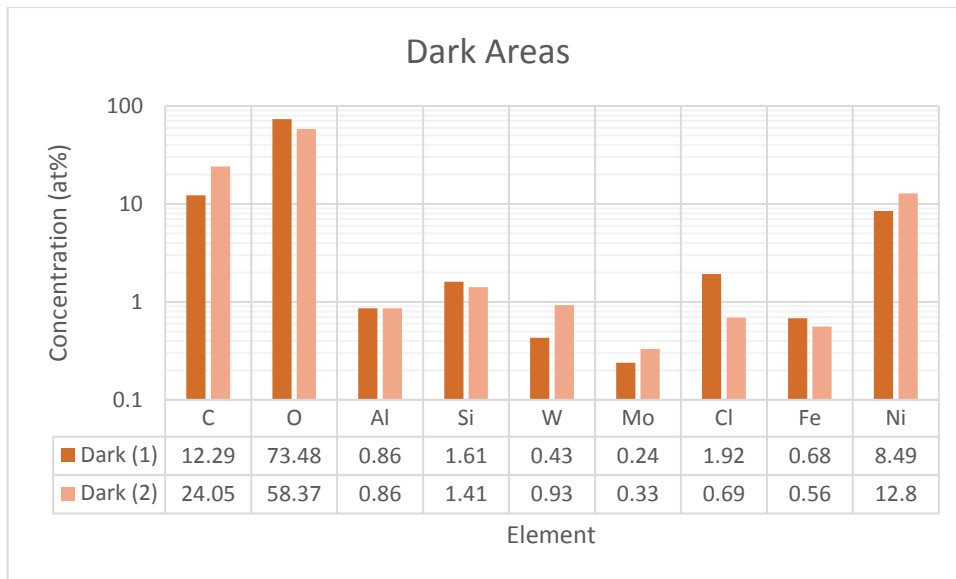


Figure 106: The quantification of the dark areas of the ILW1 IWGL outer (27) shown in Figure 104.

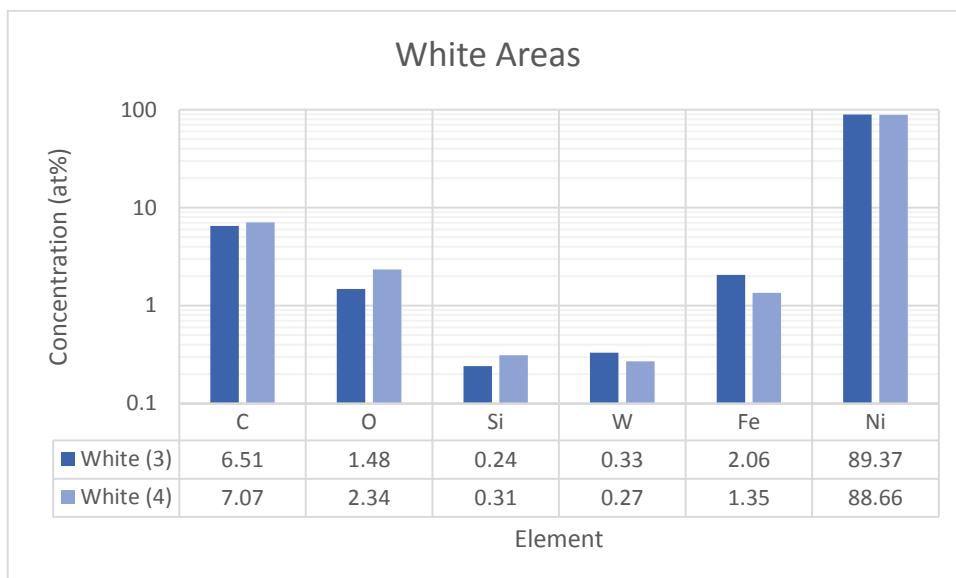


Figure 107: The quantification of the white areas of the ILW1 IWGL outer (27) shown in Figure 104.

The SEM images of the ILW1 IWGL outer (27) with different magnifications and the chosen areas are shown in Figure 104. Ni is the dominant element ((61.72 – 63.89) at%) on the surface of the sample (Figure 105), while C, O, W and Fe are also detected. For the chosen areas, the dark areas (Figure 106) are rich in O ((58.37 – 73.48) at%), while the white areas are rich in Ni ((88.66 – 89.37) at%). C, Si, W and Fe are detected on both areas, while Al, Mo and Cl were detected only on dark areas. The ^2H milli-beam spectrum shows that a part of top beryllium have been left and the Ni interlayer have been revealed. The SEM images confirm this conclusion as we observed the Ni interlayer on the surface of the sample. Thus, the conclusion is that Ni interlayer is revealed through the partial erosion of the top beryllium layer.

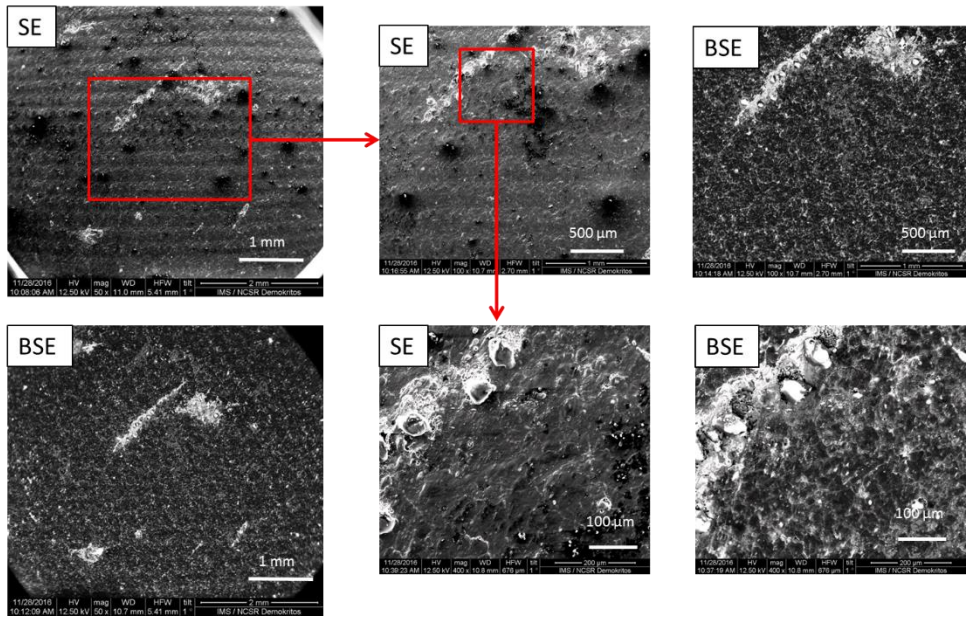


Figure 108: SEM images of ILW2 IWGL outer (191) with different magnifications.

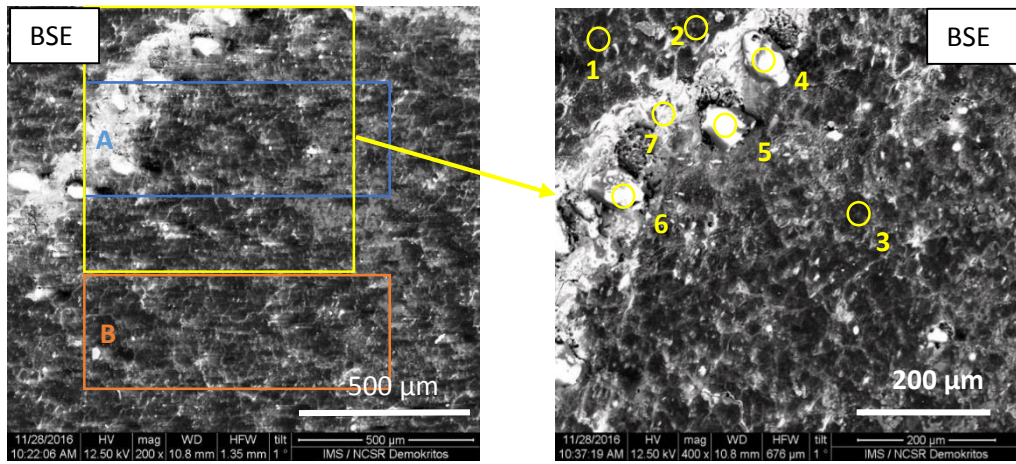


Figure 109: SEM images and the quantified areas of the IWL2 IWGL outer (191).

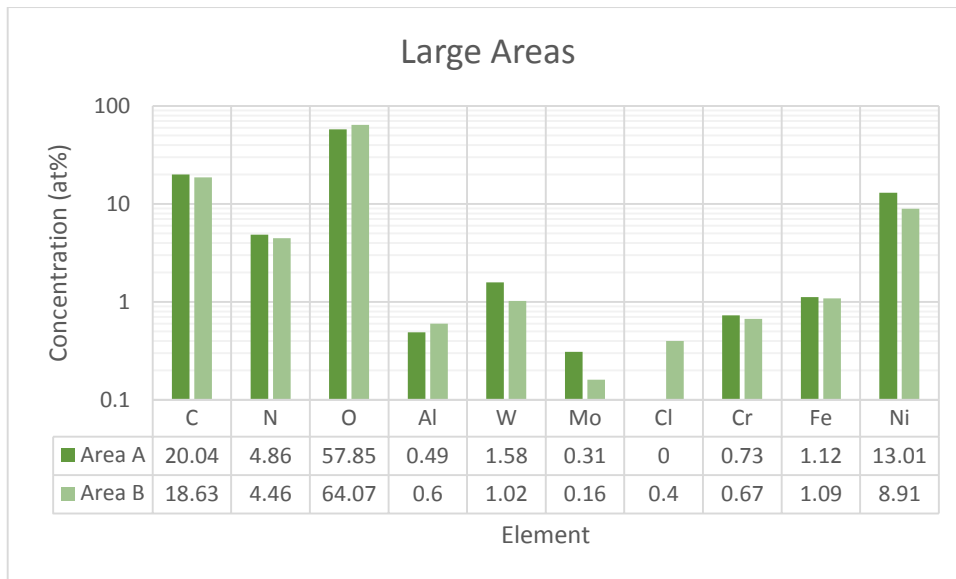


Figure 110: The quantification of the large areas of the ILW2 IWGL outer (191) shown in Figure 109.

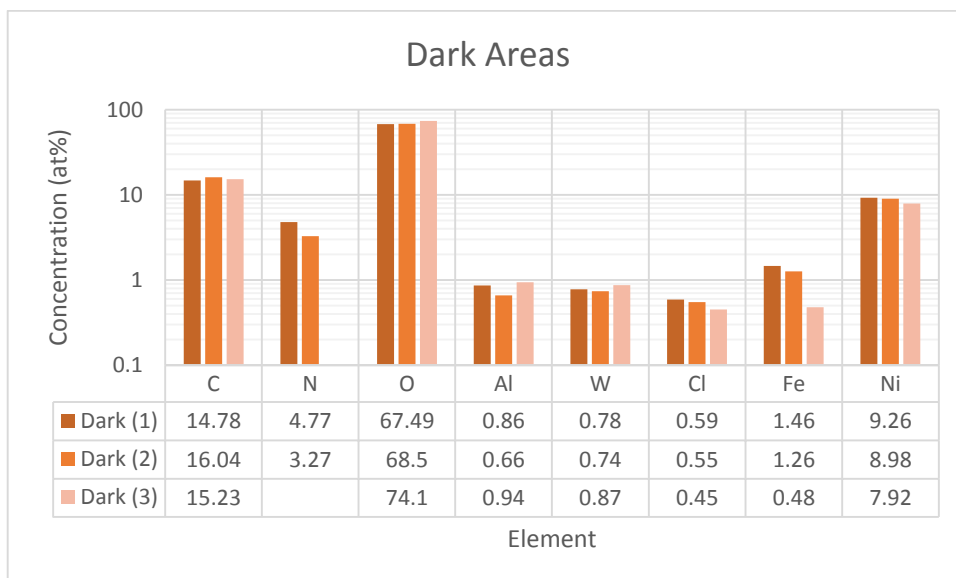


Figure 111: The quantification of the dark areas of the ILW2 IWGL outer (191) shown in Figure 109.

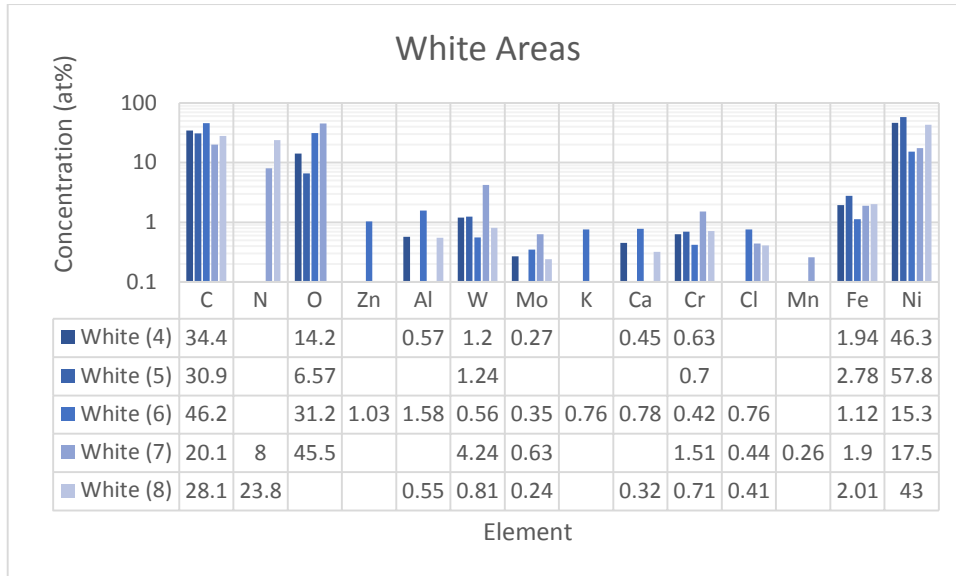


Figure 112: The quantification of the white areas of the ILW2 IWGL outer (191) shown in Figure 109.

Figure 108 presents the SEM images of the ILW2 IWGL outer (191) with different magnifications. The analysed areas were presented in Figure 109. A white strip and areas with different composition are observed on the upper region (Figure 109). The surface has high O ((57.85 – 64.07) at%) concentration while C, N, Al, W, Mo, Cl, Cr, Fe and Ni are also detected (Figure 110). The dark areas (Figure 111) are rich in O, while the white ones have high concentration of C, Ni or O (Figure 112). The common elements are C, O, Al, W, Cl, Fe and Ni; while Zn, Mo, K, Ca, Cr and Mn are observed only on some white areas. The NRA technique (Figure 68) shows that the Ni interlayer is still under the top Be layer and it is confirmed by the XRF results so the conclusion is that particles rich in Ni, which were detected by SEM technique (Figure 108 and Figure 109) have been deposited on the surface of the ILW2 IWGL outer (191) and they are not from the Ni interlayer of the sample.

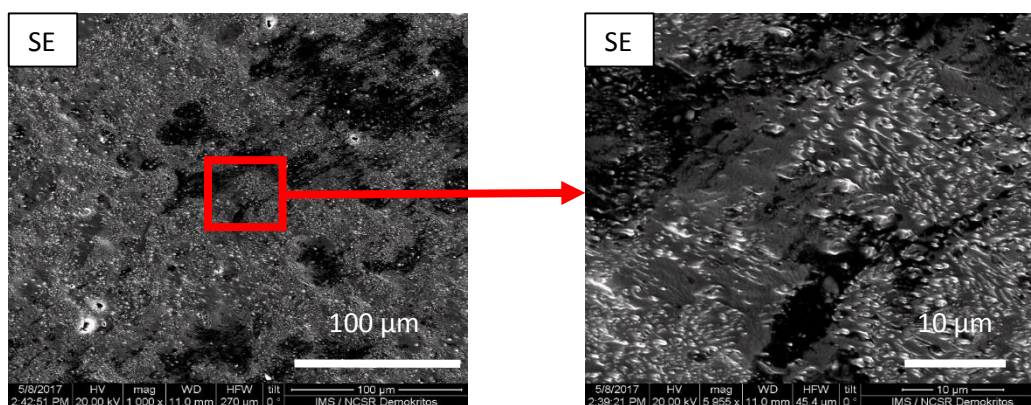


Figure 113: SEM images of ILW1 IWGL centre (174) with different magnifications.

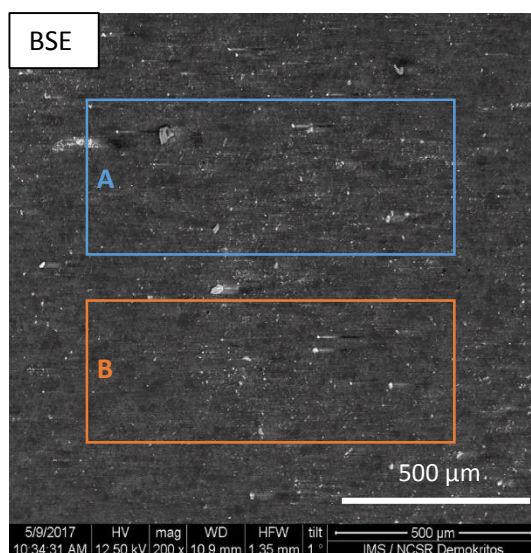


Figure 114: SEM image and the large areas of the ILW1 IWGL centre (174)

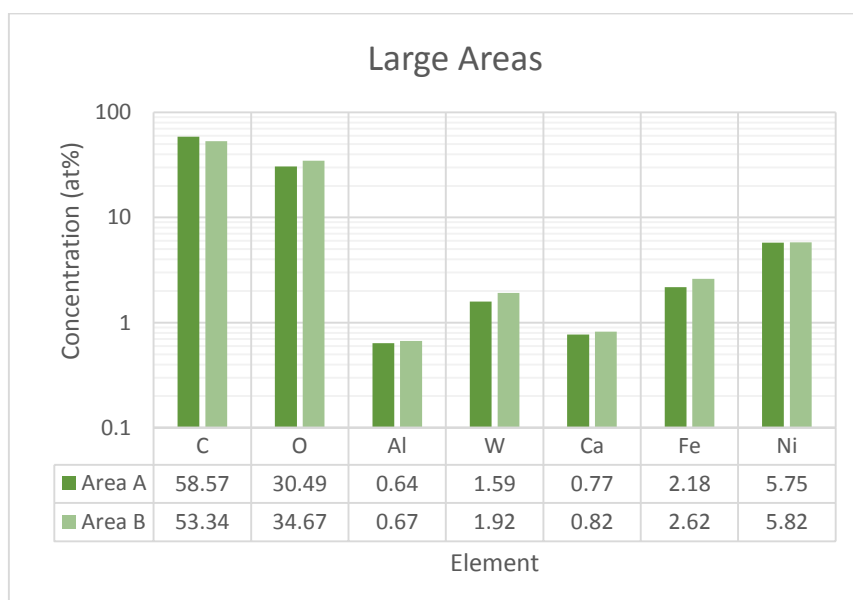


Figure 115: Quantification of the large areas of the ILW1 IWGL centre (174) shown in Figure 114.

From the secondary electron images of the ILW1 IWGL centre (174) (Figure 113) we conclude that the surface has suffered melting. Figure 114 depicts the quantified areas and Figure 115 the quantitative results of these areas. C and O were detected in high concentration ((53.34 – 58.57) at% and (30.49 – 34.67) at%, respectively), the rest elements are Al, W, Ca, Fe and Ni. According to NRA measurements the Ni interlayer is absent (Figure 68), which is confirmed with the XRF (Figure 81) and the surface has only some small areas of Ni. The conclusion is that the ILW1 IWGL centre (174) has been eroded for depths larger than 11 μm in agreement with the results of the [155].

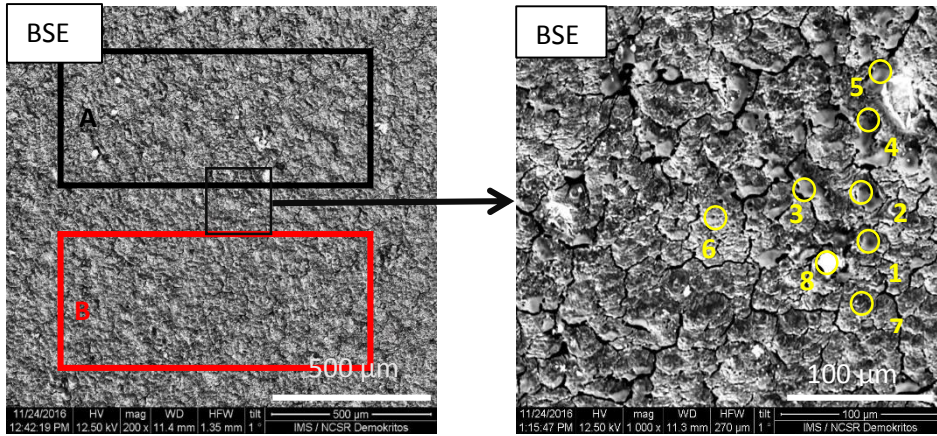


Figure 116: SEM images and the quantified areas of the IWL1 IWGL wing (76).

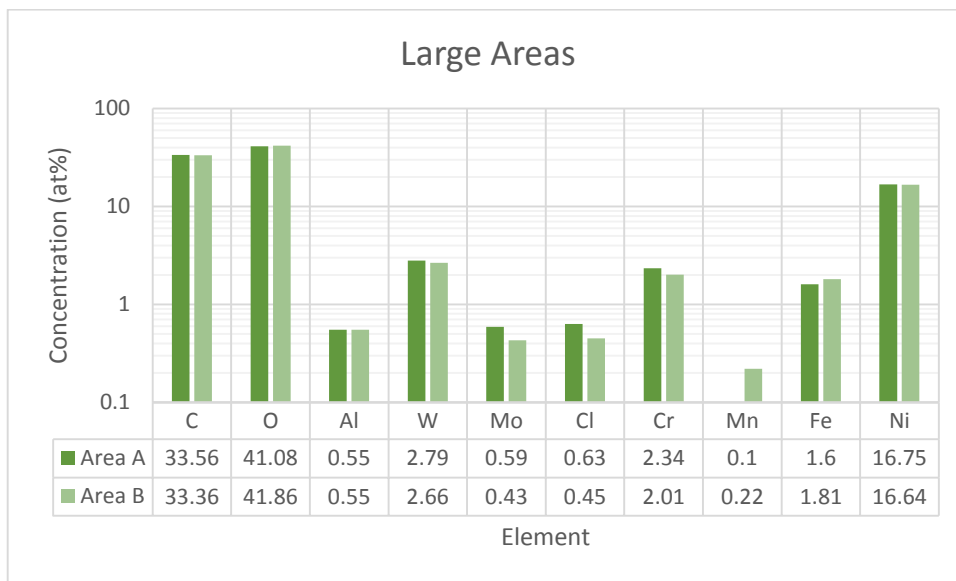


Figure 117: The quantification of the large areas of the ILW1 IWGL wing (76) shown in Figure 116.

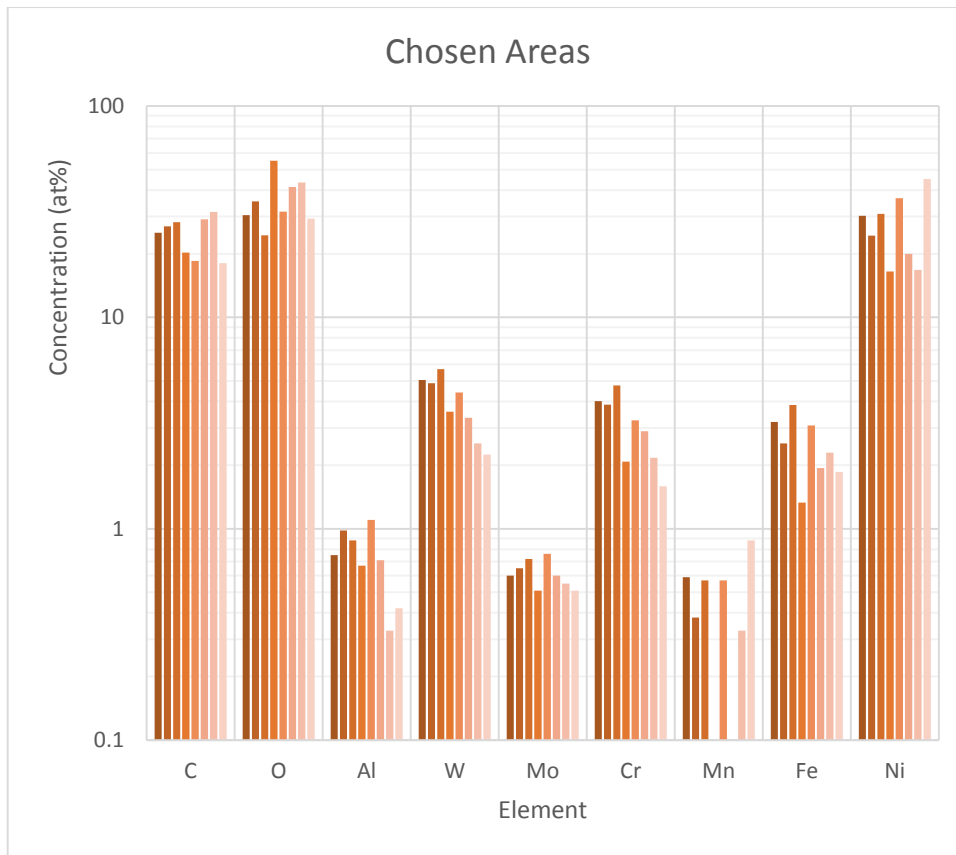


Figure 118: The quantification of the chosen areas of the ILW1 IWGL wing (76) shown in Figure 116.

Figure 116 depicts the SEM images of surface of the ILW1 IWGL wing (76) with different magnifications and Figure 117 the quantification of the large areas. The sample seems to have undergone melting. C and O are the dominant elements ((33.36 – 33.56) at% and (41.08 – 41.86) at%, respectively), and Ni is also present at high concentration ((16.64 – 16.75) at%). Al, W, Mo, Cl, Cr, Mn and Fe were also detected. Chosen areas has same elements and similar concentrations with the large areas. The Ni interlayer still exists and is under the Be top layer (Figure 68) no areas rich in Ni are observed (Figure 116) so there is no indication of erosion.

Figure 119 presents the average values of the large areas of all samples. C, O, Fe, Ni and W were detected in all samples. C, O and Ni are the elements with the highest concentration. The concentration of the Ni is correlated with the erosion and the Ni deposition. Specifically, on IWL1 IWGL centre (174) and ILW2 IWGL outer (191) low Ni concentration was detected, the former sample has suffered strong erosion, while for the latter one no erosion or Ni deposition was observed. On the other hand, ILW1 OPL (120) and ILW1 IWGL outer (27) have the highest Ni concentration as the Be top layer has suffered erosion and the Ni interlayer was detected. Additionally, the ILW2 OPL (320) has suffered enhanced erosion but the high Ni concentration was observed as same particles rich in Ni were detected, either they are remains form the interlayer or they were deposited after the erosion. As the concentrations of the elements are relative we cannot draw any other conclusion, for example the IWL IWGL centre (174) has high relative C concentration according to EDS measurements (Figure 119) but its amount is quiet small according to the NRA results (Table 9) comparing with the rest samples.

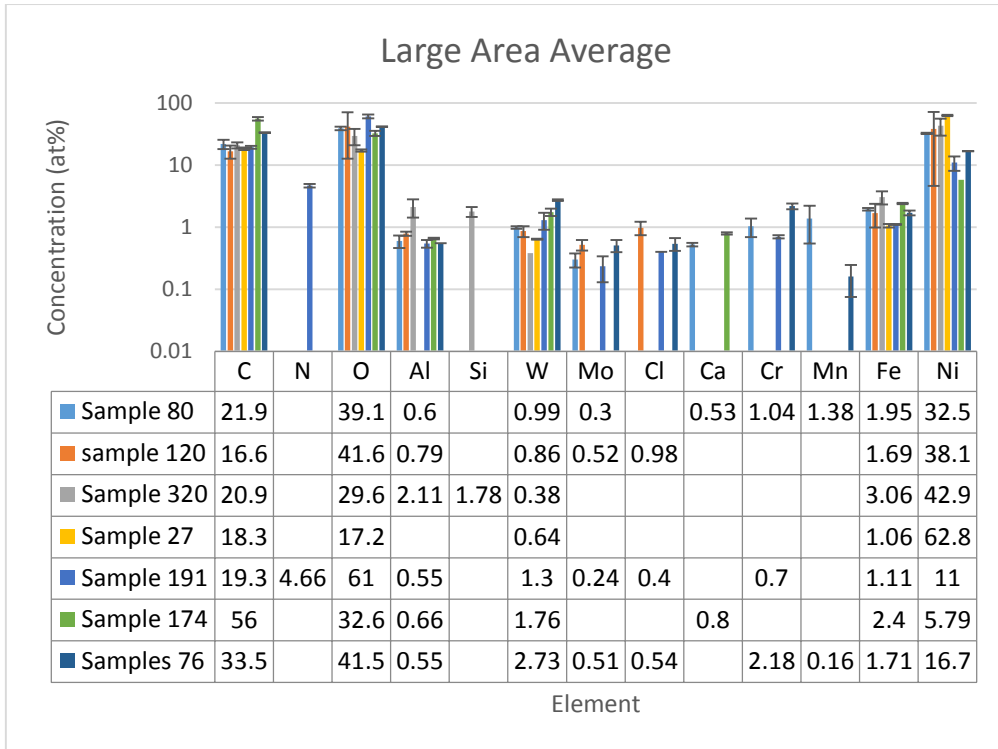


Figure 119: The average quantitative results of all samples.

5.1.7 X-ray Diffraction Results

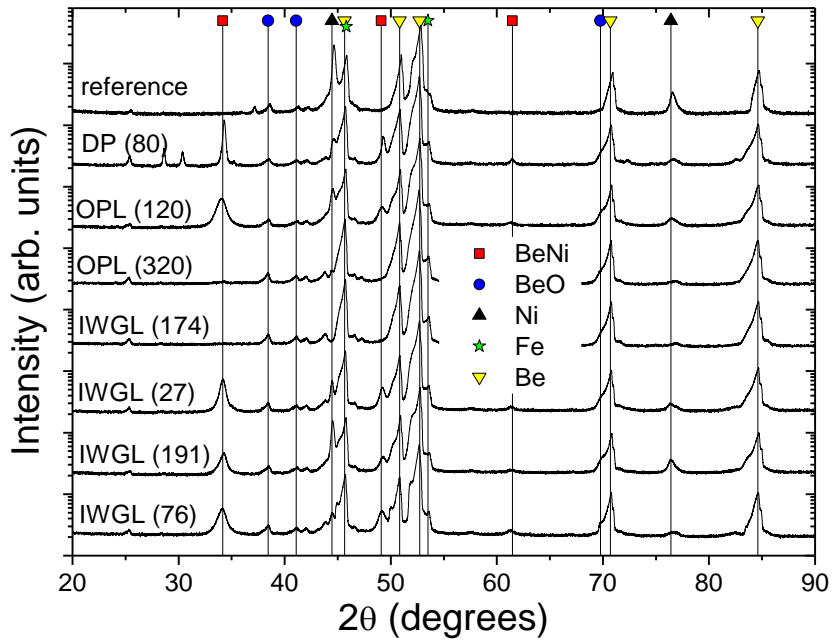


Figure 120: XRD spectra of the samples in logarithmic scale and the detected phases.

The XRD spectra (Figure 120) show the presence of BeO in all samples including the reference one. BeO is crystallized in the hexagonal system with Space Group 186. The oxidation of beryllium is a common phenomenon and the increase of the temperature enhances the oxidation [156].

Furthermore, the BeNi alloy and Ni were detected in all samples except for ILW-2 OPL (320) and ILW-1 IWGL centre (174). This finding agrees with the NRA and XRF results and shows that in these two samples the Be top layer and the Ni interlayer have been eroded. BeNi is crystallized in the cubic system with Space Group 221.

5.1.8 Summary and Conclusions

Different samples from the beryllium limiter tiles retrieved after the first and the second campaigns of the JET-ILW main chamber were investigated by a set of material analysis techniques. The C amount on the PFS ranges from $(0.35 \pm 0.07) \times 10^{17}$ at/cm² to $(11.8 \pm 0.6) \times 10^{17}$ at/cm²; while for the castellation sides near the PFS of the samples the C amount is between $(3.2 \pm 0.2) \times 10^{17}$ at/cm² and $(59 \pm 4) \times 10^{17}$ at/cm². For all samples except for ILW1 IWGL centre (174), the C amount behaviour with the depth in the grooves for different castellation sides of each sample is similar. The C maps from the castellation sides and an area up to 1.5 mm from the PFS show that, in general, the carbon amount on the investigated castellation sides either stays constant or reduces with depth from the edge of the PFS. No systematic difference is observed in carbon deposition on the front side facing, the ion drift and the other ones.

Concerning deuterium, the PFS of the majority of the samples has retained less amount than that detected on the castellation sides. From the first to the second campaign the deuterium amount of the PFS decreases, while on the castellation sides it increases. The deuterium distribution on the PFS is homogeneous while on the castellation sides it decreases with depth for the large majority of the samples. Additionally, the carbon amount is, in general, higher than the deuterium one. No systematic correlation between the carbon and the deuterium amount has been observed.

The spatial distribution investigation of the heavy element deposition on the castellation sides shows the formation of a zone rich in Al, Cl, Ca, Mo and W at depths up to about 200 μ m from the PFS. Ni is inhomogeneously distributed on the PFS and its distribution agrees with SEM images.

Combining all experimental techniques the following conclusion can be drawn. Regarding the samples from the same area and different ILW campaign, it is found that the right hand OPL area during the ILW2 campaign has undergone complete erosion of the Be top layer and the Ni interlayer, whereas during the ILW1 campaign the Be top layer and the Ni interlayer have been partially eroded. Furthermore the surface C content in the right hand OPL area is higher during the first ILW campaign than the second one. In the IWGL area no significant differences were found concerning the C content and the erosion of Be and Ni. Moreover, the areas with the lowest carbon content show the highest erosion. Cr, Mn, Fe, Ni, Ti and W are detected by XRF spectroscopy in both the plasma exposed samples and the reference one. The higher content of Cr, Fe, Mn and Ti in the plasma exposed samples compared to the reference one is attributed to the erosion of the Inconel parts present in the JET main chamber. A much higher Fe:Cr ratio is found than that expected from an Inconel alloy, whereas the Fe:Mn and Fe:Ti ratios are close to those expected. W may originate from either the divertor and/or the W coated inconel in the main tokamak chamber. XRD measurements demonstrate the formation of BeNi intermetallic compound.

5.2 JET Tokamak Main Chamber After ILW1-3 and ILW3

In the current subchapter, the results of investigation of the samples from the JET tokamak main chamber after the three or the third experimental campaigns are presented. Specifically, the samples 23 and 38 from the ILW1-3 IWC 412, the samples 390 and 418 ILW1-3 DP 2A8 and ILW3

DP 449 and 451 (Table 7) were analysed using the NRA, SEM with EDS, XRF and XRD techniques. The aim of the analysis is to determine the material deposition (C, O or heavier elements), to depict changes on the surface morphology (areas with melting, erosion or deposition), to quantify the elemental concentration of deeper layers and determine the compounds and the crystallography.

5.2.1 Carbon and Oxygen Quantification

The NRA measurements were carried out with ^2H milli-beam and the conditions that are described in Section 2.1.4.1. Figure 121 shows the representative experimental and simulated spectra of the ILW1-3 IWC 412 23 sample. The C and O amounts as determined using NRA measurements are presented in Table 10. The ILW1-3 IWC 412 23 sample has the highest C and O amount, with $(8 \pm 2) \times 10^{17}$ at/cm² and $(28 \pm 8) \times 10^{17}$ at/cm², respectively. On the other hand, the ILW1-3 3A8 418 sample has the lowest C content, of $(0.9 \pm 0.3) \times 10^{17}$ at/cm² while the O amount is under detection limit. Comparing the samples from the same tile, the sample from the region A of IWL1-3 IWC 412 has more carbon and oxygen ($(8 \pm 2) \times 10^{17}$ at/cm² and $(28 \pm 2) \times 10^{17}$ at/cm², respectively) than the region B ($(4.5 \pm 1.0) \times 10^{17}$ at/cm² and 15×10^{17} at/cm², respectively). This result agrees with the work [27] that the region A is richer in C and O than region B. Regarding the tile ILW1-3 3A8, sample 390 has four times more carbon ($(3.6 \pm 0.7) \times 10^{17}$ at/cm²) than sample 418 ($(0.9 \pm 0.3) \times 10^{17}$ at/cm²) whereas O is under detection limit on sample 418. The samples from the ILW3 2B2C have similar C amount of $(2.3 \pm 0.2) \times 10^{17}$ at/cm², while the O content of the sample 449 is 2.5 larger than that of the sample 451. The samples from the IWC-412 and the ILW3 2B2C 390 has similar O/C ratio (3.33 – 3.54) (Table 10), while the samples from the 2B2C have lower ratios (1.04 and 2.61). Comparing the C deposition of the ILW1 DP (80) with the ILW3 DP (449) which are from the same place but different periods, we observe that the C content have been reduced from the first ($(11.8 \pm 0.6) \times 10^{17}$ at/cm²) to the third campaign ($(2.3 \pm 0.2) \times 10^{17}$ at/cm²).

Figure 122 presents the C and O depth profiles of the analysed samples. The C concentration is reduced drastically after the first layer. The carbon concentration of the first layer ranges from 1.2 at% (ILW1-3 3A8 418) to 4 at% (ILW1-3 IWC412 23), while the maximum depth where carbon was detected is more than 5 μm in ILW1-3 IWC412 23. It is difficult to assess the O depth profile so we assume that there is a layer with constant O concentration, with the layer thickness varying between 0.5 μm and 1 μm .

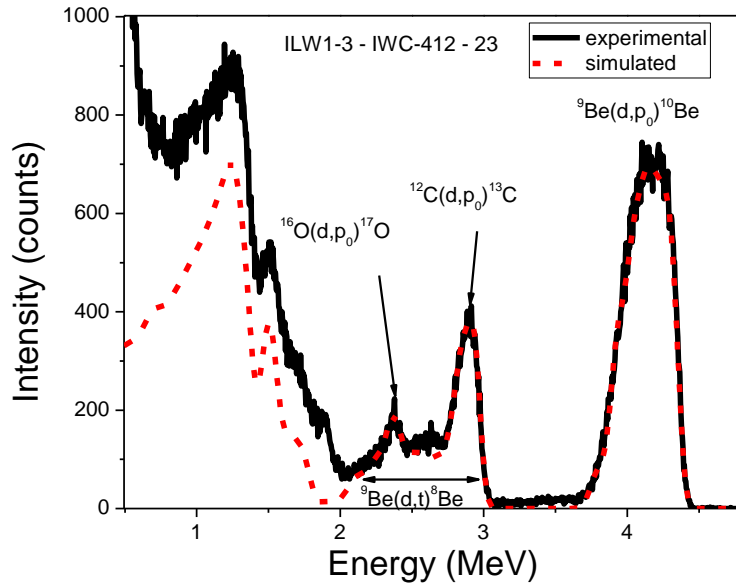
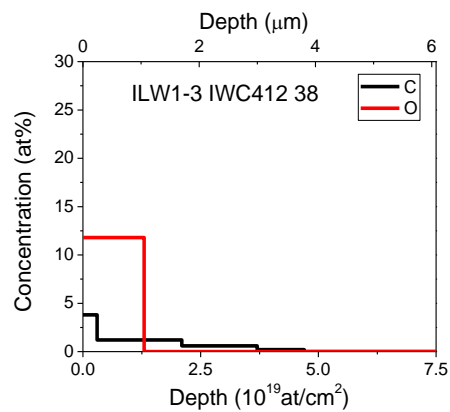
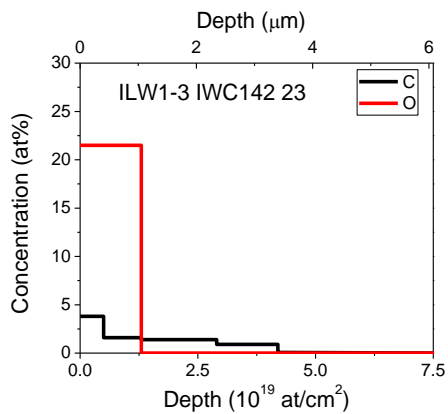


Figure 121: The experimental (black) and simulated (red) spectra of the ILW1-3 IWC412 23 sample.

Table 10: Main chamber sample description and the determined C and O content and ratio by NRA.

Exp. Campaign	Tile	Sample No	C content (10^{17} at/cm ²)	O content (10^{17} at/cm ²)	O/C
ILW1-3	IWC 412	23	7.9 ± 2	28 ± 2	3.54
ILW1-3	IWC 412	38	4.5 ± 1	15 ± 2	3.33
ILW1-3	3A8	390	3.6 ± 0.7	12 ± 1	3.33
ILW1-3	3A8	418	0.9 ± 0.3	-	-
ILW3	2B2C	449	2.3 ± 0.2	6 ± 1	2.61
ILW3	2B2C	451	2.3 ± 0.2	2.4 ± 0.6	1.04



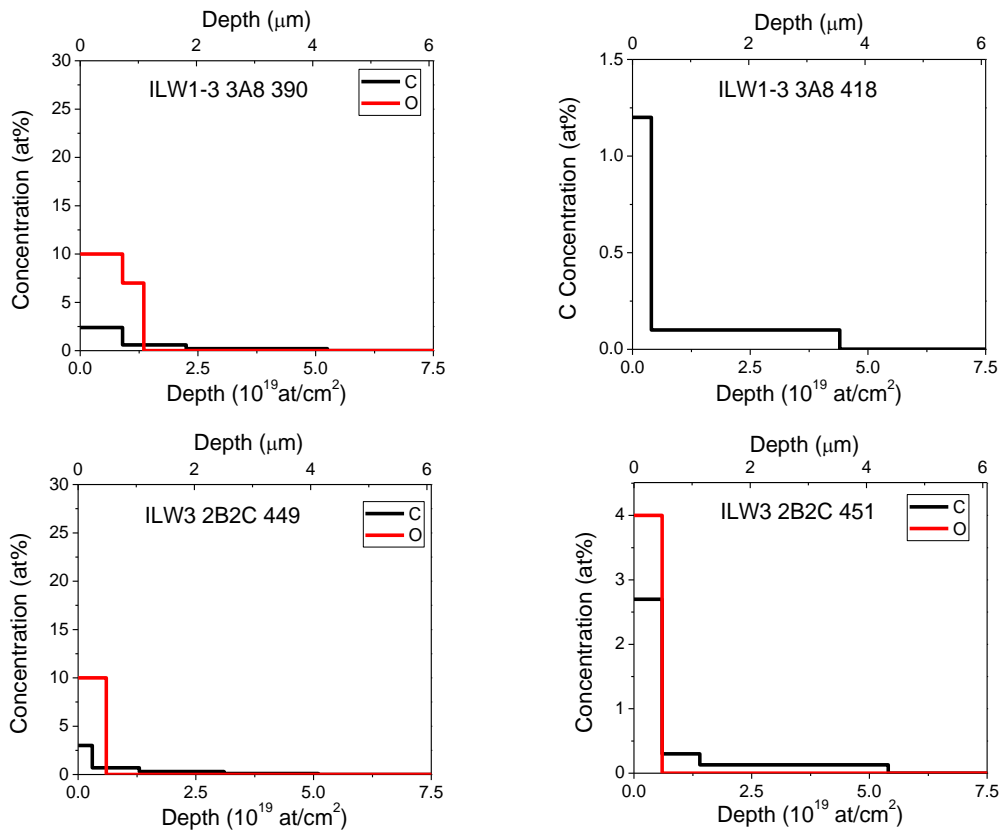


Figure 122: Carbon and oxygen depth profile of the analyzed samples.

5.2.2 X-ray fluorescence spectroscopy results

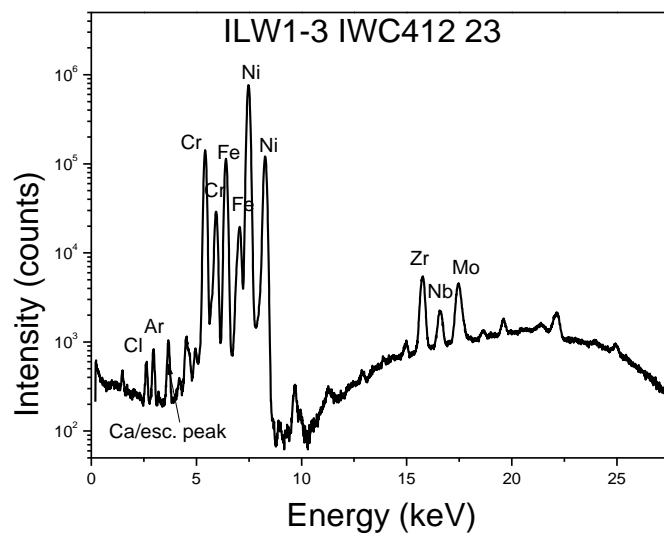


Figure 123: The XRF experimental spectrum and the peak identification of the ILW1-3 IWC 412

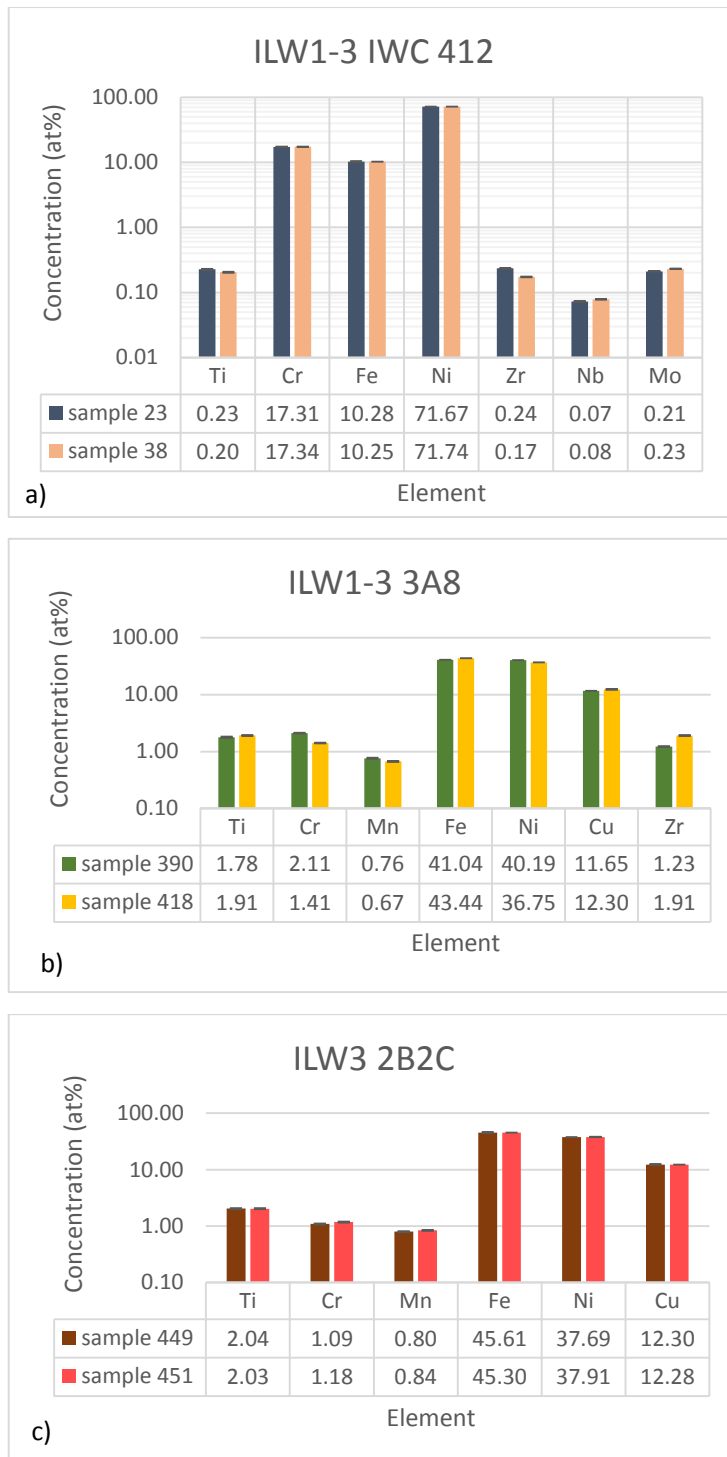


Figure 124: The XRF quantitative results of a) ILW1-3 IWC 412, b) ILW1-3 3A8 and c) ILW3 2B2C

Figure 123 presents the experimental spectrum and the peak identification of the ILW1-3 IWC 412 23 using the XRF measurement. Ti, Cr, Fe and Ni are detected in all samples. Figure 124 shows the quantitative results of analysis of the XRF spectra. Samples from the same area have also same elements with similar concentrations. Ni (73 wt%), Cr (16 wt%) and Fe (10 wt%) are the dominant element in the samples from the IWC412 and their concentrations are similar to the Inconel (Ni ≥ 72 wt%, Cr (14 – 17) wt%, Fe (6 – 10) wt%). This result indicates that the detected elements are

from the substrate of the samples, which means that the samples have not suffered material deposition. In the ILW1-3 3A8 samples apart from the common elements with the rest samples, Mn, Cu and Zr were detected. Mn and Cu are also observed in samples from the ILW3 2B2C.

5.2.3 Surface Morphology and Stoichiometry

The analysis of the SEM with EDS was carried out using electron beam with energy of 25 keV. The EDS were carried out on large areas with dimensions of about 2mm × 1mm. The chosen are characterized by the color in the BSE image.

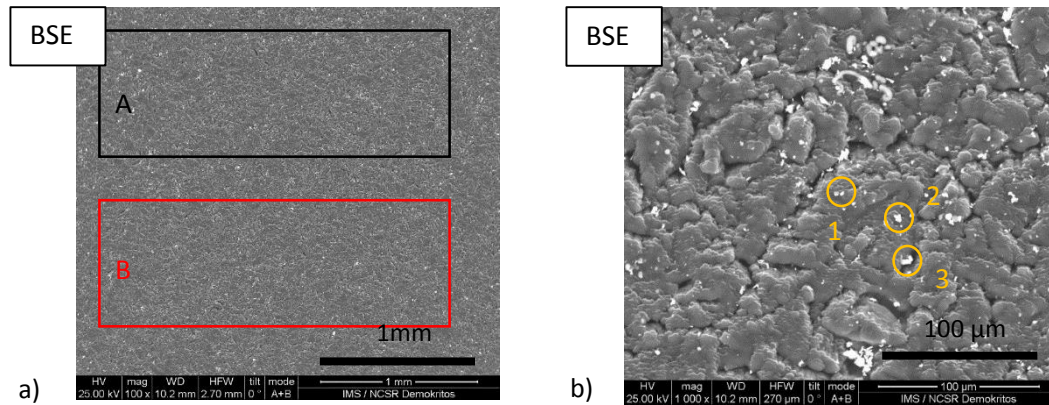


Figure 125: a) The BSE image with low magnification and the large areas and b) the BSE image with higher magnification and the selected white areas of the ILW1-3 IWC412 23

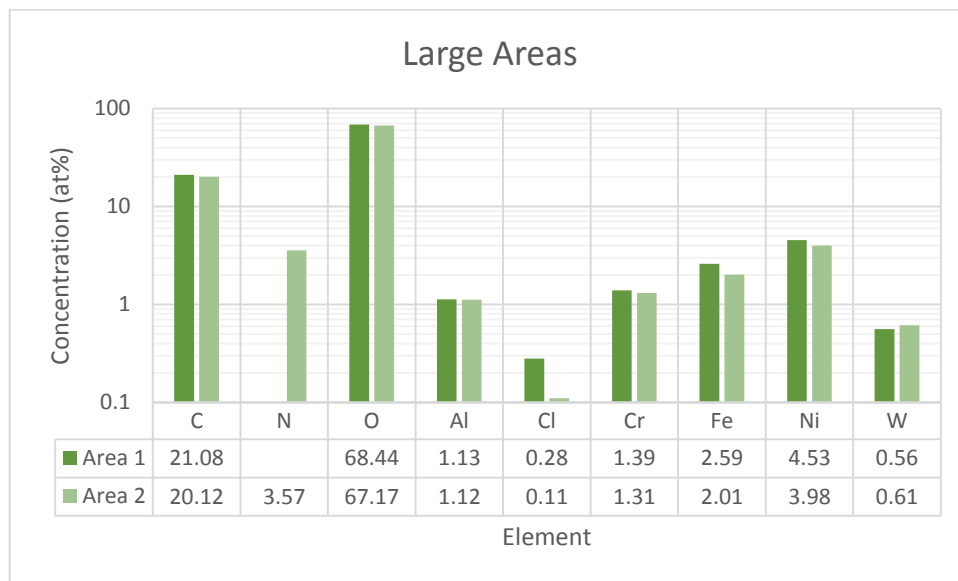


Figure 126: The quantification of the large areas of the ILW1-3 IWC412 23 shown in Figure 125.

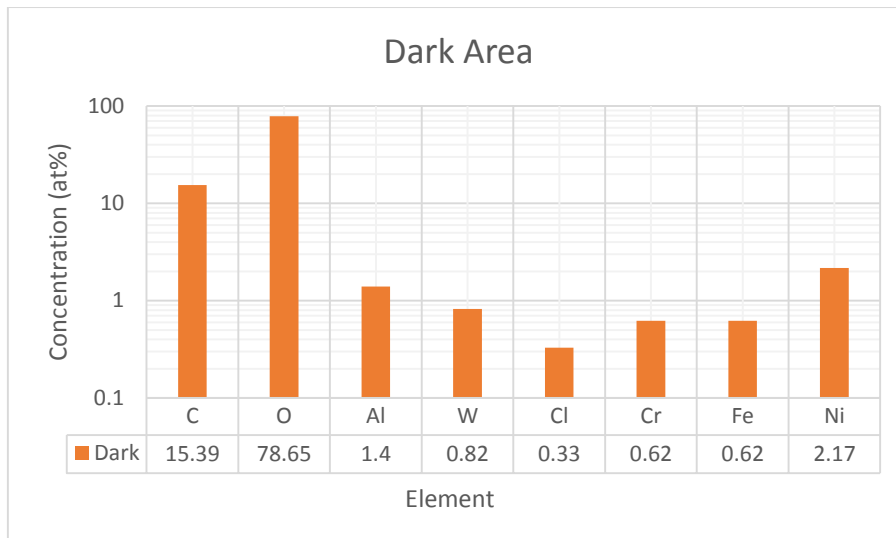


Figure 127: The quantification of the dark area of the ILW1-3 IWC412 23 shown in Figure 125.

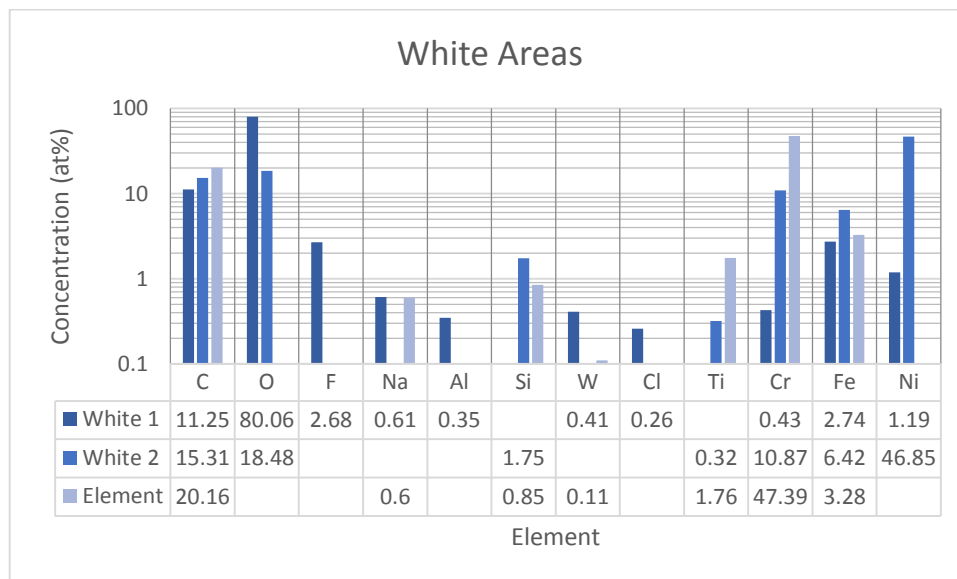


Figure 128: The quantification of the white areas of the ILW1-3 IWC412 23 shown in Figure 125.

Figure 125 present the BSE images of the ILW1-3 IWC412 23 with different magnifications and the quantified areas. The surface is quite rough and homogeneous which implies mild interaction with plasma. O is the dominant element on the large analysed areas ((67.17 – 68.44) at%), while high concentration of C ((20.12 – 21.08) at%) was also detected. The high O concentration confirms the results of the NRA measurements. The presence of N, Al, Cl, Cr, Fe, Ni and W is also observed (Figure 126). The dark areas (Figure 127) have similar composition as the large areas. On the white areas the detected elements are: C, O, F, Na, Al, Si, W, C, Ti, Cr, Fe and Ni. Each white areas have different dominant element (O, Ni and Fe) (Figure 128).

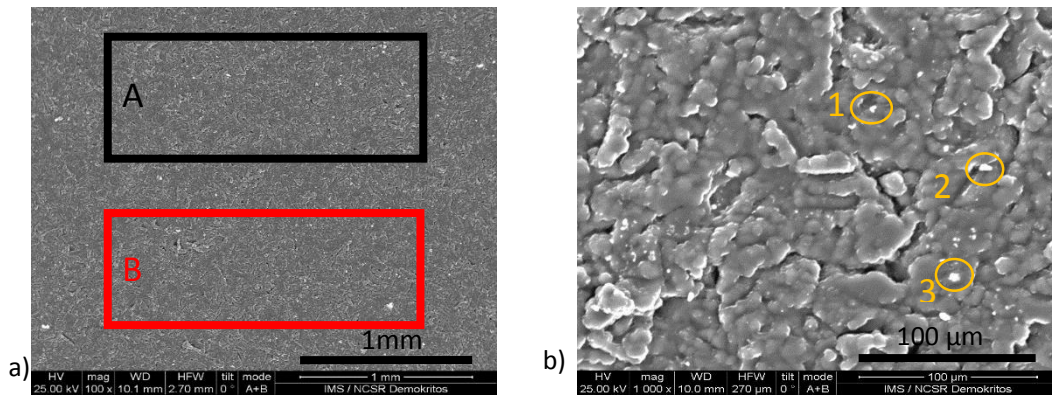


Figure 129: a) The BSE image with low magnification and the large areas and b) the BSE image with higher magnification and the selected white areas of the ILW1-3 IWC420 38.

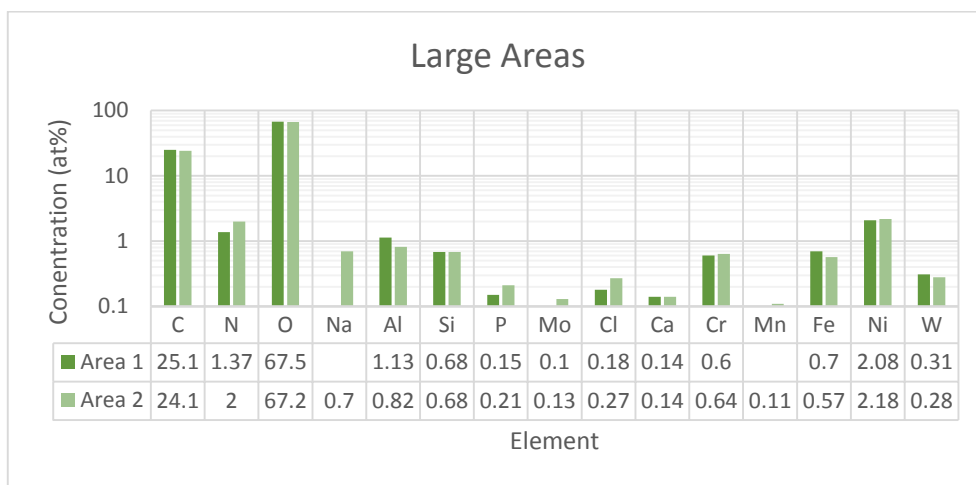


Figure 130: The quantification of the large areas of the ILW1-3 IWC412 38 shown in Figure 129.

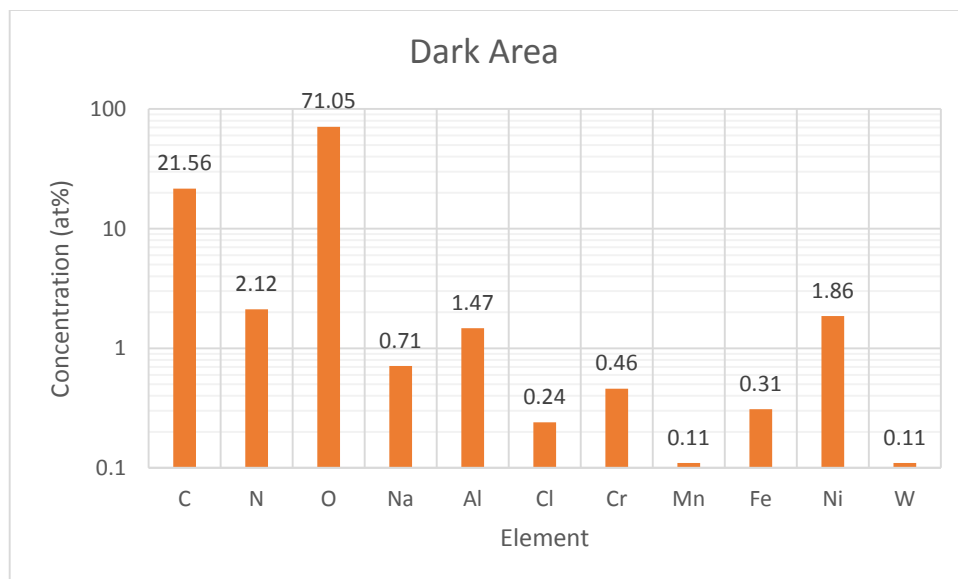


Figure 131: The quantification of the dark area of the ILW1-3 IWC412 38 shown in Figure 129.

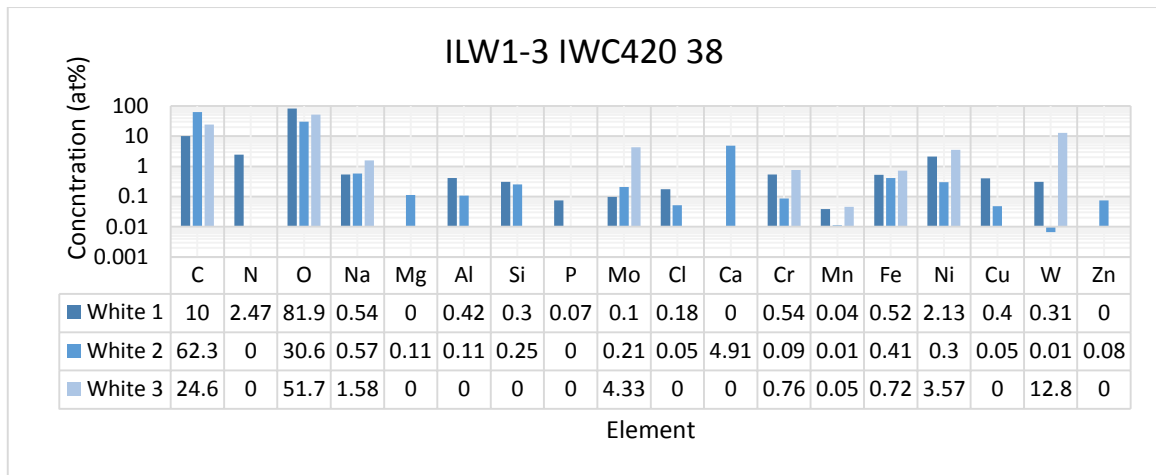


Figure 132: The quantification of the white areas of the ILW1-3 IWC412 38 shown in Figure 129.

Figure 129 shows the BSE images of the ILW1-3 IWC420 38 with different magnifications and the quantified areas. The surface of the sample is quite similar to the ILW1-3 IWC420 23. On the large areas (Figure 130) the dominant element is also the O ((67.2 – 67.5) at%) (as ILW1-3 IWC420 23) in agreement with NRA results, but much more impurities were detected (the extra elements are: Na, Si, P, Mo, Ca, Mn). The dark area has similar composition as large areas (Figure 131); however Si, P, Mo and C are not detected. Two of the white areas are rich in O with concentration of 81.9 at% and 51.7 at%, while the other is rich in C (62.3 at%) (Figure 132).

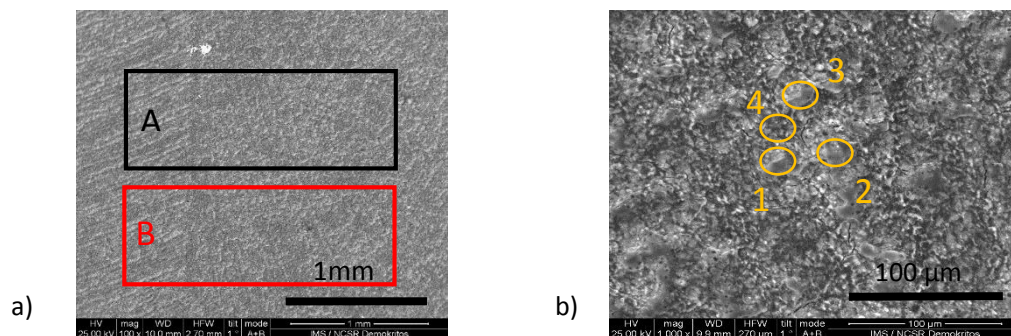


Figure 133: a) The BSE image with low magnification and the large areas and b) the BSE image with higher magnification and the chosen areas of the ILW1-3 3A8 390

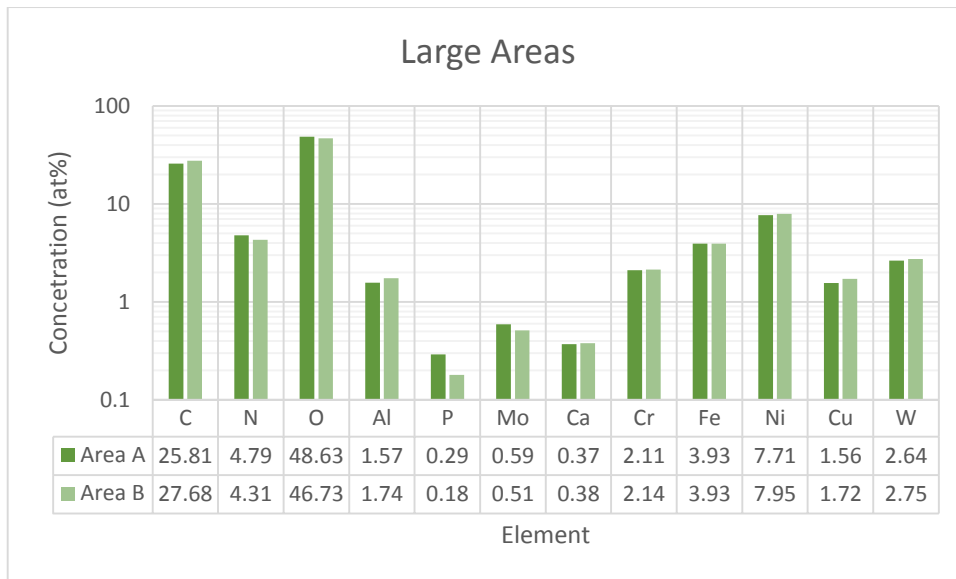


Figure 134: The quantification of the large areas of the ILW1-3 3A8 390 shown in Figure 133.

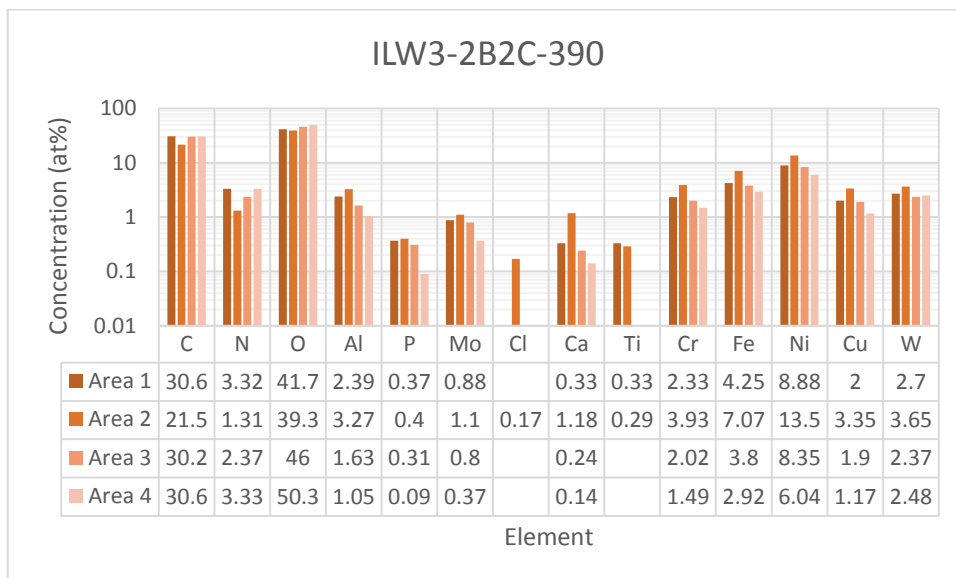


Figure 135: The quantification of the chosen areas of the ILW1-3 3A8 390 shown in Figure 133.

Figure 133 depicts the BSE images of the ILW1-3 3A8 390 with different magnifications and the quantified areas. The surface is quite smooth with some local melts (chosen areas) so the interaction between the sample and the plasma was intense. O is the dominant element ((46.73 – 48.63) at%), while C has also high concentration ((25.81 – 27.68) at%), as a confirmation of the NRA results. Other detected elements are: N, Al, P, Ca, Cr, Fe, Ni, Cu and W (Figure 134). The chosen areas have similar composition to each other and to the large ones (Figure 135). The Areas 1, 2 and 3 have different morphology as they have suffered melting.

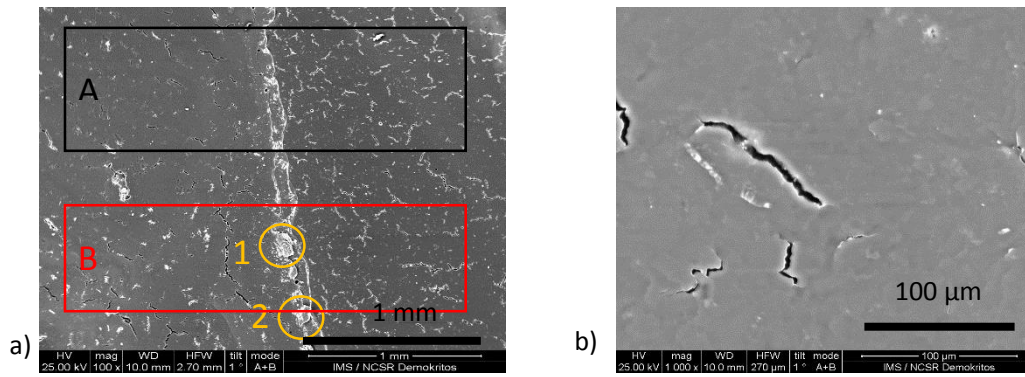


Figure 136: a) The BSE image with low magnification, the large and the white areas and b) the BSE image with higher magnification of the ILW1-3 3A8 418.

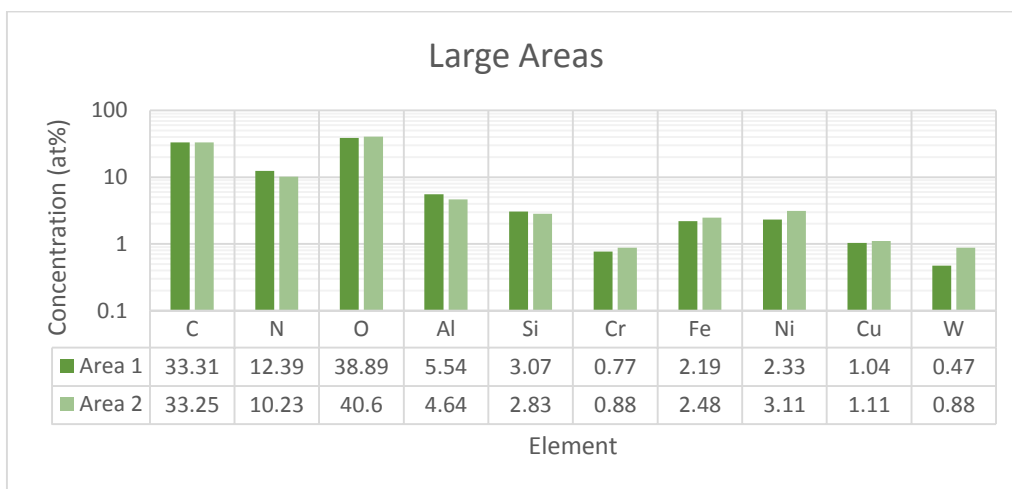


Figure 137: The quantification of the large areas of the ILW1-3 3A8 418 shown in Figure 136.

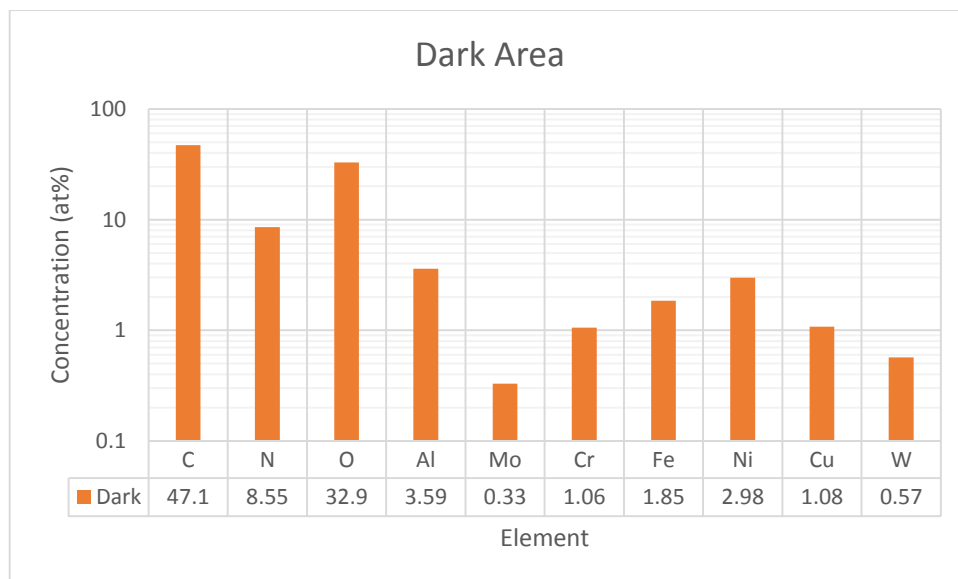


Figure 138: The quantification of the dark area of the ILW1-3 3A8 418 shown in Figure 136.

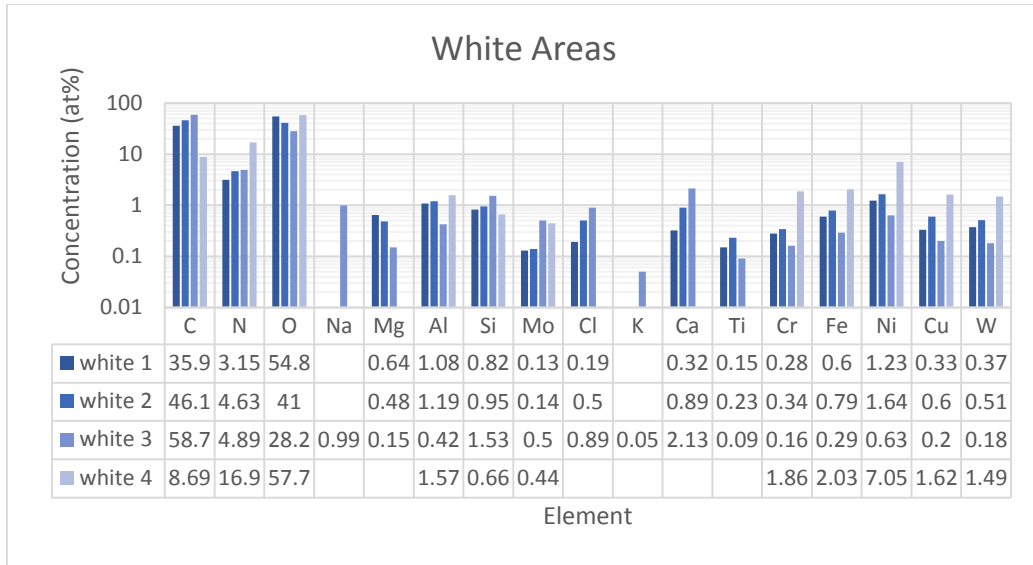


Figure 139: The quantification of the white areas of the ILW1-3 3A8 418 shown in Figure 136.

Figure 136 illustrates the BSE images of the ILW1-3 3A8 418 with different magnifications and the quantified areas. The sample has suffered melting in macroscopic scale (Figure 64a) and the SEM images confirm this observation. Large (Figure 137) and dark (Figure 138) areas have similar composition with high C ((33.25 – 33.31) at% and 47.1 at%, respectively) and O ((38.89 – 40.6) at% and 32.9 at%, respectively) concentrations and many elements with lower concentration: N, Al, Si, Cr, Fe Ni, Cu, Mo and W. The white areas has more element than the large and the dark ones: C, N, O, Na, Mg, Al, Si, Mo, Cl, K, Ca, Ti, Cr, Fe, Ni, Cu and W. C or O is the dominant element, while high N and Ni was detected on one area (16.9 at% and 7.05 at%, respectively)

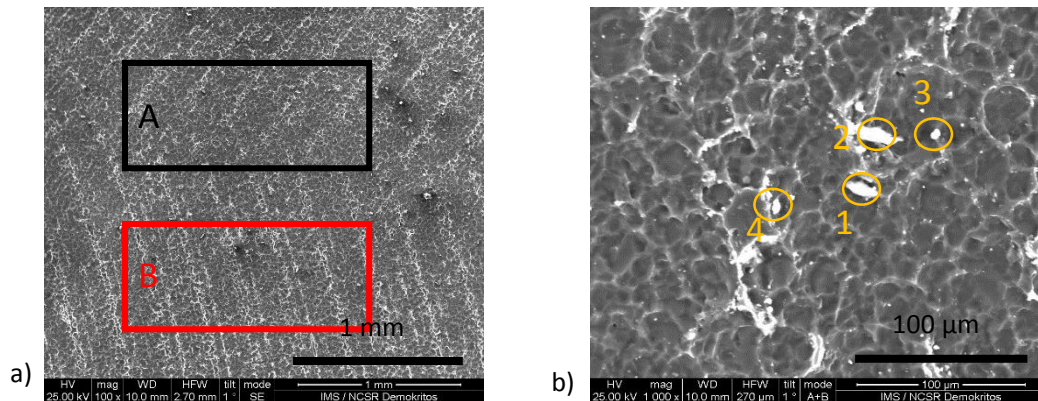


Figure 140: a) The BSE image with low magnification and the large areas and b) the BSE image with higher magnification and the selected white areas of the ILW3 2B2C 449.

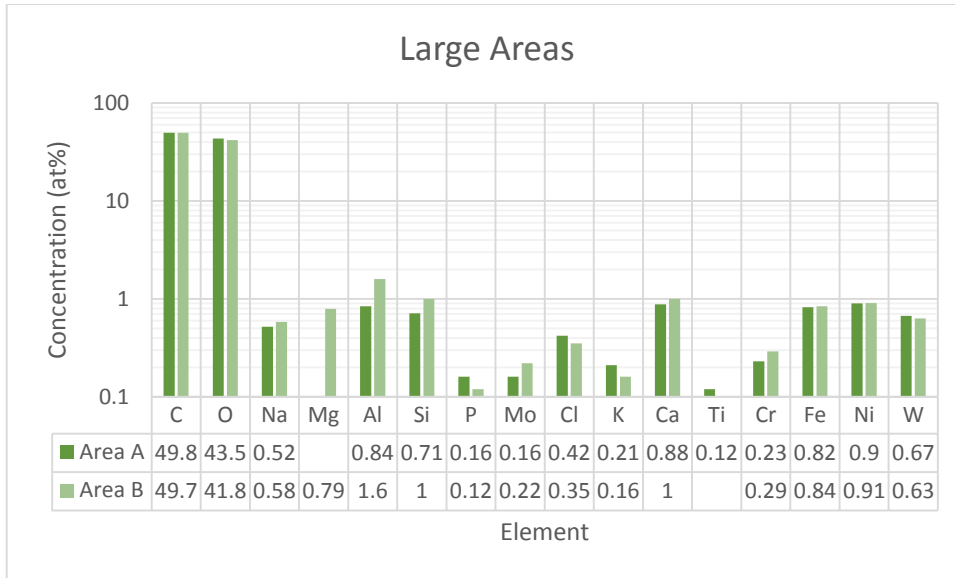


Figure 141: The quantification of the large areas of the ILW3 2B2C 449 shown in Figure 140.

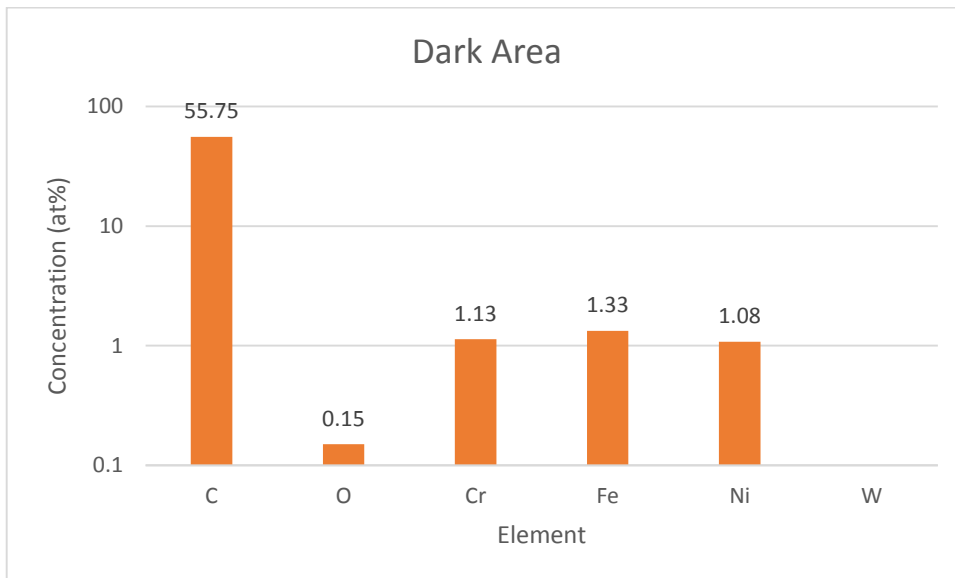


Figure 142: The quantification of the dark area of the ILW3 2B2C 449 shown in Figure 140.

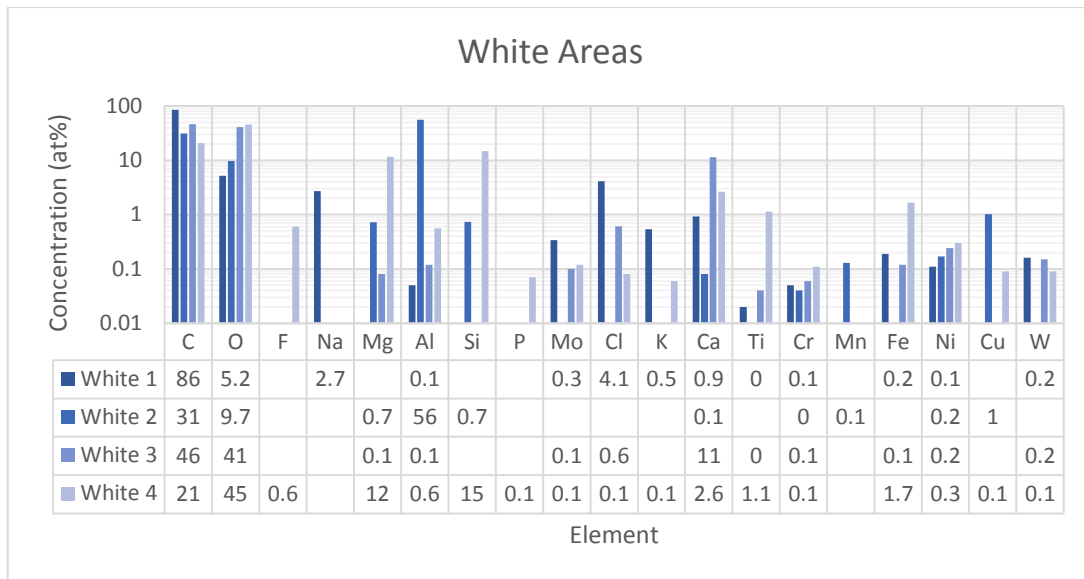


Figure 143: The quantification of the white areas of the ILW3 2B2Cc 449 shown in Figure 140.

Figure 140 presents the BSE images of the ILW3 2B2C 449 with different magnifications and the quantified areas. White lines with two different directions are observed with the low magnification (Figure 140a). The higher magnification (Figure 140b) shows that the surface has suffered melting. The large areas have high concentration of C ((49.7 – 49.8) at%) and O ((41.8 – 43.5) at%) and a lot of elements with lower concentration: Na, Mg, Al, S, Si, P, Mo, Cl, K, Ca, Ti, Cr, Fe, Ni and W. The dark area has also high C and O concentration (40.56 at% and 55.75 at%, respectively) but much fewer other elements (Cr, Fe, Ni and W). The white areas have also high concentration of C ((21 – 86) at%) and O ((9 – 45) at%) but in one of them Al (45 at%) is the dominant element (white area 2). Many other elements (F, Na, Mg, Al, Si, P, Mo, Cl, K, Ca, Ti, Cr, Mn, Fe, Ni, Cu, W) were detected. On some areas, the detected elements, other than C and O, have significant concentration: Na (2.7 at%) and Cl (4.1 at%) on White 1, Ca (11 at%) on white 3 and Mg (12 at%), Si (15 at%) and Ca (11 at%) on White 4.

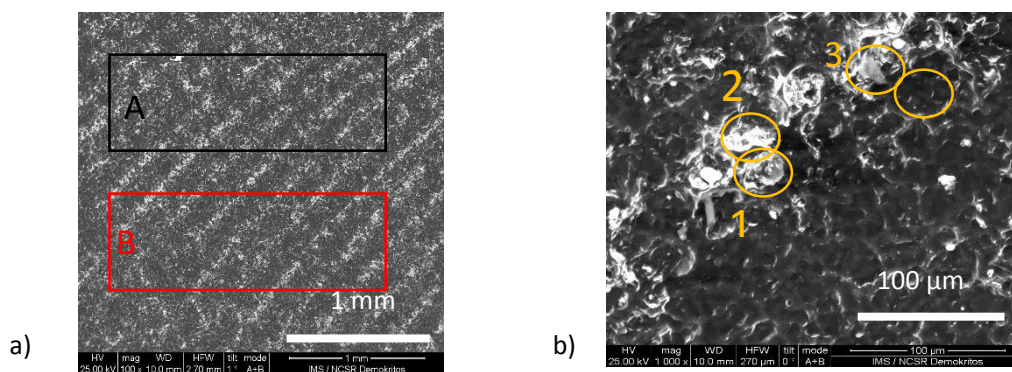


Figure 144: a) The BSE image with small magnification and the large areas and b) the BSE image with higher magnification and the selected white areas of the ILW3 2B2C 451.

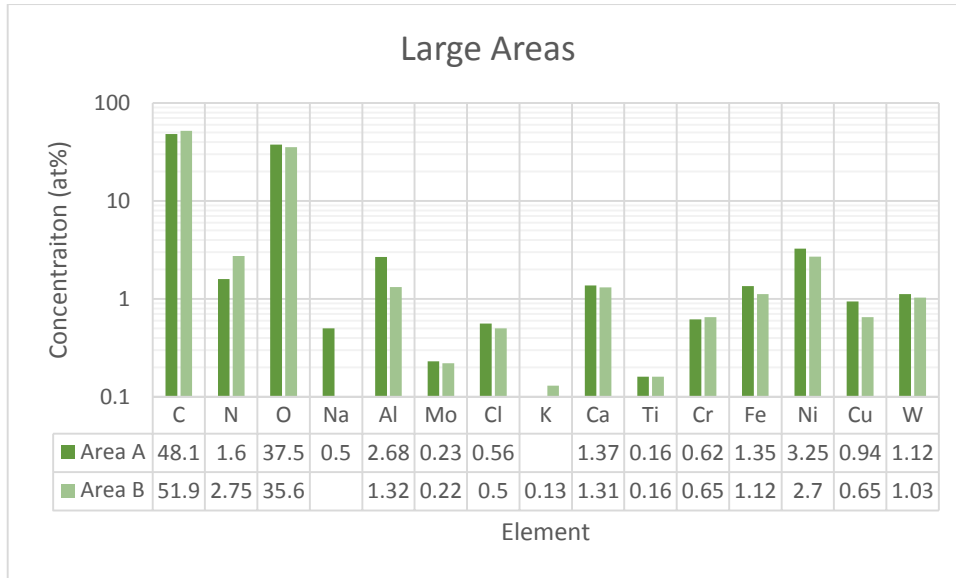


Figure 145: The quantification of the large areas of the ILW3 2B2C 451 shown in Figure 144.

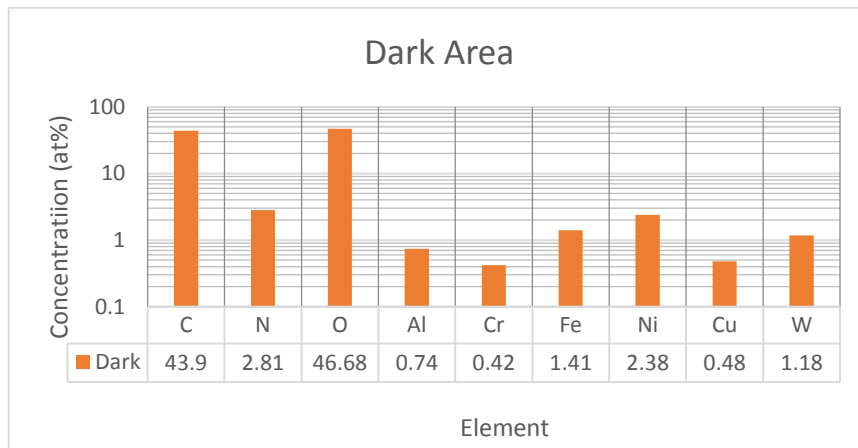


Figure 146: The quantification of the dark area of the ILW3 2B2C 451 shown in Figure 144.

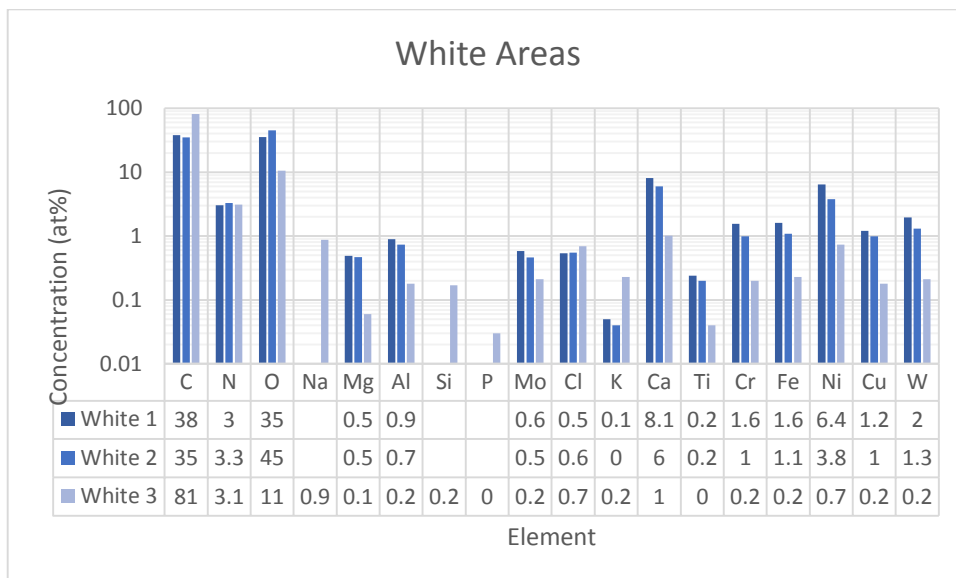


Figure 147: The quantification of the white areas of the ILW3 2B2C 451 shown in Figure 144.

Figure 144 shows the BSE image of the ILW3 2B2C 451 with different magnifications and the quantified areas. White oriented strips are observed on the surface. C ((48.1 – 51.9) at%) and O ((35.6 – 37.5) at%) are the dominant elements of the large areas (Figure 145) while a lot of elements: N, Na, Al, S, Cl, K, Ca, Ti, Cr, Fe, Ni, Cu and W were detected, some of which: N ((1.6 – 2.75) at%), Al ((1.32 – 2.68) at%), Ca ((1.31 – 1.37) at%), Ni ((2.7 – 3.25) at%) and W ((1.03 – 1.12) at%) have significant (>1% at) concentration. The dark areas (Figure 146) are also rich in C (43.9 at%) and O (46.68 at%) concentration, while the rest detected elements are N, Fe, Ni and W. C ((35 – 81) at%) and O ((11 – 45) at%) are the dominant elements of the white areas (Figure 147), a lot of elements were detected (N, Na, Mg, Al, Si, P, Mo, Cl, K, Ca, Ti, Cr, Fe, Ni, Cu, W), while white 1 and 2 have high concentration of Ca ((6 – 8.1) at%) and Ni ((3.8 – 6.4) at%).

Figure 148 presents the average elemental concentration of the samples from the IWC and the DP. C, O, Al, Cr, Fe, Ni and W were detected on all samples. N were detected on all samples apart from ILW3 2B2C 451. The samples from the IWC have the highest O concentration ((67.3 – 67.8) at%) in agreement with NRA results (Section 5.2.1). Samples from the ILW3 2B2C has the highest C concentration ((49.8 – 50.0) at%). The samples from the DP 3A8 present the highest concentration of most of the rest elements. Specifically, the ILW1-3 3A8 390 has the highest concentration of P, Mo, Cr Fe, Ni and W, while the highest concentration of N, Al and Si is detected on ILW1-3 3A8 418. The high concentration of these elements might be attribute to the low C and O amount as presented in the NRA results (Section 5.2.1).

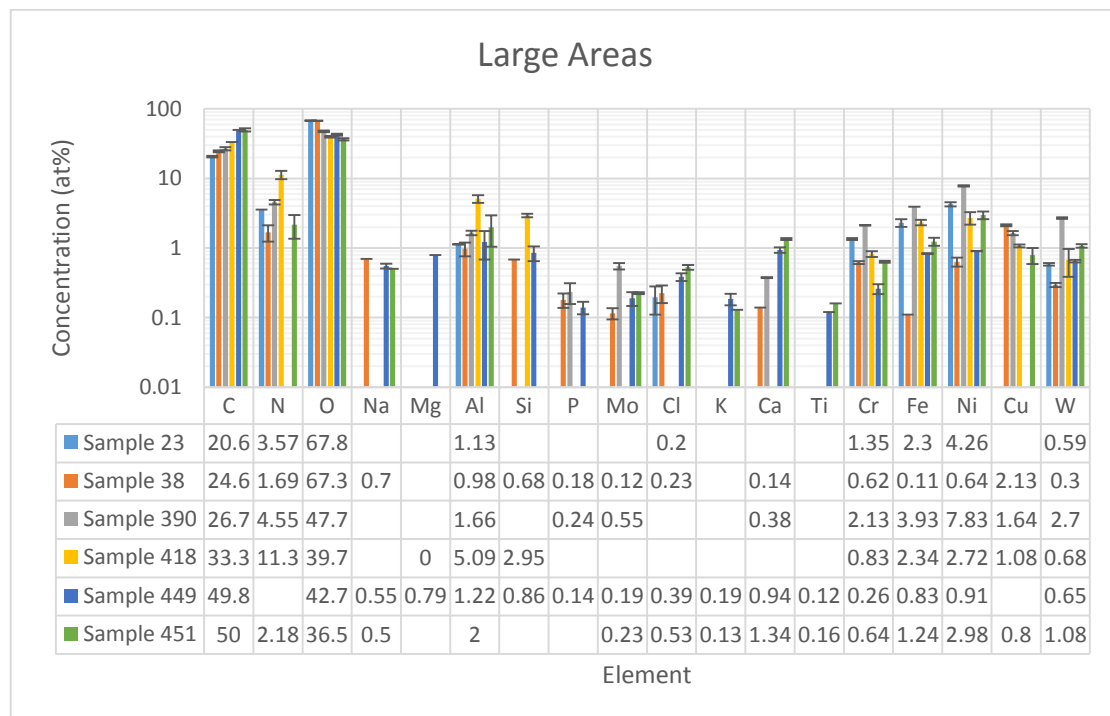


Figure 148: The average elemental concentration of large areas for all samples from IWC and DP.

5.2.4 X-ray Diffraction Results

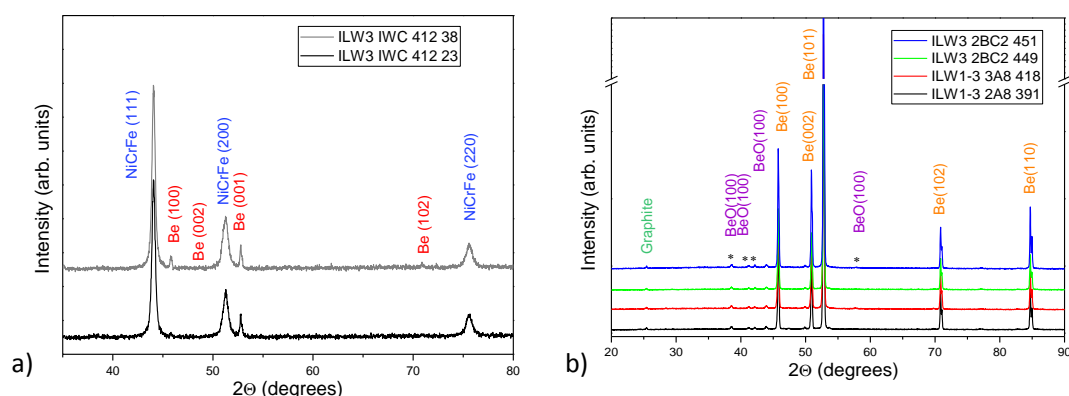


Figure 149: XRD spectra of the Be samples from (a) the IWC and (b) the DP.

Beryllium crystallizes in P63/mmc space group. Regarding the Be samples from IWC which are deposited on inconel, the NiCrFe Bragg peaks were detected (Figure 149a). In the samples from the DP BeO bromellite crystallizing in hexagonal P63mc space group and graphite were detected (Figure 149b).

5.2.5 Summary and Conclusions

Samples from different areas (IWC and DP) of the JET tokamak divertor main chamber after ILW3 or ILW1-3 campaigns were investigated using NRA, XRF, SEM with EDS and XRD techniques. The samples from the IWC have the highest carbon amount ($7.9 \pm 2 \times 10^{17}$ at/cm² and $4.5 \pm 1 \times 10^{17}$ at/cm²). Additionally, their surfaces seem unchanged and the Inconel substrate was found to have the initial composition. X-ray diffraction revealed the formation of NiCrFe. The samples from the IWL1-3 3A8 present large variation in carbon deposition and both samples have suffered melting. the sample 390 has suffered melting in microscopic scale. The C amount on the samples from the ILW3 2B2C is similar and oriented strips have been formed on the surface of both of them. On the surface of all samples, the dominant elements are C and O, but plenty of elements (N, Na, Mg, Al, Si, P, Mo, Cl, K, Ca, Ti, Cr, Fe, Ni Cu and W) were detected, with significant concentration in some areas.

Chapter 6: JET Tokamak Divertor Lamellae

In this chapter the results of the investigation of samples from W lamellae of the ILW JET tokamak divertor tile 5 using NRA, SEM with EDS, XRF and XRD are presented. The aim of the investigation is to quantify the material deposition (Be, C, O and heavier elements), determine the surface morphology changes after plasma exposure and the deposition areas, assess the stoichiometry from deeper layers and the formation of any compounds.

6.1 Carbon, Beryllium and Oxygen Deposition

The samples from the W lamellae presented in section 4.2 were measured with ^2H milli-beam with the condition described in section 2.1.4.1. Figure 150 presents representative NRA experimental and simulated spectra from the ILW-1 C14 15. From higher to lower energy we observe the peaks of $^9\text{Be}(d,p_0)^{10}\text{Be}$, the $^9\text{Be}(d,a_{0,1})^7\text{Li}$, the $^{12}\text{C}(d,p_0)^{12}\text{C}$ and $^{16}\text{O}(d,p_0)^{17}\text{O}$ nuclear reactions, the pile up and the backscattered deuteron from the $\text{W}(d,d)\text{W}$. The determined C, Be and O amounts and their ratios are presented in Table 11. ILW1 C3 12 sample presents the highest C $((25.5 \pm 3) \times 10^{17}$ at/cm 2) and O $(18.0 \times 10^{17}$ at/cm 2) amount. The second highest C amount $((10.1 \pm 0.5) \times 10^{17}$ at/cm 2) was detected on ILW2 C23 72, where the highest Be content $(16.4 \times 10^{17}$ at/cm 2). The lowest C amount $(1.4 \pm 0.2 \times 10^{17}$ at/cm 2) was detected on ILW2 C13 61, the lowest Be amount $(2.1 \times 10^{17}$ at/cm 2) on ILW2 A23 51 and the lowest O amount $(1.9 \times 10^{17}$ at/cm 2) on ILW2 C22 70.

Regarding the Be/C ratio (Table 11) the sample can be classified in three groups: sample with ratio below 1.0 (ILW1 A23 1 and C3 12), between 1.0 and 1.5 (ILW1 C14 15, ILW2 A23 48 and 51, IWL2 C22 and ILW3 A23 93) and between 1.6 and 2.0 (ILW1 A23 7, ILW2 C13 ILW 2 C14 63 and 67 and ILW2 C23 72). Additionally, samples from the same lamellae: ILW2 A23 and C14 have similar ratio (1.12-1.18 and 1.79 – 2.0, respectively), however the samples from the lamella ILW1 A23 have different ratios, where sample 1 has 0.56 while sample 7 has 1.58. For the O/Be ratio, the samples from the second campaign and the stack C have a ratio between 0.3 and 0.8, while the rest lamellae have ratio between 2 and 3.3. The O/C ratio ranges between 0.5 and 3.7. Samples from ILW2 A23 present similar O/C ratios.

The C and Be amounts of samples from the same lamella lines are presented relative to the strike point time as a function of S coordinate in Figure 151. The strike point evolution versus S coordinate is taken from Pintsuk et al [157]. For the three different lines the C and Be amounts increase with the increase of the strike point time. For example, the ILW2 A23 51 with S coordinate 1085 mm which is characterized by low strike point time has Be amount of 2.1×10^{17} at/cm 2 and C amount of 1.7×10^{17} at/cm 2 , while the ILW2 A23 72 with S coordinate 1249 mm and high strike point time (around 200 s/mm) has eight times higher Be amount and six times higher C amount. In Figure 152 the Be, C and O amounts of samples from the same positions and different experimental campaigns are shown. From the first to the second campaign, the Be deposition increases by 30% (from 3×10^{17} at/cm 2 to 3.9×10^{17} at/cm 2) for A23 lamella and by 57% (from 7×10^{17} at/cm 2 to 11×10^{17} at/cm 2) for C14 lamella. C deposition either decreases, from 5.3×10^{17} at/cm 2 to 3.5×10^{17} at/cm 2 for A23, or remains almost constant ($6.3 - 6.2 \times 10^{17}$ at/cm 2) for C14. O amount either increases (from 8.1×10^{17} at/cm 2 to 10×10^{17} at/cm 2) for A23 or decreases (13.8×10^{17} at/cm 2 to 4.9×10^{17} at/cm 2) for C14. From ILW2 to IWL3, the content of C and Be become more than double (from $(1.7 \pm 0.2) \times 10^{17}$ at/cm 2 to $(4.0 \pm 0.4) \times 10^{17}$ at/cm 2 and from 2.1×10^{17} at/cm 2 to 4.3×10^{17} at/cm 2 , respectively), while the O content increases by about 1.5 times.

Figure 153 presents the comparison of the C and Be content of the current work with the results of M. Mayer et al [158] for the common samples. Generally, the absolute values of the current

work are higher than that of the previous one, however there is an agreement that the Be amount is higher than the carbon one. Additionally, we observe that there is an agreement in classification as for lines 13 and 14 (Figure 153b), ILW2 C14 63 has the most C ($(6.2 \pm 0.3) \times 10^{17}$ at/cm²) and Be (11.0×10^{17} at/cm²) amount, ILW2 C13 61 has the less content ($(1.4 \pm 0.2) \times 10^{17}$ at/cm² and 2.5×10^{17} at/cm², respectively), while the results for ILW2 C14 67 are between them ($(4.1 \pm 0.4) \times 10^{17}$ at/cm² and 8.3×10^{17} at/cm², respectively). For lines 23 and 24, in Figure 153b the C and Be content of ILW2 A23 48, ILW2 A23 51 and ILW2 C22 70 are similar while the values for ILW2 C23 72 are higher.

Figure 154 presents the depth profile of Be, C and O of the analysed samples. O cannot be detected in depth higher than about 1 μm due to the pile up effect as shown in Figure 150. The maximum depth of C deposition is also not distinct as the end of the $^{12}\text{C}(d,p_0)^{13}\text{C}$ is overlapped with the $^{16}\text{O}(d,p_0)^{17}\text{O}$ and the pile up. The C and Be concentrations are reduced with depth in a similar way, namely either abruptly as in ILW1 A23 1 (Figure 154a), ILW2 A23 51 (Figure 154f), ILW2 C13 61 (Figure 154g), ILW2 C22 70 (Figure 154j) and ILW3 A23 93 (Figure 154l) or smoothly as in ILW1 A23 7 (Figure 154b), ILW1 C3 12 (Figure 154c), ILW1-C14-15 (Figure 154d), ILW2 A23 48 (Figure 154e), ILW2 C14 63 (Figure 154g), ILW2 C14 67 (Figure 154i) and ILW2 C23 72 (Figure 154k). ILW1 C3 12 has the highest surface C concentration with more than 30 at% with a layer thickness of about 0.6 μm , while the next highest C concentration is on ILW3-A23-93 with 25 at% but in a very thin layer of around 0.1 μm . The highest Be concentration was detected on the surface of the ILW1 C14 15 with 15 at%.

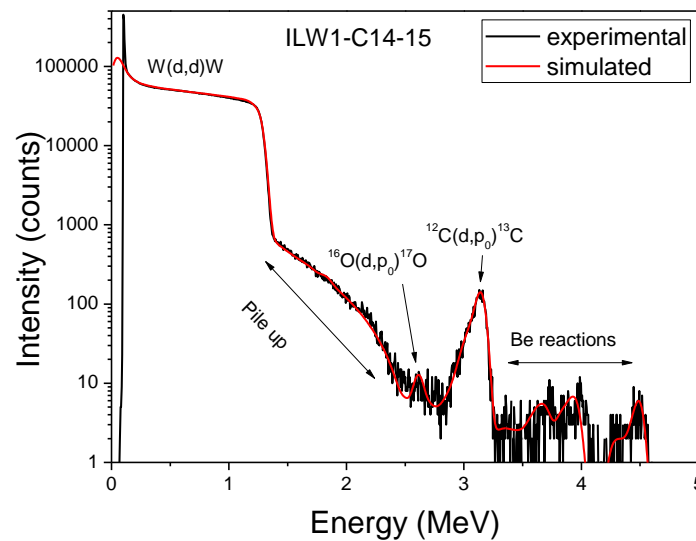
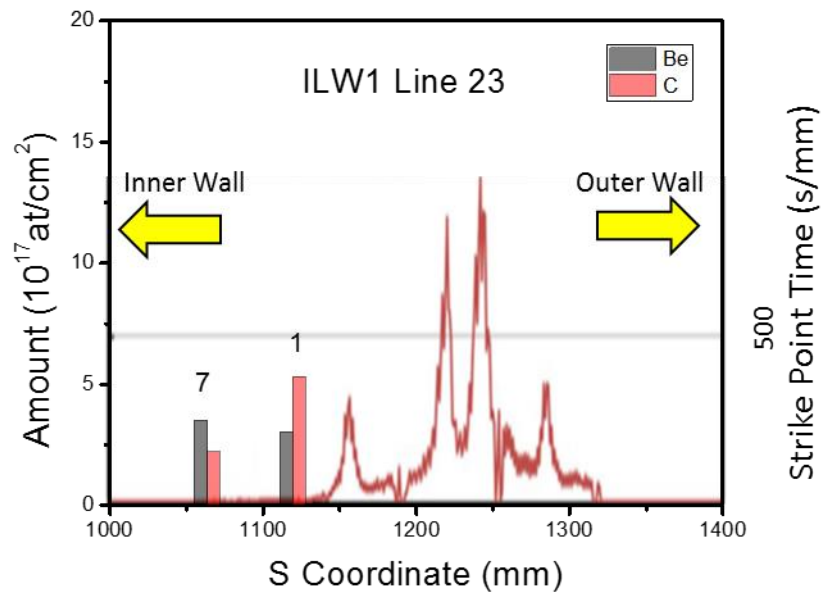


Figure 150: the experimental (black) and simulated (red) spectra of the ILW1 C14 15.

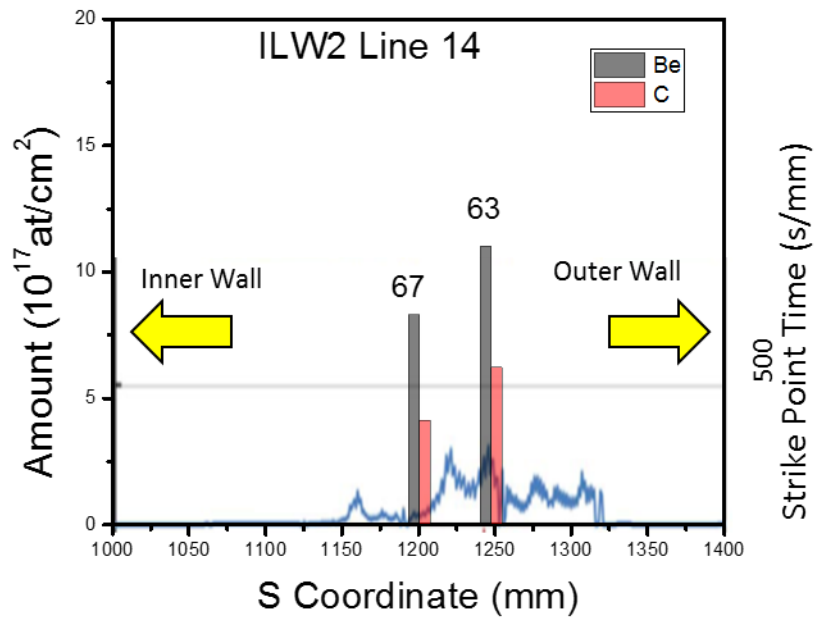
Table 11: W lamella sample description and elemental content determined by NRA.

Exp. Period	W Lamella	Sample No	Position	S-Coordinate	C Be O			Be/C	O/C	O/Be
					(10 ¹⁷ at/cm ²)					
ILW1	A23	1	as 48	1120	5.3 ± 0.5	3.0	8.1	0.56	1.52	2.70
	A23	7		1064	2.2 ± 0.3	3.5	8.2	1.58	3.71	2.34
	C3	12		1191	25.5 ± 3.0	5.5	18.0	0.22	0.71	3.27

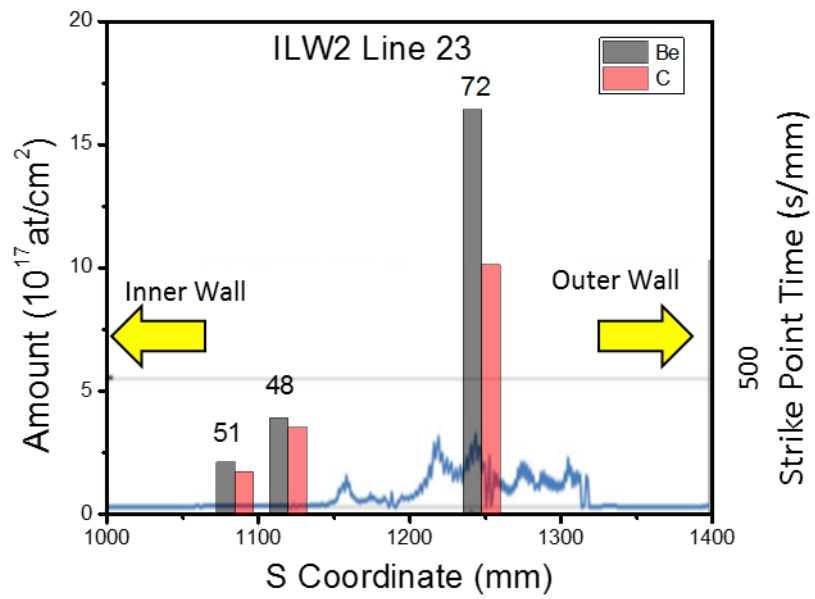
	C14	15	as 63	1248	6.3 ± 0.3	7.0	13.8	1.12	2.19	1.96
ILW2	A23	48	as 1	1248	3.5 ± 0.2	3.9	10.0	1.12	2.90	2.60
	A23	51	as 93	1085	1.7 ± 0.2	2.1	6.1	1.18	3.53	2.98
	C13	61		1248	1.4 ± 0.2	2.5	2.0	1.75	1.40	0.80
	C14	63	as 15	1248	6.2 ± 0.3	11.0	4.9	1.79	0.80	0.44
	C14	67		1201	4.1 ± 0.4	8.3	5.5	2.00	1.33	0.67
	C22	70		1248	1.8 ± 0.2	2.3	1.9	1.30	1.06	0.82
	C23	72		1248	10.1 ± 0.5	16.4	5.3	1.62	0.52	0.32
ILW3	A23	93	as 51	1084	4.0 ± 0.4	4.3	9.1	1.05	2.25	2.14



a)



b)



c)

Figure 151: C and Be amount of samples from the a) ILW1 Line 23, b) ILW2 Line 14 and c) ILW2 Line 23 as a function of S coordinate position relative to the strike point time. The strike point evolution is taken from Pintsuk et al [157].

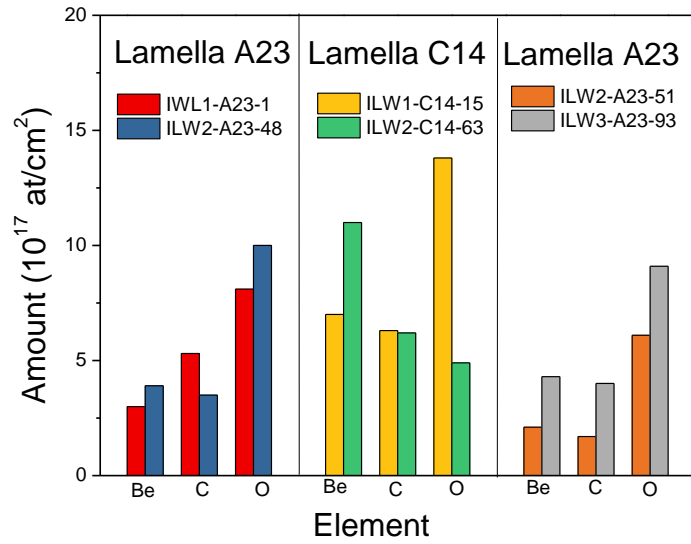


Figure 152: The element amount of the same positions and different experiment campaigns

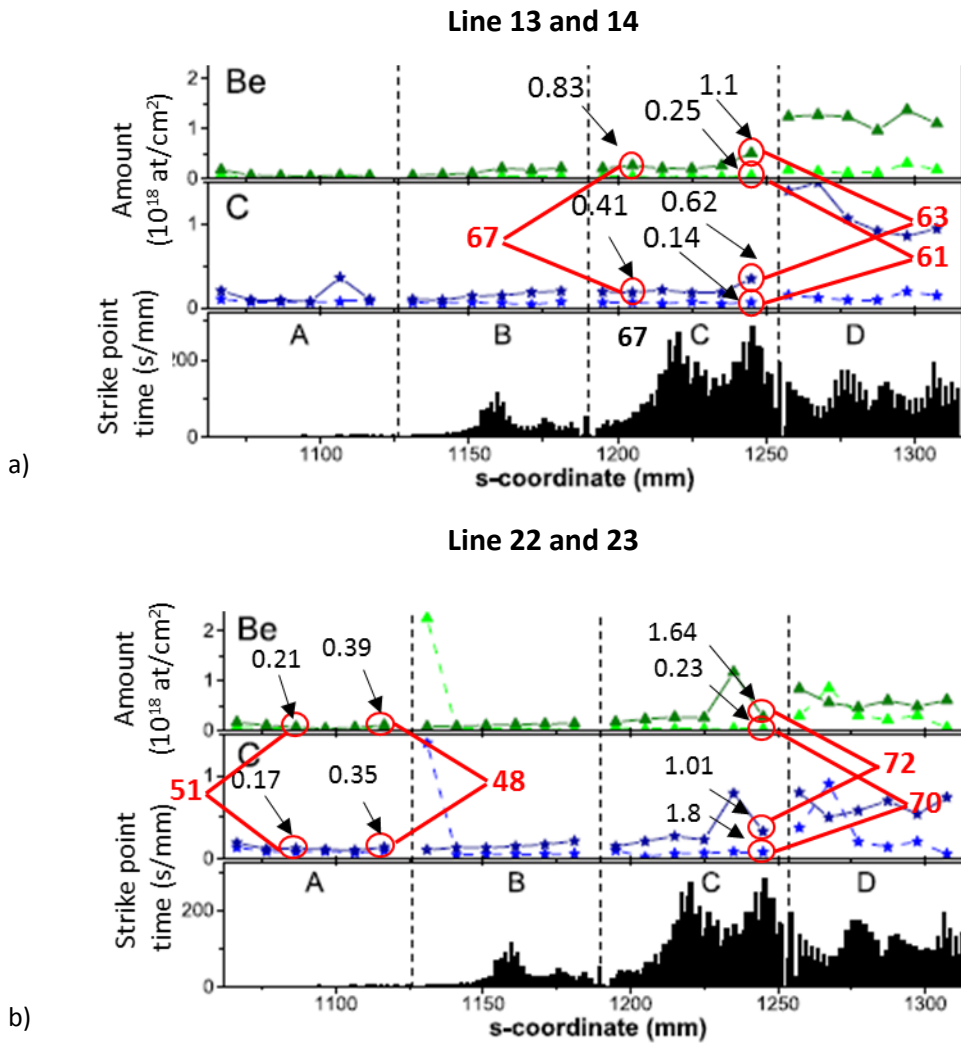
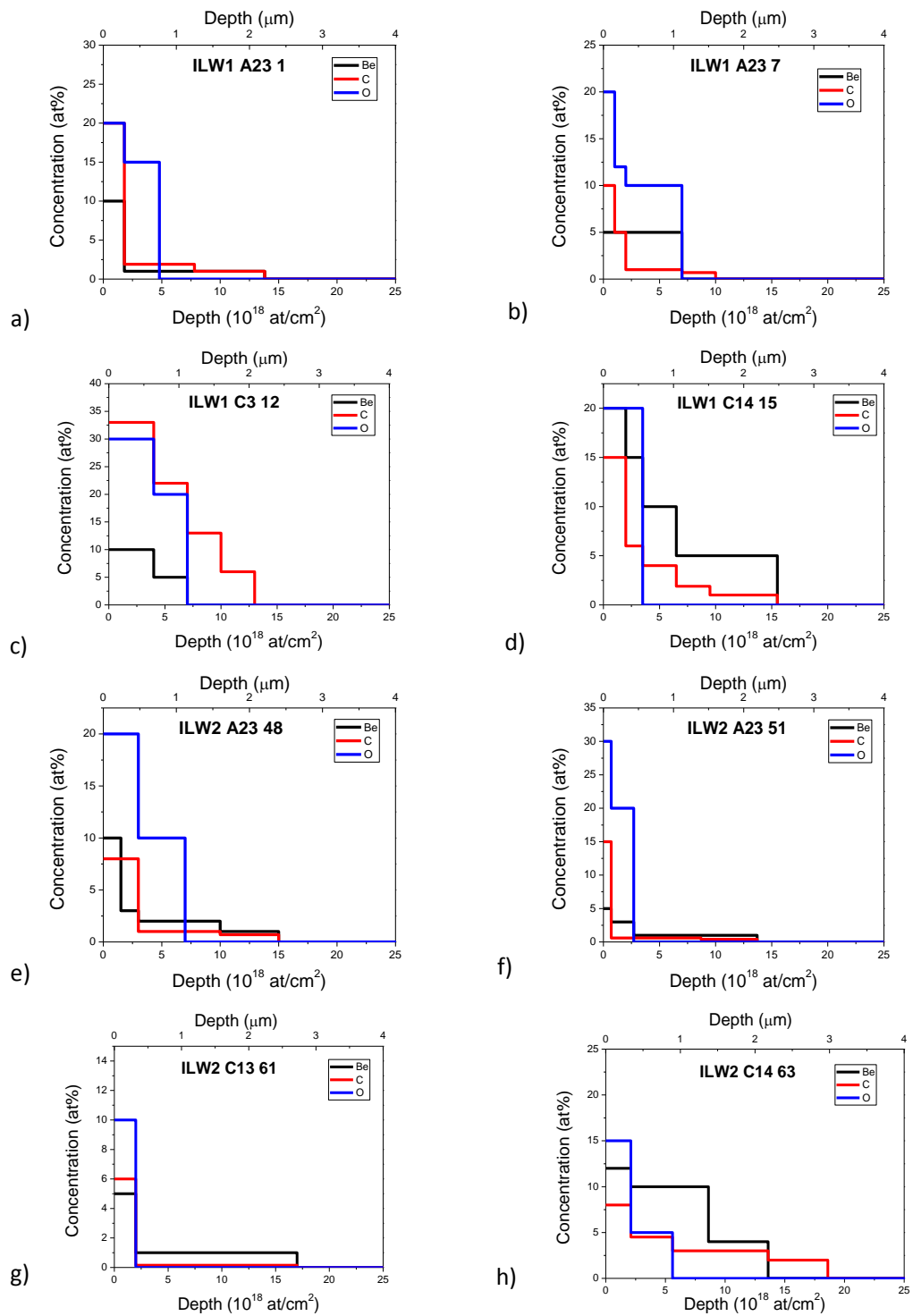


Figure 153: Comparison between the results of the current work with the results of the M. Mayer [158]. The red numbers are the name of the samples and the black ones the values of the current work. or a) line 13 and 14 and b) lines 22 and 23.



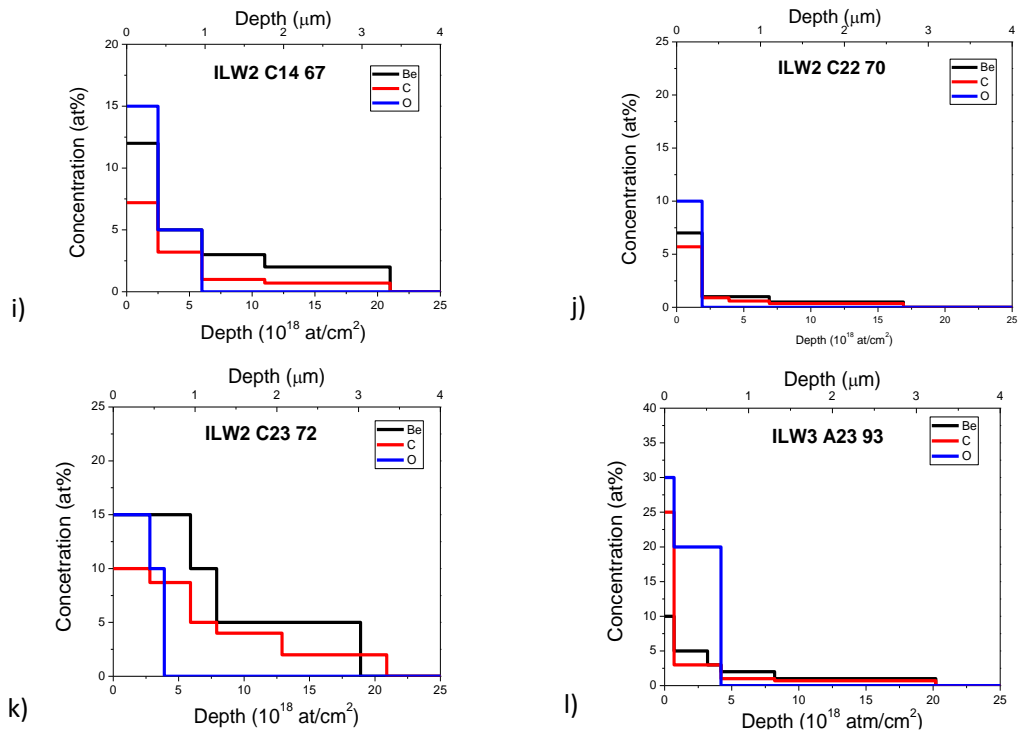


Figure 154: The depth profile of the Be, C and O of the ILW JET tokamak divertor tile 5 as determined with NRA measurement.

6.2 X-ray Fluorescence Spectroscopy Results

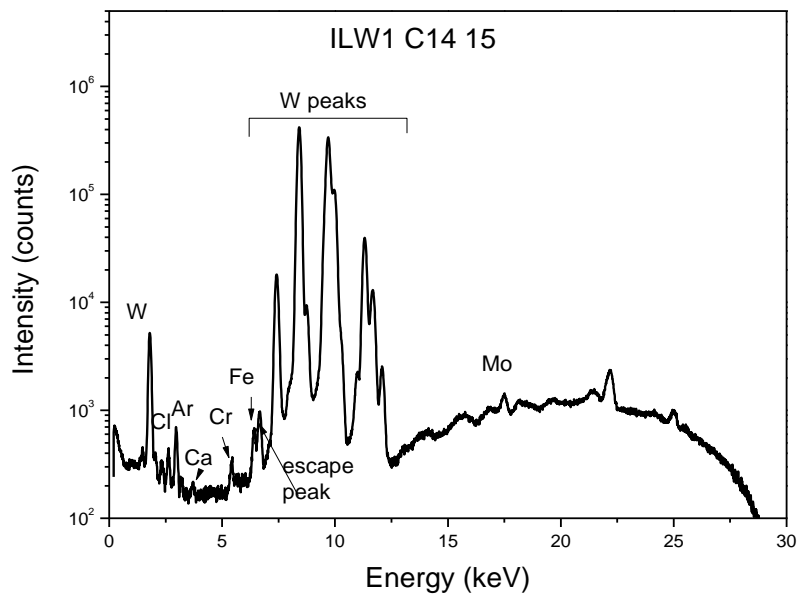


Figure 155: The XRF experimental spectrum and the peak characterization of the ILW1 C14 15.

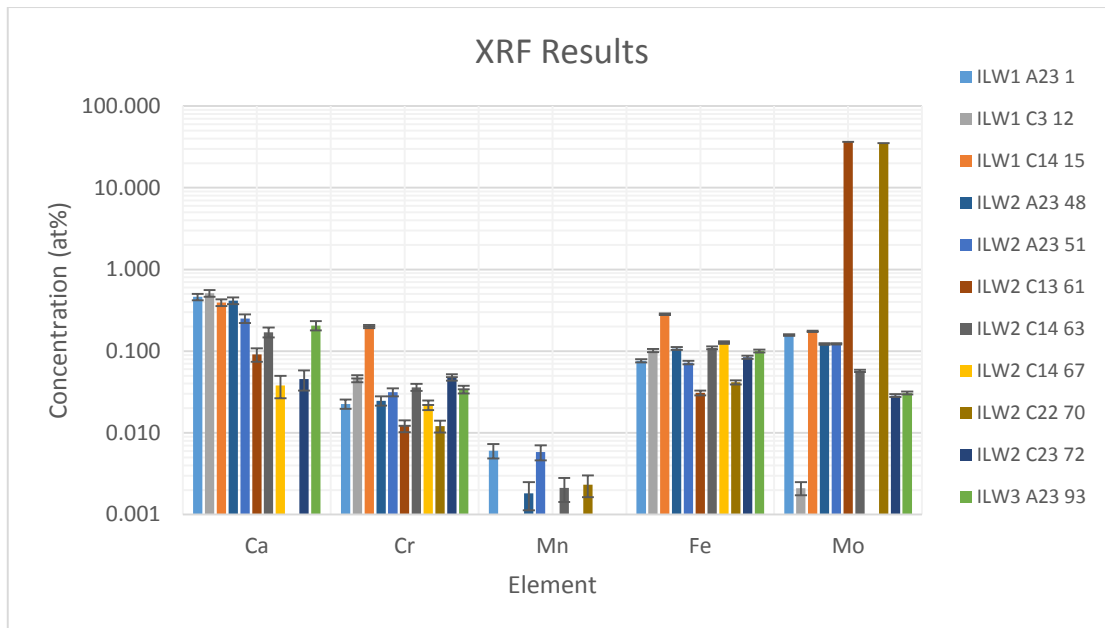


Figure 156: The results of the SEM analysis for all exposed samples except for ILW1-A23-7. The concentration of W is not presented.

Figure 155 shows the experimental spectrum and the peak identification. W is the dominant element as structural material. The other elements detected by XRF in the samples under investigation are: Ca, Cr, Mn, Fe and Mo. Cr, Fe and W are present in all samples. Figure 156 shows the quantitative results of all samples apart from ILW1 A23 7, which has surface smaller than the spot beam. W is not presented as its concentration is near 100%. Ca is observed in all samples except for ILW2 C22 70, Mo in all samples apart from ILW2 C14 67 and Mn in ILW1 A23 1, ILW2 A23 48, ILW2 A23 51, ILW2 C14 63 and ILW2 C22 70. ILW2 C13 61 and ILW2 C22 70 are the marker samples which have a Ni interlayer of 6 μm between the top W layer (6 μm) and the bulk W. The high Mo concentration can be attributed to the interlayer which means that these samples have not suffered erosion higher than 12 μm . The ILW1 C14 15 has the highest Cr and Fe concentration (0.2 at%, 0.1 at%, respectively), a result that agrees with the EDS results (see below, section 6.3). The ILW1 C3 12 has high Ca concentration (0.4 at%) in agreement with the EDS results. No correlation between the elements is observed.

6.3 Surface Morphology and Stoichiometry

Figure 157 presents the backscattered electron (BSE) images of the reference and plasma exposed samples. On the non-exposed sample, a micro-crack network is apparent (Figure 157a). Similar networks were detected on the surface of all samples from the Lamella A23 after the three campaigns, on the ILW1 C3 12 and the ILW1 C14 15. Additionally, the roughness of their surfaces is similar to the reference one, so the interaction between these samples and the plasma can be characterized as mild. On the other hand, the width and the density of the micro-cracks have been reduced on ILW2 C14 63, ILW2 C14 67, ILW2 C22 70 and ILW2 C32 72. Furthermore, the surface of these samples is smoother than the reference one which suggests significant heat transfer to these areas of the divertor. No micro-crack was detected on ILW2 C13 61 which indicates that the surface of this sample had suffered melting.

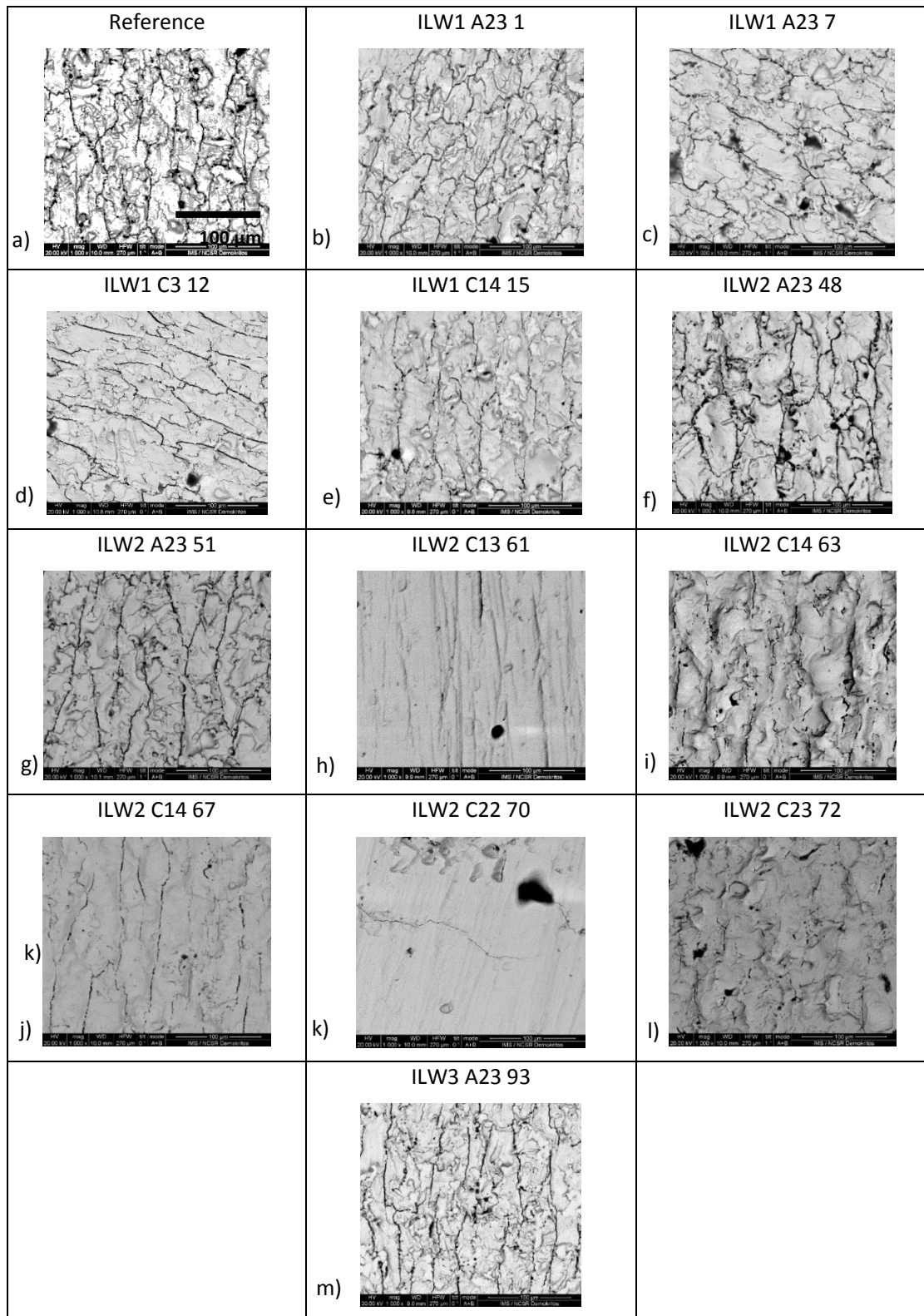


Figure 157: The BSE images of reference and the analysed exposed samples using the same magnification.

In the next Figures the surface morphology via SE and different phases via BSE images and the quantification of different areas via EDS analysis are presented for each sample. EDS analysis was

carried out in two large areas of about 1 x 2 mm² and in chosen areas with different phases, rich in either low Z elements (“dark” areas) or high Z elements (“white” areas).

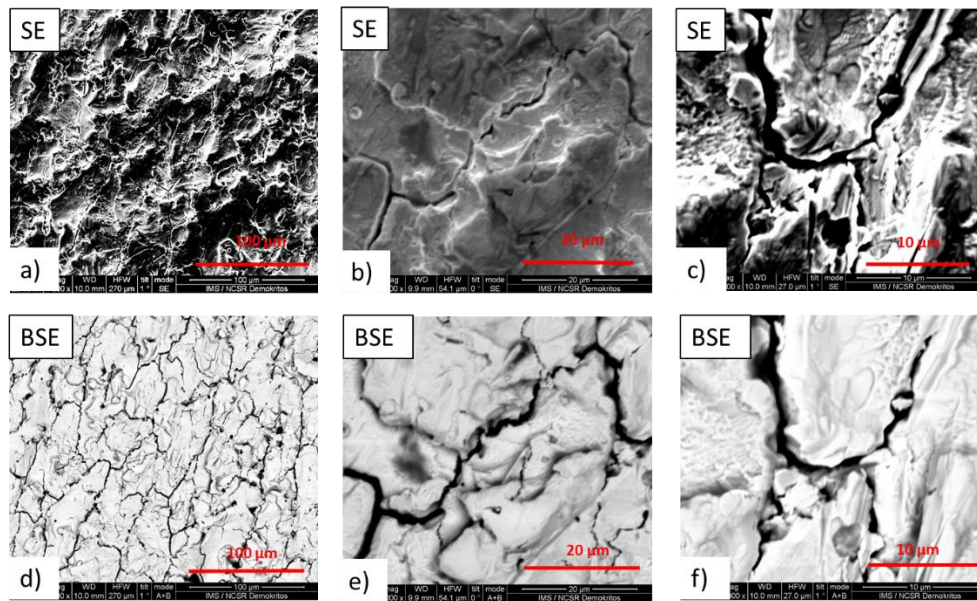


Figure 158: The secondary and backscattered electron images of the ILW1 A23 1 sample using different magnifications.

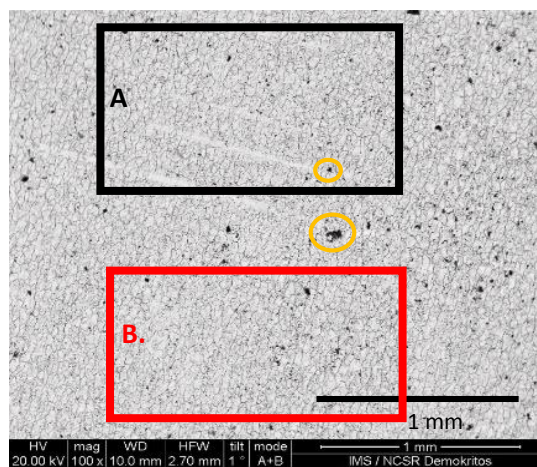


Figure 159: The BSE image and large and dark areas of the ILW1 A23 1.

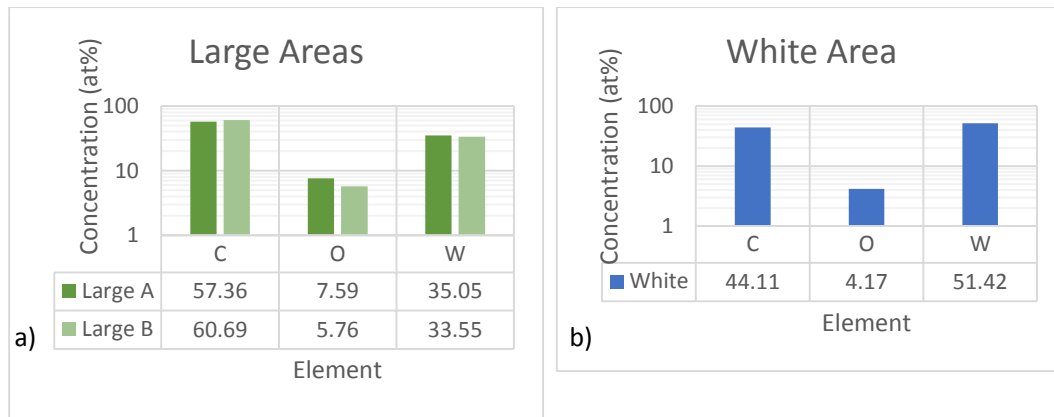


Figure 160: The quantification of a) large and b) white areas of ILW1 A23 1 shown in Figure 159.

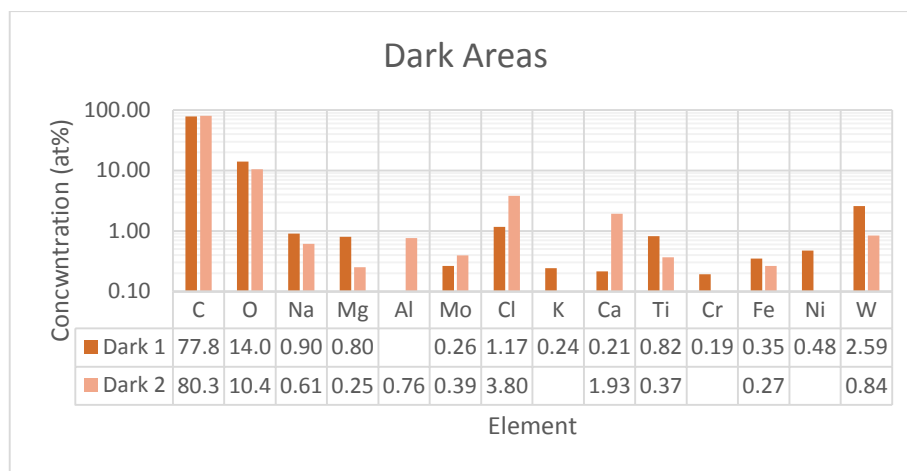


Figure 161: The quantification of the dark areas of ILW1 A23 1 shown in Figure 159.

Figure 158 presents the SE and BSE images of ILW1 A23 1 with different magnifications. Figure 159 shows the large and dark areas selected to be investigated. The cracks are intense and the surface rough. The quantification of large and white areas is presented in Figure 160. C, O and W are the only three elements detected on these areas. Higher C ((57.36 – 60.69) at%) and O ((5.76 – 7.59) at%) concentration is detected on large areas than on white one (44.11 at% and 4.17 at%) as there is a contribution of the dark areas. Figure 161 presents the quantitative results of the dark areas. The common elements are C, O, Na, Mg, Mo, Cl, Ca, Ti, Fe, W. On one of the areas Al (Dark 2), K, Cr and Ni (Dark 1) were detected. On both dark areas the dominant element is C ((77.8 – 80.3) at%). Additionally, high O concentration ((10.4 – 14.0) at%) is also observed. For the common elements large area has higher concentration of Na, Mg, Ti, Fe and W.

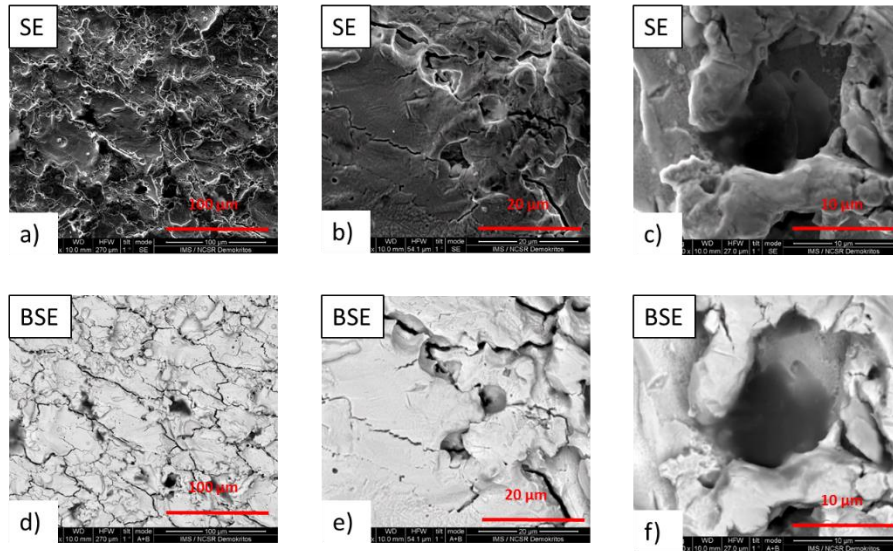


Figure 162: The SE and BSE electron images of the ILW1 A23 7 sample using different magnifications.

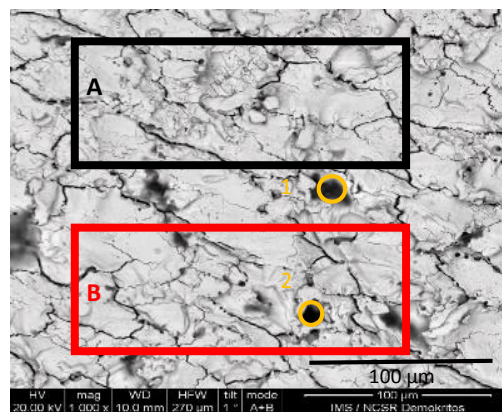


Figure 163: The BSE image and the quantified areas of the ILW1 A23 7.

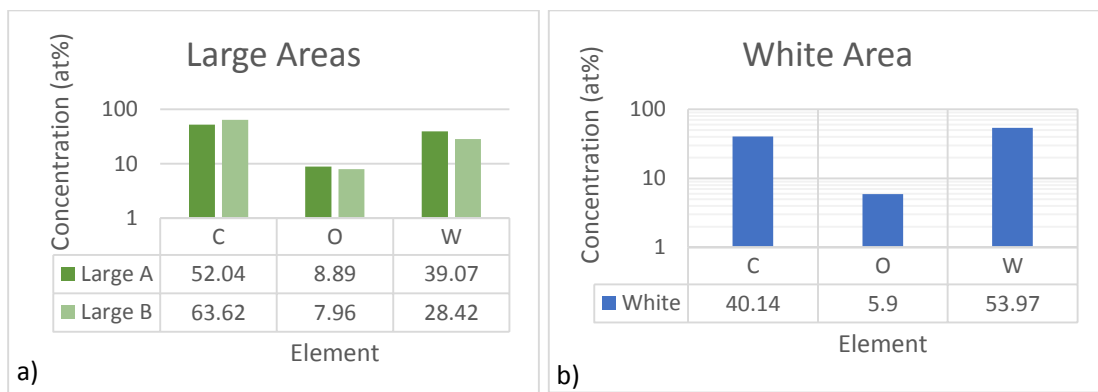


Figure 164: The quantification of the a) large and b) white areas of the ILW1 A23 7 shown in Figure 163.

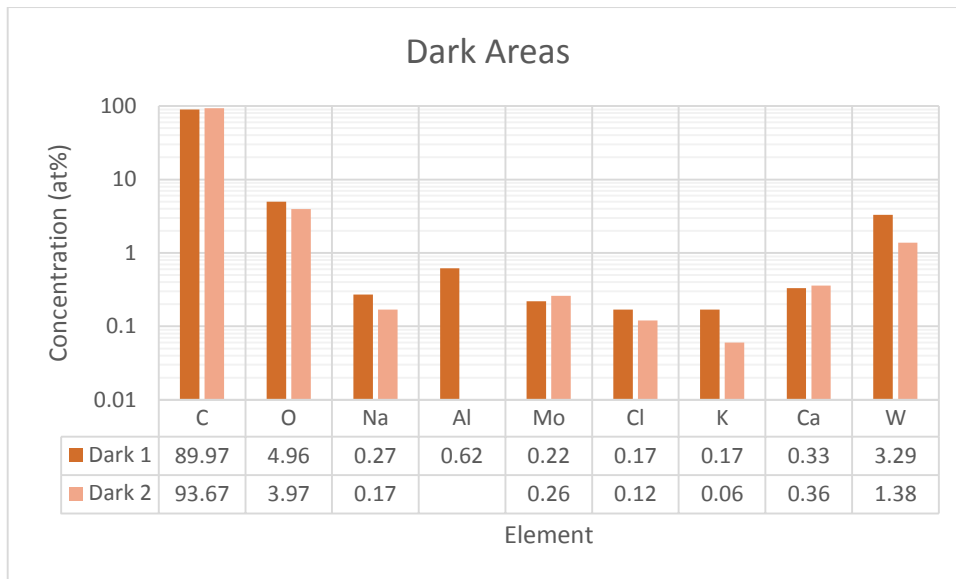


Figure 165: The quantification of the dark areas of ILW1 A23 7 shown in Figure 163.

Figure 162 shows the SE and BSE images of ILW1 A23 7 with different magnifications. Figure 163 shows the BSE image and areas selected for the quantitative measurements. The surface is rough and the micro-cracks are intense. Additionally, we observe that the deposition areas are inside the caves of the surface (Figure 162c and f). Figure 164 presents the quantification of the large and white areas. C, O and W are the only elements that were detected on both areas. The large areas present higher C ((52.04 – 63.62) at%) and O ((7.96 – 8.89) at%) concentration than white ones (40.14 at% and 5.9 at%, respectively) as include the dark ones. The quantitative results of darks areas are shown in Figure 165. The common elements are C, O, Na, Mo, Cl, K, Ca and W. Al was detected only on dark are 2. The two areas have similar elemental concentration. C has by far the highest concentration and only O and W have concentration higher than 1%.

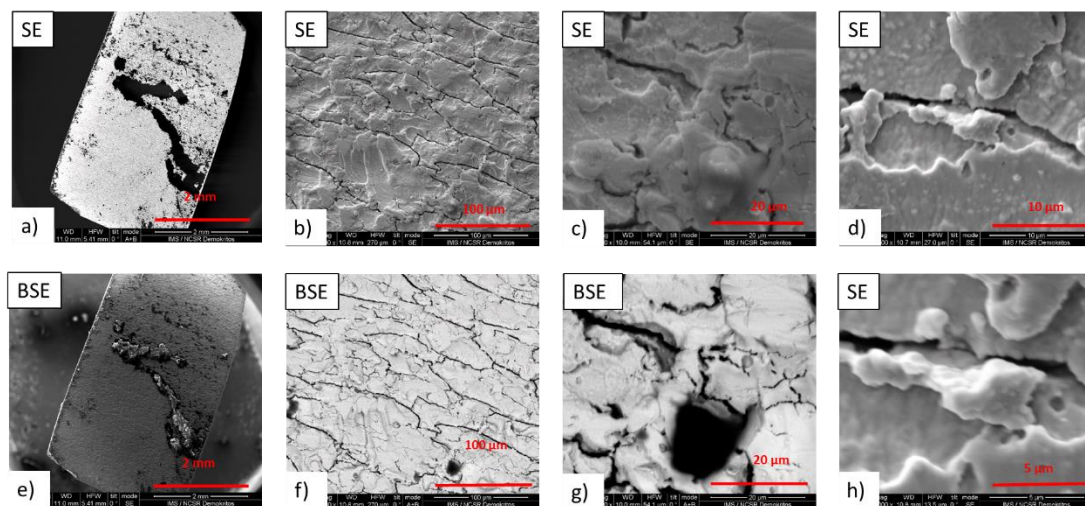


Figure 166: The SE and BSE images of the ILW1 C3 12 sample using different magnification.

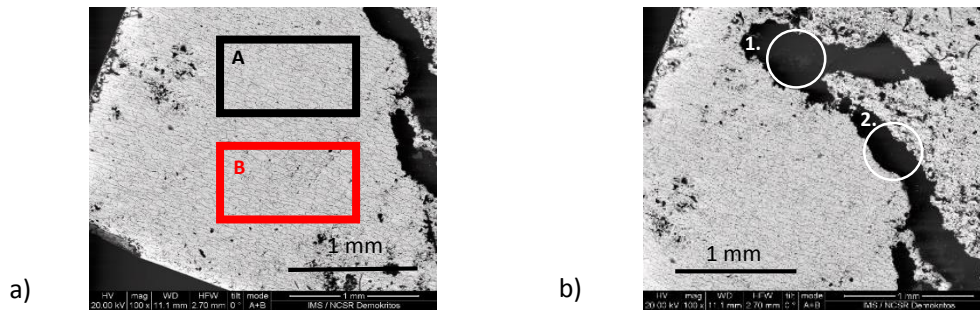


Figure 167: The BSE images and the a) large and b) dark areas of ILW1 C3 12.

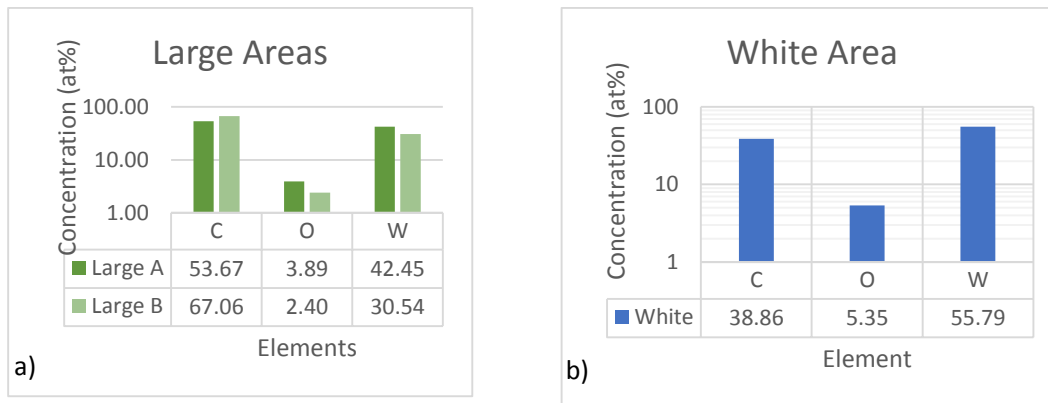


Figure 168: The quantification of a) large and b) white areas of ILW1 C3 12 shown in Figure 167.

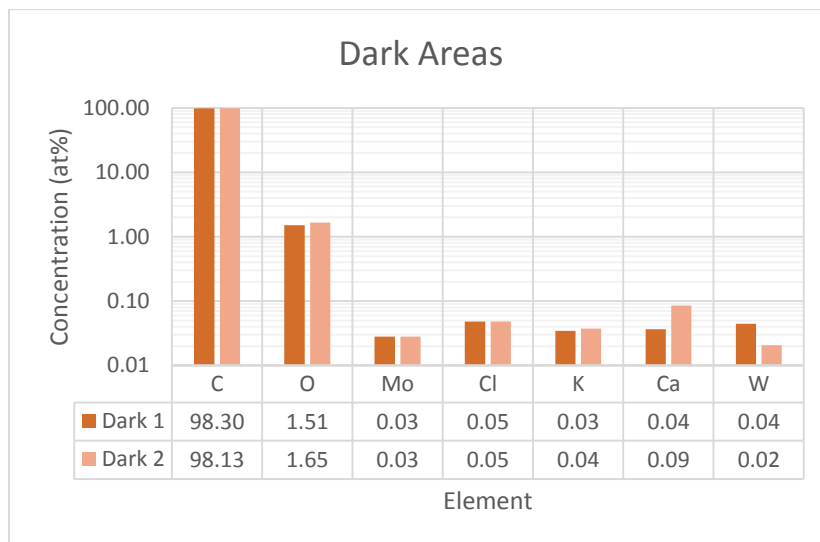


Figure 169: The quantification of dark areas of ILW1 C3 12 shown in Figure 167.

Figure 166 shows the BSE and SE images of ILW1 C3 12 with different magnification. Figure 167 shows the chosen areas for quantification in the BSE images. The cracks are intense and the surface rough. On the centre of the sample intensive carbon deposition is observed (Figure 166a and e), explaining the results of the NRA measurements (Table 11). The upper part of the sample have larger deposition areas than the bottom on (Figure 166a and e). The quantitative results of large and white areas are presented in Figure 168. C, O and W are the only elements

detected on large and white areas. The large areas have higher C concentration ((53.67 – 67.06) at%) than white one (38.28 at%) due to the dark areas. Figure 169 shows the quantification of the large dark areas (Figure 167b). Both of them consist of C ((98.13 – 98.30) at%) with low O ((1.51 – 1.65) at%) concentration and impurities of Mo, Cl, K, Ca and W.

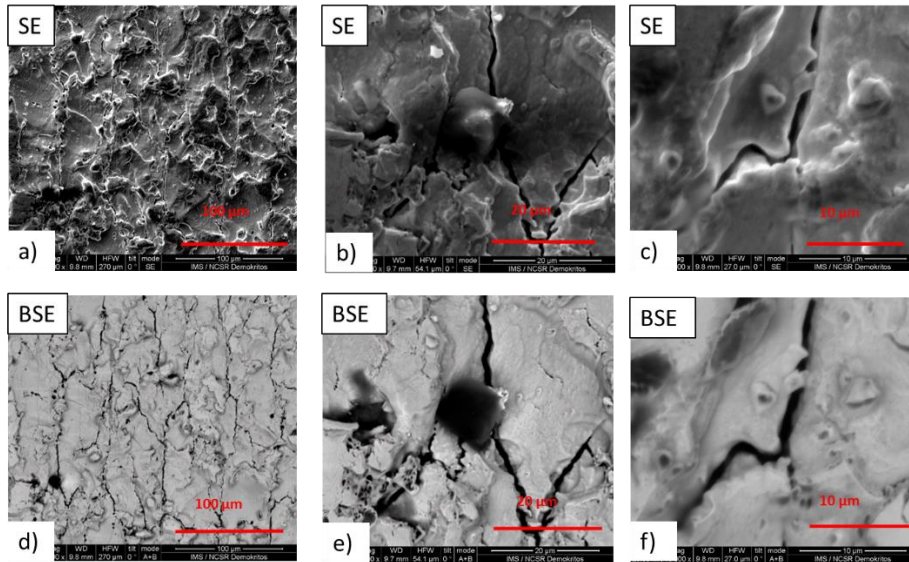


Figure 170: The SE and BSE images of the ILW1 C14 15 sample using different magnification.

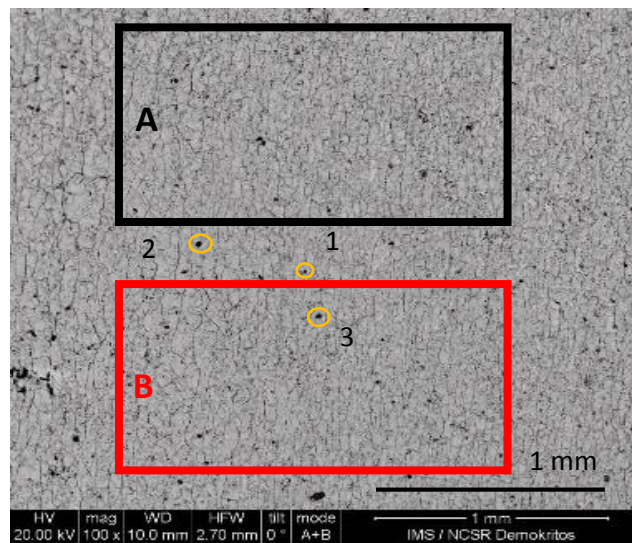


Figure 171: BSE image and quantified areas of ILW1 C14 15.

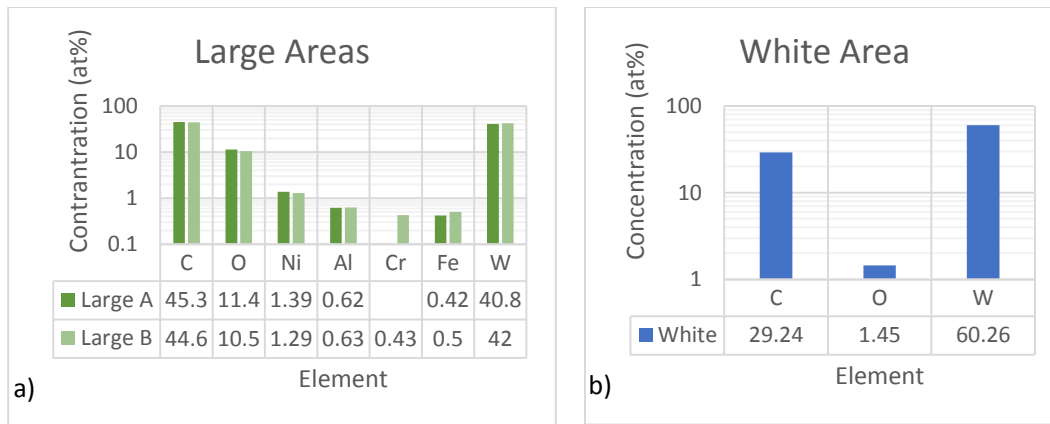


Figure 172: The quantification of a) large and b) white areas of ILW1 C14 15 shown in Figure 171.

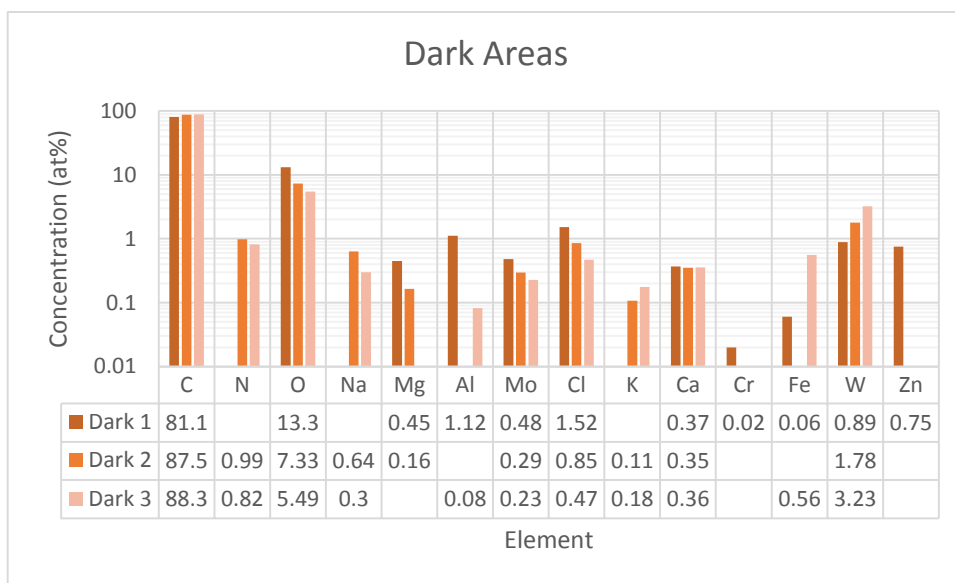


Figure 173: The quantification of dark areas of ILW1 C14 15 shown in Figure 171.

Figure 170 shows the SE and BSE images of ILW1 C14 15 with different magnifications. Figure 171 presents the BSE image and the quantified areas. The cracks and morphology are similar to the reference sample. The deposition spots prefers the flat areas surrounded by the bumps. The quantification of large and white areas is presented in Figure 172. The common elements of both areas are C, O and W. Only on large areas (Figure 172a) Ni, Al, Cr and Fe were also detected. Their concentration are close (Ni) or less (Al, Cr and Fe) than 1 at%. Figure 173 presents the quantitative results of dark areas. C, O, Mo, Cl, Ca and W were detected on all areas. N, Na, Mg, Al, K and Fe were detected on two of them, while Cr and Zn were detected only on Dark area 3. C has by far the higher concentration. O has also high concentration. For the rest elements the concentration is near 1 at% or lower.

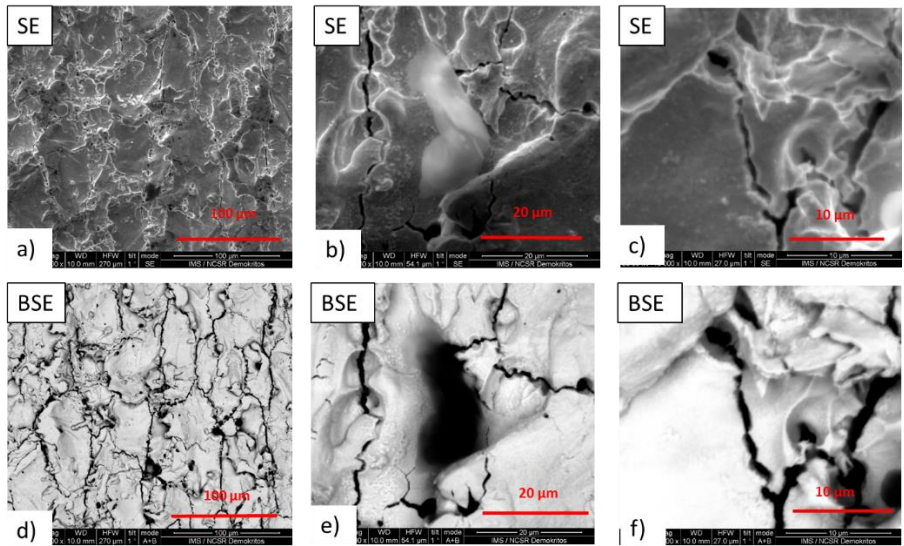


Figure 174: The SE and BSE images of the ILW2 A23 48 sample using different magnifications.

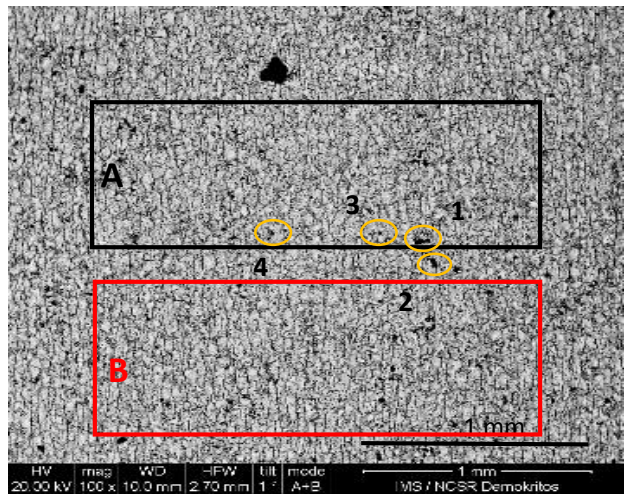


Figure 175: BSE image and quantified areas of ILW2 A23 48.

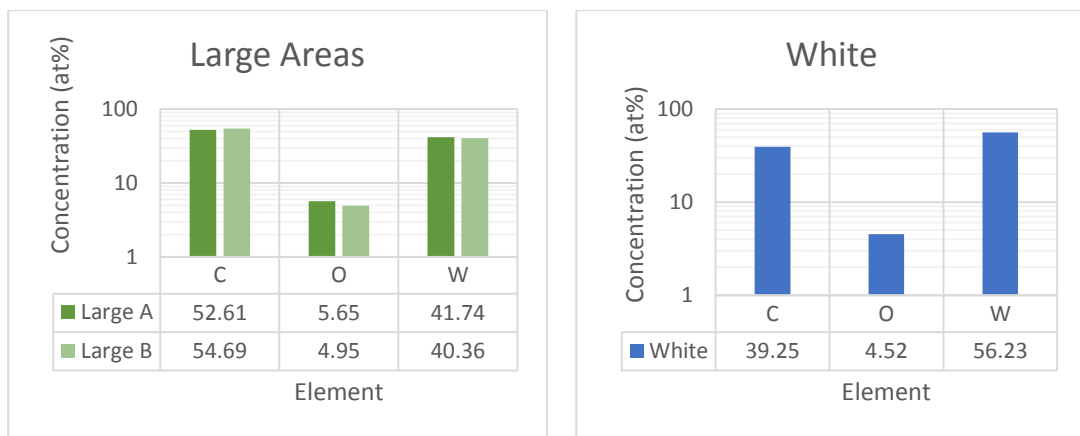


Figure 176: The quantification of a) large and b) white areas of ILW2 A23 48 shows in Figure 175.

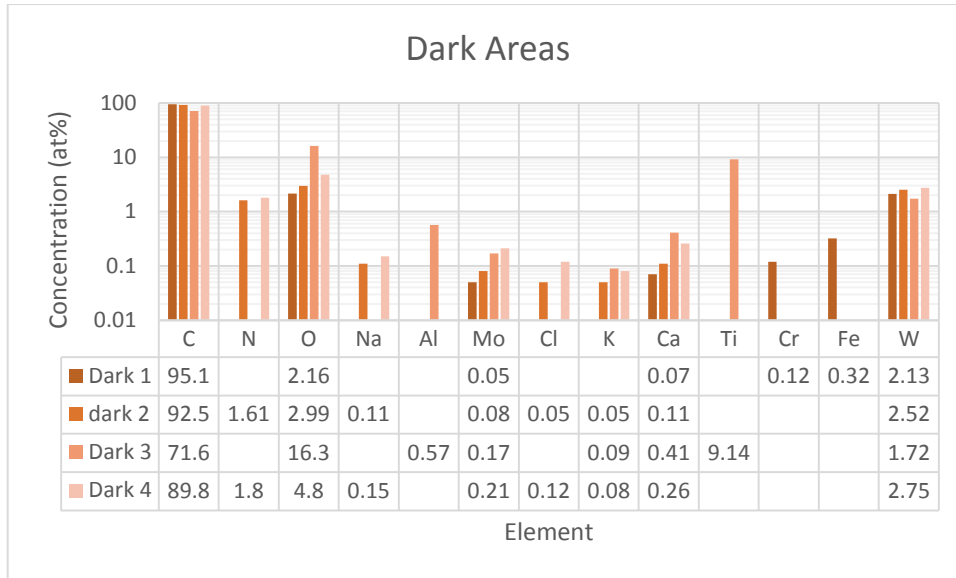


Figure 177: The quantification of dark areas of ILW2 A23 48 shown in Figure 175.

Figure 174 shows the SE and BSE images of ILW2 A23 48 with different magnifications. Depositions near to surface edges are observed (Figure 174b and e). Figure 175 presents the quantified areas on the BSE image. The cracks are intense and the surface rough. The deposited elements accumulate near the surface bumps. Figure 176 presents the quantification of large and white areas defined in Figure 175. The only detected elements are C, O and W. The large areas have more C and O due to dark areas contribution. The quantitative results of dark areas are shown in Figure 177. C, O, Mo, Ca and W were detected on all areas. K was detected on three of them with very low concentration ((0.05 – 0.08) at%). N, Na and Cl were detected on two of them (Dark 2 and Dark 4). Al and Ti were detected only on Dark 3 and Cr and Fe only Dark 1. Generally, Dark 1 has the highest C concentration (95.1 at%) and is the only area with Cr (0.12 at%) and Fe (0.32 at%). Dark 2 and 4 are similar. On the other hand Dark 3 is unique as high Ti (9.14 at%) and O (16.3 at%) concentration was detected.

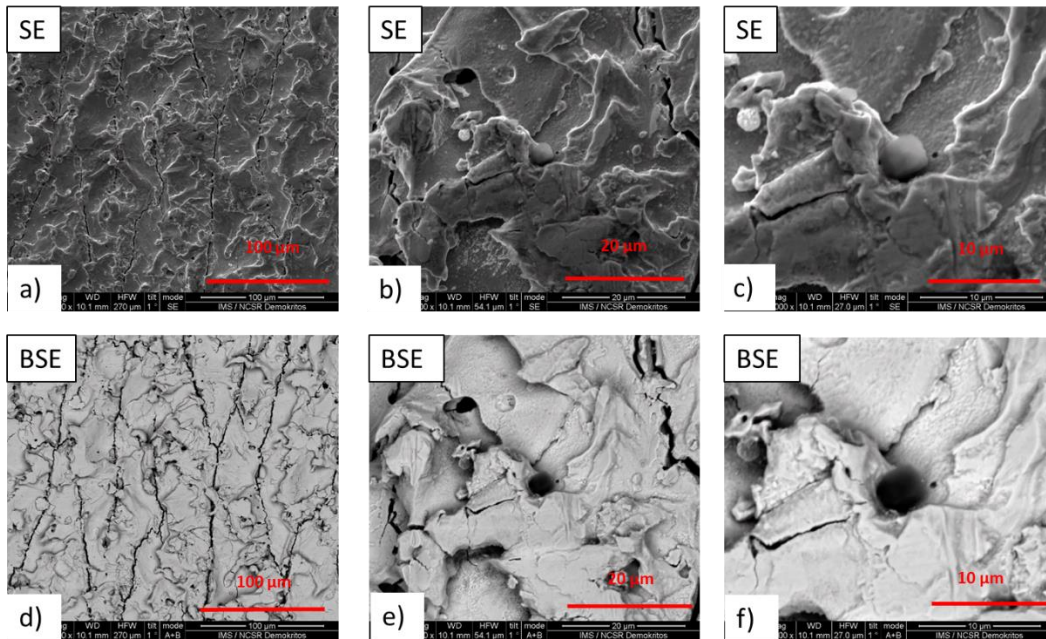


Figure 178: The SE and BSE images of the ILW2 A23 51 using different magnifications.

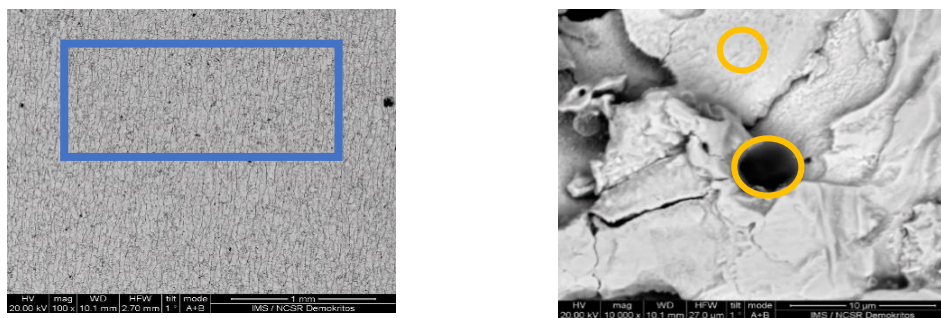


Figure 179: BSE images and a) large, b) white and dark areas of ILW2 A23 51.

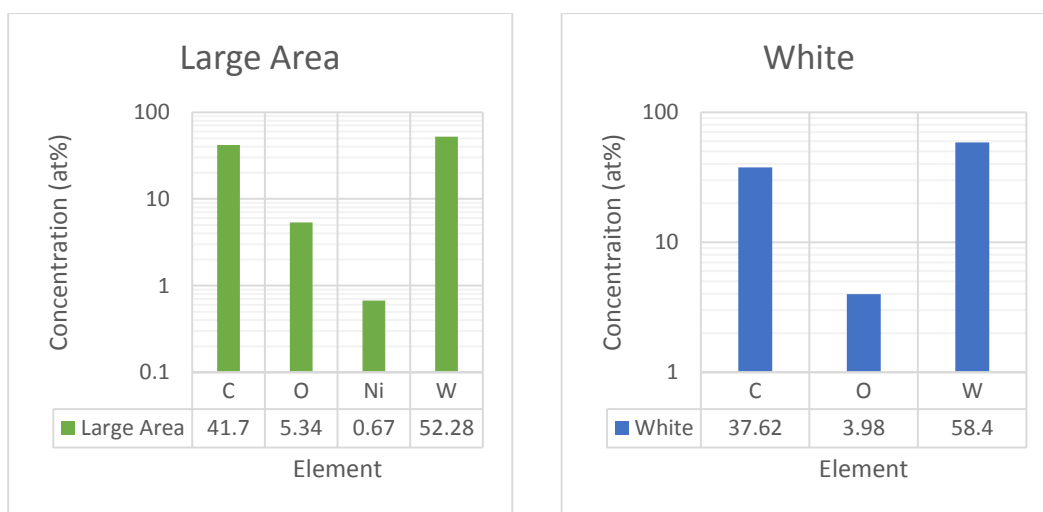


Figure 180: The quantification of large and white areas of ILW2 A23 51 shown in Figure 179.

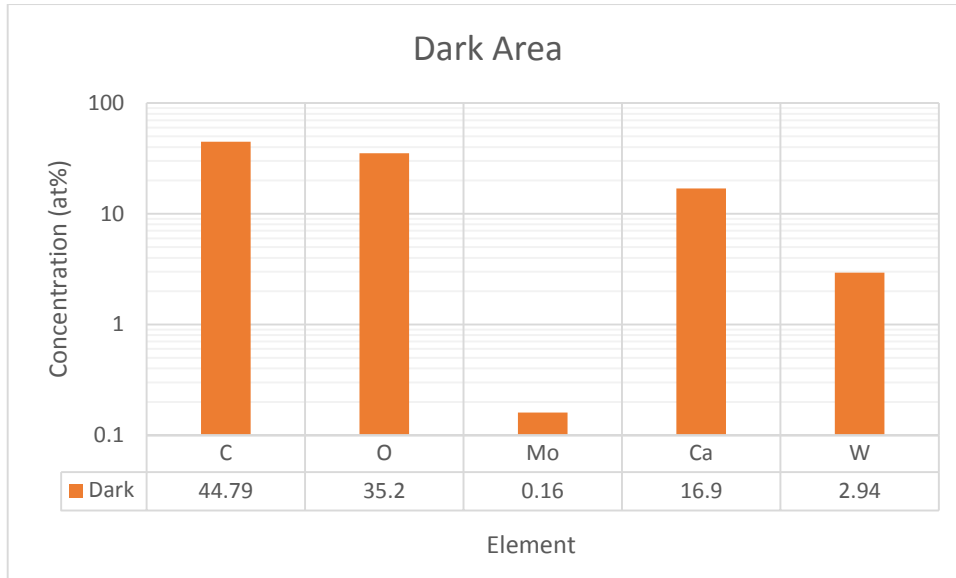


Figure 181: The quantification of dark area of ILW2 A23 51 shown in Figure 179.

Figure 178 shows the SE and BSE images of ILW2 A23 51 with different magnifications. The deposition is near the edges of the surface (Figure 178b and e). Figure 179 present the large, white and dark areas on the BSE image where the elemental quantification was performed. We observe that the deposition areas accumulate near the bumps. The cracks and morphology are similar to this of the reference sample. The quantitative results of the large and the white areas are shown in Figure 180. The C, O and W were detected on large and white areas, while on large area Ni (0.67 at%) was also detected. On large area the C (41.7 at%) and O (5.34 et%) concentration is higher than on white one (37.62 at% and 3.98 at%, respectively). Figure 181 presents the quantification of dark area. C, O, Mo, Ca and W are observed. C (44.76 at%) and O (35.2 at%) have the highest concentration, while high Ca concentration (16.9 at%) was also detected.

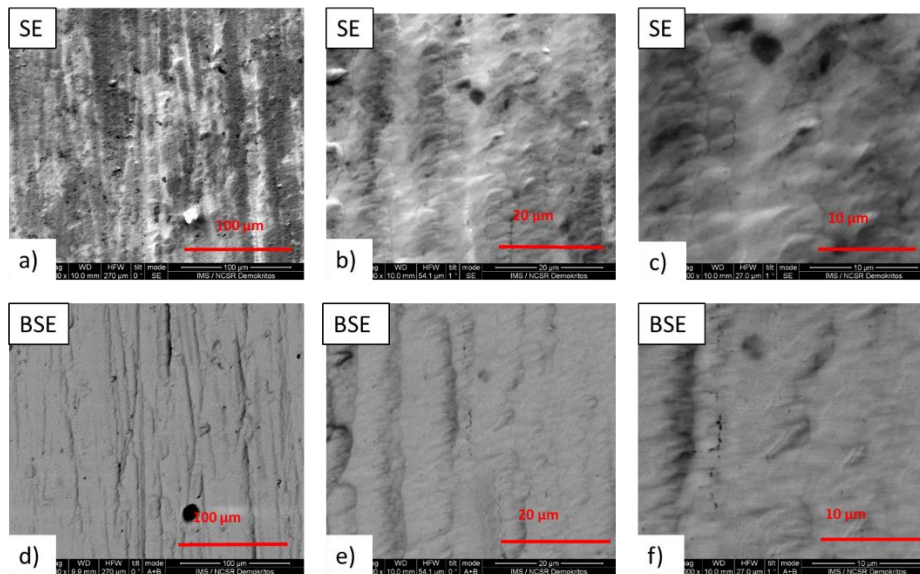


Figure 182: The SE and BSE images of the ILW2 C13 61 using different magnification.

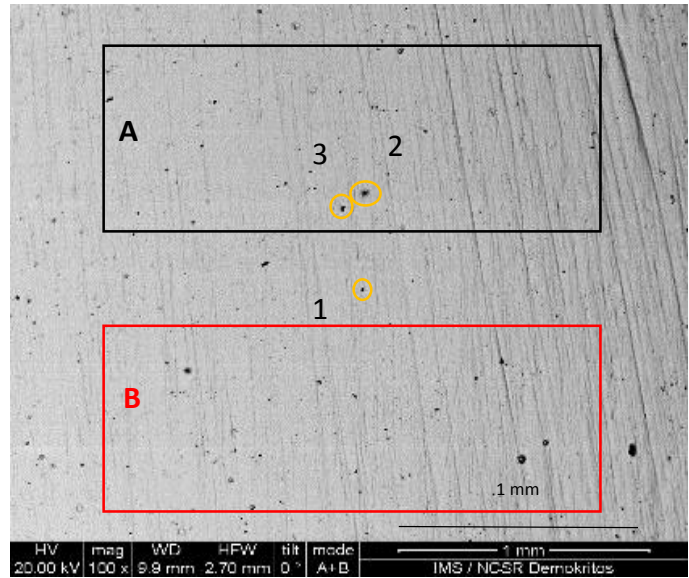


Figure 183: BSE image and quantified areas of ILW2 C13 61.

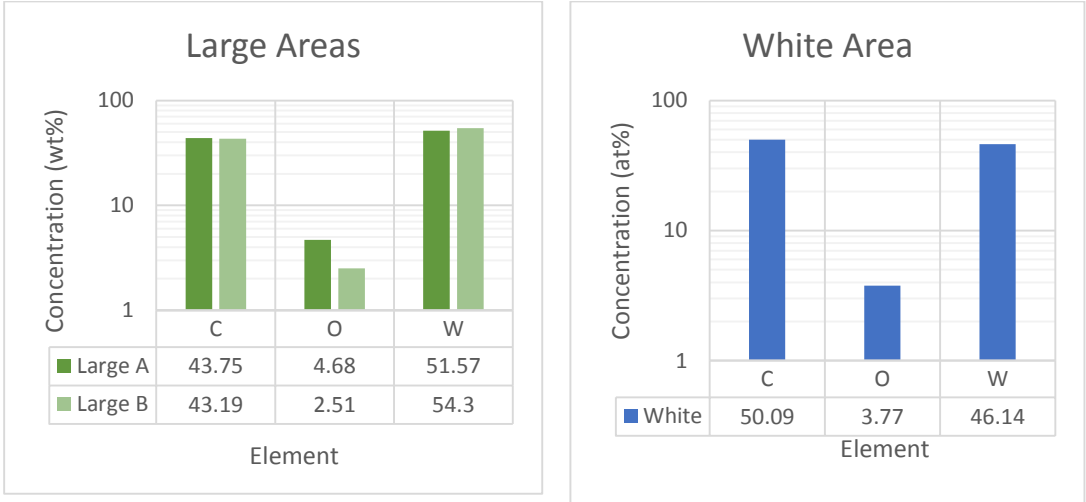


Figure 184: The quantification of a) large and b) white areas of ILW2 C13 61 shown in Figure 183.

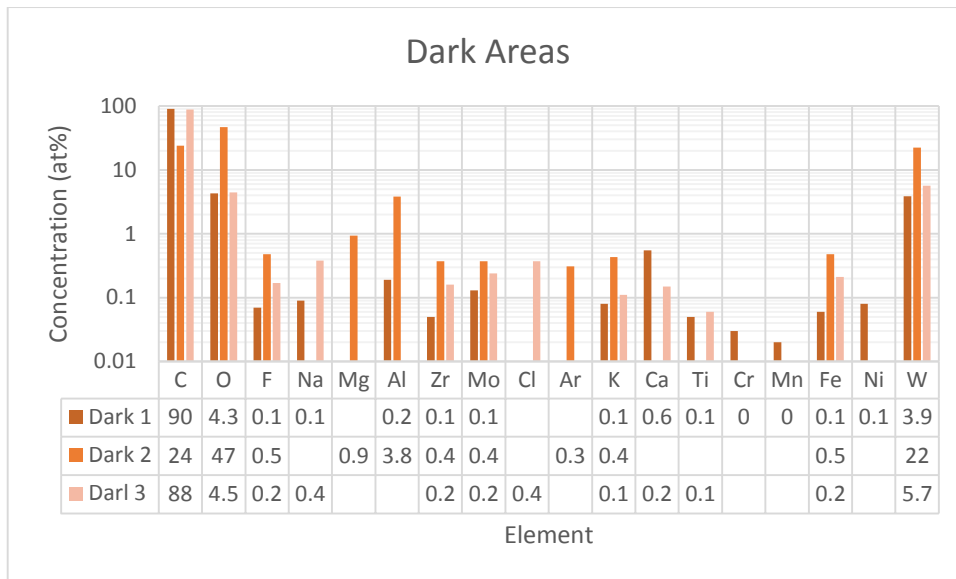


Figure 185: The quantification of dark areas of ILW2 C13 61 shown in Figure 183.

Figure 182 shows the SE and BSE images of ILW2 C13 61 with different magnifications. The surface seems quite clear with rare and small deposition areas. Figure 183 presents the quantified areas on the BSE image. The surface is smooth and there are on initial cracks. The quantification of large and white areas is presented in Figure 184. C, O and W were detected on large and white areas. It is remarkable that on white area we observe less W (46.14 at%) than on large areas ((51.57 – 54.3) at%). Figure 185 shows the quantitative results of dark areas defined in Figure 183. C, O, F, Zr, Mo, K, Fe and W were detected on all areas. Na, Al, Ca and Ti were detected on two of them, while Mg Cl, Ar, Cr, Mn and Ni were observed on only one. Dark areas 1 and 3 have similar concentration of the most of the element with very high C concentration ((88 – 90) at%). On the other hand O is the dominant element (47 at%) of Dark area 2, while F, Zr Mo, K, Fe and W have higher concentration than the other areas. Additionally, Mg and Ar were detected only on this area.

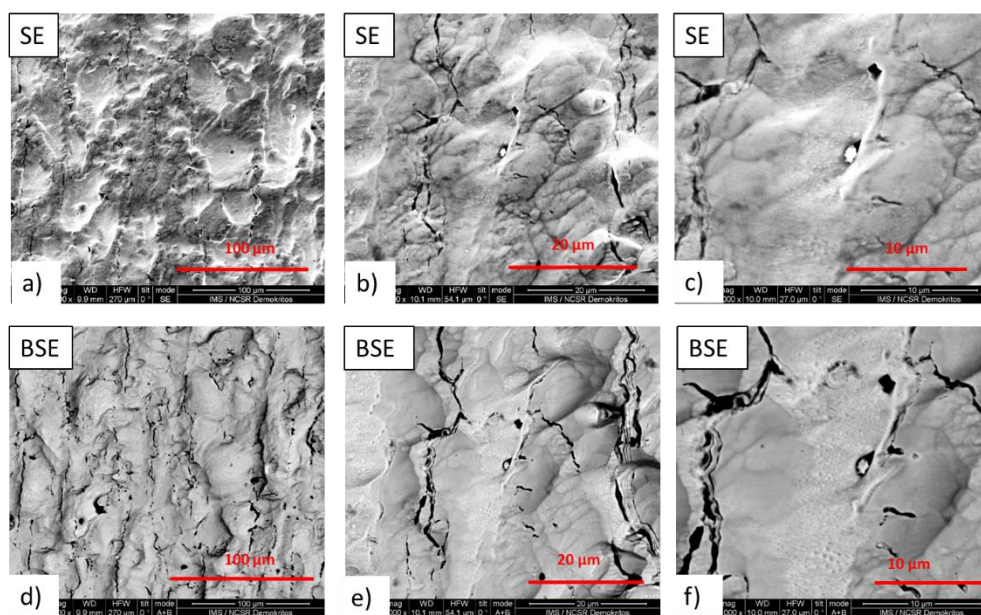


Figure 186: The SE and BSE images of the ILW2 C14 63 using different magnifications.

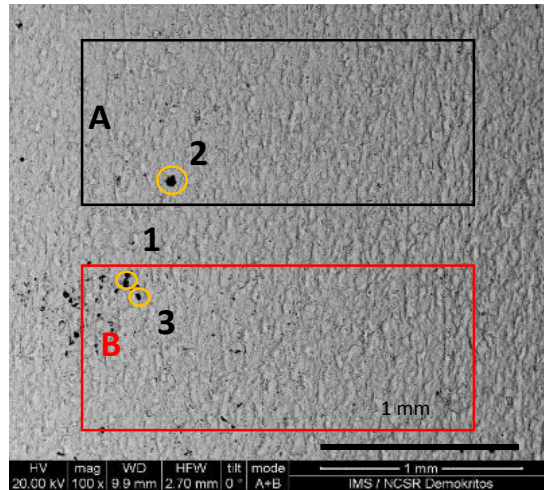


Figure 187: BSE image and the quantified areas of the ILW2 C14 63

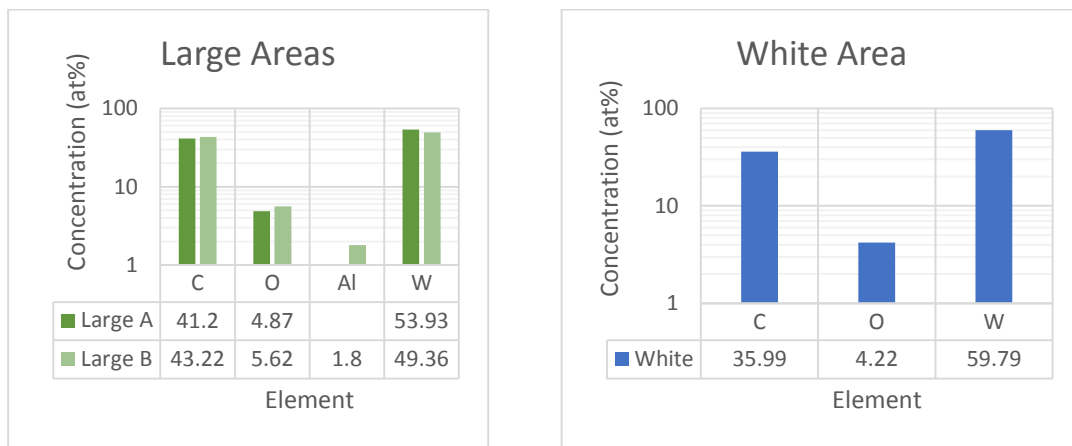


Figure 188: The quantification of large areas of the ILW2 C14 63 shown in Figure 187.

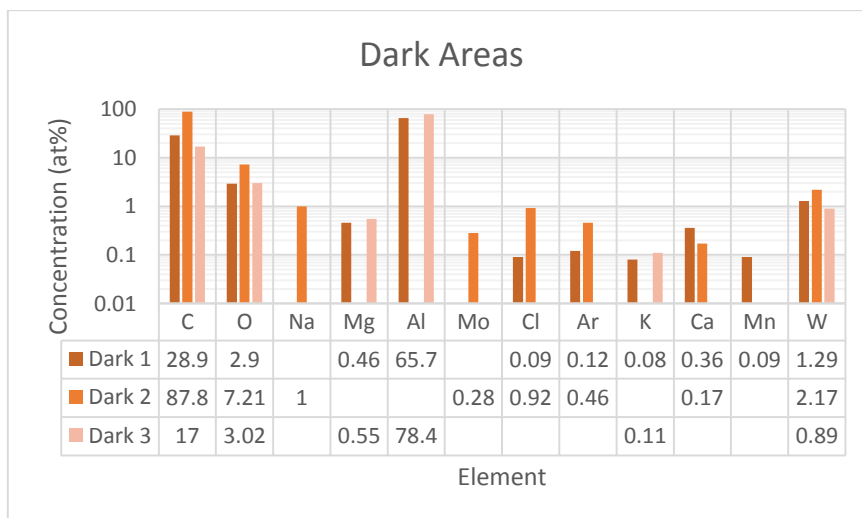


Figure 189: The quantification of dark areas of the ILW2 C14 63 shown in Figure 187.

Figure 186 shows the SE and BSE images of ILW2 C14 63 with different magnifications. Figure 187 presents the BES image and the quantified places. The surface is smoother than that of the reference sample and the micro-cracks have been partially covered with surface material. The deposition areas are concentrated in a small area (down left Figure 187), while the rest surface seems quite clean. The common elements between large (Figure 188a) and white areas (Figure 188b) are C, O and W, while Al (1.8 at%) was detected on one large area. The large areas have similar elemental concentrations with higher C ((41.2 – 43.22) at%) and O ((4.87 – 5.62) at%) concentration than white one due (35.99 at% and 4.22 at%, respectively) to the deposition areas. Figure 189 presents the quantification of the dark areas. C, O, Al and W are observed on all areas. Mg, Cl, Ar, K and Ca were detected on two of them, while Na, Mo and Mn were detected on one area. It is remarkable that Al is the dominant element on two areas (dark 1 and 3) (65.7 at% and 78.4 at%, respectively), while C is the dominant (87.8 at%) on the third one (dark 2). Dark 1 and 3 have similar concentrations of the common elements.

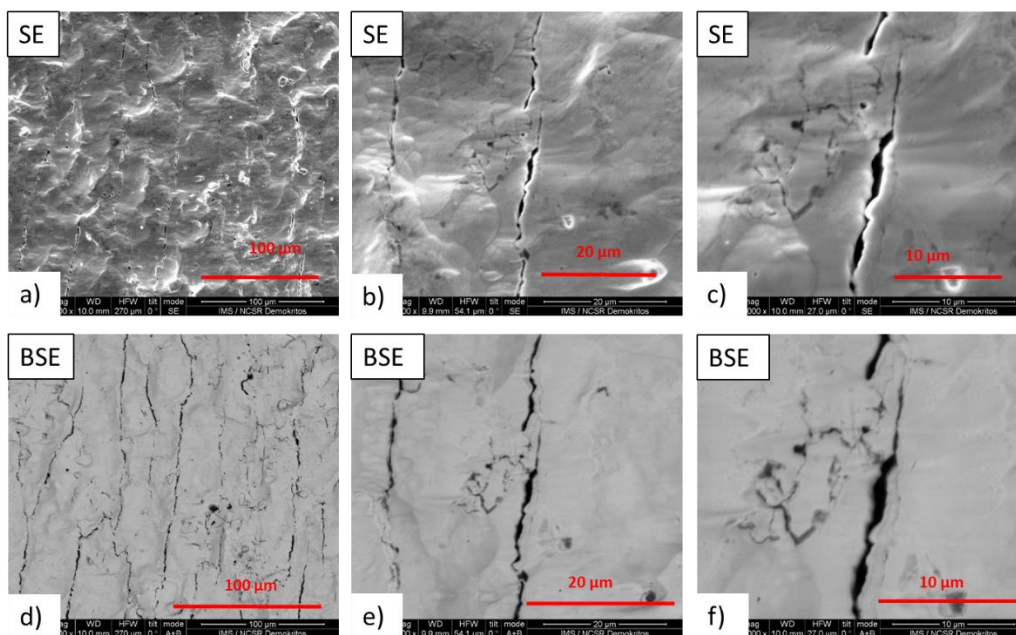


Figure 190: The SE and BSE images of the ILW2 C14 67 using different magnifications.

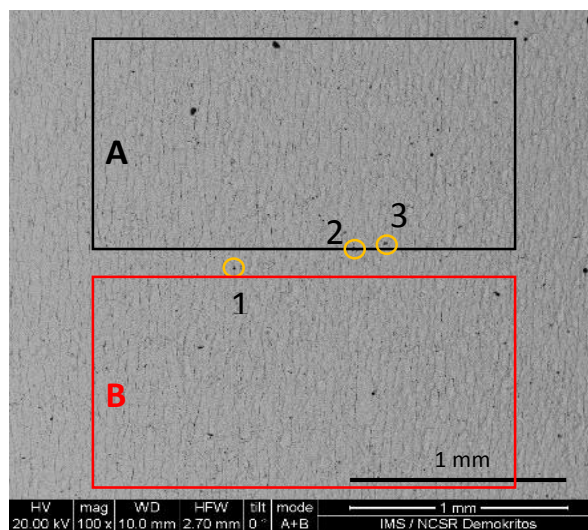


Figure 191: BSE image and quantified areas of the ILW2 C14 67.

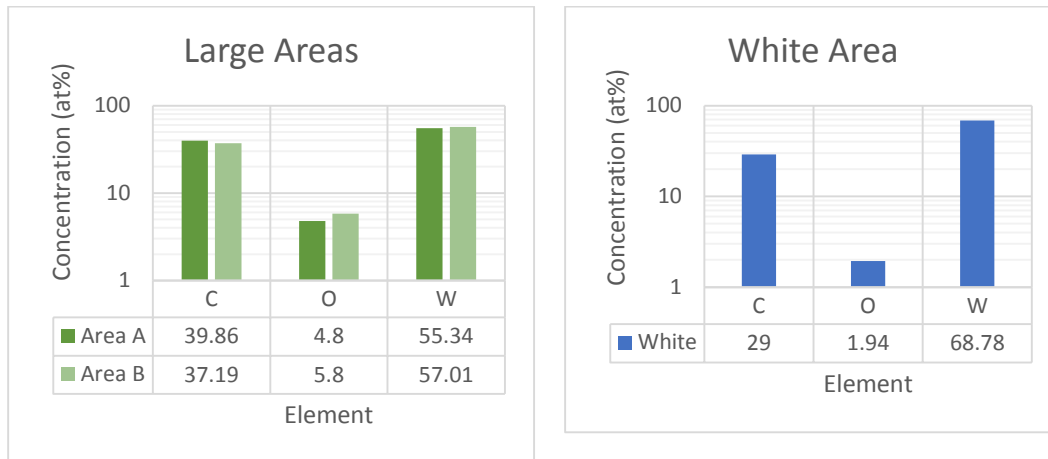


Figure 192: The quantification of large and white areas of the ILW2 C14 67 shown in Figure 191.

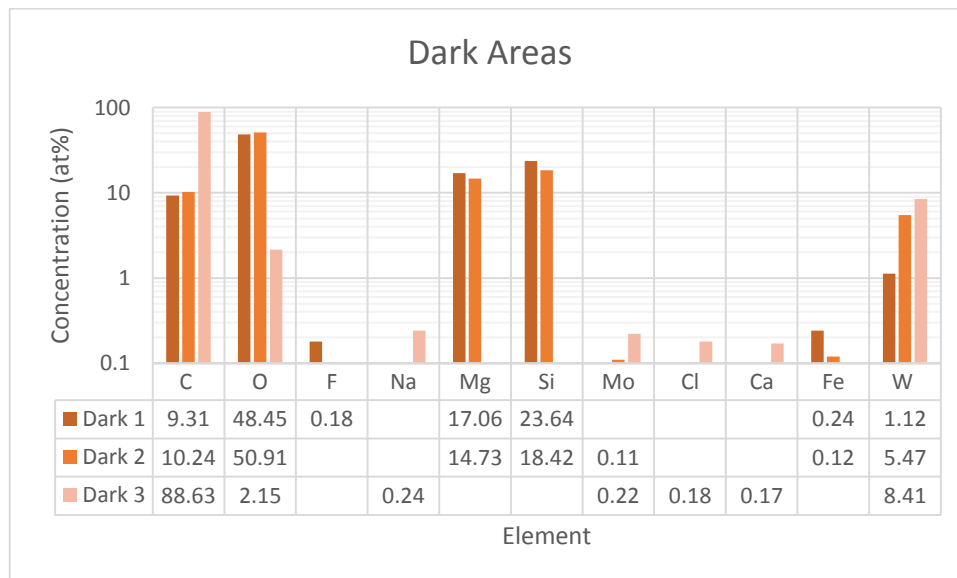


Figure 193: The quantification of dark areas of the ILW2 C14 67 in Figure 191.

Figure 190 shows the SE and BSE images of ILW C14 67 with different magnifications. Figure 191 presents the BSE image and the quantified areas. The surface is smooth and the micro-cracks have been partially covered by surface material. The surface looks quite clean with some small deposition spots. Figure 192 presents the large and white areas. C, O and W were detected on large and white areas. The C ((37.19 – 39.86 at%) and O (4.8 – 5.8 at%) concentration is higher on large areas than on white one (29 at% and 1.94 at% respectively) due to the deposition spots. Figure 193 shows the quantitative results of the dark areas. C, O and W are the only elements detected on all areas. Dark 1 and 2 have similar composition, where O is the dominant element (50.91 at% and 48.45 at%, respectively), while high concentration of Mg (17.06 at% and 14.73 at%, respectively), Si (23.64 at% and 18.42 at%, respectively) and C (9.31 at% and 10.24 at%, respectively) were detected. On the dark 3 the C has by far the highest concentration (88.63 at%).

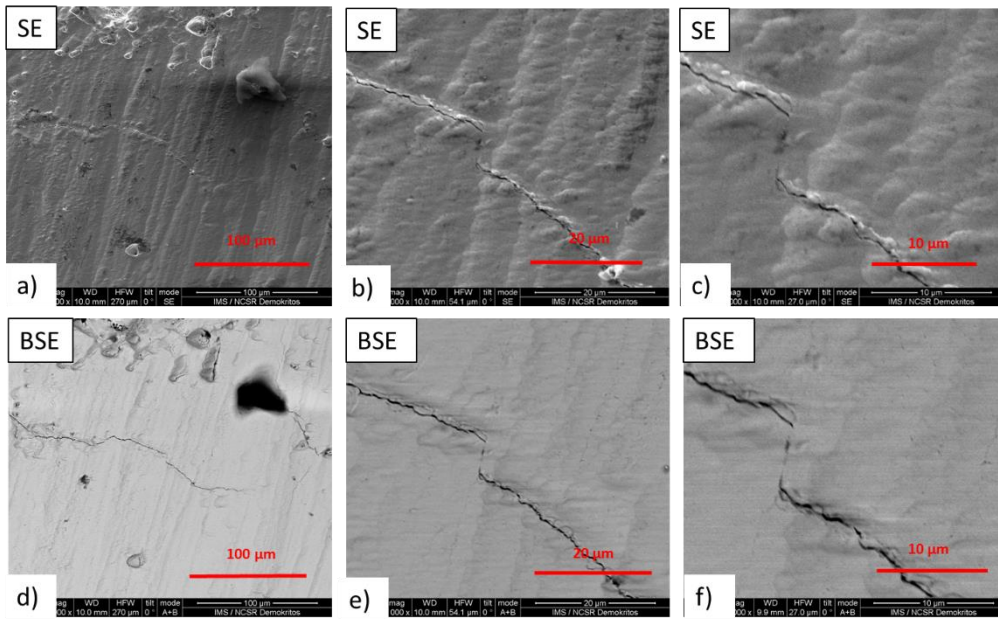


Figure 194: The SE and BSE images of the ILW2 C22 70 using different magnifications.

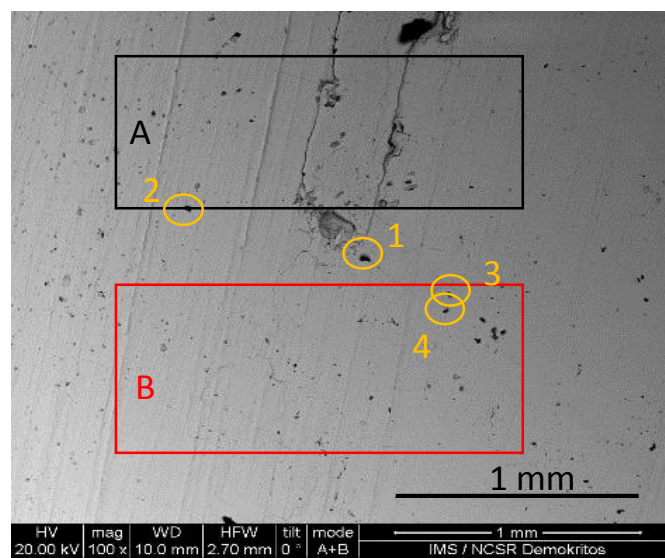


Figure 195: BSE image and quantified areas of the ILW2 C22 70.

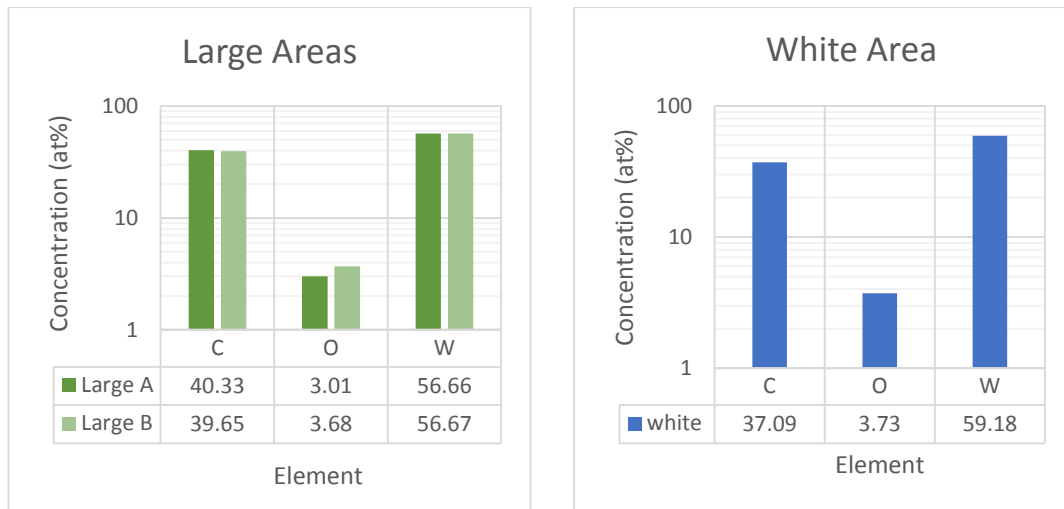


Figure 196: The quantification of a) large and b) white areas of the ILW2 C22 70 shown in Figure 194.

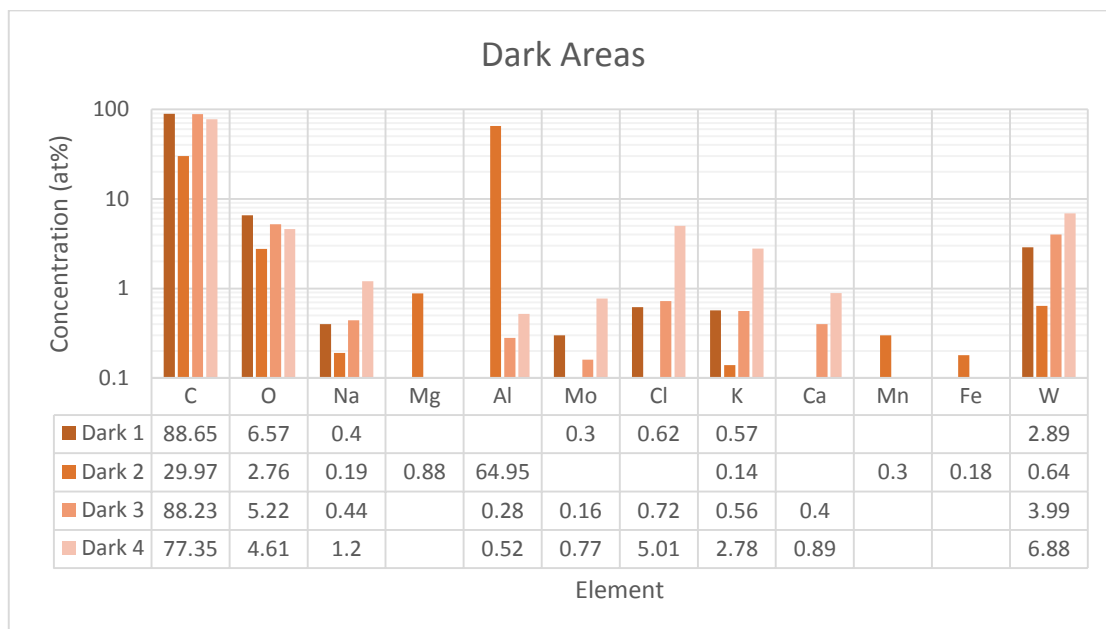


Figure 197: The quantification of dark areas of ILW2 C22 70 in Figure 194.

Figure 194 shows the SE and BSE images of ILW2 C22 70 with different magnifications. Figure 195 presents the BSE image and the quantified areas. The surface is smooth and only few micro-cracks are observed. Moreover the surface is clean with only some small deposition areas. Figure 196 presents the quantification of the large and white areas. The detected elements on these areas are C, O and W. Large and white areas have similar composition which means that the deposition spots are too small to change the elemental concentration of the large areas. The quantitative results of the dark areas are presented in Figure 197. C, O, Na, K and W were detected on all areas. On Dark 1 and 3 the concentrations of the common elements have similar values and C has by far the highest concentration (88.65 at% and 88.23 at%, respectively). On Dark 2 the dominant element is Al (64.95 at%). Mg (0.88 at%), Mn (0.3 at%) and Fe (0.18 at%) were detected only on this area. On dark 4 the highest Na (1.2 at%), Cl (5.01 at%), K (2.78 at%), Ca (0.89 at%) and W (6.88 at%) concentrations are observed.

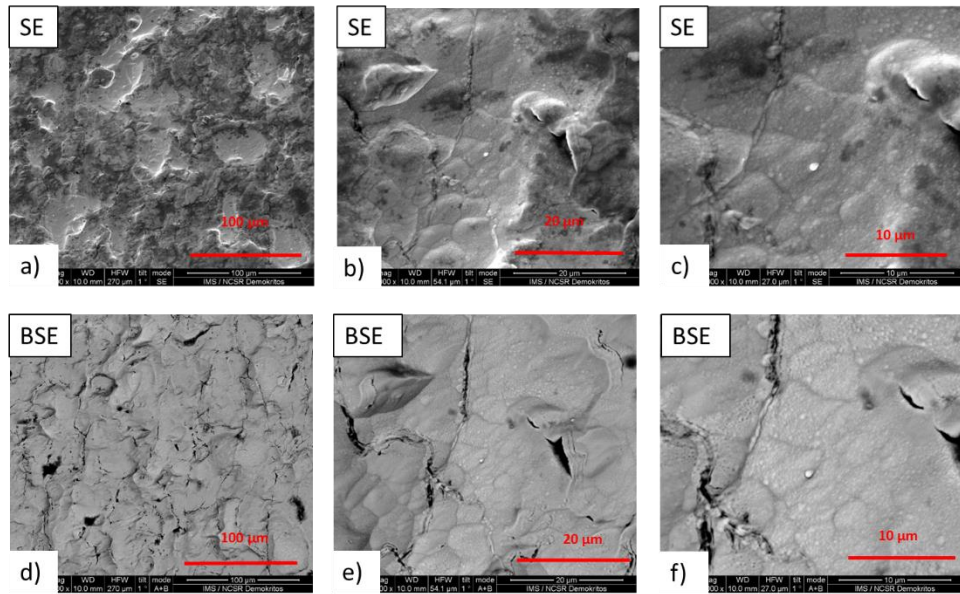


Figure 198: The SE and BSE images of the ILW2 C23 72 using different magnifications.

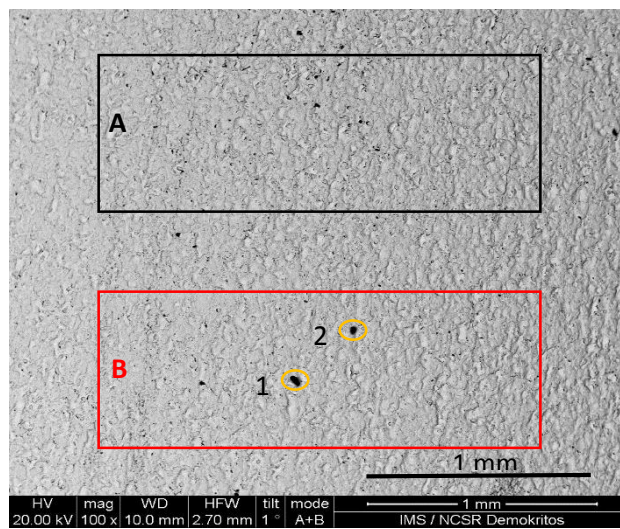


Figure 199: BSE image and quantified areas of ILW2 C23 72.

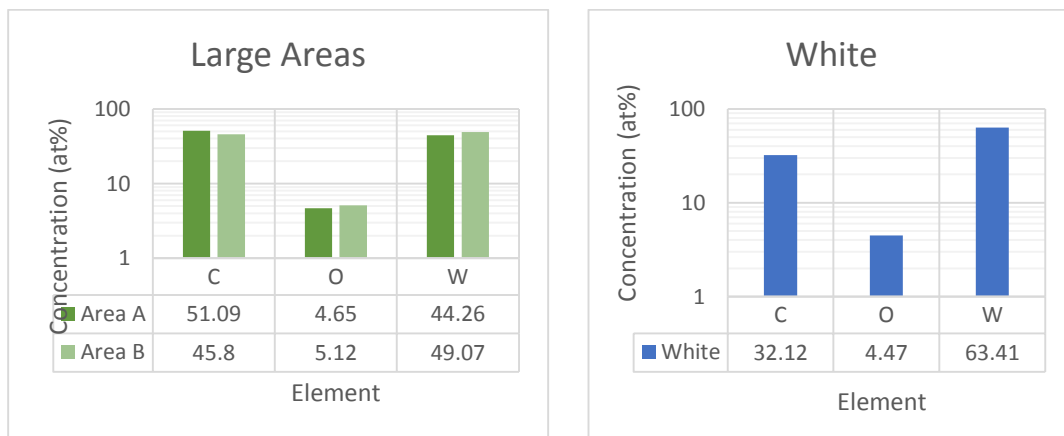


Figure 200: The quantification of large areas of the ILW2 C23 72 shown in Figure 199.

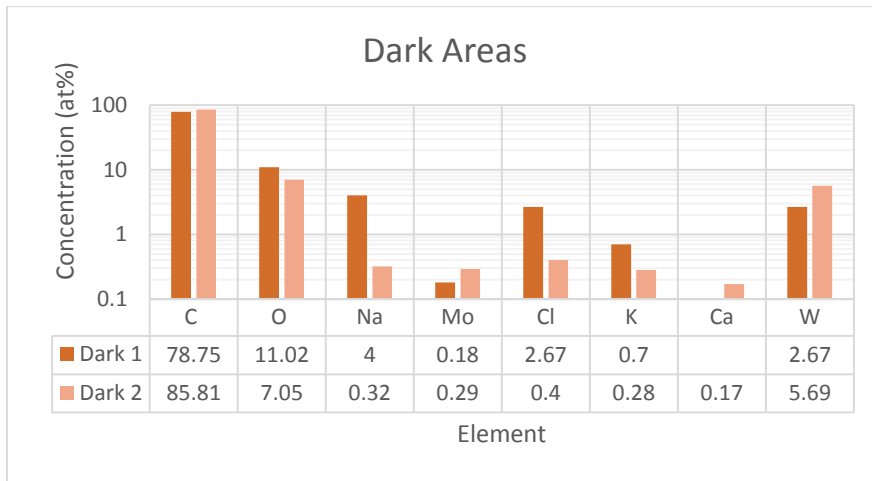


Figure 201: The quantification of dark areas of the ILW2 C23 72 in Figure 199.

Figure 198 shows the BSE and SE images of ILW2 C23 72 with different magnifications. Figure 199 presents the BSE image and the quantified areas. The surface of the samples looks quite smooth and the micro-cracks have almost been covered. Additionally, it looks very clear with only few deposition spots. Figure 200 presents the quantification of large and white areas. C, O and W were the only elements detected on these areas. The large areas have higher C ((45.8 – 51.09) at%) and O ((4.65 – 5.12) at%) concentration than the white one (32.12 at% and 4.47 at%, respectively) due to the deposition spots. The quantitative results of the dark areas are presented in Figure 201. C, O, Na, Mo, Cl, K and W were detected on both areas, while Ca (0.17 at%) was detected only on the second area. Dark area 1 has more O (11.02 at%), Na (4 at%), Cl (2.67 at%) and K (0.7 at%) than the other one.

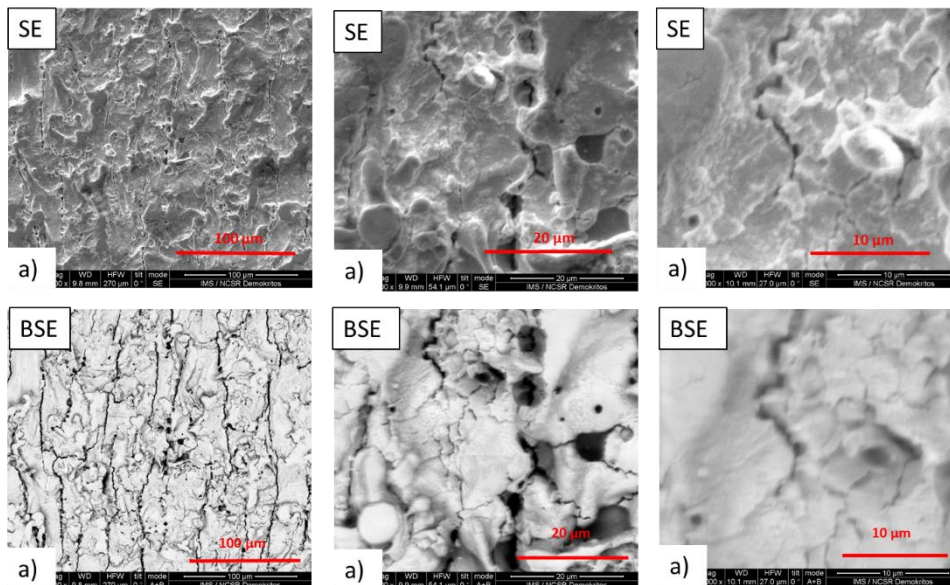


Figure 202: The SE and BSE images of the ILW3 A23 93 using different magnifications.

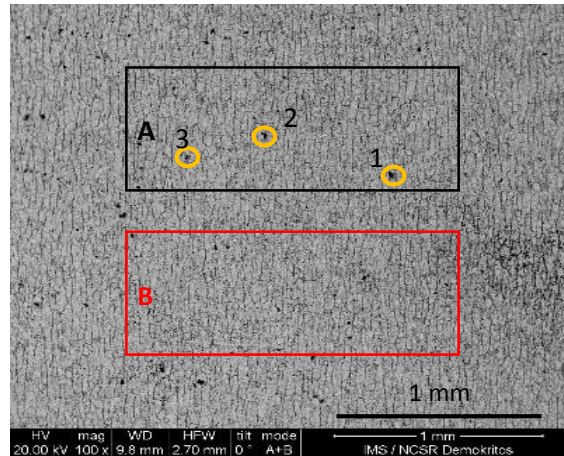


Figure 203: BS image and quantified areas of the ILW3 A23 93.

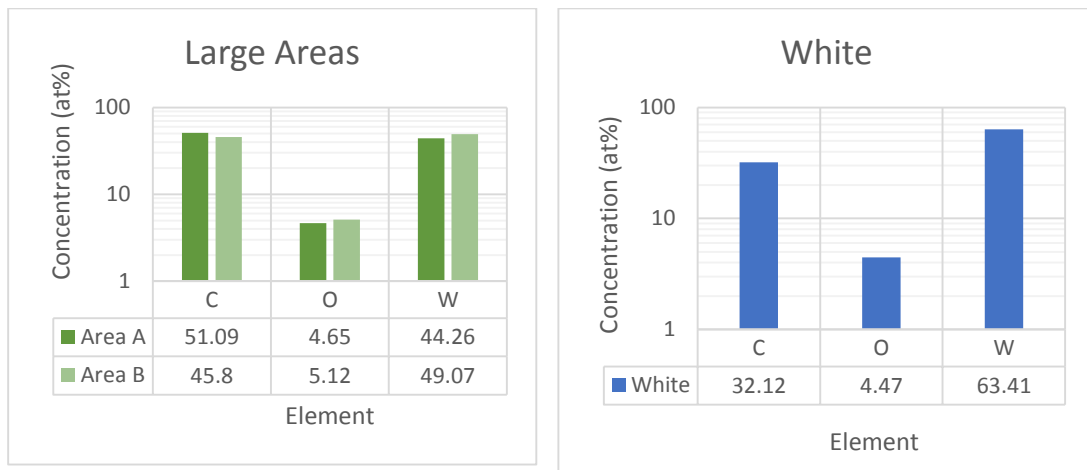


Figure 204: The quantitative analysis of large areas of the ILW3 A23 93 shown in Figure 203.

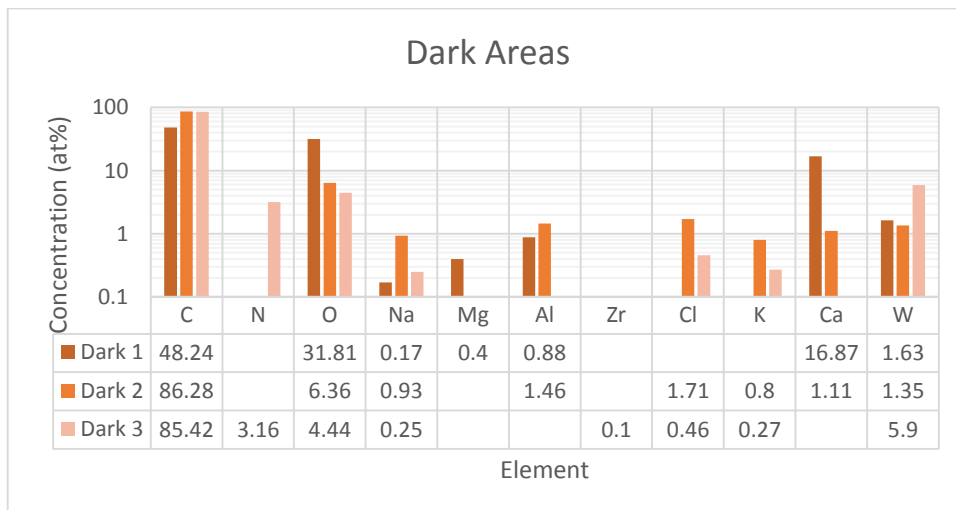


Figure 205: The quantitative analysis of dark areas of the ILW3 A23 93 shown in Figure 203.

Figure 202 shows the SE and BSE images of ILW2 A23 with different magnification. Figure 203 presents the BSE image and the quantified areas. The surface is rough and the micro-cracks are distinguishable. Deposition spots are observed throughout the surface. Figure 204 presents the quantification of the large and the white areas. The quantitative results of the dark areas are presented in Figure 205. C, O, Na and W were detected on all areas. Al, Cl, K, and Ca on two of them. N and Zr were detected only on dark area 3 and Mg only on dark area 1. Dark area 1 has lower C (48.24 at%) than the other two ((85.42 – 86.28) at%) but it has high O (31.81 at%) and Ca (16.87 at%) concentration. On the other hand, on dark areas 1 and 2 the C has by far the highest concentration.

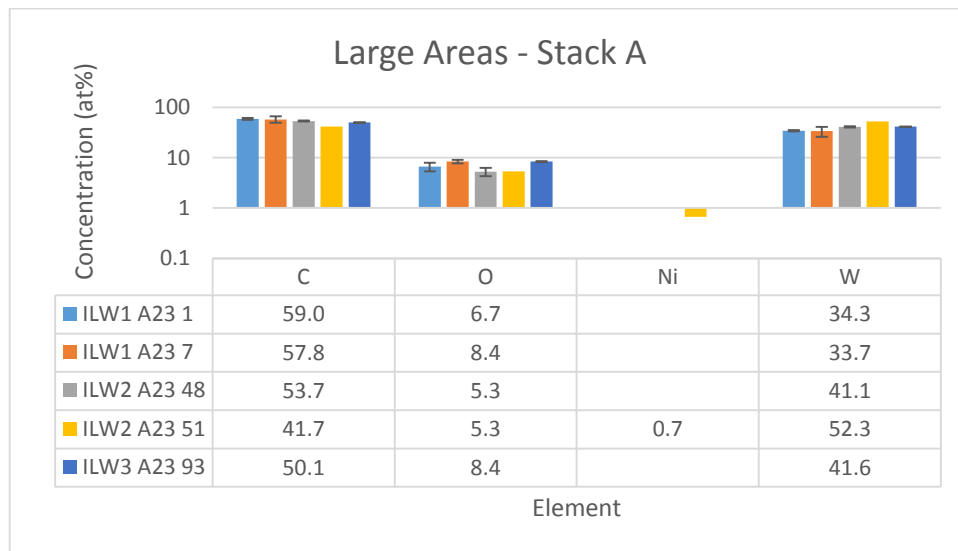


Figure 206: The average of the large areas of Stack A

Figure 206 shows the average quantitative results of the large areas from the samples of Stack A. C, O and W were detected on all samples, while Ni was detected only on ILW2 A23 51. This sample has also the lowest C (41.7 at%) and O (along with ILW A23 48) (5.3 at%) concentration. The C concentration of the rest samples ranges between 50.1 at% (ILW3 A23 93) and 59 at% (ILW1 A23 1). ILW A23 7 and ILW3 A23 93 have the highest O concentration (8.4 at%).

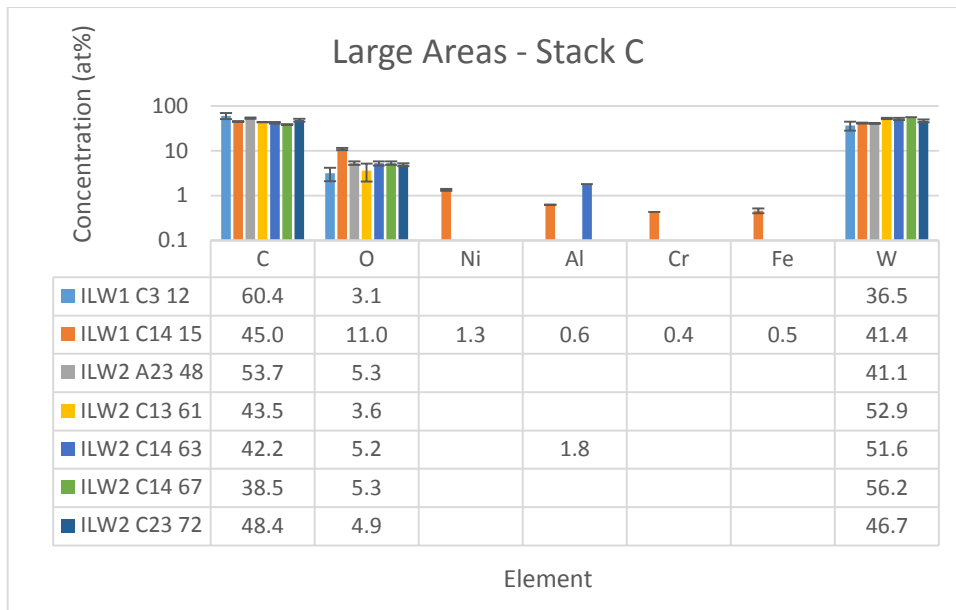


Figure 207: The average of the large areas of Stack C

Figure 207 presents the average quantitative results of the large areas of samples from Stack C. C, O and W were detected on all samples. Al was detected on ILW1 C14 15 and ILW2 C14 63. In, Cr and Fe were detected only on ILW1 C14 15. ILW1 C3 12 has the highest C (60.4 at%) and the lowest O (3.1 at%) concentration. ILW2 C14 67 has the lowest C concentration (38.5 at%) and ILW1 C14 15 has the highest O concentration (11.0 at%).

Table 12: Changes in the surface morphology and the C/W, O/W and O/C ratios of the large areas of the samples from tile 5 W lamellae.

Exp. Period	W Lamella	Sample No	Surface morphology	Large Area Range EDS		
				C/W	O/W	O/C
ILW1	A23	1	Intact	1.72	0.19	0.11
	A23	7	Intact	1.71	0.25	0.15
	C3	12	Intact	1.65	0.09	0.05
	C14	15	Intact	1.09	0.27	0.24
ILW2	A23	48	Intact	1.31	0.13	0.10
	A23	51	Intact	0.80	0.10	0.13
	C13	61	No cracks	0.82	0.07	0.08
	C14	63	Reduction of cracks density and width	0.81	0.10	0.12
	C14	67	Reduction of cracks density and width	0.67	0.09	0.14
	C22	70	Reduction of cracks density and width	0.71	0.06	0.08

	C23	72	Reduction of cracks density and width	1.10	0.10	0.09
ILW3	A23	93	Intact	1.20	0.20	0.17

Table 12 presents the C/W, O/W and O/C ratios of the large area analysis. It is observed that the C/W ratio is reduced significantly in most of the samples in which the crack density and crack width has been decreased after plasma exposure, which means that on areas where we have melting the C is reduced.

6.4 X-ray Diffraction Results

The XRD spectra showed that W reference lamella crystallizes in bcc structure (Figure 208). No extra compound formation were detected.

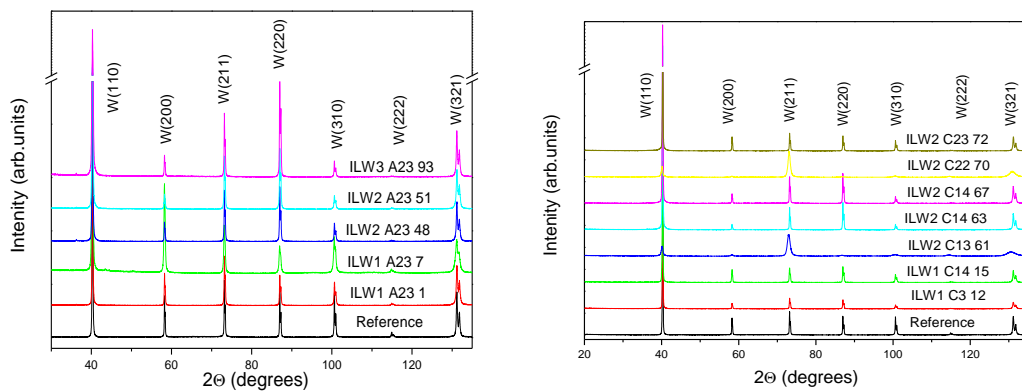


Figure 208: XRD spectra of the W lamellae samples from (a) stack A and (b) C.

6.5 Conclusions

Samples from different lamellae of the JET divertor tile 5 after ILW1, 2 or 3 experimental period were analysed using d-NRA, SEM with EDS, XRF and XRD. With the NRA measurements, Be, C and O amount and depth profile were determined. The C content of the different samples presents a wide range varying from $(1.4 \pm 0.2) \times 10^{17}$ at/cm² to $(25.5 \pm 3) \times 10^{17}$ at/cm². The Be amount presents values between 2.05×10^{17} at/cm² and 16.4×10^{17} at/cm² and the O content ranges from 1.9×10^{17} at/cm² to 13.8×10^{17} at/cm². The C and Be amount increases with the strike point time. Be deposition increases from the first to the second campaign and from the second to the third campaign. C deposition decreases from the first to the second campaign and increases from the second to the third campaign. Comparing the C and Be amounts of the current work with those of Mayer et al [158] there is general agreement. The C and Be concentration is reduced similarly with depth, either smoothly or abruptly. The O depth profile is difficult to be determined and only two layers were detected.

The reference sample surface is rough with a network of micro-cracks. The samples from the A23 lamella and from the stack C after the first campaign present similar surface morphology as the reference. On the other hand, the micro-cracks of the samples from the stack C after the second campaign have been partially or totally covered by the melted W from the surface. Additionally, the surface of these samples is smoother than that of the reference one. On most of the surfaces

only O, C and W were detected -exception constitutes ILW1 C 15 where Ni, Al, Cr and Fe were also detected. However, focusing on the deposition areas plenty elements are observed: C, N, O, F, Na, Mg, Al, Si, Cl, K, Ca, Ti, Cr, Mn, Fe, Ni, Zn, Zr, Mo and W. In some areas one or more of these elements have significantly high concentration (for example Ti on ILW2 A23 48, Ca on ILW23 A23 51 and Al on ILW2 C14 63). The marker tiles have not suffered erosion higher than 6 μm as W top layer and the Ni interlayer were detected.

Chapter 7: Summary, Conclusions and Future Perspectives

The aim of the work is to investigate the effect of the interaction between the plasma and the PFMs at the JET tokamak having an ITER-like metallic wall (ILW), i.e. Be in the main chamber and W in the divertor. Be have been chosen due to the low Z in order to limit the dilution and the cooling of the plasma core. Additionally, Be presents low fuel retention –the main advantage over C, the previous wall material. Moreover, Be constitutes a good O getter reducing the O impurities in the plasma core. On the other hand, tungsten because of its attractive properties, such as high melting point, high thermal conductivity, low swelling, thermal stress and shock resistance, and high-temperature strength, is the prime candidate material for the first wall of the future fusion reactors. The interaction of the plasma – PFMs causes the erosion of the surface of the first wall. Physical and chemical sputtering as well as sublimation are the main mechanisms which cause the Be erosion, while tungsten is resilient against erosion due to a high threshold energy for physical sputtering. W is mainly eroded by impinging impurities such as C, Be and seeding gases, however it is still the optimum material choice to withstand erosion. The eroded atoms can be deposited/co-deposited on the same area or migrate via SOL and be deposited/co-deposited on different parts of the tokamak. The co-deposition may include materials from the first wall or the fuel itself (fuel retention). Retention can also be caused by the fuel implantation. Additionally, a part of eroded material can potentially enter the center plasma, diluting and cooling the plasma. Other results of the interaction are the melting of the surfaces and the formation of compounds.

In order to achieve our aim, samples from different areas of the ILW JET tokamak main chamber and divertor and after the various experimental campaigns were investigated using a suite of experimental techniques. ^2H micro- and milli-beam were used in order to determine the C amount, depth profile and spatial distribution as the $^{12}\text{C}(^2\text{H},\text{p}_0)^{13}\text{C}$ is the most suitable reaction for the C determination. Additionally, the Be and O amounts and depth profile were determine via $^9\text{Be}(^2\text{H},\text{p}_0)^{10}\text{Be}$ and $^{16}\text{O}(^2\text{H},\text{p}_0)^{17}\text{O}$ reactions, respectively. ^3H micro-beam was chosen to determine the D amount and spatial distribution via the $\text{D}(^3\text{He},\text{p}_0)^4\text{He}$ reaction. With the same beam the spatial distribution of the heavier detected elements was performed. The SEM technique was used to depict the morphology and the different phases on the surface of the investigated samples. The detection and the quantification of the elements on different phases were performed using the EDS technique. The quantification of elements in deeper layers was performed using XRF. The XRD was used to determine the compounds that have been formed during the plasma – PFMs interaction. Moreover, the differential cross sections of the ^2H reactions on Be were measured in order to have reliable quantitative results.

The differential cross sections of $^9\text{Be}(^2\text{H},\text{p}_0)^{10}\text{Be}$, $^9\text{Be}(^2\text{H},\text{p}_0)^{10}\text{Be}$, $^9\text{Be}(^2\text{H},\text{a}_0)^7\text{Li}$ and $^9\text{Be}(^2\text{H},\text{a}_1)^7\text{Li}$ reactions were determined in the energy range of 0.75-2.2 MeV and at detection angles of 120° , 140° , 150° , 160° and 170° . The target of the measurements was a Si_3N_4 membrane coated with a Be layer. P and O beam measurements were carried out in order to determine the thickness of the target and the cross section of the $^{\text{nat}}\text{Si}(\text{d},\text{d})^{\text{nat}}\text{Si}$ to determine the cross sections of the deuteron reactions on Be. From the results, it is clear that the B excitation level with energy of 16.4 MeV affects the cross sections. Additionally, we observe an agreement between the current results and those of A. S. Deineko et al [143] as far as the cross sections of the $^9\text{Be}(\text{d},\text{p}_{0,1})^{10}\text{Be}$ reactions are concerned, while for the $^9\text{Be}(\text{d},\alpha_{0,1})^7\text{Li}$ reactions the current results agree with those of A. Saganek et al [152]. For the validity of the results, the benchmarking was carried out using a sample consisting of bulk Be coated with a thin Au layer. The benchmarking shows that the energy dependence of the differential cross section is consistent with the acquired thick target spectra for

all the detection angles with the difference between the experimental and the simulated spectra not exceeding 10%.

Samples from the Be marker tiles (Ni interlayer between top beryllium layer and bulk beryllium) of the limiters of the JET tokamak main chamber exposed to the ILW1 or ILW2 campaigns were investigated. The C deposition and D retention and their spatial distribution on the PFSs and the castellation sides were determined. The C amount throughout the castellation sides from the PFS edge up to around 6 mm was determined with milli-beam. For each sample the C amount changes with the depth in the same way for the different castellation sides. Additionally, for the majority of the samples the C amount is higher on the castellation sides than on the PFS. The C spatial distribution -determined using micro-beam- on the castellation sides near the edge of the PFS (up to 1.5 mm) either stays constant or decreases with the depth. Moreover, C agglomerates were detected on two of the samples. No systematic differences are observed among castellation sides with different orientations to ion drift direction. The D retention is higher on the castellation sides than on the PFS for the majority of the samples. From ILW1 to ILW2 campaign the deuterium retention on the PFSs increases, while on the castellation sides decreases. The D distribution on the PFS is homogeneous while on the castellation sides decreases with depth for the large majority of the samples. Additionally, the carbon amount is, in general, higher than the deuterium one. No systematic correlation between the C and the D amount has been observed. The distribution of heavier elements was depicted using the PIXE technique. On the PFSs only Ni presents inhomogeneous distribution where an agreement between the PIXE maps and the SEM images is observed. On the castellation sides a strip rich in Al, Cl, Ca, Mo and W were detected at depths up to about 200 μm . Combining the NRA spectra, the XRF results and the SEM images and EDS quantification, the erosion and the deposition areas were assessed. We conclude that the deposition increases with the decrease of the erosion. BeO was detected on all samples, while BeNi was not detected on samples that have suffered enhanced erosion.

Samples from the IWC and DP of the JET tokamak main chamber after ILW3 or ILW1-3 were investigated. The highest C and O amounts are observed on the surface of the ILW3 IWC samples. Their surfaces are rough and unchanged from the interaction with plasma. Moreover the Inconel substrate of ILW3 IWC was detected unchanged. Sample from the DP exposed to three experimental campaigns have the lowest C and O amount and have suffered melting on a macroscopic scale. The samples from the DP after the third campaign present oriented strips on their surface.

W samples from tile 5 of the JET tokamak divertor exposed to ILW1, ILW2 or ILW3 campaigns were investigated. Two of the investigated lamellae consist of a molybdenum interlayer between top tungsten and bulk tungsten in order to assess the surface erosion. In the majority of the samples the C amount is lower than the Be and the O one. On all the samples from A23 lamellae and from stack C after the first campaign the O amount is higher than that of Be, while the opposite is true for the stack C after the second campaign. Additionally, the C and Be amounts increase with the strike point time. The C amount decreases from ILW1 to ILW2 but increases from ILW2 to ILW3. The Be amount increases from the first to the second campaign and from the second to the third one. The amount of O does not present any pattern throughout the different campaigns. The unexposed sample presents a rough surface with a network of micro-cracks. Similar morphology is observed on the surface of the samples from the A23 lamellae and the stack C after the ILW1 campaign. On the other hand, the surfaces of the samples from the stack C and the second campaign have suffered melting due to plasma interaction as they are smoother and the density and width of micro-cracks have been reduced. C, O and W are the detected elements on the macroscopic areas of the majority of the samples. Focusing on the deposition areas, plenty of elements were detected (C, N, O, F, Na, Mg, Al, Si, Cl, K, Ca, Ti, Cr, Mn, Fe, Ni, Zn, Zr, Mo and W)

some of which (Mg, Al, Si, Ca and Ti) have significantly high concentration (≥ 10 at%). With the XRF measurements, the Mo interlayer in the marker samples was detected indicating that these lamellae have not suffered enhanced erosion.

The current work constitutes the completion of a more general investigation of PFMs after the plasma exposure which started in 2014 with analysis of samples from the divertor of the ILW JET tokamak [159]. This investigation offers a comprehensive view of material deposition, fuel retention, erosion and changes of the surface morphology from different areas and campaigns of the ILW JET tokamak. Knowing that C retains high amounts of fuel, we decided to measure it with accuracy in different areas and correlate it with the deuterium retention. The sources of the C in the ILW JET tokamak are the C residuals from the C-wall and the CFC substrates of the W tiles from the divertor. So, C amount was quantified with accuracy, additionally its depth profile and spatial distribution were determined. The D amount and spatial distribution were also assessed. The correlation between the C deposition and D retention was investigated for first time in samples from the main chamber of ILW JET tokamak. The correlation of the light detected element amount (D, Be, C and O) with different conditions inside the tokamak -different experimental campaign, ion drift and strike point time- was also investigated. The relative concentration of all detected elements was assessed, focusing on the deposition areas. Additionally, the changes of the surface morphology were assessed and the compound formation due to plasma exposure was determined. The differential cross sections of the deuteron reactions on Be were measured and checked with benchmarking in order to obtain reliable Be quantification with the NRA technique.

The NRA technique employing ^2H is suitable to quantify light elements: N, Be and C amounts are determined with high accuracy, while the determination of D and O amounts is difficult. ^3He beam has accuracy in D and Be, while C and O can be also detected and quantified but with less accuracy. Moreover the use of the micro-beam provides information about the spatial distribution. SEM with EDS depicted the surface morphology, the areas with the different phases and the relative concentration of the detected elements. XRF measures the relative concentration of heavy elements with accuracy in deeper layers. Moreover, the thickness of thin layers on samples with rough surface can be assessed. XRD presents the compound on the surface. It is clear that this set of complementary experimental techniques is a powerful tool to investigate PFMs not only from the JET tokamak but from any fusion device as well. Of course these techniques are not limited to material from fusion devices but they have also a widespread use.

According to the current study, the presence of C does not affect the D retention in the investigated samples. This investigation should be extended to samples from other areas of the JET tokamak. In this direction, investigation in controlled conditions simulating the conditions of a fusion machine should also be performed and complement the literature. Moreover, the other mechanisms of fuel retention namely co-deposition with beryllium or implantation should be also investigated. The current set of techniques is not appropriate to determine Be deposition on Be or to distinguish whether the detected elements have been implanted. Different experiments and techniques should be used for this investigation.

The different cross sections used in this work are reliable. However, it would be useful to measure the differential cross section of $\text{D}(^2\text{H},\text{p})^3\text{He}$ reaction as the data in the literature are not reliable and it would be very interesting to determine the C and D simultaneously with ^2H beam. Additionally, the research on the different cross section measurements for NRA and RBS techniques continues.

8. References

- [1] N. Khelurkar, S. Shah and H. Jeswani, *A review of radioactive waste management, 2015 International Conference on Technologies for Sustainable Development (ICTSD)*, Mumbai, 2015, pp. 1-6. [10.1109/ICTSD.2015.7095849](https://doi.org/10.1109/ICTSD.2015.7095849)
- [2] M. Kikuchi and N. Inoue, *Role of fusion energy for the 21 century market and development strategy with international thermonuclear experimental reactor*, 2009.
- [3] K. Tokimatsu et al, *Energy analysis and carbon dioxide emission of Tokamak fusion power reactors*, Fusion Eng. Des. 48, 2000, 483-498. [https://doi.org/10.1016/S0920-3796\(00\)00157-5](https://doi.org/10.1016/S0920-3796(00)00157-5)
- [4] R. Toschi, *Nuclear fusion, an energy source*, Fusion Eng. Des. 36, 1997, 1-8 [https://doi.org/10.1016/S0920-3796\(97\)00007-0](https://doi.org/10.1016/S0920-3796(97)00007-0)
- [5] https://commons.wikimedia.org/wiki/File:Binding_energy_curve_-_common_isotopes.svg
- [6] <https://www.iter.org/sci/MakingitWork>
- [7] M. Rubel, *Structure Materials in fusion reactors: Issues related to tritium, Radioactivity and radiation-induced effects*, Fusion Sci. and Technol., 57, 2010, p. 474-482 <https://doi.org/10.13182/FST10-A9438>
- [8] M. Kikuchi, K. Lackner and M. Q. Tran, *Fusion Physics*, Vienna: International Atomic Energy Agency, 2012, ISBN 0978-92-0130410-0
- [9] H. Bethe, *Energy Production In Stars*, Physcal Review, Vol 55, Issue 5, 1939 pp. 434-456 <https://doi.org/10.1103/PhysRev.55.434>
- [10] <https://solarscience.msfc.nasa.gov/interior.shtml>
- [11] <https://lasers.llnl.gov/science/icf/how-icf-works>
- [12] L. L. Snead and M. Ferraris, 4.18 - *Carbon as a Fusion Plasma-Facing Material*, Comprehensive Nuclear Materials, Vol 4, 2012, p. 583-620 [10.1016/B978-0-08-056033-5.00119-1](https://doi.org/10.1016/B978-0-08-056033-5.00119-1)
- [13] R. Neu, *Tungsten as a Plasma Facing Material in Fusion Devices*, 2003
- [14] K. L. Wilson et al, *Beryllium-a better tokamak plasma facing material?*, J Vac. Sci. Technol A, 8, 1990. <http://dx.doi.org/10.1116/1.576843>
- [15] J.P. Coad et al, *Material migration and fuel retention studies during the JET carbon divertor campaigns*, Fusion Eng. Des 138, 2019, 78 <https://doi.org/10.1016/j.fusengdes.2018.10.002>
- [16] J. Roth et al, *Recent analysis of key plasma wall interactions issues for ITER*, J. Nucl. Mater. 390-391, 2009, 1-9 <https://doi.org/10.1016/j.jnucmat.2009.01.037>
- [17] G.F. Matthews et al, *Overview of ITER-like Wall Project*, Phys. Scr. T128, 2007, 137. <https://doi.org/10.1088/0031-8949/2007/T128/027>
- [18] V. Philipps et al, *Overview of the JET ITER like wall project*, Fusion Eng. Des., Vol 85, Issues 7-9, 2010, p. 1581-1586 <https://doi.org/10.1016/j.fusengdes.2010.04.048>
- [19] M. Rubel et al, *Overview of erosion-deposition diagnostic tools for the ITER-like Wall*, J Nucl. Mater. 438, 2013, S1204 – S1207 <http://dx.doi.org/10.1016/j.jnucmat.2013.01.266>
- [20] S. Brezinsek et al, *Fuel retention studies with ITER-Like Wall in JET*, Nucl. Fusion 53, 2013, 083023 <https://doi.org/10.1088/0029-5515/53/8/083023>
- [21] H. Meister, R. Fischer, L. D. Horton, C.F. Maggi, D. Nishijima and ASDEX Upgrade Team, Z_{eff} from spectroscopic bremsstrahlung measurements at ASDEX Upgrade and JET, Rev. Sci. Instrum. 75, 2004, 4097 <https://doi.org/10.1063/1.1787167>
- [22] C. H. Wu, U. Mszanowski, *A comparison of lifetimes of beryllium, carbon, molybdenum and tungsten as divertor armour materials*, J. Nucl. Mater. 218, 1995, p. 293 - 301 [https://doi.org/10.1016/0022-3115\(94\)00675-X](https://doi.org/10.1016/0022-3115(94)00675-X)
- [23] G. De Temmerman et al, *Data on erosion and hydrogen fuel retention in Beryllium plasma-facing materials*, Nucl. Mater. Energy 27, 2021, 100994 <https://doi.org/10.1016/j.nme.2021.100994>

-
- [24] G. Pintsuk, Tungsten as a Plasma-Facing Material, *Compr. Nucl. Mater.* 4, 2012, 551-581
- [25] J. Roth et al, *Recent analysis of key plasma wall interactions issues for ITER*, *J. Nucl. Mater.* 390-391, 2009, p. 1 – 9 <https://doi.org/10.1016/j.jnucmat.2009.01.037>
- [26] H. Maier et al, *Tungsten and Beryllium Armour Development for the JET ITER-like Wall Project*, *Nucl. Fusion* 75, 2007, 222 <https://doi.org/10.1088/0029-5515/47/3/009>
- [27] L. Dittrich et al, *Fuel retention and erosion-deposition on inner wall cladding tiles in JET-ILW*, *Phys. Scr.* 98, 2021, 124071 <https://doi.org/10.1088/1402-4896/ac379e>
- [28] C. P. Lungu et al, *Beryllium coatings on metals for marker tiles, at JET: development of process and characterization layers*, *Phys. Scr.* T128, 2007, 157-161 <https://doi.org/10.1088/0031-8949/2007/T128/030>
- [29] <https://www.iter.org/newsline/-/2516>
- [30] J. Roth, *Erosion and impurity production of C and Be: a comparison*, *J. Nucl. Mater.* 145 – 147, 1987, p. 87 – 95 [https://doi.org/10.1016/0022-3115\(87\)90313-8](https://doi.org/10.1016/0022-3115(87)90313-8)
- [31] M. Rubel et al, *Fusion Neutrons: Tritium Breeding and Impact on Wall Materials and Components of Diagnostic Systems*, *J Fusion Energ* 38, 2019, 315 – 329 <https://doi.org/10.1007/s10894-018-0182-1>
- [32] W. Eckstein, *Calculated Sputtering, Reflection and Range Values*, *Materials Science S36*, 2002, p. 313
- [33] J. Roth et al, *Flux dependence of carbon chemical erosion by deuterium ions*, *Nucl. Fusion* 44, 11, 2004, L21 – L25 <https://doi.org/10.1088/0029-5515/44/11/L01>
- [34] R. A. Pitts et al, *Edge and divertor physics with reversed toroidal field in JET*, *J. Nucl. Mater.* 337 – 33, 2005, p. 146-153 <https://doi.org/10.1016/j.jnucmat.2004.10.111>
- [35] K. Heinola et al, *Fuel retention in JET ITER-like Wall from post-mortem analysis*, *J. Nucl. Mater.* 463, 2015, p. 961 - 965 <https://doi.org/10.1016/j.jnucmat.2014.12.098>
- [36] K. Heinola et al, *Long-term fuel retention in JET ITER-like wall*, *Phys. Scr.* T167, 2016, 014075 (7pp) <https://doi.org/10.1088/0031-8949/T167/1/014075>
- [37] X. Litaudon et al, *Overview of the JET results in support to ITER*, *Nucl. Fusion* 57, 10, 2017, 102001 (41 pp) <https://doi.org/10.1088/1741-4326/aa5e28>
- [38] J. P. Coad et al, *Surface analysis of the tiles and samples exposed the first JET campaigns with the ITER-like wall*, *Phys. Scr.* T159, 2014, 014012 (5pp) [doi:10.1088/0031-8949/2014/T159/014012](https://doi.org/10.1088/0031-8949/2014/T159/014012)
- [39] K. Heinola et al, *Tile profiling analysis of sample from the JET ITER-like wall and carbon wall*, *Phys. Scr.* T159, 2014, 014013 <https://doi.org/10.1088/0031-8949/2014/T159/014013>
- [40] N. Catarino et al, *Assessment of erosion, deposition and fuel retention in the JET-ILW divertor from ion beam analysis data*, *Nucl. Mater. Energy* 12, 2017, 559-563 <https://doi.org/10.1016/j.nme.2016.10.027>
- [41] M. Mayer et al, *Erosion and deposition in the JET divertor during the first ILW campaign*, *Phys. Scr.* T167, 2016, 0144051 (9pp) <https://doi.org/10.1088/0031-8949/T167/1/014051>
- [42] J. Likonen et al, *Investigation of deuterium trapping and release in the JET divertor during the third ILW campaign using TDS*, *Nucl. Mater. Energy* 19, 2019, p. 300 - 306 <https://doi.org/10.1016/j.nme.2019.03.012>
- [43] P. Petersson et al, *Co-deposited layers in the divertor region of JET-ILW*, *J. Nucl. Mater.* 463, 2015, p. 814-817 <https://doi.org/10.1016/j.jnucmat.2014.12.077>
- [44] A. Baron-Wiechec et al, *Global erosion and deposition in JET with the ITER-like wall*, *J. Nucl. Mater.* 463, 2015, p. 157-161 <https://doi.org/10.1016/j.jnucmat.2015.01.038>
- [45] S. Krat et al, *Comparison of erosion and deposition in JET divertor during the first three ITER-like wall campaigns*, *Phys. Scr.* T171, 2020, 014059 (8pp) <https://doi.org/10.1088/1402-4896/ab5c11>
- [46] Y. Zhou et al, *Microanalysis of deposited layers in the inner divertor of JET with ITER-like wall*, *Nucl. Mater. Energy* 122, 2017, 412-417 <https://doi.org/10.1016/j.nme.2017.02.015>
- [47] Y. Oya et al, *Comparison of Hydrogen Isotope Retention in Divertor Tiles of JET with the ITER-Like Following Campaigns in 2011-2012 and 2015-2016*, *Fusion Sci. and Technol.* 76, 2020, 439-445 <https://doi.org/10.1080/15361055.2020.1716455>

-
- [48] Y. Hatano et al, *2D Tritium Distribution on Tungsten Tiles used in JET ITER Wall Project*, J. Nucl. Mater. 463, 2015, p. 966 – 969 <https://doi.org/10.1016/j.jnucmat.2014.12.041>
- [49] Y. Hatano et al, *Tritium distributions on W-coated divertor used in the third JET ITER-like wall campaign*, Nucl. Mater. Energy 18, 2019, p. 258-261 <https://doi.org/10.1016/j.nme.2019.01.001>
- [50] A. Widdowson et al, *Material migration patterns and overview of first surface analysis of the JET ITER-like wall*, Phys. Scr. T159, 2014, 014010 <https://doi.org/10.1088/0031-8949/2014/T159/014010>
- [51] I. Jepu et al, *Beryllium melting and erosion on the upper dump plates in JET during three ITER-like wall campaigns*, Nucl. Fusion 59, 2019, 086099
- [52] J. P. Coad, P. L. Andrew, A. T. Peacock, *Carbon deposition and hydrogen isotope retention in JET*, Phys. Scr. T81, 1999, 7-12 <https://doi.org/10.1238/Physica.Topical.081a00007>
- [53] M. Rubel et al, *Fuel inventory and co-deposition in grooves and gaps of divertor and limiter structures*, Phys. Scr. T111, 2004, 112-117 <https://doi.org/10.1238/Physica.Topical.111a00112>
- [54] J. P. Coad, M. Rubel, C. H. Wu, *The amount and distribution of deuterium retained in the jet divertor after the C and Be phases in 1994-1995*, J. Nucl. Mater. 241-243, 1997, 408-413 [https://doi.org/10.1016/S0022-3115\(97\)80073-6](https://doi.org/10.1016/S0022-3115(97)80073-6)
- [55] M. Rubel, J. P. Coad, R. A. Pitts, *Overview of co-eposition and fuel inventory in castellated divertor structures at JET*, J. Nucl. Mater. 367-370, 2007, 1432-1437 <https://doi.org/10.1016/j.jnucmat.2007.04.007>
- [56] M. Rubel, J. P. Coad, D. Hole, *Overview of long-term fuel inventory and co-deposition in castellated beryllium limiters at JET*, J. Nucl. Mater. 386-388, 2009, 739-732 <https://doi.org/10.1016/j.jnucmat.2008.12.287>
- [57] S. Krat et al, *Beryllium film deposition in cavity samples in remote areas of the JET divertor during the 2011-2012 ITER-like wall campaign*, Nucl. Mater. Energy 12, 2017, 548-552 <https://doi.org/10.1016/j.nme.2016.12.005>
- [58] S. Brezinsek, JET-EFDA contributors, *Plasma interaction in the Be/W environment: Conclusions drawn from the JET-ILW for ITER*, J. Nucl. Mater. 463, 2015, 11-21 <https://doi.org/10.1016/j.jnucmat.2014.12.007>
- [59] N. Catarino et al, *Deposition in the tungsten divertor during the 2011-2016 campaigns in JET with ITER-like wall*, Phys. Scr., Vol. 2020, Num T171, 2020 <https://doi.org/10.1088/1402-4896/ab4df7>
- [60] A. Hakola et al, *Effect of composition and surface characteristics on fuel retention in beryllium-containing co-deposition layers*, Phys. Scr. T171, 2020, 014038 (8pp) <https://doi.org/10.1088/1402-4896/ab4be8>
- [61] Y. Oya et al, *Comparison of Hydrogen Isotope Retention in Divertor Tiles of JET with the ITER-Like Following Campaigns in 2011-2012 and 2015-2016*, Fusion Sci. and Technol. 76, 2020, 439-445 <https://doi.org/10.1080/15361055.2020.1716455>
- [62] P. Stom et al, *Analysis of deposited layers with deuterium and impurity elements on samples from the divertor of JET with ITER-like wall*, J. Nucl. Mater 516, 2019, 202-213 <https://doi.org/10.1016/j.jnucmat.2018.11.027>
- [63] S. Moon et al, *Fuel inventory and impurity deposition in castellated tungsten tiles in KSTAR: experiment and modelling*, Phys. Scr. T171, 2020, 014049 (8pp) <https://doi.org/10.1088/1402-4896/ab51f4>
- [64] L. Sun et al, *Ex-situ diagnosis of deuterium retention and carbon deposition on shaped tungsten castellated blocks exposed in KSTAR by laser-induced breakdown spectroscopy*, Fusion Eng. Des. 173, 112811 <https://doi.org/10.1016/j.fusengdes.2021.112811>
- [65] Y. Oya et al, *Effect of carbon impurity reduction on hydrogen isotope retention in QUEST high temperature wall*, Fusion Eng. Des. 146, 2019, 1480-1484 <https://doi.org/10.1016/j.fusengdes.2019.02.110>
- [66] A. Koike et al, *Evaluation of hydrogen retention behaviour in tungsten exposed to hydrogen plasma in QUEST*, Nucl. Mater. Energy, 26, 2021, 100856 <https://doi.org/10.1016/j.nme.2020.100856>

-
- [67] D. Schlessner et al, *Hydrogen isotope inventories in the ASDEX-Upgrade tungsten coated divertor tiles*, J. Nucl. Mater. 266-269, 1999, 1296-1302 [https://doi.org/10.1016/S0022-3115\(98\)00570-4](https://doi.org/10.1016/S0022-3115(98)00570-4)
- [68] K. Sugiyama et al, *Deuterium inventory in the full-tungsten divertor of ASDEX Upgrade*, Nucl. Fusion 50, 2010, 035001 <https://doi.org/10.1088/0029-5515/50/3/035001>
- [69] V. Philipps et al, *Experiments with tungsten limiters in TEXTOR-94*, J. Nucl. Mater. 258-263, 1998, 858-864 [https://doi.org/10.1016/S0022-3115\(98\)00385-7](https://doi.org/10.1016/S0022-3115(98)00385-7)
- [70] T. Tanabe et al, *Material mixing on W/C twin limiter in TEXTOR-94*, Fusion Eng. Des. 49-50,2000, 355-362 [https://doi.org/10.1016/S0920-3796\(00\)00396-3](https://doi.org/10.1016/S0920-3796(00)00396-3)
- [71] M. Rubel et al, *An overview of fuel retention and morphology in a castellated tungsten limiter*, Fusion Eng. Des 83,2008, 1049-1053 <https://doi.org/10.1016/j.fusengdes.2008.05.011>
- [72] K. Krieger et al, *Formation of deuterium-carbon inventories in gaps of plasma facing components*, J. Nuc. Mater., 363-365, 2007, 870-876 <https://doi.org/10.1016/j.jnucmat.2007.01.155>
- [73] Y. Oya et al, *Enhancement of hydrogen isotope retention capacity for the impurity deposited tungsten by long-term plasma exposure in LHD*, Fusion Eng. Des. 88, 2013, 1699-1703 <https://doi.org/10.1016/j.fusengdes.2013.03.002>
- [74] Y. Oya et al, *Comparison of hydrogen isotope retention for tungsten probes in LHD vacuum vessel during the experimental campaigns in 2011 and 2012*, Fusion Eng. Des. 89, 2014, 1091-1095 <https://doi.org/10.1016/j.fusengdes.2013.12.018>
- [75] I. Bizyukov et al, *Principal processes occurring at simultaneous bombardment of tungsten by carbon and deuterium ions*, J. Appl. Phys., 102, 2007, 074923 <https://doi.org/10.1063/1.2786113>
- [76] V. Kh. Alimov et al, *Deuterium retention in tungsten exposed to low-energy, high-flux clean and carbon-seeded deuterium plasmas*, J. Nucl. Mater., 375, 2008, 192-201 <https://doi.org/10.1016/j.jnucmat.2008.01.008>
- [77] F. C. Sze et al, *Growth of redeposited carbon and its impact on isotope retention properties on tungsten in a high flux deuterium plasma*, J Nucl. Mater. 266-269, 1999, 1212-1218 [https://doi.org/10.1016/S0022-3115\(98\)00636-9](https://doi.org/10.1016/S0022-3115(98)00636-9)
- [78] Y. Ueda et al, *Deuterium permeation in tungsten by mixed ion irradiation*, Fusion Eng. Des. 87, 2012, 1356-1362 <https://doi.org/10.1016/j.fusengdes.2012.03.006>
- [79] Y. Oya et al, *Behaviour of Deuterium Retention and Microstructure change of Tungsten Simultaneously Implanted with Carbon and /or Helium Ions*, Materials Transaction 54, 2013, 430-436 <https://doi.org/10.2320/matertrans.MG201205>
- [80] M. Fukumoto et al, *Deuterium retention in tungsten coating layers irradiated with deuterium and carbon ions*, J. Nucl. Mater. 462, 2015, 354-359 <https://doi.org/10.1016/j.jnucmat.2015.02.041>
- [81] Y. Oya et al, *Behavior of hydrogen isotope retention in carbon implanted tungsten*, J. Nucl. Mater., 390-391, 2009, 622-625 <https://doi.org/10.1016/j.jnucmat.2009.01.175>
- [82] M. Poon, J.W. Davis and A. A. Haasz, *Effect of carbon pre-implantation on deuterium retention in tungsten*, J. Nucl. Mater. 283-287, 2000, 1062-1067 [https://doi.org/10.1016/S0022-3115\(00\)00167-7](https://doi.org/10.1016/S0022-3115(00)00167-7)
- [83] O. V. Ogorodnikova, *Deuterium retention in tungsten in dependence of the surface conditions*, J. Nucl. Mater. 313-316, 2003, 469-477 [https://doi.org/10.1016/S0022-3115\(02\)01375-2](https://doi.org/10.1016/S0022-3115(02)01375-2)
- [84] V. Kh. Alimov et al, *Retention of ion-implanted deuterium in tungsten pre-irradiated with carbon ions*, J. Nucl. Mater. 282, 2000, 125-130 [https://doi.org/10.1016/S0022-3115\(00\)00422-0](https://doi.org/10.1016/S0022-3115(00)00422-0)
- [85] T. Taguchi et al, *Dynamic deuterium recycling on tungsten under carbon-deuterium implantation circumstance*, J. Nucl. Mater. 438, 2013, 1117-1120 <https://doi.org/10.1016/j.jnucmat.2013.01.246>
- [86] D. A. Komarov et al, *Role of grain boundaries and carbon deposition in deuterium retention behavior of deuterium plasma exposed tungsten*, J. Nucl. Mater. 290-293, 2001, 433-436 [https://doi.org/10.1016/S0022-3115\(00\)00511-0](https://doi.org/10.1016/S0022-3115(00)00511-0)
- [87] S. Nagata et al, *Retention and release of deuterium implanted in W and Mo*, J. Nucl. Mater. 266-269, 1999, 1151-1156 [https://doi.org/10.1016/S0022-3115\(98\)00520-0](https://doi.org/10.1016/S0022-3115(98)00520-0)

-
- [88] R. A. Anderl et al, *Deuterium retention in W, W1%La, C-coated W and W₂C*, J. Nucl. Mater. 290-293, 2001, 38-41 [10.1016/S0022-3115\(00\)00622-X](https://doi.org/10.1016/S0022-3115(00)00622-X)
- [89] G. M. Wright et al, Carbon film growth and hydrogenic retention of tungsten exposed to carbon-seeded high density deuterium plasmas, J. Nucl. Mater. 396, 2010, 176-180 <https://doi.org/10.1016/j.jnucmat.2009.11.002>
- [90] W. Wang et al, Deuterium trapping in and release from tungsten carbide, J. Nucl. Mater. 241-243, 1997, 1087-1092 [https://doi.org/10.1016/S0022-3115\(97\)80199-7](https://doi.org/10.1016/S0022-3115(97)80199-7)
- [91] V. Kh. Alimov, *Deuterium Retention in Pure and Mixed Plasma Facing Material*, Phys. Scr. T108, 2004, 46-56 <https://doi.org/10.1238/Physica.Topical.108a00046>
- [92] J. P. Roszell, *D retention in C- and O-contaminated tungsten during D⁺ irradiation*, J. Nucl. Mater., 427, 2012, 193-199 <https://doi.org/10.1016/j.jnucmat.2012.04.004>
- [93] Y. Oya et al, *Impact of temperature during He⁺ implantation on deuterium retention in tungsten tungsten with carbon deposit and tungsten carbide*, Phys. Scr. T167, 2016, 014037 <https://doi.org/10.1088/0031-8949/T167/1/014037>
- [94] R. A. Anderl, G.R. Longhust, R.J. Pawelko and M.A. Oates, *Implanted Deuterium Retention and Release in Carbon-Coated Beryllium*, Journal of Fusion Energy, Vol. 16, Nos1/2, 1997 [10.1023/A:1022569130666](https://doi.org/10.1023/A:1022569130666)
- [95] M. I. Guseva, V. M. Gureev, L. S. Danelyan, B. N. Kolbasov, S. N. Korshunov, Yu. V. Sereda, V.G. Stolyarova, V.V. Zatekin, and V.S. Kulikauskas, Effect of Carbon on Accumulation of Deuterium in beryllium Irradiated with Stationary Plasma, Journal of Surface Investigation Vol. 2, No. 2, 2008, pp. 274-276 <https://doi.org/10.1134/S1027451008020201>
- [96] C. Porosnicu, A. Anghel, K. Sugiyama, K. Krieger, J. Roth, C.P. Lungu, *Influence of beryllium carbide formation on deuterium retention and release*, J. Nucl. Mater. 415, 2011, S713-S716 [10.1016/j.jnucmat.2010.12.238](https://doi.org/10.1016/j.jnucmat.2010.12.238)
- [97] S. Brezinsek et al, *Residual carbon content in the initial ITER-Like Wall experiments at JET*, J. Nucl Mater 438, 2013, p. S303 - S308 <https://doi.org/10.1016/j.jnucmat.2013.01.122>
- [98] A. F. Gurbich, *SigmaCalc recent development and present status of the evaluated cross-sections for IBA*, Nucl. Instr. Meth. B371, 2016, 27-32 <https://doi.org/10.1016/j.nimb.2015.09.035>
- [99] J. F. Ziegler, J. P. Biersack and U. Littmark, *The Stopping and Range of Ions in Solids*, vol. 1 of *The Stopping and Ranges of Ions in Matter*, Pergamon Press, New York, 1985, ISBN 008021603X
- [100] H. R. Verma, *Atomic and Nuclear Analytical Methods*, Springer, 2007, ISBN-10 3-540-30277-8, -13 978-3-540-30277-3
- [101] R. E. Philips and S. T. Thornton, *A FORTRAN PROGRAM FOR RELATIVISTIC KINEMATIC CALCULATIONS IN TWO-BODY NUCLEAR REACTIONS*, 1967, OAK RIDGE NATIONAL LABORATORY
- [102] Cheng Xu et al, *On the Electron-Transfer Mechanism in the Contact-Electrification Effect*, Advanced Materials 30 (15), 2018 <https://doi.org/10.1002/adma.201706790>
- [103] https://en.wikipedia.org/wiki/File:Van_de_Graaff_Generator.svg
- [104] V. E. Krohn, Emission of Negative Ions from Metal Surfaces Bombarded by Positive Cesium Ions, J. Appl. Phys. 33, 1962, 3523, <https://doi.org/10.1063/1.1702439>
- [105] <https://www.pelletron.com/products/snics/>
- [106] D. C. Faircloth, *Particle Sources*, Proceedings of the CERN-Accelerator-School: Introduction to Accelerator Physics, Chavannes de Bogis, Switzerland, 2021 <https://doi.org/10.48550/arXiv.2103.13231>
- [107] G. R. Choppin, J.- O. Liljenzin, J. Rydberg, *Radiochemistry and Nuclear Chemistry* (third Edition), 2002, 978-0-7506-7463-8
- [108] <http://www.microbeams.co.uk/index.html>
- [109] M. Bogovac et al, *Data acquisition and scan control system for nuclear microprobe and other multiparameter experiments*, Nucl. Instrum. Methods Phys. Sect., Sect. B, 89, 1994, 219-222 [https://doi.org/10.1016/0168-583X\(94\)95176-4](https://doi.org/10.1016/0168-583X(94)95176-4)
- [110] V. Kh. Alimov, M. Mayer, J. Roth, *Differential cross-section of the D(3He,p)4He nuclear reaction and depth profiling of deuterium up to large depths*, Nucl. Instr. Meth. Phys. Res. B, 234, 2005, p. 169 <https://doi.org/10.1016/j.nimb.2005.01.009>

- [111] N. P. Barradas et al, *Determination of the $9\text{Be}(3\text{He},\pi)11\text{B}$ ($i=0,1,2,3$) cross section at 135 degrees in the energy range 1-2.5 MeV*, Nucl. Instr. Meth. Phys. Res. B, 346, 2015, 21-25
<https://doi.org/10.1016/j.nimb.2015.01.037>
- [112] M. Mayer, *SIMNRA, a simulation program for the analysis of NRA, RBS and ERDA*, AIP Conference Proceedings, AIP, 1999, pp. 541–544. <https://doi.org/10.1063/1.59188>
- [113] N. Bohr, *On the Constitution of Atoms and Molecules*, Part I. Philos. Mag. 26 (151): 1-24, 1913 <https://doi.org/10.1080/14786441308634955>
- [114] E. Scerri, *The Electronic Configuration Model*, Quantum Mechanics and Reduction, Br. J. Philos. Sci. 42, 1991, 309-325 https://doi.org/10.1142/9781848164260_0003
- [115] U. Fano, *Gamma-ray attenuation, Part I: Basic processes*, Nucleonics 11 (8): 8-12; Part II: Analysis of penetration, Nucleonics 11 (9): 55-61, 1953
- [116] J. H. Hubbell (1969), *Photon Cross Sections, Attenuation Coefficients and Energy, and Energy Absorption Coefficients From 10 keV to 100 GeV*, National Bureau of Standards Report NSRDS-NBS 26, Washington, DC: Government Printing Office
- [117] O. Klein and O. Nishina, *On the Scattering of Radiation by Free Electrons According to Dirac's New Relativistic Quantum Dynamics*, Physik 52, 1929, 853—868
https://doi.org/10.1142/9789814571616_0015
- [118] J. M. Jauch and F. Rohrlich, *The theory of Photons and Electrons*, Cambridge: Addison-Wesley, 1955 <https://link.springer.com/book/10.1007/978-3-642-80951-4>
- [119] G. White-Grodstein, *X-ray Attenuation Coefficients from 10 keV to 100 MeV*, NBS Circular 583, 1957
- [120] XCOM: Photon Cross Sections Database <https://www.nist.gov/pml/xcom-photon-cross-sections-database>
- [121] R. Jenkins, et al, *Nomenclature System for X-ray Spectroscopy*, X-ray Spectrometry, Vol. 20, 1991,149-155 <https://doi.org/10.1002/xrs.1300200308>
- [122] NPL: National Physical Laboratory, table: X-ray adsorption edges and characteristic X-ray line energies (keV),
http://www.kavelaby.npl.co.uk/atomic_and_nuclear_physics/4_2/4_2_1.html
- [123] E. Haug, W. Nakel, *The Elementary Process of Bremsstrahlung*, World Scientific, 2004, ISBN 981-238-578-9
- [124] <http://amptek.com/>
- [125] H. R. Verma, *Atomic and Nuclear Analytical Methods*, Springer, 2007, ISBN-10 3-540-30277-8, -13 978-3-540-30277-3
- [126] G. F. Knoll, *Radiation detection and measurement*, USA: Wiley, 2000, ISBN: 9780471073383, 0471073385
- [127] Amptek Silicon Drift Detectors-Application Note AN-SSD-003. s.l. : Amptek Inc
- [128] R. Redus, Amptek Application Note XRF-1: XRF Spectra and Spectra Analysis Software, 2008
- [129] <https://www.amptek.com/>
- [130] NIST SRM 160b, https://www-s.nist.gov/srmors/view_cert.cfm?srm=160B
- [131] R. Browning et al, *Empirical from for the electron atom elastic scattering cross sections from 0.1 to 30 keV*, Journal of Applied Physics 76, 2016 (1994) <https://doi.org/10.1063/1.346400>
- [132] L. Reimer, *Scanning Electron Microscopy Physics of Image Formation and Microanalysis*. Munster : Springer, 1998. ISBN 978-3-642-08372-3.
- [133] M. Dufek, *The Quanta Inspect User Operation Manual*. s.l. : FEI COMPANY, 2005.
- [134] https://en.wikipedia.org/wiki/Scanning_electron_microscope
- [135] <https://www.matsusada.com/column/sem-tech2.html>
- [136] https://en.wikipedia.org/wiki/Scintillation_counter
- [137] B.D. Cullity, S.R. Stock, *Elements of X-ray diffraction*, Pearson: 2014, ISBN 10: 1-292-04054-8
- [138] A. P. Manage, *BSc Sem VI Solid state physics*, D.M.S. Mandal's B. K. College, Belgaum
- [139] S. Rath, *Comparison of CPFEM and spectral solution methods in prediction of strains near grain boundaries in a uniaxially loaded oligocrystalline tensile specimen*, thesis
<10.13140/RG.2.2.28150.32320>

-
- [140] T. Ishimatsu, et al., *Angular Distribution and Excitation Functions of the $Be^9(d,p)Be^{10}$ Ground-State Reaction*, J. Phys. Soc. Jpn 16, 1961, 367-371. <https://doi.org/10.1143/JPSJ.16.367>
- [141] E. Friedland, H. W. Alberts, J. C. van Staden, *Deuteron induced reactions on 9Be at low energies*, Jour. Zeitschrift fuer Physik 267, 1974, p. 97. <https://doi.org/10.1007/BF01668635>
- [142] I. I. Bondouk, F. Asfour, F. Machali, *An Experimental Investigation of the Reaction $^9Be(d,p_0)^{10}Be$ and $^9Be(d,p_1)^{10}Be$* , Jour. Atomkernenergie 24, 1974, 62.
- [143] A. S. Deineko, et al., *Features of Reaction $^9Be(d(pol),p)^{10}Be$ at low Polarized-Deuteron Energies*, Jour. Izv. Rossiiskoi Akademii Nau Ser. Fiz. 44, 1980, 2652.
- [144] M. Tsan, W.F. Hornyak, *B^{10} Levels from Elastic Scattering of Protons by Be^9* , Phys. Rev. 287, 1969, 1220. [10.1103/PhysRev.187.1220](https://doi.org/10.1103/PhysRev.187.1220)
- [145] N. Catarino, et al., *Determination of $^9Be(p,p_0)^9Be$, $^9Be(p,d_0)^8Be$ and $^9Be(p,a_0)^6Li$ cross sections at 150° in the energy range 0.5-2.35 MeV*, Nucl. Instr. Meth. B 371, 2016, 50-53. <https://doi.org/10.1016/j.nimb.2015.10.062>
- [146] Z. Liu, R. Wang, *Non-Rutherford elastic scattering cross sections for 170o backscattering of 0.15-3.00 MeV protons from beryllium*, Nucl. Instr. Meth. B 93, 1994, 404-408. [https://doi.org/10.1016/0168-583X\(94\)95626-X](https://doi.org/10.1016/0168-583X(94)95626-X)
- [147] N. Patronis, et al., *Study of $^{nat}Mg(d,d_0)$ reaction at detector angles between 90° and 170° , for the energy range $E_{d,lab}=1660-1990$ keV*, Nucl. Instr. Meth. B 337, 2014 97-101 <https://doi.org/10.1016/j.nimb.2014.07.027>
- [148] E. Ntemou, et al., *Differential cross-section measurements for deuteron elastic scattering on ^{nat}Si for elastic backscattering purposes*, Nucl. Instr. Meth. B 450, 2019, 24-30 <https://doi.org/10.1016/j.nimb.2019.08.032>
- [149] OriginPro, 8.5. OriginLab Corporation, Northampton, MA, USA
- [150] <https://www.nuclear-power.com/nuclear-power/reactor-physics/nuclear-engineering-fundamentals/neutron-nuclear-reactions/compound-nucleus-reactions/>
- [151] J. A. Biggerstaff, et al., *Differential cross sections for (d,a) and (d,t) reactions in Be^9* , Nucl. Phys. 35, 1962, 631-641. [https://doi.org/10.1016/0029-5582\(62\)90488-1](https://doi.org/10.1016/0029-5582(62)90488-1)
- [152] A. Saganeck, et al., *$^9Be(d,a_0)^7Li$ (ground State) and $^9Be(d,a_1)^7Li^*(470$ keV) Reactions In the 0.9-2.2 MeV Energy Range*, Jour. Acta Physica Polonica B 2, 1971. 473
- [153] V. Riccardo et al, *Design, Manufacture and Initial Operation of the Beryllium Component of the JET ITER-Like Wall*, Fusion Eng. and Des. 88, 2013, 585-589 <https://doi.org/10.1016/j.fusengdes.2013.01.084>
- [154] G. Arnoux, I. Balboa, M. Clever, S. Devaux, P. De Vries, T. Eich, M. Firdaouss, S. Jachmich, M. Lehnen, P. J. Lomas, G.F. Matthews, Ph. Martens, I. Nunes, V. Riccardo, C. Ruset, B. Sieglin. D.F. Valcarcel, J. Wilson, K-D Zastrow and JET-EFDA contributors, *Power handling of the JET ITER-like wall*, Phys. Scr. T159, 2014, 014009 <https://doi.org/10.1088/0031-8949/2014/T159/014009>
- [155] E. Pajuste et al., *Comparison of the structure of the plasma-facing surface and tritium accumulation in beryllium tiles from JET ILW campaigns 2011-2012 and 2013-2014*, Nucl. Mater. Energy 19, 2019, 131-136 <https://doi.org/10.1016/j.nme.2019.02.011>
- [156] J. Roth et al., *Oxidation of beryllium and exposure of beryllium oxide to deuterium plasmas in PISCES B 2013* J. Nucl. Mater. 438, 2013, S1044-S1047 <https://doi.org/10.1016/j.jnucmat.2013.01.228>
- [157] G. Pintsuk et al, *Metallography and mechanical parameters of plasma-exposed plasma-facing materials and components*, Phys. Scr. T171 (2020), 014042 <https://doi.org/10.1088/1402-4896/ab4d72>
- [158] M. Mayer et al., *Erosion and deposition in the JET divertor during the second ITER-like wall campaign*, Phys. Scr. T170, 2017, 014058 <https://doi.org/10.1088/1402-4896/aa8ff9>
- [159] A Lagoyanis et al, *Surface composition and structure of divertor tiles following the JET tokamak operation with the ITER-like wall*, Nucl Fusion 57, 7, 2017, 076027 (7pp) <https://doi.org/10.1088/1741-4326/aa6ec1>